Rita Joana Vaz dos Santos

TOWARDS AN EFFICIENT FILTRATION AND CHARACTERIZATION OF AIRBORNE NANOPARTICLES

· U C ·

UNIVERSIDADE DE COIMBRA

University of Coimbra

Faculty of Sciences and Technology

Department of Mechanical Engineering

Towards an Efficient Filtration and Characterization of Airborne Nanoparticles

Rita Joana Vaz dos Santos

Thesis presented for the degree of Doctor of Philosophy in the scientific area of Mechanical Engineering and the specialization of Nanomaterials and Microfabrication, submitted to the Department of Mechanical Engineering, Faculty of Sciences and Technology, University of Coimbra.

September 2016

Technical Sheet

Title: Towards an Efficient Filtration and Characterization of Airborne Nanoparticles

Author: Rita Joana Vaz dos Santos

Editor: Department of Mechanical Engineering, Faculty of Sciences and Technology of University of Coimbra

Cover: Nanotomographic image performed by FIB, of the nanoporous thin film deposited by F1 onto Anopore: AnoT_F1_2.55_89_60_O.

"I have not failed.

I've successfully discovered 10,000 things that won't work."

Thomas A. Edison

Acknowledgments

The PhD journey was an evolving process and an unforgettable experience. However, this work would not be possible without the support and help of several persons and entities.

Firstly, I would like to express my sincerest gratitude to my academic advisor, Professor Doctor Maria Teresa Vieira, for her guidance, encouragement and support, for opening me "the doors" of nanotechnology and for the efforts that she has made to create conditions to continue the scientific work, over all these years. Also, for her suggestions that are always the solution of everything and for letting me pursue my ideas.

I would also like to specially thank to all persons that actively contributed to this work:

To Professor Doctor Sandra Carvalho from the Centre of Physics of University of Minho for providing me the necessary resources to develop the porous anodic aluminum oxide membranes and her valuable suggestions.

To Professor Doctor Teresa Rosete from the Center for Neuroscience and Cell Biology (CNC) of University of Coimbra for her teachings and efforts in performing *in vitro* toxicity tests, and also to Isabel Ferreira for her help.

To Professor Doctor José Paixão from Physics Department of University of Coimbra and to Doctor André Cavaleiro for actively participating in the X-ray nanotomography characterization of the nanoporous thin films at European Synchrotron Radiation Facility (ESRF), from the collaboration on the proposal and the characterization of thin films at Grenoble, to all subsequent work on image processing.

To Professor Doctor Andrey Chuvilin from nanoGUNE who volunteered to perform the characterization by Focused Ion Beam (FIB) of the nanoporous structures and for the email discussions which gave me insightful perspectives.

To Professor Doctor João Gomes from Lisbon Engineering Superior Institute (ISEL) of Lisbon Polytechnic for lending equipment that were essential in the study of nanoparticles on industrial environments.

I would also to express my gratitude to the colleagues that have crossed my path in Centre for Mechanical Engineering of the University of Coimbra (CEMUC), for the friendship, support and contribution, each one of them in a different way.

I would also like to say a heartfelt thank you to my parents for the unconditional support and motivation in the less good times.

Last, but not least, I would like to thank to my husband for his technical, scientific and emotional support which contributed to keep my focus.

Resumo

Nos últimos anos, os avanços científicos e tecnológicos têm levado a uma maior presença de nanopartículas (NPs) nos espaços de trabalho de indústrias convencionais e de base nanotecnológica. Isto tem preocupado a comunidade científica, uma vez que as NPs representam potenciais efeitos nocivos para a saúde do ser humano e para o ambiente, devido ao seu "ultrapequeno" tamanho e "ENORME" área de superfície. Em todo o mundo os trabalhadores da indústria estão expostos diariamente a elevados níveis de NPs, que a longo prazo podem comprometer irreversivelmente a sua saúde. Assim, têm de ser tomadas medidas de proteção, apesar de no mercado não existirem soluções eficazes capazes de filtrar as NPs, em particular as de menor dimensão. O estudo realizado propõe novas soluções com estruturas nanoporosas capazes de filtrar eficientemente as NPs. Por outro lado, contribui com uma análise detalhada de ambientes ocupacionais, quantificando e recolhendo NPs, que permitiu não só a sua caracterização físico-química, mas também com recurso a metodologias *in vitro*, demonstrar o seu carácter toxicológico.

As estruturas nanoporosas foram produzidas por pulverização catódica em modo magnetrão por deposição de filmes finos de alumínio em substratos porosos, sendo os nanoporos criados através do método M (reduzindo o tamanho do poro do substrato) e do método F1 (controlando os parâmetros de deposição e a inclinação do substrato). O método F2 (co-deposição de YSZ+Sn com posterior remoção do material sacrificial (Sn)) não teve sucesso devido à ausência de porosidade aberta aquando do desaparecimento do material sacrificial ou pela formação de um óxido do material sacrificial. As estruturas porosas revelaram poros com tamanhos mínimos na ordem dos 20 nm (métodos M e F1). A deposição de filmes finos de Al em substratos porosos aumenta substancialmente a área de superfície e o volume dos poros, mantendo a porosidade aberta do topo até à base.

Uma série de estudos de monitorização de ambientes ocupacionais foi conduzida durante períodos de 24 horas, em indústrias baseadas em processos eletrolíticos aditivos (anodização e lacagem de alumínio) e subtrativos (electroerosão e maquinagem a laser). Em ambas ocorreu a presença de NPs não intencionais emitidas de processos convencionais, sendo que a concentração de NPs durante a electroerosão com elétrodos apresentou valores superiores àqueles recomendados como limiar provisório. A electroerosão por fio foi o processo que emitiu a maior concentração de partículas ($36{,}20 \times 10^6$ partículas/cm^3) com o menor tamanho médio (23 nm). Por este motivo, este processo de fabrico foi o escolhido para recolher as NPs para posterior caracterização. Estas estruturas nanoporosas retiveram partículas maiores que 20 nm com uma eficiência de cerca de 95%. As NPs recolhidas exibiam uma gama alargada de tamanhos (tamanho médio de 27 nm determinado por microscopia eletrónica de transmissão) e diferentes formas, estruturas e características de superfície.

Em termos da caracterização toxicológica, os ensaios preliminares *in vitro* em macrófagos Raw 264.7 demonstraram que para a concentração de NPs estudadas, houve produção de óxido nítrico, relacionada com mecanismos pro-inflamatórios. Contudo, não foram observados efeitos negativos na viabilidade celular.

Os resultados deste estudo contribuem para soluções eficazes de filtração de NPs, capazes de proteger a saúde dos trabalhadores, uma vez que a exposição a NPs, presentes em ambientes industriais convencionais, representa um risco inesperado.

Abstract

In the recent years, scientific and technological advancements have led to an increased presence of airborne nanoparticles (NPs) in conventional and nanotechnological industrial workplaces. This has concerned scientific community, since NPs represent potential harmful effects to the human health and to the environment, due to their "very small" size and "ENORMOUS" surface area. Worldwide, industrial workers are exposed every day to high levels of NPs that, at long term can irreversibly compromise their health. Thus, protective measures have be taken, despite the nonexistence in the market of efficient solutions, capable of filtering NPs, in particular the smallest ones. The conducted study proposes novel solutions with nanoporous structures capable of efficiently filtering NPs. In addition, it contributes with a detailed analysis of occupational environments, by quantifying and collecting NPs, which allowed not only their physicochemical characterization, but also through *in vitro* methodologies to demonstrate their toxicity.

Nanoporous structures were produced by magnetron sputtering through the deposition of aluminum thin films onto porous substrates, being nanopores created by method M (reducing the substrate pore size) and method F1 (controlling the sputtering conditions and the substrate tilt). Method F2 (co-deposition of YSZ+Sn with posterior removal of sacrificial material (Sn)) was unsuccessful due to the absence of open porosity when the loss of sacrificial material, or to the formation of an oxide of sacrificial material. Porous structures revealed pores with minimum sizes of about 20 nm (methods M and F1). The deposition of the Al thin films onto porous substrates substantially increases the surface area and the pores volume, while keeping the open porosity from top to bottom.

A series of monitoring studies of occupational environments was conducted during periods of 24 hours, in industries based on additive (anodizing and lacquering of aluminum) and subtractive (electrical discharge and laser machining) electrolytic processes. In both occurred the presence of unintended NPs emitted from conventional processes, with the concentration of NPs during sinker electrical discharge machining presenting higher values than those recommended as provisional limits. The wire electrical discharge machining was the process that emitted the largest concentration of particles (36.20×10^6 particles/cm^3) with the smallest average size (23 nm). For this reason, this manufacturing process was chosen to collect NPs for posterior characterization. Such nanoporous structures retained particles bigger than 20 nm with an efficiency of around 95%. The collected NPs exhibited a wide range of sizes (average size of 27 nm determined by transmission electron microscopy) and different shapes, structures and surface characteristics.

In terms of toxicological characterization, preliminary *in vitro* assays in macrophages Raw 264.7 demonstrated that for the concentration of NPs studied, these induced the production of nitric oxide, which is related to pro-inflammatory mechanisms. However, negative effects in the cellular viability were not observed.

The outcomes of this study contribute with effective solution of filtration of NPs, able to protect the health of workers, since the exposure to NPs, that are present in conventional industrial environments, represents an unexpected risk.

x

List of acronyms

AAO	Anodized Aluminum Oxide
AB	Anodizing Baths
AFM	Atomic Force Microscopy
ALD	Atomic Layer Deposition
AnoB	Anopore Bottom surface
AnoT	Anopore Top surface
BAuA	Federal Institute for Occupational Safety and Health
BET	*Brunauer, Emmett and Teller*
BSI	British Standard Institution
CCD	Charge-Coupled Device
CMAR	Carcinogenic, Mutagenic, Asthmagenic and Reproductive toxicants
CNTs	Carbon NanoTubes
DC	Diffusion Charger
DC sputtering	Direct Current sputtering
DLS	Dynamic Light Scattering
DMEM	Dulbecco's Modified Eagle Medium
DNA	DeoxyriboNucleic Acid
EDM	Electrical Discharge Machining
ELISA	Enzyme Linked Immunosorbent Assay
ELPI	Electrical Low Pressure Impactor
ELS	Electrophoretical Light Scattering
EPI	Epiphaniometer
EPMA	Electron Probe Micro Analyzer
ESRF	European Synchrotron Radiation Facility
FFF-ICP-MS	Field Flow Fractionation - Inductively Coupled Plasma - Mass Spectrometry
FIB	Focused Ion Beam
FTIR	Fourier Transform InfraRed
FWHM	Full width at half maximum
GDE	General Dynamic Equation
GLAD	Glancing Angle Deposition
HEPA	High Efficiency Particulate Arrestor
HXN	Hard X-ray Nanoprobe
ICSD	Inorganic Crystal Structure Database
ISO	International Organization for Standardization
LAL	*Limulus Amebocyte Lysate* test
LB	Lacquering baths
LDH	Lactate Dehydrogenase
LP	Lacquering Paint
LPCVD	Low Pressure Chemical Vapor Deposition
MTT	3-(4,5-dimethylthiazol-2-yl)-2,5-diphenyltetrazolium bromide
N/A	Not Applicable
N/D	Not Defined
NAS	Nanometer Aerosol Sampler
NIOSH	National Institute for Occupational Safety and Health
NPs	Nanoparticles
NRVs	Nano Reference Values
NSAM	Nanoparticle Surface Area Monitor
OAD	Oblique Angle Deposition
OECD	Organization for Economic Co-operation and Development
OELs	Occupational Exposure Limits

OPC	Optical Particle Counter
PCR	Precaution Characterization Ratio
PVDF	Polyvinylidene fluoride
REACH	Registration, Evaluation, Authorization and Restriction of Chemicals
RF	Radio Frequency
SAED	Selected Area Electron Diffraction
SEM	Scanning Electron Microscopy
SEM-EDS	Scanning Electron Microscopy - Energy Dispersive X-ray Spectroscopy
SER	Social and Economic Council
SF	Safety Factor
SMPS	Scanning Mobility Particle Sizer
SRB	Sulforhodamine B
STP	Standard Temperature and Pressure
TEM	Transmission Electron Microscopy
TEM-EDX	Transmission Electron Microscopy – Energy Dispersive X-ray
TEOM	Tapered Element Oscillating Microbalance
TUNEL	Terminal Uridine Nucleotide End Labeling
TWA	Time Weighted Average
UV/Vis	UltraViolet/Visible
XRD	X-Ray Diffraction
YSZ	Yttria Stabilized Zirconia

Contents

List of figures

List of tables

Introduction

Humans have been exposed since ever to nanomaterials, that according to the most recent European Commission definition "means a natural, incidental or manufactured material containing particles, in an unbound state or as an aggregate or as an agglomerate and where, for 50% or more of the particles in the number size distribution, one or more external dimensions is in the size range 1 nm – 100nm" [1].

In the last decades, industrial development and the nanotechnology evolution led to a large increase in the concentration of airborne nanoparticles (NPs) either unintended from conventional industry and daily life activities, or engineered from the nanotechnology industry. Millions of industrial workers worldwide are exposed to NPs, since industrial activities generate plenty of NPs, whatever is the dimension of the material used.

This fact has concerned the scientific community, since nanosized materials exhibit a significantly different behavior from the bulk materials. Nanomaterials are potentially toxic as by decreasing the size of a given material, it significantly increases its surface area per mass unit which may enhance the material reactivity and consequently its toxicity. When inhaled, NPs can cross the olfactory nerve and reach the brain, or through the respiratory tract penetrate into the alveoli. Due to their small size, they easily cross alveoli until the blood stream reaching tissues and organs [2].

Therefore, it becomes essential to study physicochemical characteristics of airborne NPs present in workplaces, especially according to 5 S's characterization: Size, Size distribution, Shape, Structure and Surface [3]. In addition to physicochemical characterization, also the *in vitro* toxicity of NPs must be assessed. According to the recent trend, *in vitro* tests are preferred over the *in vivo* tests due to the lower associated costs, no need of animals and rapid and reliable results. The effects of NPs at a cellular level should be evaluated by studying the cellular responses triggered in different human cell models. Although some toxicity studies have been conducted for several single nanomaterials, nanotoxicity studies of airborne NPs real samples are almost absent. When together, particles with different characteristics may behave differently than when present as a single particle. For example,

tungsten carbide as NPs has not acutely toxicity, according to *in vitro* tests of mammalian cells. However, in the same conditions, if these particles are mixed with NPs of Co in a system WC-Co, the toxicity effect increases significantly [4]. Therefore, there are many unanswered issues that must be addressed, since studies present in literature are insufficient in this subject.

Assuming the presence of potential toxic NPs in workplaces, control strategies and preventive measures must be taken, such as, the implementation of ventilation and air filtration systems and the use of adequate clothes, glasses and breathing respirators by the workers. However, the effectiveness of breathing respirators available on the market against NPs is not suitable for efficiently filtering NPs. Thus, it is imperative the emergence of scientific studies in this field, namely in what concerns the development of efficient and reliable nanoporous structures which can act as effective physical barriers to NPs, and to develop effective *in vitro* tests to assess their human toxicity.

The full characterization of airborne NPs will assist in making protective measures to be taken by workers, as well as the limits to which they can be exposed during working tasks. Thus, it will be possible to overcome the absence of definitive occupational exposure limits to NPs based on the reliable metrics (number), since for now only provisional limits are available. Moreover, *in vitro* studies will be a contribution in the development of predictive nanotoxicological models.

Motivation and goals

As the amount of NPs in the environment is rapidly increasing as a consequence of research, development of nanotechnologies, and conventional industrial processes, there are still many unanswered questions and concerns over their consequences for environment and human health. In this context, it is imperative to avoid the unnecessary exposure to NPs, by using effective filtration systems, while it is not well understood the underlying mechanisms on toxicity effects of NPs.

In the frame of the present thesis, there were three main goals to be achieved:

- Tuning nanoporous structures by magnetron sputtering using three different approaches, and then to assess the effectiveness of these structures against NPs. Nanoporous structures with open pores and with controlled size, shape and pore size distribution should be able to retain NPs and act as a nanoporous filter. The developed structures will be fully characterized, making possible to establish the best methodology for reproducibility, which implies choosing parameters to obtain the most promising filter. The possibility to control the morphology and porosity of thin films showed to be a promising strategy for a variety of applications.

- Monitoring airborne particles present in conventional industries. Particle size distribution, total number of particles and surface area deposited per human lung will be assessed. The provisional exposure limits present in literature will be applied to evaluate the workers exposure.

- Characterizing a set of metal-based NPs of realistic samples of NPs, collected from a specific real industrial environment. These NPs will be fully characterized physicochemically, based on 5 S's characterization. Furthermore, *in vitro* tests will be performed assessing the toxicity of different concentrations of NPs. Thus, these results may contribute to infer about the real risks of NPs to the human health.

Finally, it is expected that this work can provide scientific contributions in order to establish non-provisional number/surface-based occupational exposure limits of real workplaces environments, and in predictive nanotoxicological models.

Thesis outline

This thesis has four main chapters and a final section dedicated to the main conclusions and future work (Figure I. 1).
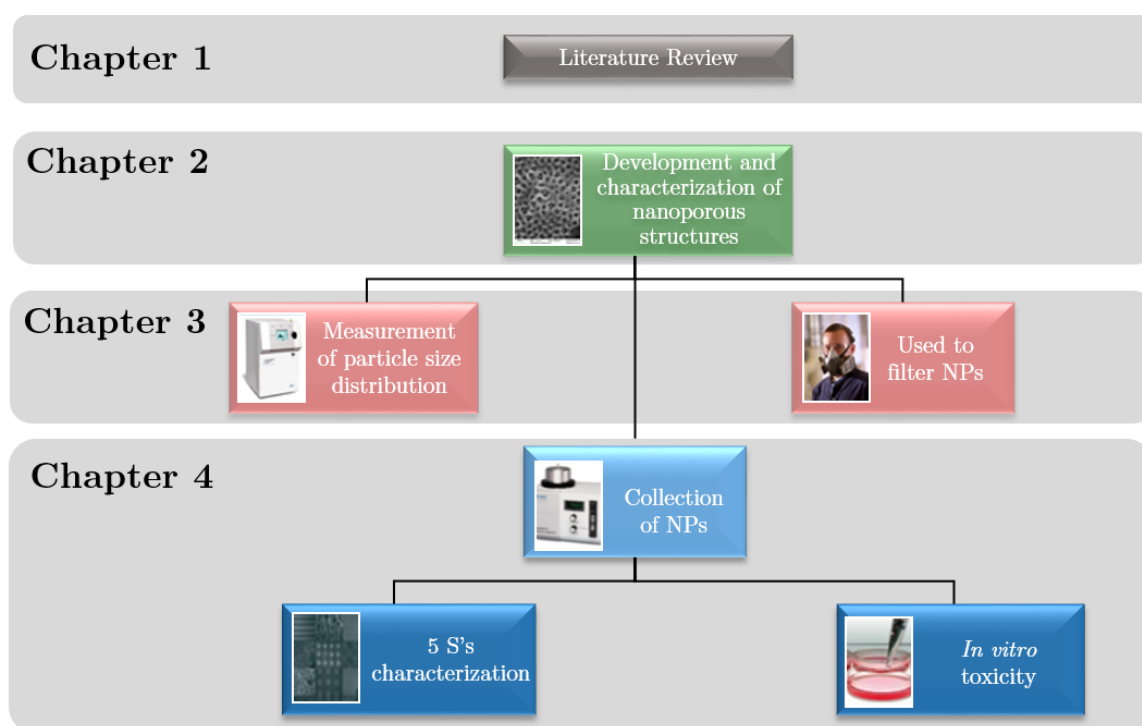
Figure I. 1 - Schematic illustration of the structure of the thesis.

Chapter 1 covers the literature review on NPs, their behavior and the current state of the art in quantification and characterization of NPs. Some works approaching the development of porous structures, are mentioned. Furthermore, a survey on interactions of nanomaterials with biological human system and related toxicity, and the available exposure limits are also provided.

The other chapters, covering different interconnected subjects, are self-contained including experimental procedure, results, discussion and key conclusions.

Chapter 2 describes the production and characterization of nanoporous structures, by three main approaches: reducing the substrate pore size; controlling sputtering conditions; and sputtering two materials.

In chapter 3, occupational environments and daily activities are monitored in terms of temporal size distribution, total number of particles and surface area deposited per human lung. Moreover, the capacity of filtration of nanoporous structures produced in chapter 2, is assessed.

Chapter 4 focuses on the characterization of airborne particles captured in occupational environments, according to 5 S's (size, size distribution, shape, structure and surface) and *in vitro* nanotoxicity.

Finally, the last section is dedicated to expose the major outcomes and conclusions and to point relevant future work.

Chapter 1
Literature Review

Nanoparticles are nanomaterials with a great industrial impact, due to their special properties, if voluntary produced. However, they can be unintentionally emitted from conventional activities. Due to their physicochemical characteristics, nanoparticles may represent potential toxicity to the health of human being and environment, and thus should not be neglected.

This chapter introduces recent applications of NPs and approaches the human exposure and the research efforts to avoid nanotoxicological effects. The behavior of NPs in airborne environments and the importance of assessing human exposure through a fully characterization, are also referred. Nanoporous filters must be used to collect airborne NPs and to play an important role in protecting workers against their adverse effects. Therefore, a review on nanoporous structures particularly developed by the sputtering technique is present. The importance of establishing safety standards and reference values for human exposition are also highlighted in this chapter, as well as, a brief description of several biological impacts in human.

1.1 Nanoparticles

Nanoparticles are present on the Earth for millennia, either from natural or anthropogenic sources. *Esquivel* and *Murr* [5] found aggregates of NPs, nanopowders and carbon nanotubes in an age-dated ice (10.000 years old) from Greenland. Furthermore, the Lycurgus Cup is an evidence of silver and gold NPs handling during the 3rd century AD. Examples of natural nanomaterials sources are volcanoes, forest fires and dust storms, whereas anthropogenic nanomaterials are arising from man-made processes, as products of combustion and manufacturing.

In the last years, technological advancements, in particular in nanotechnology field, led to a growing number of nanomaterials applications, especially NPs. Therefore, the term "nanoparticle" is frequently used nowadays and for this reason should be clarified. In Table 1. 1 are listed several definitions of "nanoparticle" implemented by diverse organizations and standardization committees, such as, International Organization for Standardization (ISO), Scientific Committee on Emerging and Newly Identified Health Risks (SCENIHR), European Union – Scientific Committee on Consumer Products (EU-SCCP) and International Union of Pure and Applied Chemistry (IUPAC).

Table 1. 1 - Overview on the definition of "nanoparticle".

Organization	Nanoparticle

ISO [6]	Nano-object with all external dimensions in the nanoscale where the lengths of the longest and the shortest axes of the nano-object do not differ significantly
	    Nano-object: discrete piece of material with one, two or three external dimensions in the nanoscale
	    Nanoscale: length range approximately from 1 nm to 100 nm

SCENIHR [7]	A discrete entity which has three dimensions of the order of 100 nm or less
EU SCCP [8]	Particle with one or more dimensions at the nanoscale Nanoscale: having one or more dimensions of the order of 100 nm or less
IUPAC [9]	Microscopic particle whose size is measured in nanometers, often restricted to so-called nanosized particles (<100 nm in aerodynamic diameter) Aerodynamic diameter: the size of a spherical particle of unit density

The growing number of nanomaterials applications leads to increase the human exposure. However, this increase is not only due to nanotechnology, but instead mainly to conventional industry.

As nanomaterials, which include NPs, behave differently from the bulk materials, they are very interesting in several applications mainly due to their ability to enhance the materials properties and to reduce raw materials and energy consumption. The main factors which can differentiate nano from bulk materials are the surface area and quantum effects. When particles get smaller, the relative surface area per unit of mass increases and consequently the number of atoms at surface too, leading to a change in the surface material reactivity. Furthermore, the confinement of the electrons in very small particles (few dozen nm) induces changes in their optical, electrical and magnetic behavior.

Among many fields of nanomaterials applications, currently the main explored ones are electronics, transports, telecommunications, biomedicine, cosmetics and others. Already in the beginning of this century, some potential uses of nanomaterials have been pointed (Figure 1. 1).

Nowadays, there is a special concern regarding nanoparticulate materials and their interactions with environment and biological systems. Since thin films are composed by nanostructured elements which are fixed, they are considered reliable. Conversely, free NPs can easily be released into environment and consequently reaching the human being in many ways. In the beginning of this century several researchers in this field, namely

Oberdörster [10] [11] and *Maynard* [12], had already made aware for the possible harmful effects of NPs in humans. Due to their small size, NPs can easily travel from the respiratory system crossing the alveolar barrier until the blood and thus reaching the body tissues and organs, since lungs are not able to filter such small particles.

Figure 1. 1 - Potential applications of nanomaterials [13].

Despite their importance and input on the society, the nanotoxicity studies go at a slow rate comparing to the number of publications for the possible applications of NPs. This is mainly due to their many different varieties, i.e., NPs can present different characteristics, such as chemical composition, morphology, size, agglomeration/aggregation state, structure, topography, and others, which could result in different interactions with biological systems. Thus, a full physicochemical characterization of NPs is essential to understand their toxicological effects. As ISO/TR 27628 [14] suggests, one of the first approaches to evaluate airborne NPs is through physical measures, namely particles concentration and specific surface area. Nevertheless, for toxicological studies further characterization must be performed, based on the principle of 5 S's characterization (Size, Size distribution, Shape, Structure and Surface).

According to the Elsevier Scopus database, the number of publications comprising the physicochemical and nanotoxicological characterization of NPs presented a rising trend since 2005. The search on Scopus database was conducted with the follow keywords: "nanotoxicology", "oxides", "metals", "carbon", "polymers", "multiple materials", "nanoparticles", "incidental" and "engineered".

Comparing particle types (Figure 1. 2 a)), in the last years the oxides are the most studied materials, and in the opposite side are the studies covering multiple materials. Despite some studies focus in particles classified as multiple, a large percentage of them involves the characterization of different NPs, but separately. Which means, there are very few studies characterizing physicochemical and/or toxicologically NPs of different materials when they are together.

The same database classifies particles as engineered (NPs produced for a given application) and incidental (unintended NPs mainly originated from industrial processes). The number of publications over the eleven years (Figure 1. 2 b)), clearly shows that engineered NPs are the focus of researchers, while the incidental ones are almost disregarded.
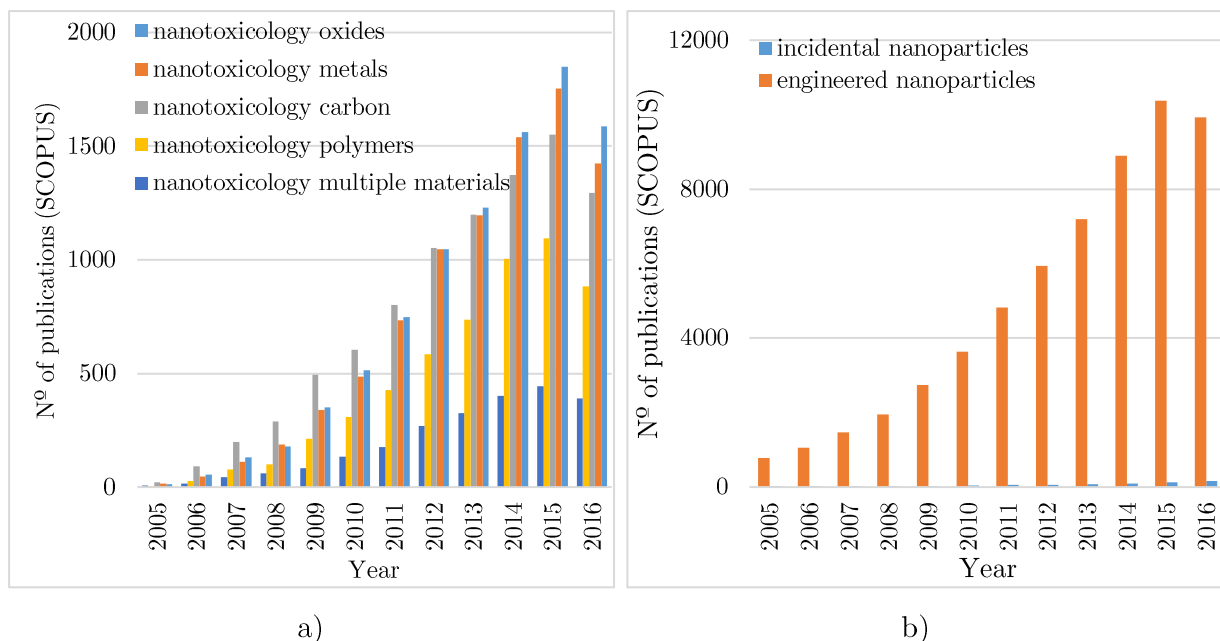
Figure 1. 2 - Statistic data comparing the number of publications over the years regarding: a) the types of NPs and b) the NPs production method.

1.2 Measurement and characterization of airborne nanoparticles

Since it is not yet established the relation between the potential toxicity of NPs and their properties, it is crucial to understand their behavior and to create methods for NPs measurements and characterization.

1.2.1 Behavior of airborne nanoparticles

Particles present in a fluid, e.g. air, move according three phenomena: diffusion, Brownian motions and external forces [15]. In diffusion, they are transported in a convective movement by the difference in air concentrations, from the highest to the lowest concentration. The Brownian motion explains the stochastic movement of particles subjected to collisions with molecules in the vicinities. Assuming Brownian motion, a given particle can be characterized by its diffusion coefficient (D) which is expressed by the Stokes-Einstein equation 1.1:

$$D = \frac{KT}{3\pi\eta d}$$

Eq 1. 1

where:
  K   Boltzmann constant
  T   absolute temperature
  η   viscosity of the fluid
  d   particle diameter

Airborne particles can also move in the air due to external forces, which include the gravity effect (presents a minimum effect, since NPs are almost absent of mass), electrical forces, aerodynamic effects and others [15].

Particles can collide between them which may lead to coalescence, by agglomeration or aggregation, and consequently to increase their diameter. While agglomerates are a group of particles joined by weak forces (as Van der Waals, electrostatic and surface tension), aggregates are particles held together by strong forces (ionic or covalent bonds) (Figure 1. 3).
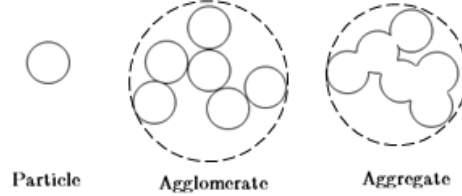
Figure 1. 3 - Scheme of different particles configurations.

As the size of one NP is closely related to its mobility, being inversely proportional, the smaller the particle is, the greater is its mobility. Thus, in nuclei mode NPs tend to agglomerate very quickly forming big particles. Increasing size, the mobility is reduced and the growth rate decreases. This fact defines the accumulation mode. For particles larger than 2000 nm, it prevails the coarse mode, which is characterized by the bonding of agglomerates to create aggregates and vice versa [16]. Figure 1. 4 shows an example of diesel engine concentration of particles according to the size and respective modes.
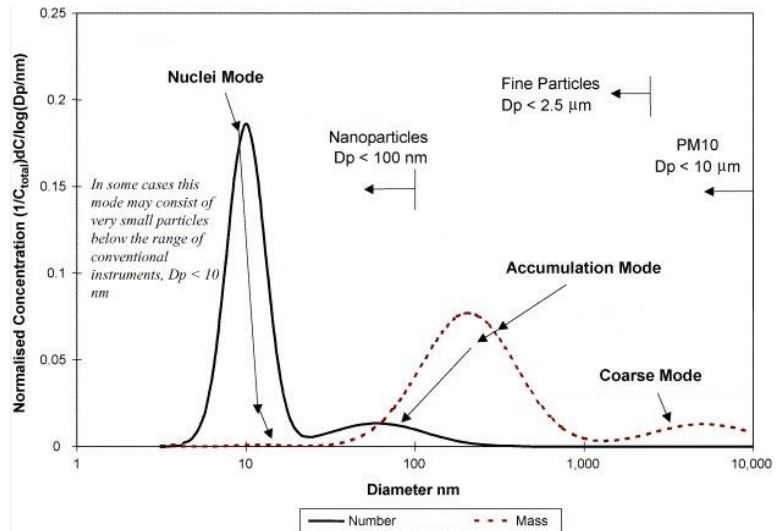
Figure 1. 4 - Concentration of particles of a diesel engine in different modes (adapted from [17]).

For the transport of particles dispersed in a fluid, Friedlander proposed in 1977 the first equation describing the process, so-called general dynamic equation (GDE) [18]. This well-known model was kept until present days as the most used model for aerosol dynamics, and it is expressed by equation 1.2:

$$\frac{\partial n_k}{\partial t} = -\nabla \cdot n_k v + \nabla \cdot D \nabla n_k + \left[\frac{\partial n_k}{\partial t}\right]_{growth} + \left[\frac{\partial n_k}{\partial t}\right]_{coalescence} - \nabla \cdot c n_k \qquad \text{Eq 1. 2}$$

where:

n_k concentration of particles with size k

t time

v particle velocity vector

D diffusion coefficient

c particle velocity vector associated with external forces

The GDE allows the determination of the concentration of particles, during a period of time, where $\nabla \cdot n_k v$ is related to the convective movement of particles, as described above, the diffusion movement. $\nabla \cdot D \nabla n_k$ refers to the Brownian motions of particles, while $\nabla \cdot c n_k$ is associated with external forces. $\left[\frac{\partial n_k}{\partial t}\right]_{growth}$ and $\left[\frac{\partial n_k}{\partial t}\right]_{coalescence}$ are elements which express the particles formation by growth - the gas-to-particles conversion (condensation or nucleation processes); and by coalescence - when they aggregate/agglomerate reducing their total number [19].

Meteorological conditions, in particular temperature and relative humidity, play also an important role on airborne particles concentration and size. These two factors exhibit anti-correlational behavior, so when increasing the temperature, relative humidity decreases, and vice-versa.

The decreasing temperature influences particles in two ways: increases the atmospheric supersaturation ratio which causes the formation of nuclei mode particles; promotes the condensation leading to the particles growth [20], [21] and [22]. Besides, other study [23] shows that the number of particles smaller than 100 nm rises with the increase of temperature.

Regarding relative humidity, according to several authors [22], [24] and [25], the higher the atmospheric relative humidity is, the greater the concentration of particles with bigger diameters. This effect is due to their hygroscopic ability, which results in the condensation of surrounding gaseous precursors, usually water vapor, causing the growth of smaller particles.

Since several factors influence the concentration and characteristics of particles in atmospheric environments, it is extremely important to develop strategies to evaluate *in situ* and in real-time the number of particles and their size distribution for which the human being are exposed to.

1.2.2 Exposure assessment - detection and quantification

Usually, in industrial environments there is a complex mixture of particles, from indoor and outdoor air, with different sizes, shapes and chemical compositions. They can be sourced of the industrial activity itself, but also originated by natural phenomena. Due to this complexity in airborne environments, quantitative determination of particles is an enormous challenge. Nowadays, several approaches can be taken for the detection of particles in a particular environment. Different instruments commercially available, allow the determination of particles in terms of mass, number or surface area. Examples of

equipment indicated for mass analysis are: the Electrical Low Pressure Impactor (ELPI), the Tapered Element Oscillating Microbalance (TEOM) and the piezobalance. In terms of number concentration, calculation devices as Optical Particle Counter (OPC), Scanning Mobility Particle Sizer (SMPS) and Electron microscopes (SEM and TEM) can be used. For surface area determination, the Epiphaniometer (EPI) or the Diffusion Charger (DC) are options. Table 1. 2 presents a survey of instruments used for NPs quantification, their operating principles and resolution, commercialized model and related works.

Table 1. 2 - Examples of available equipment for detection of particles.

Metric	Equipment	Operating Principle (in short)	Resolution (model/ company)	Ref.
Mass	ELPI	Airborne particles are collected by gravimetric size distribution into different substrates. Knowing the substrate weight, the particle mass is determined.	6nm - 10µm (ELPI+^{TM}/ Dekati)	[26] [27]
	TEOM	The air flows until a substrate on the tip of an oscillating glass tube. The resonance frequency of the tube is related with the mass of particles.	<1µm (1405-F TEOM / Thermo Scientific)	[28]
	Piezobalance	Particles are forced to deposit on a crystal. By determining the crystal resonance, their mass is calculated.	0.1 -10µm (3521 / Kanomax USA)	[29]
Number Concentration	OPC	By detection the light scattered when a particle passes through a beam of light, it is possible to estimate the particle size.	0.3 - 5µm (3887 / Kanomax USA)	[30] [31]
	SMPS	Through determining the mobility diameter of the particles, the equipment is able to provide the particle size distribution.	10-487nm (3034 / TSI)	[32] [33]
	Electron microscope (SEM/TEM)	By analyzing images and using appropriate software, it is possible to estimate the number of particles.	>0.1nm (H-9500 / Hitachi)	[34]
Surface Area	EPI	Particles are submitted to an environment with lead isotopes which adhere to their surface. Then, the radiation level is detected and correlated with total surface area of particles.	53nm - 2µm (developed in laboratory)	[35]
	DC	A corona needle assigns electric charge to the particles, being then trapped in a filter. Through the filter current, it is possible to determine the total surface area of the particles set.	10-1000nm (3550 / TSI)	[36]

Since the beginning of this century, there has been an intense debate within the scientific community concerning the establishment of the best metric to be applied in the determination of the particles content in different environments. For instance, *Oberdörster* [37] concluded that mass was not the best metric, since the same mass dose can be non-toxic for larger particles and become toxic for nanoparticles. Therefore, the latest standards [14] [38] already suggest as the best option, the application of parameters as the number of particles or even the surface area. However, in recent studies the mass remains the most widely used metric. This fact is mainly due to the easy application of this metric in toxicological tests, *in vitro* and *in vivo*, and consequently the easiness in establishing a relationship between dose and toxicity. In EuroNanoForum 2013 (Dublin), several researchers already mentioned the surface potential reactivity as the preferential metric to

be applied in a near future. As mentioned, the number of particles, including their size distributions, is one of the most suitable metrics for characterizing an environment. Thus, it was the metric selected to be applied in the present research work. Finally, Table 1. 3 summarizes some relevant studies focused on a quantitative determination of particles from selected environments.

Table 1. 3 - Studies focused on number concentration of NPs from different sources.

Processes		Size Range (nm)	Equipment	Total number (#/cm³)	Period of time	Ref.
Industrial Processes Emissions	Welding	5-1100	CPC GmbH	10^6	100 min	[39]
		10-487	SMPS TSI 3034	9.75-11.4×10^3	3 min	[40]
	Glaze ceramic firing	10-487	SMPS TSI 3034	2.5×10^5	3 min	[41]
	Wire EDM of Aluminum	10-1000	CPC TSI 3007	4.65×10^5	6 min	[42]
Engineered Nanomaterials	Test aerosol of NaCl	7-300	SMPS TSI 3071A/3010	3.19×10^4	20 min	[30]
	Test aerosol of TiO₂	7-300	SMPS TSI 3071A/3010	1.37×10^4	20 min	[30]
	Test aerosol of SiO₂	7-300	SMPS TSI 3071A/3010	9.2×10^3	20 min	[30]
	Test aerosol of Fe₂O₃	7-300	SMPS TSI 3071A/3010	10^4	20 min	[30]
Daily Life Activities	Cigarette	10-1000	CPC TSI 3007	1.1×10^6	1 cigarette	[43]
	Cigarette	5-350	SMPS+C 5400 Grimm	4.23×10^5	1 cigarette	[44]
	Burning candle	5-350	SMPS+C 5400 Grimm	1.3×10^6	1 candle	[44]
	Cooking	7.6-289	SMPS TSI 3936L85	0.03-5.03×10^4	1 min	[45]
	Office printer	7-3000	CPC TSI 3025A	3×10^3	8h	[46]
Transports	Ship emission	20-600	SMPS TSI 3081	2.1×10^5	ship exhaust event	[47]
	Aircraft emission	14-800	SMPS TSI 3936	2.6×10^4	8h	[48]
	Vehicle emission	10-290	SMPS TSI 3080L 3025A	2.29×10^5	2h	[49]

These studies show that NPs are present everywhere and therefore humans are constantly exposed to them. Their concentrations may vary enormously up to 10^6 particles/cm³ or more, depending on the measurement time and the range of particles size evaluated by the equipment.

1.2.3 Physicochemical characterization

In the exposure assessment as function of particles number, the most used parameter for obtain the size distribution is the diameter. This term is quite complex in nature, since the majority of the particles does not present a perfect spherical shape. Particles with low aspect ratio morphology can be presented as ovals, pyramids, cubes and others, while those with high aspect ratio include wires, helices, pillars, tubes... Then, it became indispensable to use a term that could be applied in all cases, the so-called equivalent diameter. The equivalent diameter can be defined as the diameter of a spherical particle which behaves

in the same way that the real one, under the same conditions. The agglomeration/aggregation state of the particles also contributes for the use of equivalent diameter, once particles are bonded for weak or strong forces, equipment consider it only as a single particle (Figure 1. 3). Understanding the particles surface behavior is another priority, since it is the surface that is in contact with organs/tissues and cells and it is usually the first characteristic responsible for the toxicological effect. The surface charge has also a significant role on the adhesion and the tendency to agglomeration or aggregation. On the other hand, chemical composition and structure are others characteristics that play an important role on the behavior of NPs. It is therefore of great importance to evaluate the main physicochemical characteristics of particles by means of a variety of analytical techniques and methods. In Table 1. 4 there is a list of some equipment and methods that can be used.

Table 1. 4 - List of equipment and methods available to characterize NPs.

Characteristic	Equipment/Method*
Shape	FFF-ICP-MS, SEM, TEM, AFM, DLS
Surface topography	SEM, TEM, AFM
Surface charge	AFM, Zeta potential, electrophoretic mobility
Surface chemistry	Optical method, XRD, HXN
Chemical composition (general)	FFF-ICP-MS, UV/Vis, EPMA, FTIR, TEM-EDX
Crystallographic structure	XRD, TEM
Aggregation/agglomeration state	DLS, AFM, SEM

*For abbreviations, please see page xi with acronyms

In terms of occupational exposure, it will be essential to fully characterize workplace environments in order to perceive the possible toxicological effects to the workers and therefore to develop control and preventive strategies that will lead to an exposure reduction.

1.3 Porous structures

The studies and development of porous structures to capture small airborne particles have started more than half a century ago. The first to be in the market was the "HEPA" (High Efficiency Particulate Arrestor), which was developed during the World War II to capture radioactive particles, specifically iodine. These particles occurred in the nuclear reactors vicinities and their diameters were around 300 nm. In 1960s the particles capture systems started being used in hospitals and later to protect atmospheres of computers apparatus [50]. Meanwhile, with technological innovation, particularly in the nanotechnology field, the scientific community became interested in the aerosol filtration by nanoporous structures for respiratory protection, air cleaning, processing of hazardous materials and removal of NPs. In the present study, the term nanoporous is related to materials having pores with at least one dimension ranging from 1 to 100 nm [51], which is not according to IUPAC nomenclature which considers 3 classes of porous materials: microporous (< 2 nm), mesoporous (2 - 50 nm) and macroporous (> 50 nm). These structures possess unique surface and structural properties, underlying their increasingly importance in several other applications, such as energy storages [52], catalyzers [53], filters [54], biomedical devices

[55] and sensors [56]. Although the study and development of nanoporous materials advanced at a slow rate, in the last decade there was a boom in this field reflected in the research work, with studies using several techniques and a wide range of materials.

In spite of some limitations, polymeric structures are one of the most commonly used in nanoparticles filtration. For instance, when exposed to hydrocarbons, many polymers can be swollen or even plasticized causing irreversible damages [57]. Typically, they are composed by fibers [58] enabling a wide range of pores sizes, but it is also possible to combine a polymer with carbon [59], carbon nanotubes (CNTs) [60] and NPs [61] [62].

Among ceramic nanoporous materials, the most common are definitely the silica [63] [64] [65]. Alumina [66] and titania [67] are either examples of ceramics usually employed as nanoporous structures. In contrast, the number of publications regarding the metallic porous structures is the lowest, being then the less studied porous structures.

The main characteristics of the materials of nanoporous structure are summarized in Table 1. 5. This information may be essential for the selection of the material to be used in a given application.

Table 1. 5 - Characteristics of nanoporous materials (adapted from [68]).

	Porosity	Strength	Thermal stability	Chemical stability	Costs	Life
Polymer	Low	Medium	Low	Low-medium	Low	Short
Ceramic	Low	Strong	Good	High	High	Long
Metal	Low	Strong	High	High	Medium	Long

Nanoporous structures can be a physical barrier built onto a porous substrate or alternatively, it can present a porous planar geometry that is prepared on any non-porous substrate with posterior substrate removal. Depending on the methods used to fabricate those porous structures, they can present a unimodal or a wide distribution of pores sizes. In literature, many methodologies are described for membranes or thin films manufacturing, by additive or subtractive processes [69] [70]. Some examples are listed below:

- Additive processes:
    Physical vapor deposition; chemical vapor deposition; spray deposition; atomic layer deposition; pulsed laser deposition; sol-gel.
- Subtractive processes:
    Chemical etching; electrochemical etching; e-beam etching.

1.3.1 Synthesis of nanoporous materials by electrochemical anodizing

The fabrication of porous structures by electrochemical anodizing, especially of aluminum, has been performed since 1950s [71], despite the process to achieve a self-ordered porous alumina structure has only been established in 1995 [72].

Nowadays, anodizing is a very popular method used to produce nanoporous structures despite its environmental impact, once it is simple, cheap, scalable and easily controllable regarding pore size and shape.

Porous Anodic Aluminum Oxide (AAO) membranes are formed by passing a direct current through an acidic electrolytic bath, usually with oxalic, phosphoric or sulfuric acids. The Al^{3+} ions, which are released by the application of the current on the Al (anode), and the O^{2-} ions from the water based electrolyte promote the formation of a barrier oxide layer (Al_2O_3). This barrier is continually regenerating and the oxide layer begins to present a semi-spherical shape, which is the bottom of the pores and from where they start growing (Figure 1. 5) [73].
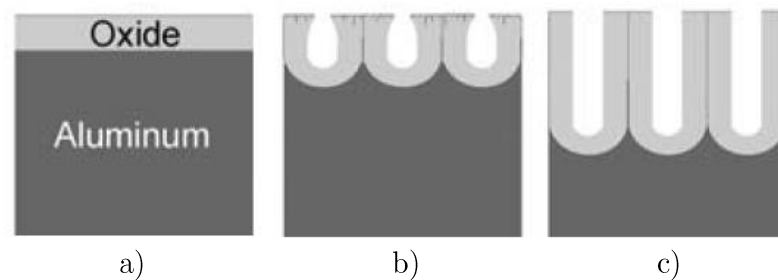
Figure 1. 5 - Mechanism of pore formation of AAO: a) barrier oxide layer formation; b) pore formation; c) pore growth (adapted from [72]).

The highly self-ordered porous AAO was firstly achieved by *Masuda* and *Fukuda* [72], by implementing a double anodizing process. The initial pores, with a less organized configuration, are removed by etching giving rise to an ordered semi-spherical pits. During the second anodizing, pits serve as seeds for the pores growth in an orderly manner.

Nevertheless, the formation of the porous nanostructure is closely related to a precise control of parameters during anodizing, such as: electrolyte acid, concentration, temperature and applied voltage/current.

Kushwaha [74] studied the influence of different electrolytes on the pore structure (Figure 1. 6) and AAO showed a typical morphology for each kind of acid. The use of sulfuric acid gives rise to small and not ordered pores, with thin walls. In contrast, phosphoric acid leads to the formation of bigger pores and larger walls. By the other hand, oxalic acid promotes the formation of a well ordered porous structure, with pore size and inter-pore distance in midway.
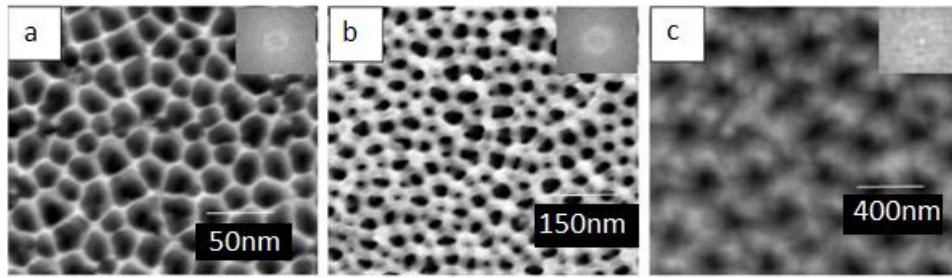
Figure 1. 6 - Morphology of AAO using different electrolytes: a) 0.3M sulfuric acid at 25 V (pore size – 33 nm; inter-pore distance – 63 nm); b) 0.3M oxalic acid at 40 V (pore size – 52 nm; inter-pore distance – 100 nm); c) 0.1M phosphoric acid at 195 V (pore size – 254 nm; inter-pore distance – 490 nm). [74]

Data from several studies [74 – 79] show the pore size dependence of anodizing voltage, type of electrolyte and respective concentration (Figure 1. 7).

For anodizing with phosphoric acid, high voltages are preferably applied, while sulfuric acid is used with low voltages. In spite of the different range of anodizing voltage used for each electrolyte, the pore size increases with the anodizing voltage.
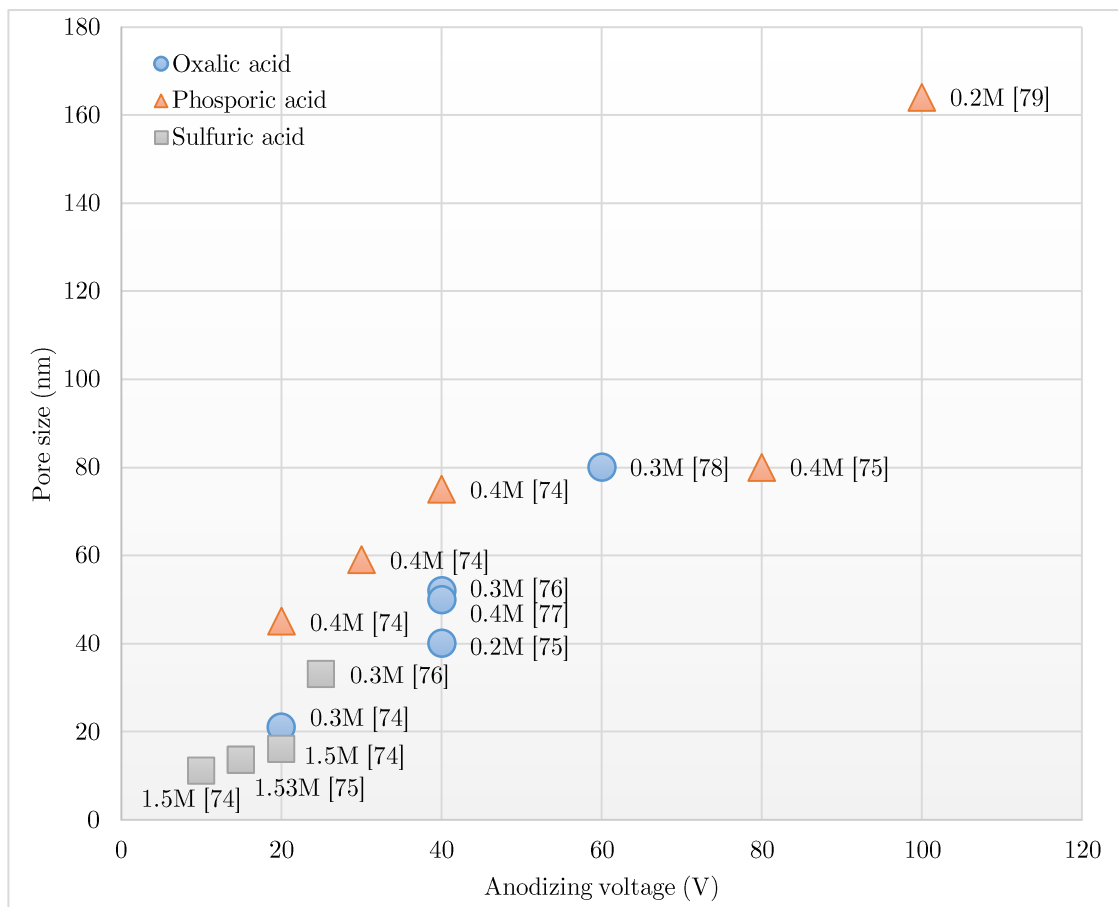
Figure 1. 7 - Pore size function of anodizing voltage, electrolyte type and concentration.

1.3.2 Synthesis of nanoporous materials by sputtering

Sputtering is a conventional process used for the deposition of thin films, with a long history in many applications. This technique is advantageous, since it is reproducible, several materials can be used and it is an environmentally friendly process. Sputtering allows the variation of a wide range of parameters and variables to attain different results, such as, substrate and deposition materials, deposition pressure, atmosphere gases, power density, temperature, substrate bias, distance target-substrate, substrate tilt. In general, this technique is used to deposit compact thin films with adhesion to substrate. However, with all these benefits, this technique is also an option for nanoporous materials applications. With this purpose, there are several approaches that can be considered for the production of nanoporous structures.

1.3.2.1 Nanoporous membranes by reducing the substrate pore size

Nanoporous materials can be produced by growing thin films on porous substrates and consequently narrowing the pore until reaching a nanometric size (Figure 1. 8). By taking advantage of the templates with uniform porous structures, thin films coating substrates exhibit self-organized pores which size depends on the thickness of the thin film. This method is widely used in a large number of application, being already referred in several patents.
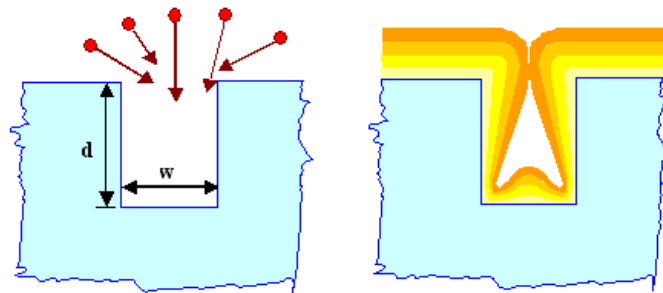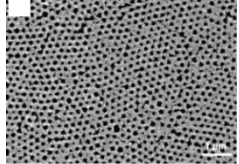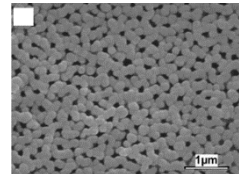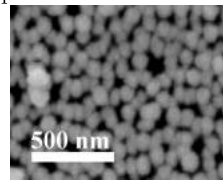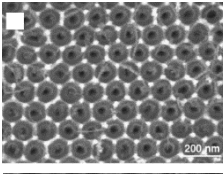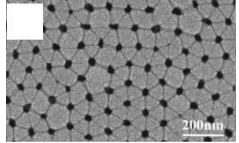
Figure 1. 8 - Thin film is deposited at the edge of the substrate, reducing the pore aperture. In case w<<d, the layer at the hole base becomes very thin or even inexistent [80].

US 7736724 B1 patent [81], titled "Fabrication of nanobaskets by sputter deposition on porous substrates and uses thereof", describes the fabrication of the so-called "nanobaskets". The inventors claim a method of coating porous substrates by sputtering, for example AAO, until just before pores close, resulting in nanoporous materials with high surface area.

Other example is the patent US 20120142016 A1 [82], named by "Array-based bioactivated nanopore devices", which nanoporous membranes are produced by sputtering a metal onto a porous structure, in order to reduce the hole sizes. This nanoporous structure is applied to biosensors, limiting the passage to only single biological molecules.
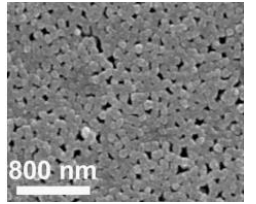
Table 1. 6 summarizes the content of different publications regarding porous structures developed by this method.

Table 1. 6 - Studies related to nanoporous structures created by reducing the substrate pore size.

Ref. Year	Substrate material/ pore size (nm)	Thin film material/ thickness (nm)	Deposition parameters	Summary	Pore size (nm) Image
[83] 2005	Porous polymer (removal of silica particles) / -	Au/Pd alloy (80/20) / 5-40	Sputtering N/D Electrical current density: 3 A/m² Pressure: 6.7 Pa Atmosphere: Ar	After sputtering, substrate is removed by oxidative degradation resulting in a freely suspended porous membrane. During the sputtering, part of the molecules is deposited on the top surface and others cross the pores without being deposited. As the thickness of the thin film increases, some cracks are formed due to its heterogeneity.	pore size: 270 ± 85nm Free-standing thin film (5nm) (SEM)
[84] 2008	AAO (commercially available) / 100-200	SiO₂ / 80-350	rf magnetron Power: 100 W Pressure:~1.33 Pa Distance target-substrate: 60 mm Atmosphere: Ar-O₂ (5:3 ratio) Temperature: 473 K Growth rate: 0.067 nm/s	The first adatoms go to inside walls and create a shadow effect which does not allow the entrance of more species into the pores. Thus, increasing the film thickness, the size of open pores decreases and are almost extinct.	pore size: <100 Thin film (250nm) deposited on porous alumina (SEM)
[85] 2008	AAO (commercially available) / 100	Pt / -	Sputtering N/D Current: 20 mA Distance target-substrate: 30 mm	Thin film grows until achieve a pore size of 20 nm after 20 min of deposition.	pore size: 20 - 90 nm Pt film on porous alumina (10 min) (SEM)
[86] 2010	AAO (developed in laboratory) / 60	Nb / 85 Hf / 85	Sputtering N/D Pressure: ~0.1 Pa Substrate rotation: 2 rpm Atmosphere: Ar Temperature: room temperature Growth rate: 0.017 nm/s	The AAO template is partially removed by etching. The pores present in Hf films seem to be bigger than in Nb films. This is explained by the high sticking factor of the Nb material, allowing also the deposition inside the pores which results in smaller pores sizes.	pore size: $d_{Nb} < d_{Hf}$ Nb and Hf films after partially substrate removal (SEM)
[87] 2015	AAO (developed in laboratory) / 67	TiO₂ / -	Sputtering N/D Power: 2000 W Atmosphere: Ar	The TiO₂ thin film is concentrated in the surface of the pores walls of AAO substrate. The pore size decreases, or may even close the pores, by increasing the deposition time.	pore size: - TiO₂ deposited on the AAO substrate (SEM)

continued

Table 1. 6 - Studies related to nanoporous structures created by reducing the substrate pore size.

Ref. Year	Substrate material/ pore size (nm)	Thin film material/ thickness (nm)	Deposition parameters	Summary	Pore size (nm) Image
[88] 2015	AAO (commercially available) / 200	Al (by sputtering) / 25 + HfO₂ (by ALD*) / 10	N/D	A thin film of aluminum is deposited onto AAO by sputtering, with a posterior coating of HfO₂ by ALD. The Al layer will act as an electrode to selectively separate ions of saline water producing pure water. The final pore size is reduced from 200 to 130 nm.	pore size: 130 nm Al/HfO₂ coating AAO (SEM)

*ALD – Atomic Layer Deposition

1.3.2.2 Nanoporous thin films by controlling sputtering conditions

The sputtering ability to produce nanoporous thin films with a controlled pore structure is due to the easy control of deposition parameters, such as: deposition rate, temperature, substrate bias, with or without substrate tilt.

A usual approach consists on the etching method by the application of a negative substrate bias voltage, which could cause the re-sputtering phenomenon, producing nanoporous structures. However, taking advantage of the shadowing effect to create nanocolumns is another common alternative. The limited surface diffusion of adatoms and/or the substrate tilt to an oblique position (oblique angle deposition) lead adatoms to stochastically form "islands" at the substrate surface (nucleation stage). As the thin film grows, these "islands" become columns which create a shadowing effect, introducing significant porosity in the thin film. The shadowing effect increases with the tilt angle, α of substrate (Figure 1. 9).

Both, oblique angle deposition (OAD) and glancing angle deposition (GLAD), being the last an extension of OAD wherein the tilted substrate rotates about its normal axis, present several advantages [89]:
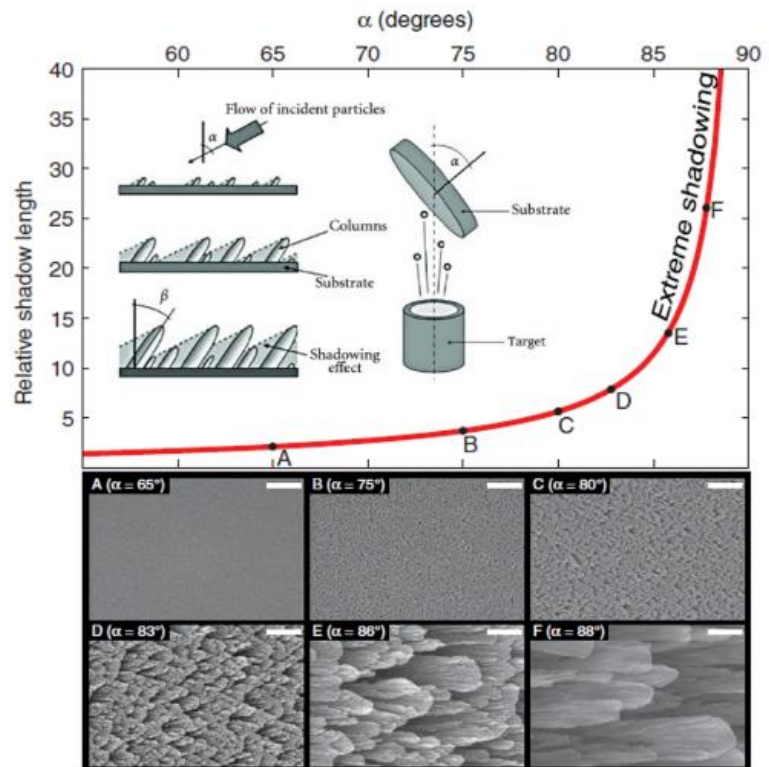
Figure 1. 9 - Shadowing effect due to the substrate tilt, in the presence of nanocolumns. The shadow length is increased with the tilt angle, α. The scale bars in all SEM images represent 100 nm (adapted from [88] and [89]).

- Morphological control at nanoscale enabling the formation of zigzag, helical and vertical nanocolumnar structures;
- Wide range of materials can be used;
- New thin films properties;
- Easy reproducibility, even at the industrial level.
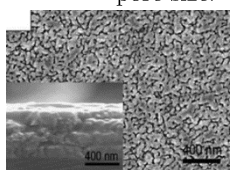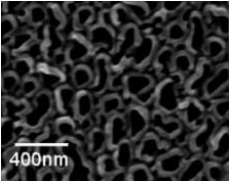
US 20090123517 A1 and US 20150027613 A1 are examples of patents related with shadowing effect used to create nanoporous structures.

In the patent named by "Medical devices for releasing therapeutic agent and methods of making the same" (US 20090123517 A1) [91], the authors claim a method to fabricate a medical device with a porous structure for controlled therapeutic agents delivery.

The patent titled "Electrochromic films and related methods thereof" (US 20150027613 A1) [92] describes a method to develop an electrochromic thin film by OAD or GLAD. The presence of nanocolumns leads to increasing the surface area, which contributes to a faster response of electrochromic devices.
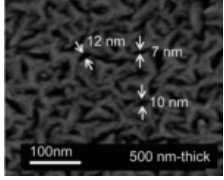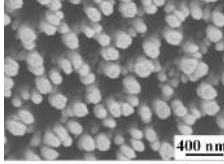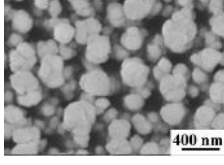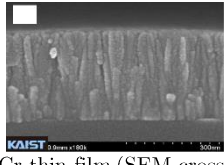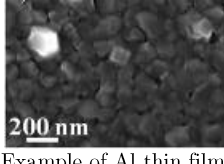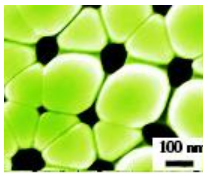
Several research works approach the development of nanoporous thin films by etching or shadowing effect, through the control of sputtering conditions (Table 1. 7).

Table 1. 7 - Studies related to nanoporous structures created by controlling sputtering conditions.

Ref. Year	Substrate material	Thin film material/ thickness (nm)	Deposition parameters	Summary	Pore size (nm) Image
etching					
[93] 2010	Silicon	CN$_x$ / -	MF magnetron (20 kHz) Power density: 650 W/m^2 Pressure: 0.5 Pa Distance target-substrate: 140 mm Atmosphere: N$_2$-Ar (2:5 ratio) Temperature: 573 K	When increasing the substrate bias from 0 to 150V, thin films porous structures are revealed. This can be explained by the re-sputtering phenomenon due to the high energy of Ar$^+$. This could easily broke unstable interface bonds creating the porous structure.	pore size: - Surface and cross section of the film deposited at -150V (SEM)
[94] 2012	Ti	Ta / 300	dc Power density: 1.36×10^4 W/m^2 Atmosphere: Ar Temperature: 373 K	The deposition of Ta under extremely high negative substrate bias (up to 800V) leads to the formation of a porous structure, which pore size increases as the applied bias is more negative.	pore size: 40-50 Ta porous thin film with a substrate bias of -800 V (SEM)

continued

Table 1. 7 - Studies related to nanoporous structures created by controlling sputtering conditions.

Ref. Year	Substrate material	Thin film material/ thickness (nm)	Deposition parameters	Summary	Pore size (nm) Image
shadowing effect – limited surface diffusion					
[95] 2012	Silicon coated in both sides with silicon nitride by LPCVD	Cr / 50-500	dc Pressure: 0.93 Pa Atmosphere: Ar	As the thin film thickness increases, prominent points continue to grow up forming columnar grains and hence the pores sizes increase. The substrate is after removed by etching, in order to make a free-standing membrane.	pore size: <10 500 nm Cr thin film (SEM)
shadowing effect – substrate tilt					
[96] 2008	Patterned Si (inverted pyramidal pit arrays)	Ta / 180-750 Al / 180-750	dc magnetron Power density: 1.13×10^5 W/m² Distance target-substrate: 100 mm Deposition angle: 84° Pressure: 0.39 Pa Atmosphere: Ar Substrate rotation speed: 80 rpm	The pores of Al thin films close easier than those of Ta. The lower melting temperature of Al leads to a large surface adatoms diffusion and consequently rod broadening by merging neighboring rods. This mechanism is responsible for the almost pores closure in Al thin films.	pore size: d_{Al}< d_{Ta}=280 Porous Ta and Al thin films with thickness 750 nm (SEM)
[97] 2010	Glass layer + electroplated Ti (20nm) layer+ electroplated Cu (1μm) layer	Cr / 300	dc Power density: 1.5×10^3 W/m² Pressure: 0.93 Pa Deposition angle: 45° Atmosphere: Ar	The deposition by dc sputtering is performed with the substrate in an oblique angle to create a shadow effect enhancing the formation of columnar grains.	pore size: ~10 Cr thin film (SEM cross section)
[98] 2011	SiO₂	Sn, Al, Au, Ru, W, RuO₂, SnO₂ and WO₃ / 50-350	dc and pulsed dc Power density: (1.42-14.22)$\times 10^4$ W/m² Distance target-substrate: 110 mm Deposition angle: 80° Pressure: 0.4 Pa Substrate rotation speed: 5 rpm	The columns size is closely related to the material melting point. Authors concluded that materials with the lowest melting point (Sn and Al) present coarse morphologies due to the high surface mobility of adatoms. Conversely, materials with the highest melting points (Au, Ru, W, RuO₂, SnO₂ and WO₃) exhibit small and isolated nanorods.	pore size: - Example of Al thin film deposited by GLAD (SEM)
[99] 2015	AAO	Mg₆₅Cu₂₅Y₁₀ / ~ 350	dc magnetron Pressure: 0.3 Pa Substrate rotation speed: 80 rpm	Thin films are deposited using the multi-targets glancing angle deposition. This configuration allows the control of pore size and shape and the chemical composition of the thin film.	pore size:~100 Nanopororous structure AAO/thin film (SEM)

1.3.2.3 Nanoporous thin films by co-deposition

The co-deposition by sputtering of two immiscible components, with posterior selective removal of one component is an approach widely disseminated in nanoporous thin films fabrication (Figure 1. 10). Usually, this removal is performed by dealloying the less noble component.
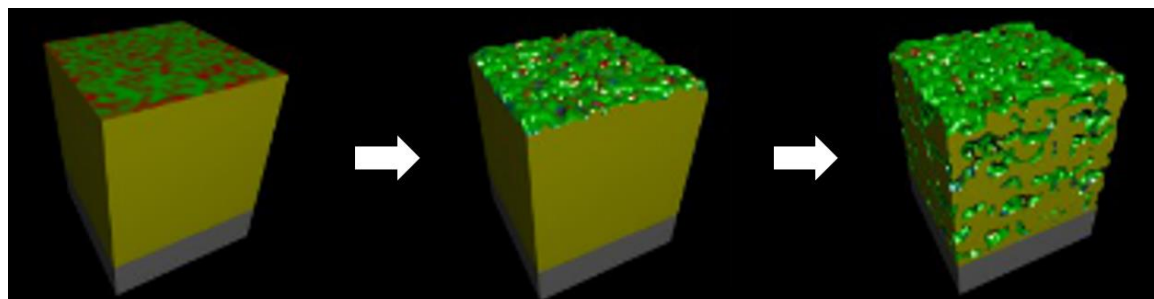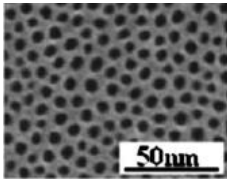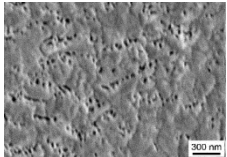
Figure 1. 10 - Schematic illustration of nanopores formation by removing one component [100].

Chemical and electrochemical dealloying are the most reported in literature (Table 1. 8), whereas few references reporting thermal dealloying are currently available [101].
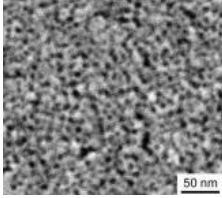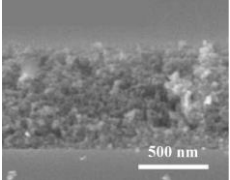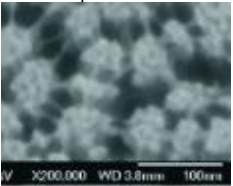
US 20060193889 A1 is a patent named "Nanoporous layers using thermal dealloying" for drug delivery applications [102]. The thermal dealloying is applied to introduce nanoporosity in a mixture or an alloy deposited, for instance, by sputtering. The heat source applied in vacuum for this thermal dealloying can be visible, infrared and ultraviolet radiations, inductive heat sources or ultrasound sources.

Table 1. 8 - Studies related to nanoporous structures created by sputtering co-deposition.

Ref. Year	Substrate material	Thin film material/ thickness (nm)	Deposition parameters	Summary	Pore size (nm) Image
Chemical dealloying					
[103] 2005	Silicon	Al-Si (Al composition 40 to 70 at.%) / 500	rf magnetron Power: 100 – 500 W Pressure: 0.1 – 0.7 Pa Atmosphere: Ar Temperature: room temperature – 573 K Growth rate: 0.125 – 0.767 nm/s	During the rf magnetron deposition, Al is arranged in nanometer sized cylinders perpendicular to the substrate. Al material is removed by a 5-wt% phosphoric acid etching solution. ↑ deposition rate, ↓ pores sizes ↑ substrate temperature, slightly ↓ pores sizes ↑ Al composition, ↑ pores sizes	pore size: 5-13 Freestanding thin film (SEM)
[104] 2007	coated silicon	Au and Ag / 1600	N/D	Ag is removed by dealloying in 32.5% HNO_3 aqueous solution. By decreasing the content of Ag, microcracks start to appear, being responsible for the film broken into small fragments.	pore size: 20-50 NiO thin film (SEM)

continued

Table 1. 8 - Studies related to nanoporous structures created by sputtering co-deposition.

Ref. Year	Substrate material	Thin film material/ thickness (nm)	Deposition parameters	Summary	Pore size (nm) Image
[105] 2010	Silicon coated with 2 nm Ta and 2nm Pd	Pd and Ni (18/82 at.%) / 90	rf magnetron Power: 35 W	The dealloying of thin film used sulfuric acid (25 vol.%) with surfactants as oleic acid and oleylamine. Surfactants and long ultrasonic agitation promote a fine porosity. The authors suggest that these parameters are responsible for the immobilization of the Pd adatoms blocking their surface diffusion.	pore size: 5 -20 PdNi thin film dealloyed with surfactants and ultrasonic agitated (SEM)
[106] 2013	Silicon	Ag/TiO$_2$ / 700-1800	rf magnetron Power density: Ag – varied; TiO$_2$ – 4.9×10^4 W/m^2 Pressure: 0.67 Pa Atmosphere: Ar Temperature: room temperature	Thin films were immersed in nitric acid (70 wt% HNO$_3$ and 30 wt% deionized water) to selectively remove Ag clusters, thus creating a TiO$_2$ nanoporous template.	pore size: 7.7 Nanoporous TiO$_2$ thin film (FE-SEM cross section)

Electrochemical dealloying

[107] 2015	Silicon	Pt$_{0.1}$Si$_{0.9}$ / 3200-3720	Sputtering N/D Power density: 1.1×10^5 W/m^2	Electrochemical dealloying removes Si from the thin film, leaving a nanoporous Pt structure. By increasing the dealloying current and time, the pores depth increases from 220 to 1110 nm.	pore size: 4-40 Dealloyed Pt thin film (SEM)

All the mentioned methods used to create nanoporous structures through sputtering produce relatively homogenous nanoporosity.

One of the limitations on producing nanoporous membranes concerns the need of a porous substrate. Commercially available porous materials, used as substrates, are very limited concerning the pores size and materials. Thus, in many cases it is firstly necessary the production of suitable substrates. In contrast, the development of nanoporous thin films onto bulk substrates for a specific application, namely for filtration of NPs, requires the detachment of the nanoporous thin film from the substrate. This action is frequently problematic, since usually nanoporous thin films are very thin and present low structural integrity.

It is important to underline that only few studies are performed with a view of a particular application in the filtration field. These are targeted for non-specified filtration or catalytic applications, and none was found referring the filtration of airborne NPs. Thus, sputtering shows to be a suitable technique for the development of nanoporous structures, although further studies are still necessary on the development of nanoporous filters capable of mechanically capturing nanosized particles.

1.4 Biological impact of nanoparticles in human being

NPs are a potential risk to human health, mainly due to their small size and large surface area. A substantial number of research groups are currently conducting studies to perceive the main routes of exposure, the possible health effects and the relationship between NPs characteristics and toxicity.

1.4.1 Exposure routes

The human being is constantly exposed to nanomaterials, whether they are natural or anthropogenic. The main nanomaterial portal routes into the human body are the respiratory, the gastrointestinal and the dermal routes. Once inside the body, NPs can reach any organ or tissue (Figure 1. 11).

The most common exposure route is the respiratory tract. Once inhaled, the deposition rate of NPs throughout the respiratory system is dependent on their size, according to a function. This function was firstly modulated in 1994 by International Commission on Radiological Protection [10] and predicts that in the range of 10-100 nm particles are mainly deposited in the alveolar region. As soon as particles get inside respiratory tract, the biological system triggers clearance mechanisms. In upper airways, particles are removed by mucociliary escalator, whereas for particles in lower respiratory tract,

Figure 1. 11 - Routes of human exposure to NPs (adapted from [108]).

macrophages will act in order to phagocyte them for future elimination [109]. However, most of the particles reaching alveoli are nanosized and those particles are not phagocyted because of their small diameters (<100 nm), allowing them to penetrate the alveolar barrier and to reach blood stream and lymphatic system [110]. However, if NPs concentration is too high, they tend to aggregate/agglomerate, generating particles bigger than 100 nm which will be then engulfed by macrophages.

Moreover, inhaled particles can be directly translocated to the brain via olfactory nerve, despite particles crossing this barrier have to present diameters compatible with olfactory axons size [111]. Additionally, NPs can also reach the brain via blood stream, although the blood-brain barrier is a physiological structure permeable to cationic components, since it presents a negative charge between blood vessels and brain. Therefore, only surface positively charged NPs are able to pass through this barrier [112]. Once NPs reach the brain, they can be responsible for neurodegenerative diseases, such as Parkinson's and

Alzheimer's [113]. Experiments with metallic NPs revealed that they can cause cellular damages affecting almost all components of the brain [114].

Regarding the blood stream route, NPs can interact with blood cells and/or be translocated to organs, such as, heart, liver, kidney and others. The uptake of NPs by red and white blood cells is dependent on the size of particles, however white cells (e.g. macrophages) are assisted by their phagocytic capabilities, that is absent in red cells [115]. In the case of platelets, the surface charge of particles dictates the effect. Positively charged NPs lead to platelet aggregation and also thrombosis [116]. When NPs reach the heart, they directly interact with its muscle cells, affecting the calcium balance, resulting in bioelectrical activities failure and muscle difficulty in contracting [117].

Endothelial cells surrounding organs can be tightly joint or not. In the case of their junctions are large enough to make possible to NPs cross this barrier, they enter into the organs. *Takenaka et al.* [110] observed silver NPs, after inhalation by rats, in their circulatory system, liver, kidney and heart. All these organs are targets for NPs absorption through gaps between endothelial cells, likewise lymphatic system. However, studies covering NPs uptake by lymphatic systems are more focused in therapeutics proposals. This is due to the higher accumulation of NPs, using as drug carriers, in lymphatic system than in blood stream, proving to be a more efficient method, for example, in cancer therapies [118].

NPs ingestion can also occurs by unintentionally transferring them from hands to the mouth, or through the inhalation process, which can lead to the passage of few NPs from airways to the digestive system. The majority of studies shows that most of the ingested NPs are excreted in feces or even through urine [11]. Conversely, some of them can be transferred to the blood and consequently, can reach several organs. NPs absorption via the gastrointestinal tract depends on their physicochemical characteristics, for instance, particle size. It is known that increasing NPs size, the uptake is decreased [119].

The absorption of NPs through the skin is still controversial. Despite, there are evidences that NPs can penetrate into the skin and eventually reach the blood stream [17], a more recent study, based on confocal microscopy, shows that NPs do not penetrate beyond the skin top layer and therefore do not reach deeper cells [120].

At a cellular scale, NPs can reach cellular structures, such as, cellular membrane, cytoplasm, mitochondria, lipid vesicles, along the nuclear membrane or even into the nucleus. Depending on size, particles can penetrate into the cells through ionic channels or membranes pores (for particles smaller than 1 nm), or they are engulfed by cells (bigger particles) [121]. When penetrating a cell, particles are able to induce several mechanisms which can lead to the cell death [122]. NPs may trigger the phagocytic process and consequently can be responsible for the production of free radicals which lead to the oxidative stress. In turn, the oxidative stress induces lipids, proteins and DNA oxidation leading to biological damage, as well as up regulates inflammatory factors generating the inflammatory process [123]. NPs can also be responsible for damaging the cellular membrane, altering metabolic activity, interfering with chromosome segregation, inhibiting the mechanism of DNA repair and altering gene expression [124].

1.4.2 Nanoparticles characteristics and related toxic effects

The unique physicochemical characteristics of NPs play critical roles in biological responses, which are associated with adverse health effects. In Table 1. 9 some characteristics of NPs and their related toxic effects are summarized, as well as, some case studies are mentioned.

Since each physicochemical characteristic contributes differently to the biological response, it is desirable a complete characterization of the material, particularly regarding their size, surface area, concentration, crystalline structure, and others.

Table 1. 9 - NPs physicochemical characteristics and toxicity effects.

Characteristic	Toxic Effect	Case Study
Dose	Typically with no correlation	The oxidation profile induced fluorescence for carbon black NPs versus particle dose is not homogeneous. The oxidation increases to a dose of approximately 50 µg/ml and then, increasing the dose, the oxidation response decreases [125].
Size	Smallest particles are typically the most toxic	Both Al_2O_3 (20nm) and TiO_2 (20nm) showed greater inflammatory response in rat lungs than Al_2O_3 (500nm) and TiO_2 (250nm) for the same dose of NPs [11].
Surface area	Largest surface areas are responsible for increased reactivity	
Concentration	High concentrations of NPs lead to particle aggregation, increasing the total size and reducing toxicity	Agglomerated/aggregated Ag NPs (with a final size >100nm) are easier phagocyted by rat alveolar macrophages, than primary NPs [110].
Crystalline structure	This characteristic influences differently cell responses	Human dermal and lung epithelial cells lines in contact with TiO_2 particles (rutile or anatase) have different responses. Anatase particles induce 100 times more toxicity than rutile [126].

1.4.3 Nanoparticles toxicity

The deep knowledge of toxicological effects of engineered or unintended NPs with enormous physicochemical characteristics combinations, may be an extremely demanding or an impracticable task regarding the time consumption, costs and experimental facilities.

The current scientific opinion agrees that the best option to determine NPs toxicity is by means of *in vitro* and *in silico* (performed in a computer or via simulation) methods, thus drastically reducing the need of animal testing. Meanwhile, *in vivo* tests are still performed by several research groups to study the toxicity of NPs.

In vitro research works present several advantages, such as, rapid and effective results with low costs associated (comparing to *in vivo* tests). Traditional *in vitro* tests cover the study of toxic cellular responses for different cell lines. Usually, the assessment of NPs toxicity is carried out in various cell lines with different doses and using diverse assays. Several tests can be used to assess NPs toxicity (Table 1. 10).

Table 1. 10 - *In vitro* assays for determining NPs toxicity [123].

Toxicity	*In vitro* assays*
Cytotoxicity	MTT, SRB, LDH, Colony forming efficiency test
Genotoxicity	DNA fragmentation assay
Gene mutations	Ames assay in *Salmonella typhimurium* and *Escherichia coli*
Apoptosis	Caspase-3 marker assay, TUNEL
Stress	Reactive oxygen species test
Inflammatory response	ELISA assay
Bacteria and endotoxins	LAL test
Hemolysis	Hemoglobin estimation

*For abbreviations, please see page xi with acronyms

A wide range of nanomaterials are subjected to nanotoxicological studies, using different methodologies and various cell lines. Nowadays it is a complex task to understand the real effects of NPs in human health, in order to perceive the mechanisms behind the toxicity of a particular NP or a set of combined NPs. As the focus of this study comprises the assessment of occupational environments, where metal-based NPs are present, in this section will not be addressed the biological impact of other nanomaterials, such as polymers or carbon based materials. Thus, a review regarding *in vitro* and *in vivo* toxicity responses of metal and metal oxide NPs in different cell lines and tissues, is outlined in Table 1. 11.

Table 1. 11 - General *in vitro* and *in vivo* toxicities of metal-based NPs [127].

NPs	Test	Comments
Au	*In vitro*	Many studies refer Au NPs as biocompatible, not cytotoxic or immunogenic. However a specific size of particles (1.4 nm) triggers toxicity, which is maybe related to the intercalation with DNA.
	In vivo	NPs accumulate rather in liver and spleen.
Ag	*In vitro*	Ag NPs induces oxidative stress, DNA damage and apoptosis. Cellular viability is dependent on the release of Ag^+ ions and particles size and shape.
	In vivo	Target organs are lungs and liver. Dose-dependent pulmonary function reduction is observed. In humans, Ag leads to skin and eyes gray discoloration, and when repeatedly inhaled may represent health risks.
Pt and Pd	*In vitro*	Pt NPs originate DNA damage, especially in smaller particles, not being observed further adverse effects. Pd NPs cause apoptosis and reduced cell viability in primary bronchial epithelial cells.
	In vivo	Inflammatory responses in mice lung tissues are triggered by Pt NPs. Nevertheless, there is no reference available in literature regarding i*n vivo* studies of Pd NPs.
Al and Al_2O_3	*In vitro*	Aluminum based NPs are generally nontoxic, however in extreme conditions (very high doses), NPs especially of Al are responsible for reducing cellular viability.
	In vivo	Inflammation and oxidative stress are observed in rats exposed to high doses of Al_2O_3.

continued

Table 1. 11 - General *in vitro* and *in vivo* toxicities of metal-based NPs [127].

NPs	Test	Comments
Cu and CuO	*In vitro*	Nanosized CuO is one of the most toxic particles, causing a massive oxidative stress and cell death due to NPs themselves and Cu ions. NPs of Cu are also toxic although the triggering mechanisms are not the same.
	In vivo	CuO NPs show to be the most toxic material among 16 different particles, via intratracheal instillation in rats, causing severe lung edema. Besides, lung tissues in contact with Cu NPs were not able to be assessed due to mortality. Cu also induces adverse effects in spleen and kidney.
Ni and NiO	*In vitro*	Citotoxicity of Nickel based NPs is size-dependent. In the same conditions, NiO NPs show to be more toxic than Ni NPs.
	In vivo	Carcinogenic to humans.
Fe_2O_3	*In vitro*	In general, iron oxide NPs induce low cytotoxicity.
	In vivo	The majority of studies do not show abnormal changes in tissues, despite some refer a dose-dependent toxicity.
TiO_2	*In vitro*	Studies regarding TiO_2 NPs toxicity have opposite conclusions. Some authors refer cell death and DNA damage, while others report no harmful effect. However, negative effects are often related to higher doses of NPs.
	In vivo	TiO_2 NPs cause genotoxic and inflammatory responses in various tissues despite being considered safety for skin applications.
ZnO	*In vitro*	ZnO NPs are reported by different authors as one of the most toxic nanomaterials, wherein Zn^{2+} ions, originated by ZnO dissolution, play the key role.
	In vivo	In lung tissues ZnO NPs induce severe cytotoxic inflammation. Toxicity is increased in acidic medium due to the dissolution of NPs, causing cell death.
SiO_2	*In vitro*	Citotoxicity of silica NPs is related to particles size and surface reactivity. Studies have shown that silica particles can penetrate into cytoplasm and the smaller ones reach the cell nucleus.
	In vivo	Crystal structure of material dictates its toxicity. Amorphous silica is considered safe, while crystalline silica is carcinogenic.

This review shows that NPs toxicological effects, as already referred, are closely related to their physicochemical characteristics, particularly the particle size, size distribution, chemical composition, surface reactivity and dissolution. Cu and Zn based-NPs are commonly the particles with the greatest toxic potential, considered highly toxic for human health [128] [129]. Conversely, Au, Fe- and Al-based NPs show often inertness or low cytotoxicity. Nevertheless, there are NPs which interact with some cell lines and in contrast do not reveal any negative response with others.

In spite of the great number of research publications in the nanotoxicology field, there is an imperative urgency in obtaining more data. The lack of standardized methods to characterize NPs and to assess their toxicity is the main concern. Regulatory bodies must establish, in a near future, proper NPs characterization methods and assays and cell lines

used to determine biological impact of NPs in humans. Moreover, mathematical approaches must be taken into account as a way to speed NPs assessment.

The recent trend points at the development of computational models (*in silico*) to link the physicochemical characteristics of NPs to the toxicological effects assessed by *in vitro* tests, and to understand underlying mechanisms that trigger NPs toxicity [130]. Here, *in vitro* approaches include both human cell lines and models of human organs using organ slices at controlled environments, in order to simulate the human body.

Computational models, as powerful and reliable tools, allow predicting toxicological outcomes based on the previous knowledge of NPs physicochemical characteristics. *Zhang et al.* [129] developed a predictive model to metal oxide NPs and used a comparative analysis of *in silico* and *in vivo* results. Figure 1. 12 shows the excellent agreement between results, proving that it is possible to use computational models to study NPs toxicity.
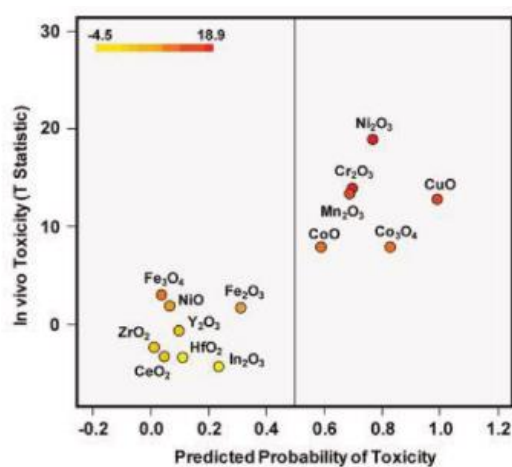
Figure 1. 12 - *In vitro* and *in silico* outcomes of lung tissues [129].

1.5 Occupational exposure limits

Since the 19th century that already exists a concern related with workers exposure to airborne materials which may cause adverse health effects (chronology in Figure 1. 13). The history on Occupational Exposure Limits (OELs) started in 1883, when *Gruber* developed a study exposing hens and rabbits to carbon monoxide, establishing the first OEL in the range of 200 to 500 parts per million. In 1916, the Phthisis Prevention Committee stated an exposure limit of 300 particles/cm³ for dust in South Africa gold mines. In United States, one of the first investigations were conducted by *Katz* and *Kenney* and led to a list of 33 OELs for different materials present in workplaces. In the 1940s, during annual meetings in American Conference of Governmental Industrial Hygienists, appeared the first OELs for chemical and toxic substances and in 1942 a list of Maximum Allowable Concentrations for atmospheric contaminants. Based on human experiences, threshold limit values were proposed by Occupational Safety and Health Act in 1970 [131].
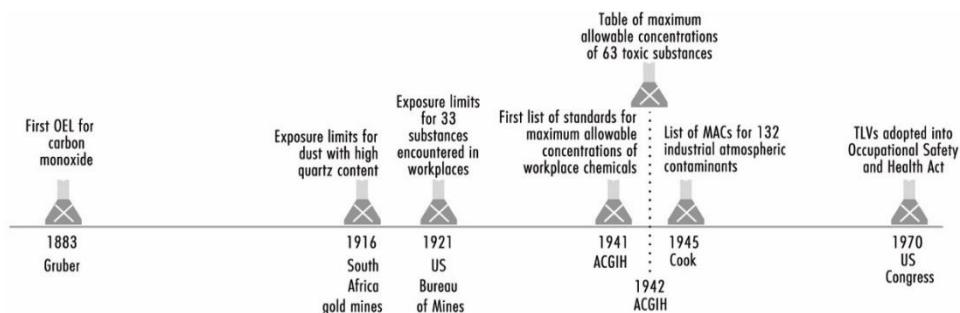
Figure 1. 13 - Chronology of OELs in last two centuries for bulk materials.

With the "recent" awareness in potential toxicity of nanoscale materials, there is a need to set exposure limits. Due to the diversity of nanomaterials on their various physicochemical combinations in the environment, classic toxicological tests are currently unable to cover the demand for the determination of reliable limits. Thus, due to the lack of regulations on the nanotechnology field, nowadays nanomaterials exposure are within the regulatory framework REACH (Registration, Evaluation, Authorization and Restriction of Chemicals), which addresses the chemical regulation of global materials, concerning environmental protection, occupational safety and health issues. Nevertheless, few OEL have been suggested by several regulatory bodies. Most of them are mass-based OELs that are not the best metric in the case of nanomaterials (section 1.2.2). This is demonstrated by a study of *Dankovic et al.* [132] where for titanium particles smaller than 2.5 µm, rats produced tumors for a dose of 250 mg/m^3, while for the same particles but with 0.1 µm, 10 mg/m^3 was enough to cause a similar tumor.

Despite in the last years some organizations, such as National Institute for Occupational Safety and Health (NIOSH), Federal Institute for Occupational Safety and Health (BAuA), Organization for Economic Co-operation and Development (OECD), Institute for Occupational Safety and Health and British Standard Institution (BSI), have made efforts in the development of OELs, currently OELs are still based on the mass metric. *Schulte et al.* [133] performed an intensive study in which they conducted an exhaustive search on the OELs state of the art topic. The Table 1. 12 summarizes some of OELs proposed for nanomaterials, where Safety Factor (SF) designates the number of times that the nanomaterial OEL is smaller than the bulk material OEL.

Table 1. 12 - OELs for nanomaterials.

Nanomaterial	Parameter	OELs	Organization (year)
CMAR*		SF=10	BSI (2007)
Insoluble	Not fibrous	SF=15	BSI (2007)
Soluble	Not fibrous	SF=10	BSI (2007)
General	0.004% risk level	SF=15	OECD (2008)
Titanium Dioxide	Particles < 100 nm	0.1 mg/m^3	NIOSH (2005)
	Tolerable risk	0.6 mg/m^3	BAuA (2008)
Photocopier Toner	2009 acceptable risk	0.06 mg/m^3	BAuA (2008)
	2018 acceptable risk	0.006 mg/m^3	BAuA (2008)
General dust		3 mg/m^3	BAuA (2009)

Recently, Institute for Occupational Safety and Health of the German Social Accident Insurance (IFA) and Social and Economic Council (SER), a Dutch government advisor organization, proposed the number-based OELs. Both organizations, IFA [134] and SER [135] suggested the implementation of provisional Nano Reference Values (NRVs) for 8-hours Time Weighted Average (TWA). Therefore, nanomaterials are classified in different groups, as has been suggested in several studies, and NRVs TWA-8hr are defined for each class. The Table 1. 13 summarizes provisional nanoreference values for different classes of nanomaterials.

Table 1. 13 - List of provisional NRVs for different classes of nanomaterials.

Class	Description	Density	NRVs TWA-8hr	Examples
1	Rigid, biopersistent nanofibers for which effects similar to those of asbestos are not excluded	-	0.01 fibers/cm³	SWCNT or MWCNT or metal oxide fibers for asbestos like effects are not excluded by manufacturer
2	Biopersistent granular nanomaterial in the range of 1 and 100 nm	>6000 kg/m³	20000 particles/cm³	Ag, Au, CeO_2, CoO, Fe, Fe_xO_y, La, Pb, Sb_2O_5, SnO_2
3	Biopersistent granular and fiber form nanomaterials in the range of 1 and 100 nm	<6000 kg/m³	40000 particles/cm³	Al_2O_3, SiO_2, TiN, TiO_2, nanoclay, carbon black, C60, dendrimers, polystyrene. Nanofibers for which asbestos like effects are excluded
4	Non-biopersistent granular nanomaterials in the range of 1 and 100 nm	-	Applicable OELs	e.g. fats, common salts (NaCl)

Making the agreements with NRVs, the background has to be considered. Background comprises outdoor airborne NPs and other airborne NPs that are not resulting from industrial activities. In other words, the background represents all the airborne NPs present in a workplace when industrial activities are not in course. The Precaution Characterization Ratio (PCR) is the parameter which defines the workplace safety levels for airborne NPs. The PCR is calculated according to the equation 1.3 [135]:

$$PCR = \frac{concentration\ of\ particles_{industrial\ activity} - concentration\ of\ particles_{background}}{NRV} \quad \text{Eq 1. 3}$$

When PCR > 1, workers are exposed to a possible harmful environment, and then some safety precautions must be employed. In any cases, it is recommended that workers protect themselves by means of personal protective equipment, such as, certified respirators, gloves, glasses, protective clothing and appropriate shoes. Companies should also adopt preventive measures. It is expected that those industries assume the responsibility for isolation or confinement of some areas where potential dangerous materials are handled. The use of mechanically driven ventilation and air filtration systems should be encouraged, and workers should be educated to implement safety procedures during cleaning, operating equipment and personal hygiene.

Despite the NRVs are provisional and not recent, they are the only available limits present in literature for monitoring workplaces. However, it should be noted that real environments are composed by a large variety of nanomaterials, and it is still unknown the real effects of these nanomaterials when they are together. When combined, they can enhance toxicity, or conversely they can cancel the toxicity of the others.

Studies of long term effects of NPs and predictive toxicity models, will be an important contribution to the implementation of definitive exposure limits in workplaces, by the regulatory bodies. In this respect, there is still much work to be made and until this goal is not reached, it should be regarded the principle "no data, no exposure".

1.6 Beyond the state of the art

According to the described state of the art, there are still many important issues that must be addressed in the occupational nanosafety field.

The current trend in studies concerning physicochemical and toxicological characteristics of NPs focuses mainly on single and engineered nanomaterials. In this context, this thesis highlights the study of realistic occupational environments, where different types of unintended airborne NPs are present. Measurements of airborne NPs regarding the number-based metric will be performed, as recommended by several organizations as being one of the most appropriated, despite not so regularly used.

To promote a safety occupational environment, efficient porous filters must be used as protective equipment. Commercially available porous filters have pores in the micrometric range, capturing NPs by impaction, interception and diffusion. The main objective of this thesis is to develop nanoporous filters with pores in nanometric range, thus preventing by interception that NPs cross the pores, which could be more effective in NPs filtration. Moreover, the thin thickness of nanoporous thin films enhances the flux of air passing through the filter, when compared to commercial filters that have a high ratio pore size/thickness.

The study is complemented with toxicity assays of NPs collected in industrial environments. *In vitro* studies with human cells go in favor to the recent trend of the American and European Scientific Communities whose emphasize to avoid using animal models, since results from animal models often cannot be transposed to human beings. Currently, cellular studies aiming the toxicity characterization of a set of different NPs combined are almost inexistent.

Therefore, it is expected that this work can contribute to the establishment of non-provisional number-based OELs and to predictive nanotoxicological models, which are not yet available. Moreover, efficient nanoporous filters would be a huge progress in the nanosafety field.

Chapter 2
Nanoporous Structures

T he demand on solutions for filtering, sensing, biomedical devices and energy conversion, has led to major and recent advances in the production and characterization of nanoporous structures. With the increasing presence of unintended and engineered NPs in environment, mainly due to nanotechnological or conventional industrial processes, it is urgent a truly effective solution in the retention of these NPs to prevent the human exposure.

This chapter describes the three main approaches selected in this study based on sputtering for producing nanoporous structures, capable of filtering airborne NPs by reducing the substrate pore size, by controlling sputtering conditions and by sputtering two materials. Nanoporous structures are fully characterized in order to select the sputtering conditions which achieve nanoporous structures with the best filtration properties.

2.1 Experimental procedure

2.1.1 Sputtering deposition

The nanoporous structures were produced by rf magnetron sputtering using three main approaches (Figure 2. 1):

1) M – Reducing the substrate pore size

   Thin films of aluminum were deposited onto different porous substrates (alumina (Al_2O_3) and polyvinylidene fluoride (PVDF)), decreasing the template pore size until a nanometric size. Parameters such as deposition time, power density and substrate rotation were varied in order to study the effect on the size and morphology of pores.

2) F1 – Controlling sputtering conditions

Sputtering parameters, such as power density, deposition pressure and atmosphere gases and variables as substrate tilt and rotation and time of deposition, were controlled in order to deposit nanoporous aluminum thin films with different porosities onto porous substrates (Al_2O_3 and PVDF) and bulk Si (as control).

3) F2 – Sputtering two materials

Co-deposition of YSZ (Yttria Stabilized Zirconia) and Sn with posterior removal of the sacrificial material with low melting temperature (Sn).
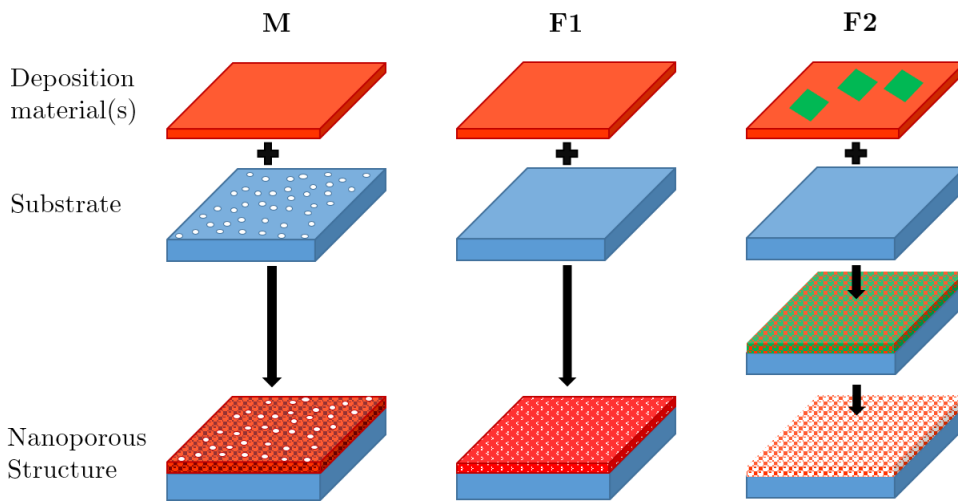
Figure 2. 1 - Production of nanoporosity.

2.1.1.1 Substrates

Thin films were deposited onto different selected substrates, according to the approach.

1) M – Reducing the substrate pore size

- Anopore – commercial Al_2O_3 Anodisc membranes with diameter of 13 mm, thickness of around 60 µm and pore size of 100 nm (Whatman[®] Anopore, UK)

- AAO – homemade porous Al_2O_3

  Metal sheets of Al 6016 alloy (20×20 mm^2 and 1 mm of thickness) were mechanical grinded until the 2400 grit size and finished with mirror-like polishing with 3 µm diamond paste. After cleaned in acetone and ethanol in ultrasonic baths, aluminum sheets were anodized in a two-steps procedure.

The anodizing apparatus, comprising a polymeric holder with a graphite rod as cathode immersed in an electrolyte and a dc power supply (Agilent Technologies, N5751A model, max. 300 V, 2.5 A), was operating on potentiostatic mode at a constant voltage of 100 V.

During the first step, aluminum sheets were anodized in a stirred 5 wt.% H_3PO_4 (phosphoric acid) electrolyte solution at $273 - 278$ K (electrochemical cell in an iced bath) for 60 min. After this first step, the initial disorderly oxide layer was selectively removed through chemical etching using a 8 wt.% H_3PO_4 + 4 wt.% CrO_3 solution at 333 K for 30 min, and then cleaned in an ultrasonic bath during 10 min. This created semi-spherical pits that served as seeds to grow the pores in the second step anodization.

The second anodization was conducted in the same conditions of the first one, creating a highly ordered porous structure of Al_2O_3 with about 2 µm of thickness.

The production of AAO membranes with open porosity in both sides is possible by a significant increase in the time of anodizing and removing the Al substrate by etching. However, this procedure leads to a long time and resources consumptions. Once size and morphology of pores of substrate surface do not show significant changes for longer anodizing processes, in the present study the deposition of thin films was performed onto the porous surface of AAO.

- Millipore – commercial PVDF Durapore membranes with diameter of 13 mm, thickness of 125 µm and pore size of 220 nm (Merck Millipore, Ireland)

2) F1 – Controlling sputtering conditions

- Anopore – commercial Al_2O_3 Anodisc membranes with diameter of 13 mm, thickness of around 60 µm and pore size of 100 nm (Whatman[®] Anopore, UK)

- AAO – homemade porous Al_2O_3 (procedure described above)

- Millipore – commercial PVDF Durapore membranes with diameter of 13 mm, thickness of 125 µm and pore size of 220 nm (Merck Millipore, Ireland)

- Bulk Si with a preferential orientation (111) (control substrate)

3) F2 – Sputtering two materials (YSZ and Sn)

- Bulk Cu (mechanical grinding until 2400 grit size and a final polishing with diamond paste of 3 µm grit size and silica colloidal OP-U)

This substrate was used to optimize the deposition process, and can be later removed by a (physical or chemical) subtractive via.

- Bulk Si with a preferential orientation (111) (control substrate)

2.1.1.2 Thin films

The depositions of nanoporous structures by rf magnetron sputtering were performed using the Edwards Coating System (model E306A) (Figure 2. 2). The system has two cathodes, allowing the co-deposition from two different targets, assisted by two rf power supplies (13.56 MHz). In this study was only used one target (placed in target 1 of Figure 2. 2), assisted by the Eni Power Systems (model OEM12-05). The sputtering chamber was evacuated until pressures of around 10^{-4} Pa and thin films depositions were carried out at 0.7 Pa in an Ar 99.999% atmosphere. This deposition system works with substrates in static or rotational mode (200 rpm) and the shortest distance target-substrate is 65 mm.

Deposition conditions varied according to the deposition method.
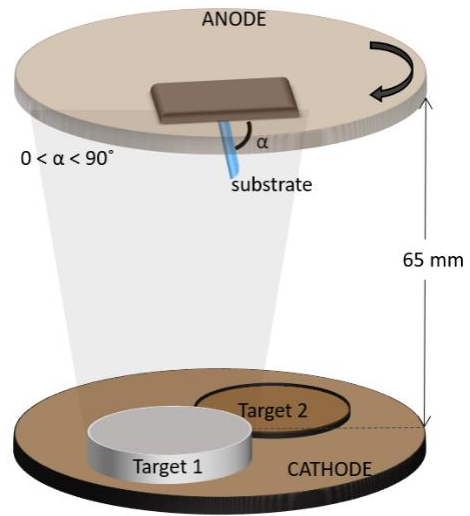
Figure 2. 2 - Schematic representation of cathode (target) and anode (substrate) (Edwards Coating System E306A).

1) M – Reducing the substrate pore size

   A target of Al with 100 mm of diameter and 5 mm of thickness was used to deposit thin films from 5 to 90 min applying different power densities (1.27×10^4, 2.55×10^4 and 3.18×10^4 W/m^2).

2) F1 – Controlling sputtering conditions

   In this approach, the depositions were carried out applying different power densities (1.27×10^4, 2.55×10^4 and 3.18×10^4 W/m^2) for 30, 60 and 90 min. In addition, substrates were tilted in three angles, 70, 85 and 89° and the variation of other sputtering conditions were also studied, for instance, increasing the deposition pressure to 1.7 Pa and injecting 5% of N$_2$ in the chamber atmosphere (reactive deposition).

3) F2 – Sputtering two materials (YSZ and Sn)

   By co-depositing two materials is possible to produce a nanoporous thin film based on a chemical and structural stabilized matrix. One of the materials must be easy to be removed by a heat treatment at low temperature. The materials more suitable to accomplish this purpose are the YSZ, due to their excellent properties,

and Sn with a limited dissolution in YSZ and a melting temperature of around 500K. Two different approaches were considered for the thin films deposition:

a) YSZ target (8% mol Y_2O_3, 99.9% pure, Cerac) with 100 mm of diameter and 6 mm of thickness, with 2 and 4 foils of Sn (5×5 mm^2) (99.99%, Goodfellow) placed in strategic places;

b) YSZ-Sn homemade target: a powder mixture composed by 70 wt.% YSZ (Innovnano) and 30 wt.% Sn (>45 µm, 99.8% pure, Sigma-Aldrich) was mixed, pressed at 37 MPa and finally heated at 510 K.

In both cases, the power density was 3.18×10^4 W/m^2 for 30, 60 and 90 min.

During the present study, the thin films are designated according to the follow nomenclature[1] (Figure 2. 3):
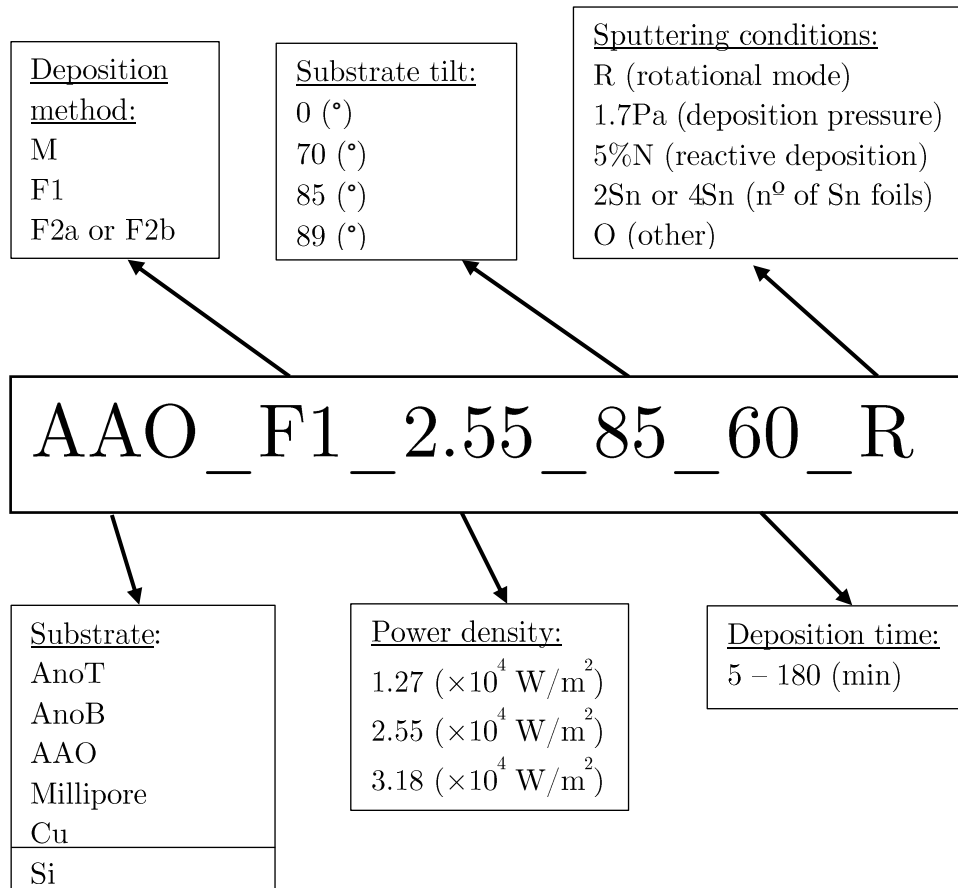
Figure 2. 3 - Thin films designation.

---

[1] The printable version has a bookmark where is provided this nomenclature for an easy reading.

2.1.2 Characterization of substrates and thin films

Substrates and thin films were characterized through the techniques listed in Table 2. 1.

Table 2. 1 - Techniques and equipment used in thin film characterization.

Characteristic	Technique	Equipment
Morphology	SEM	FEI Quanta 400 FEG, Leica S360
Surface Area and Porosity	Gas adsorption (BET)	Micromeritics ASAP 2000
Topography	AFM	Veeco diInnova
Tomography	X-ray nanotomography FIB nanotomography	ID16A Nanotomography beamline FEI Helios 450S Dual Beam™ FIB/SEM
Structure	XRD	PANanalytical X'Pert PRO (Cu Kα (λ=0.1542 nm)) PANanalytical X'Pert (Co Kα (λ=0.179 nm))

For abbreviations, please see page xi with acronyms

2.1.2.1 Morphology

All the thin films developed through the three different approaches and substrates were characterized regarding their morphology. SEM was used to observe surface and cross section morphologies, with an operating voltage of 5 and 15 kV, according to the microscope used.

In addition, image processing of SEM images of porous structures were performed using ImageTool 3.0 software to determine the pore size distribution, the average pore size, the wall thickness or column size and the thickness of thin films (Figure 2. 4). SEM images were converted to 24-bits grayscale images, and then analyzed to find the objects (pores) by manual threshold. The Feret diameter (the mean of a group of diameters that are measured by the distance between two parallel lines tangent to the perimeter of the object) of all identified pores were determined. Finally, the wall thickness and column size were evaluated by measuring 25 randomly selected walls/columns.
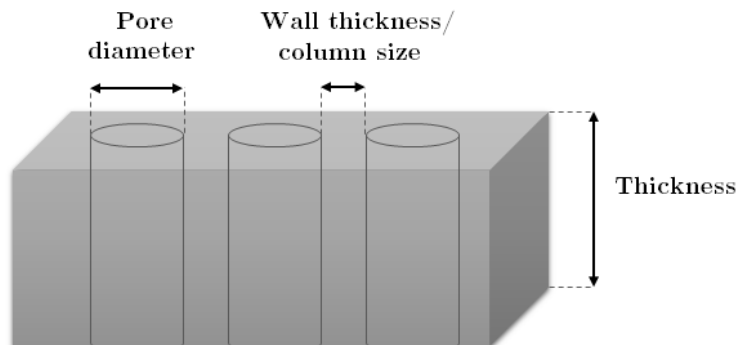
Figure 2. 4 - Scheme of characteristics measured by processing SEM images.

2.1.2.2 Surface area and porosity

Physical gas adsorption of nitrogen, is commonly used to measure the surface area and porosity. Isotherm curves of Anopore and AAO substrates and of nanoporous structures achieved by methods M and F1, were obtained. Besides, surface areas were measured through the *Brunauer, Emmett and Teller* (BET) model and the total pore volumes by the isotherm curves.

Porous structures were outgassed at 378 K during at least 3-4 hours to stabilize the pressure around 0.53 - 0.67 Pa. The adsorption-desorption N_2 measurements were conducted at liquid nitrogen temperature (77 K), with the isotherm curves being obtained with relative pressure (P/P_0 – gas pressure/gas saturation pressure) in the range of 1×10^{-3} – 0.999.

The BET model was applied to determine the surface area, assuming that a monolayer of N_2 was covering all the surface of the porous structures. The total pore volume was stated as the volume in which the relative pressure was 0.999, which corresponds to the maximum amount of gas filling the pores. Since the total pore volume was expressed in cm^3/g STP (Standard Temperature and Pressure), the value was multiplied by a conversion factor of 0.0015468. This conversion factor is the ratio between an amount of liquid N_2 at 77 K and the same amount at STP.

2.1.2.3 Topography

Surface roughness of nanoporous structures with potential applications on nanofiltration, is more than to infer the surface topography. The surface roughness plays an important role in the filtration efficiency, since the roughest the surface is, more easily it traps the particles [136]. Rougher nanoporous surfaces with curved surfaces (cavities) contribute to the deposition of particles.

Therefore, in addition to the pore size, the surface roughness is also a characteristic that must be taken into account in order to achieve nanoporous structures with a great filtration performance. Thus, there must be a balance between pore size and surface roughness, since these two characteristics are inversely correlated.

Topographies were analyzed by AFM at tapping mode with an antimony doped silicon probe (k = 5 N/m) of *Bruker* (Figure 2. 5). Data were then processed using the WSxM 4.0 software. Besides, average (S_a) and root mean square (S_{RMS}) surface roughness were evaluated.

Tip radius	8 nm
Front Angle (FA)	25°
Back Angle (BA)	15°
Tip Set Back (TSB)	15 µm
Tip Height (h)	17.5 µm
Side Angle (SA)	17.5°
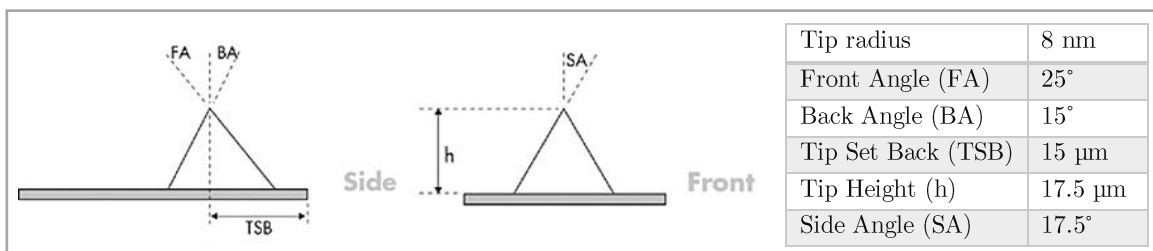
Figure 2. 5 - Schematic representation of AFM probe and its dimensions.

2.1.2.4 Tomography

3D nanotomography of thin films was studied by two different characterization techniques, the synchrotron X-ray nanotomography and the FIB (Focused Ion Beam) nanotomography.

Synchrotron X-ray nanotomography

The specimen were prepared by two different methodologies:

- The Al membrane produced by method M (AnoB_M_2.55_0_10_O) was coated with a YSZ thin film by rf magnetron sputtering for 5 hours at 0.7 Pa and 3.82×10^4 W/m². Afterwards, a cylinder with 10 µm of diameter and 60 µm of height was extracted from the specimen by FIB (FEI Helios 450S Dual Beam™) (Figure 2. 6). The region of interest (Al nanoporous thin film) is sandwiched (Al_2O_3/Al/YSZ) to avoid artifacts during X-ray nanotomography, due to different densities material/vacuum.
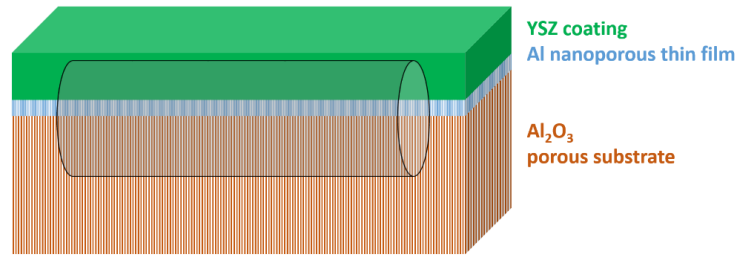
Figure 2. 6 - Schematic illustration of the FIB cut of AnoB_M_2.55_0_10_O.

- Initially, the Al thin films deposited through method F1 (AnoT_F1_2.55_85_60_O, AnoT_F1_2.55_89_60_O and AnoT_F1_2.55_85_60_R) were glued with a thin layer of epoxy-based glue with the thin films placed face-to-face (Figure 2. 7). Specimens were cut by FIB (FEI Strata dual beam 400) into cylindrical shape with 30 µm of height and diameter ranging from 15 to 20 µm.
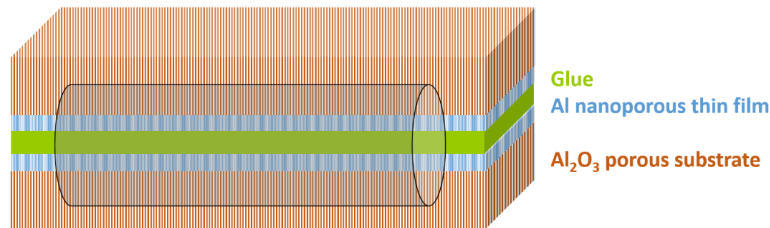
Figure 2. 7 - Schematic illustration of the FIB cut of AnoT_F1_2.55_85_60_O, AnoT_F1_2.55_89_60_O and AnoT_F1_2.55_85_60_R.

Afterwards, as a way to ensure the best resolution, it was reduced the cylinders diameters. Thus, some material was removed from the specimen until achieving 10 µm of thickness.

The nanoporous structures cut by the two different methodologies were positioned in the longitudinal axis and mounted on the specimen holder (Figure 2. 8).

a)

b)

c)

d)
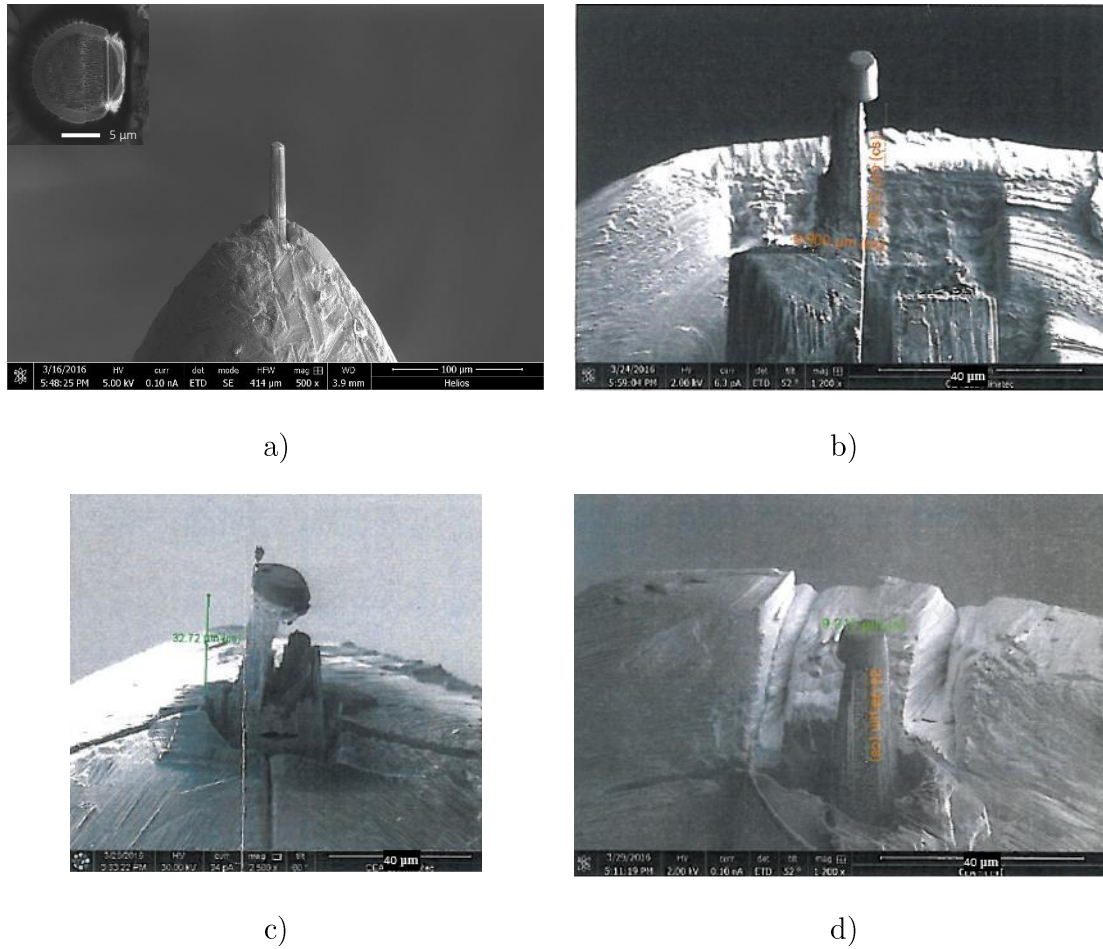
Figure 2. 8 - SEM images of nanoporous structures cut by FIB to synchrotron X-ray nanotomography: a) AnoB_M_2.55_0_10_O; b) AnoT_F1_2.55_85_60_O; c) AnoT_F1_2.55_89_60_O and d) AnoT_F1_2.55_85_60_R.

X-ray nanotomography was carried out at the European Synchrotron Radiation Facility (ESRF) Nano-imaging beamline ID16A (Figure 2. 9). Further details of this characterization technique are in Appendix A.

The technique is based on a conic beam focalized by Kirkpatrick Baez multilayer mirrors. The X-ray energy of 33.6 keV was selected to acquire radiographs with 7 nm of pixel size. A FReLoN detector (2048×2048 pixels) was used to record images at 4 predefined sample-detector distances (D1 = 2.952; 3.079; 3.585 and 4.636 mm) at 1570 angular positions for each distance (total of 6280 projections). Afterwards, those projections were processed for the phase retrieval and the tomographic reconstruction.
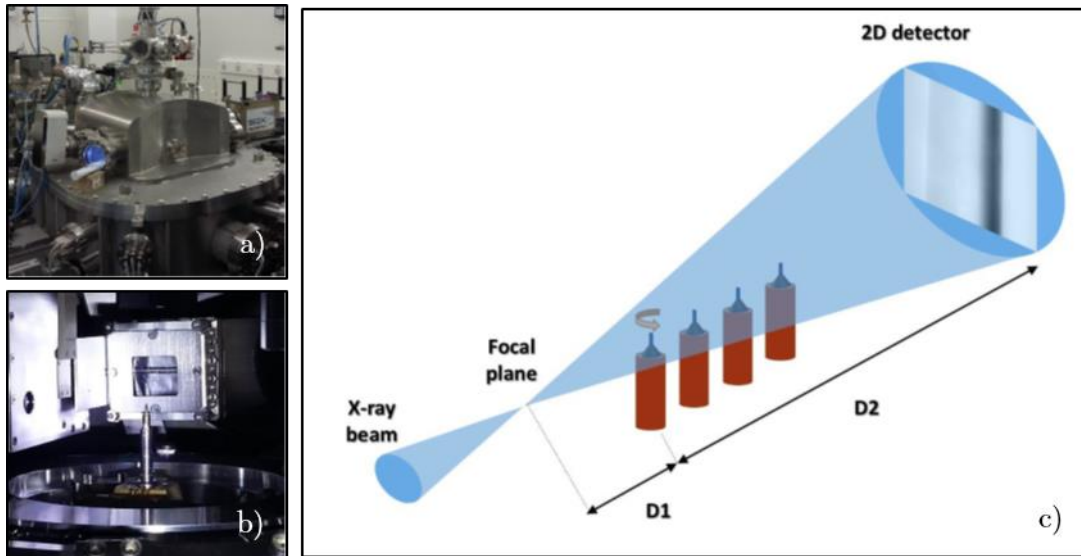
Figure 2. 9 - X-ray nanotomography at ESRF ID16A: a) end-up station; b) sample holder and c) schematic representation of the experimental setup.

FIB nanotomography

FIB nanotomography was performed using a dual-beam system FIB/SEM with a resolution of 1 nm, obtaining 3D nanotomographic images of nanoporous structures, to fully assess the internal pore structure.

AnoB_M_2.55_0_10_O, AnoT_F1_2.55_85_60_O, AnoT_F1_2.55_89_60_O and AnoT_F1_2.55_85_60_R deposited onto Anopore were pre-coated with a 150 nm Pt protective layer. Then, the sectioning was carried out by removing slices one by one parallel to the surface by FIB at an accelerating voltage of 30 kV and a beam current of 18 pA, exposing new planar sections (Figure 2. 10). The procedure was repeated in several slices with different dimensions (Table 2. 2).

Finally, the sections were observed by SEM at an accelerating voltage of 5 kV and a current of 100 pA. The process was run in automated
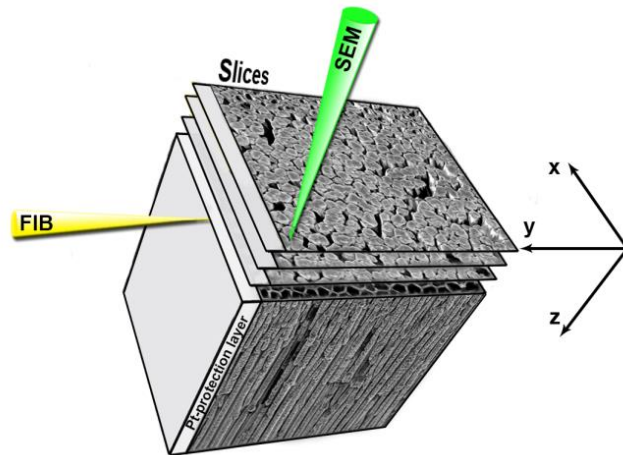
Figure 2. 10 - Schematic illustration of the procedure to obtain 3D nanotomographic images by FIB.

mode using the AutoSlice&View[TM] G3 software. The total time of acquisition for each sample was 7 hours. 2D tomographic images were post-processed, reconstructed in 3D and quantified through the FEI VSG Avizo software.

Table 2. 2 - Dimensions of volume of analysis and voxels of aluminum thin films deposited onto Anopore by methods M and F1.

		Analysis volume (µm)	Voxel matrix	Voxel size (nm)
	x	7.31	3072	2.38
AnoB_M_2.55_0_10_O	y	4.87	2048	2.38
	z	1.2	60	20
	x	8.64	1800	4.8
AnoT_F1_2.55_85_60_O	y	7.2	1500	4.8
	z	2.9	145	20
	x	5.94	512	11.6
AnoT_F1_2.55_89_60_O	y	5.94	512	11.6
	z	4.5	225	20
	x	9.04	1536	5.89
AnoT_F1_2.55_85_60_R	y	6.03	1024	5.89
	z	3.9	196	20

2.1.2.5 Phasic composition

The thin films produced by method F2 were analyzed regarding their phasic compositions. Crystal structures of Si_F2a_3.18_0_180_2Sn and Si_F2a_3.18_0_180_4Sn were analyzed by X-ray diffraction (XRD) at a wavelength of 0.1542 nm using a Cu Kα radiation at 45 kV and 40 mA. The Bragg-Brentano geometry had a constant incident beam of $\theta = 5°$ and 2θ ranging from 20 to 90°. The Si_F2b_3.18_0_30_O was performed at a wavelength of 0.179 nm using a Co Kα radiation at 40 kV and 35 mA. The constant incident beam was $\theta = 2°$ and 2θ was between 10 and 120°.

2.2 Results and discussion

2.2.1 Substrates

2.2.1.1 Morphology

The porous substrates (Anopore, AAO and Millipore) used to deposit the aluminum thin films by methods M and F1 present different morphologies, as revealed by SEM images (Figure 2. 11). The two surfaces of Anopore substrates, the top (AnoT) and the bottom surface (AnoB), present different morphologies. Based on digital image processing of the SEM images, the average pore size and the wall thickness of porous substrates were measured (Table 2. 3). Remark: due to the large average pore size of Millipore substrate, the magnification of SEM image (Figure 2. 11 c)) is much lower than for the other substrates.

Anopore   AAO   Millipore

Top

a)   b)   c)

Bottom

d)
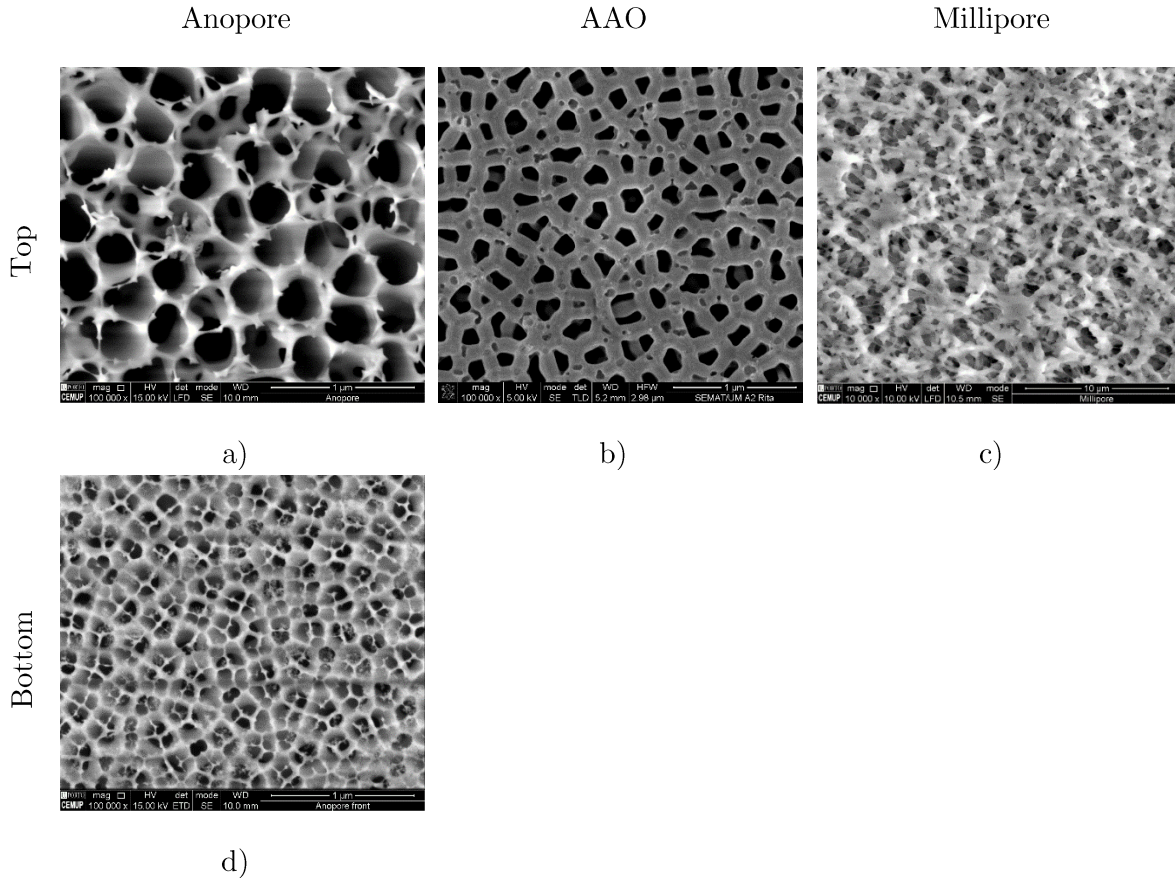
Figure 2. 11 - Top view SEM images of substrates: a) AnoT; b) AAO; c) Millipore and d) AnoB.

Table 2. 3 - Average pore size and wall thickness of substrates.

	Pore size $\pm$ σ (nm)	Wall thickness $\pm$ σ (nm)
AnoT	181 $\pm$ 16	18 $\pm$ 8
AnoB	87 $\pm$ 12	9 $\pm$ 2
AAO	120 $\pm$ 13	94 $\pm$ 15
Millipore	641 $\pm$ 57	-

Substrates reveal different porous structures, with AAO and Anopore showing more ordered porous structures and smaller pore sizes than Millipore. Millipore exhibits interconnected porous network with a wide range of pore shapes and sizes which average pore size is 641 nm. Measuring the wall thickness became a difficult task since Millipore has a very wide range of wall thickness.

The top and bottom surfaces of Anopore substrates have different morphologies. While the top surface shows cylindrical unconnected pores with an average pore size and wall thickness of 181 nm and 18 nm respectively, the bottom surface exhibits smaller sized interconnected pores (87 nm) and thinner walls (9 nm). The anodization procedure led AAO substrates to present relatively thick walls (94 nm), which is close to the average pore size (120 nm). Therefore, the wall thickness of AAO is much thicker than both sides of Anopore.

2.2.1.2 Surface area and porosity

Anopore and AAO substrates were assessed by nitrogen adsorption, being obtained the nitrogen adsorption isotherms (Figure 2. 12) and estimated the BET surface area and the total pore volume (Table 2. 4).

a)   b)
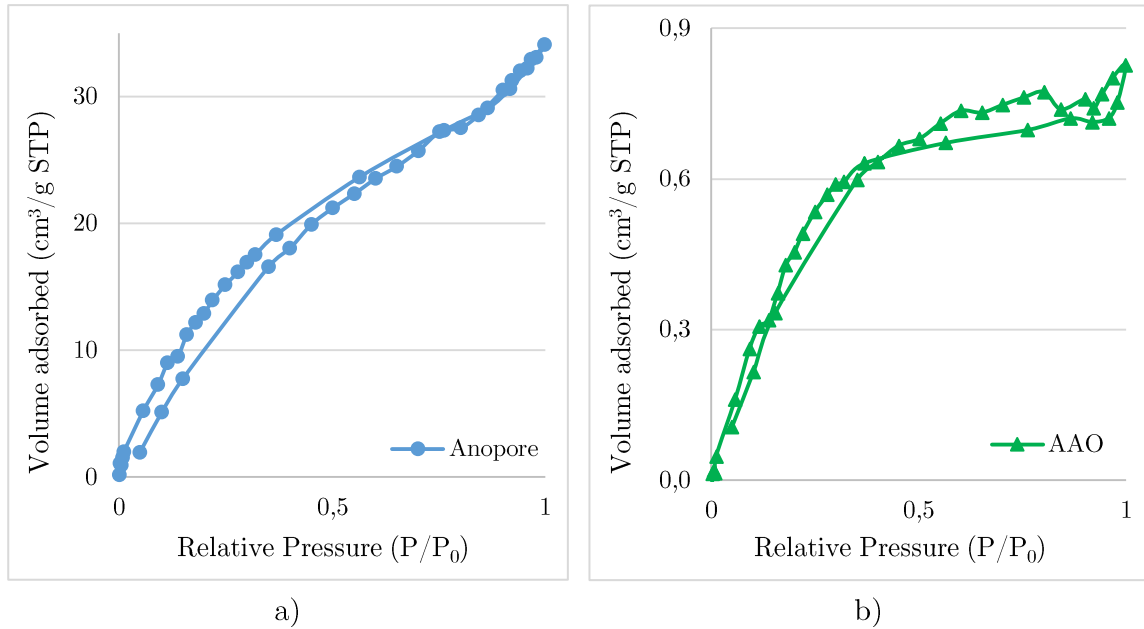
Figure 2. 12 - Nitrogen adsorption isotherms of: a) Anopore and b) AAO substrates.

Table 2. 4 – BET surface area and total pore volume of Anopore and AAO substrates.

	Surface area (m²/g)	Total pore volume (cm³/g)
Anopore	66.44	0.0530
AAO	2.40	0.0013

Both substrates present adsorption isotherms curves type H4 hysteresis [137], according to IUPAC, which is a typical isotherm curve of porous structures with a wide range of pore sizes, including nanopores, and in which the biggest pores are not completely filled. The mismatched adsorption and desorption curves are the evidence of capillary condensation, in which the processes of filling and emptying pores are different. The inflection point at lower relative pressures corresponds to the gas monolayer formation.

In Figure 2. 12 is evident that the volume of gas required to fill the porous structure is much greater in the Anopore than the AAO. These results are in accordance with the estimated total pore volume and BET surface area, and are related to the porous structures of substrates. While the Anopore is a completely porous structure, the AAO presents partial porosity, with a porous layer of about 2 µm of thickness, and a dense part which results in a lower porosity of AAO than Anopore.

2.2.1.3 Topography

AFM 3D images (1×1 µm²) of AnoT, AnoB and AAO (Figure 2. 13) reveal thick walls in AAO substrates and much thinner walls in both surfaces of Anopore, which are consistent with the SEM images.

Regarding the topography of Millipore substrate, it was not possible to use AFM due to the material deformation when the tip contacts its surface. The values of surface roughness of porous substrates and bulk Si (optical polished) are shown in Table 2. 5. In spite of the roughness of the porous structures is closely related to the pore size, the larger the pore size the greater the roughness [138], the texture of the pore walls also influences the final surface roughness.

Anopore   AAO

a)   b)   c)
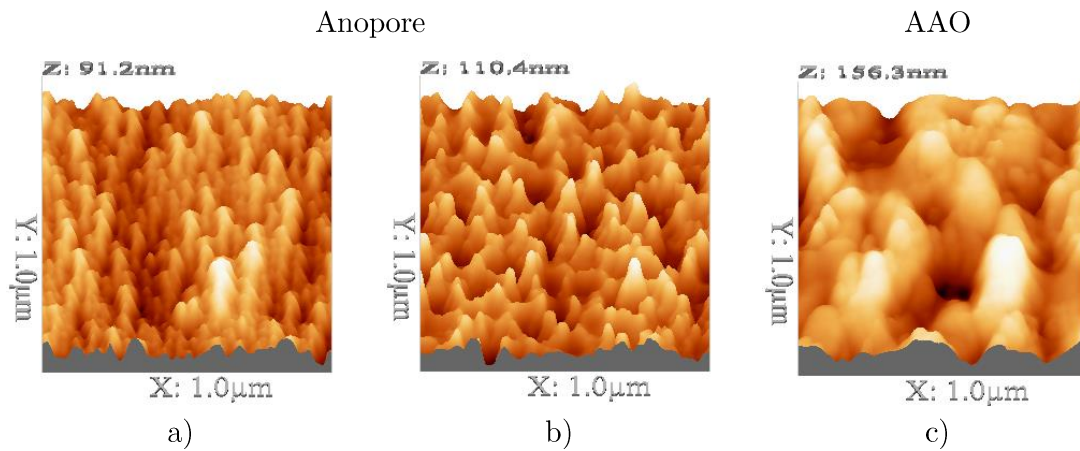
Figure 2. 13 - Topography of substrates: a) AnoT; b) AnoB and c) AAO.

Table 2. 5 - Surface roughness of substrates.

	S_a (nm)	S_{RMS} (nm)
AnoT	10	12
AnoB	12	15
AAO	21	26
Si	1	1

In this case is clear that it is not only the pore size that determines the surface roughness, but also the pore walls. S_a and S_{RMS} of AnoB are due to the presence of saw-like pores, with rough edges. AnoT reveals to be the smoothest porous surface, although its surface roughness are not so dissimilar than those of the AnoB surface. The roughest topography of the AAO substrates is maybe due to the protruded pore walls with further surface defects, such as interstitial rods.

2.2.2 Nanoporosity by reducing substrate pore size (M)

2.2.2.1 Morphology

Nanoporous membranes produced by the method M, resulted from the rf sputtering deposition of aluminum thin film onto porous substrates (Anopore, AAO and Millipore) by a conventional deposition process. The parameters, such as, the deposition time, the power density or the substrate rotation, induce different thin films morphologies.

● Deposition time

The growing mechanisms of aluminum thin films deposited onto Anopore are similar in both surfaces, AnoT (Figure 2. 14) and AnoB (Figure 2. 15). The initial steps of the growing mechanisms are easily observed in the thin films deposited onto AnoT, due to the great dimensions of pores. The nucleation phase occurs, with the adatoms reaching the substrate surface. Usually, the nucleation happens on the surface of the pore wall, creating a shadow effect. However, some adatoms pass through the pores and are deposited in the inner walls of channels (Figure 2. 14 a) and Figure 2. 15 a)). The growth of islands is observed although the discontinuous thin film. Then, these islands start coalescing, giving rise to a nanoporous thin film with the same pore location of the substrate, but with smaller sizes. The islands coalescence is also observed for thin films deposited onto AnoB.

a)   b)
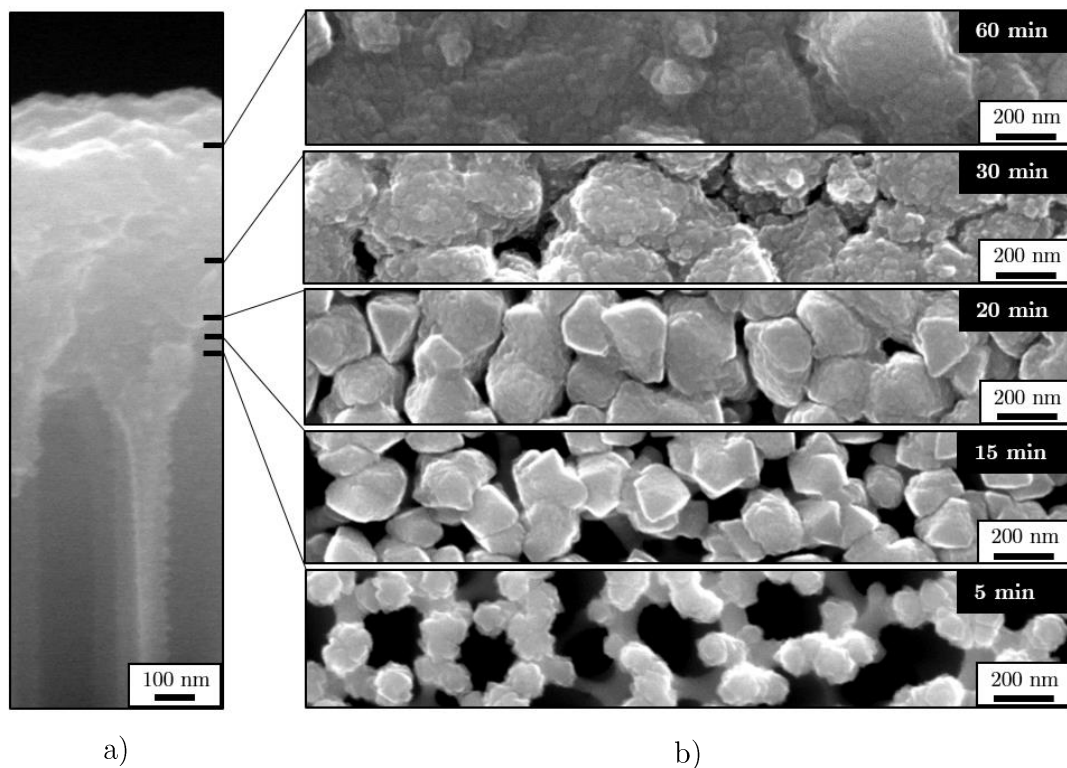
Figure 2. 14 - Growth of aluminum thin films deposited onto AnoT, function of the deposition time: a) cross section and b) top view.

Therefore, the film growth leads to the formation of V-shaped columns, increasing their size with the time of deposition: 44 nm after 5 min and 333 nm at 30 min in AnoT and in AnoB 76 nm at the first 5 min and 147 nm at 15 min (Table 2. 6).
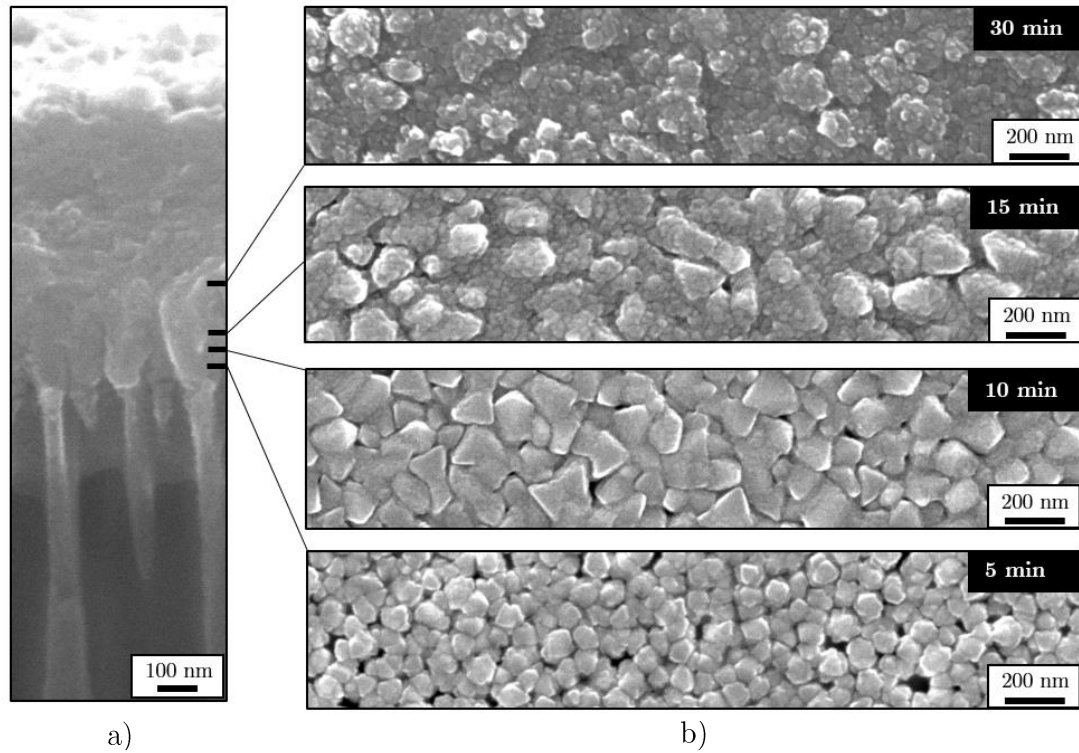
Figure 2. 15 - Growth of aluminum thin film deposited onto AnoB, function of the deposition time: a) cross section and b) top view.

Table 2. 6 - Average pore and column sizes of nanoporous membranes onto both sides of Anopore.

	Pore size ± σ (nm)	Column size ± σ (nm)
AnoT_M_2.55_0_60_O	-	-
AnoT_M_2.55_0_30_O	58 ± 5	333 ± 62
AnoT_M_2.55_0_20_O	72 ± 5	99 ± 16
AnoT_M_2.55_0_15_O	130 ± 10	139 ± 22
AnoT_M_2.55_0_5_O	172 ± 17	44 ± 7
AnoB_M_2.55_0_30_O	-	-
AnoB_M_2.55_0_15_O	20 ± 3	147 ± 24
AnoB_M_2.55_0_10_O	25 ± 3	117 ± 23
AnoB_M_2.55_0_5_O	38 ± 3	76 ± 11

By increasing the deposition time, the surface average pore size of membrane is narrowed. Thin films onto AnoB present smaller pore sizes than AnoT due to different morphologies and pore sizes of both surfaces of Anopore. For thin films deposited onto AnoT, the pore size decreases from 181 nm (substrate) to 58 nm (30 min of deposition), being required 60 min of deposition to close the pores completely. In turn, in the thin films onto AnoB the pore size is ranging from 87 nm (substrate) to 20 nm (15 min of deposition) with pores closing after 30 min of deposition (Table 2. 6). After 60 min of deposition, the thin film deposited onto AnoT has 500 nm of thickness, while the 30 min of deposition onto AnoB grows a thin film with 250 nm of thickness. Thus, the different characteristics of both surfaces of Anopore surface do not interfere significantly with the thickness of the aluminum thin films.

The same pore formation mechanism is also observed in the thin films deposited onto AAO substrates (Figure 2. 16). In the thin films deposited onto AAO, the adatoms are already fully agglomerated after 15 min but 60 min are not enough to completely close the pores. The thin films of aluminum have about 1200 µm of thickness after 60 min of deposition. These facts suggest that the largest wall thickness (94 nm) of AAO substrate contributes to the adatoms being retained on the substrate surface rather than penetrating the pores and being deposited on its walls.
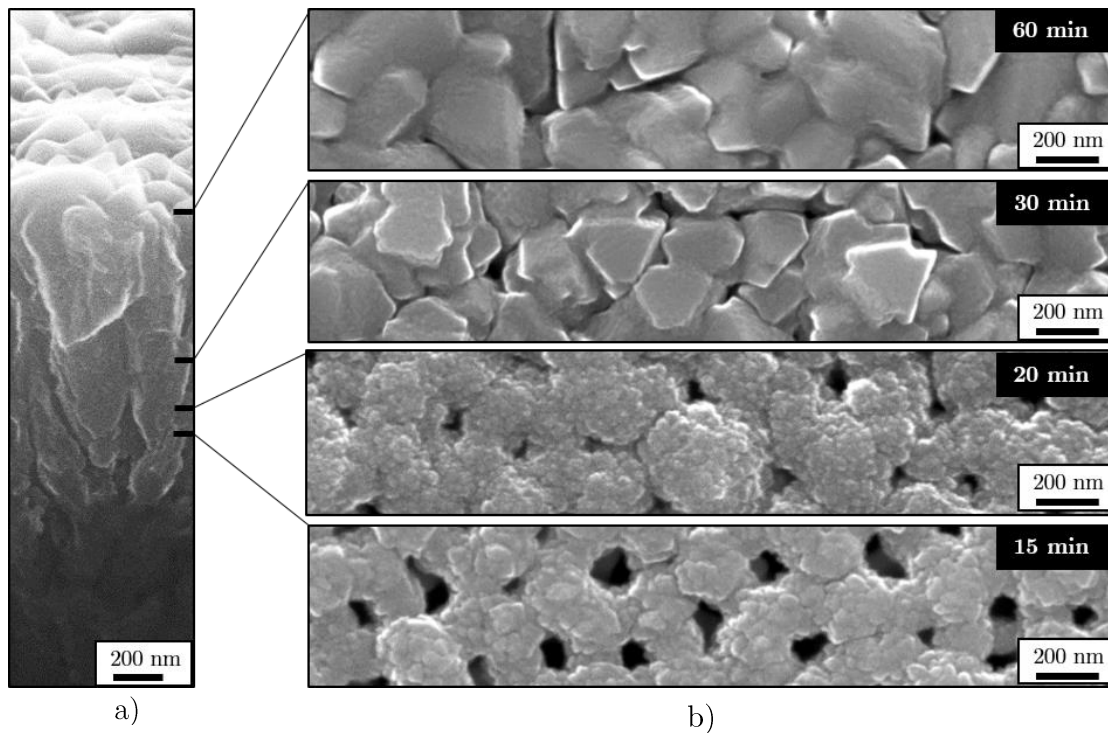
Figure 2. 16 - Growth of aluminum thin films deposited onto AAO, function of the deposition time: a) cross section and b) top view.

The pore narrowing is followed by the increasing on the size of columns, which presented a V-shape (Table 2. 7), and the smoothing of the surface (Figure 2. 16). This effect is promoted by adatoms diffusion which contributes to fill the surface discontinuities, with the deposition time [139]. The smallest average pore size (37 nm) and the largest column size (444 nm) are achieved at a deposition time of 60 min.

Table 2. 7 - Average pore and column sizes of nanoporous membranes onto AAO.

	Pore size ± σ (nm)	Column size ± σ (nm)
AAO_M_2.55_0_60_O	37 ± 3	444 ± 39
AAO_M_2.55_0_30_O	42 ± 3	290 ± 79
AAO_M_2.55_0_20_O	57 ± 3	247 ± 42
AAO_M_2.55_0_15_O	80 ± 4	183 ± 27

The aluminum thin films deposited onto Millipore substrates, with different deposition times are shown in Figure 2. 17.

Millipore substrate, with much larger pore size than that claimed by the manufacturer (641 nm), hinders the production of membranes with pores in the nanometric range. In fact, after 180 min of deposition, the average pore size has only decreased to 458 nm (Table 2. 8). Due to the large average pore size, most of the adatoms are not deposited on the surface of pore walls and some are even deposited in the walls of pores located at levels below the surface.
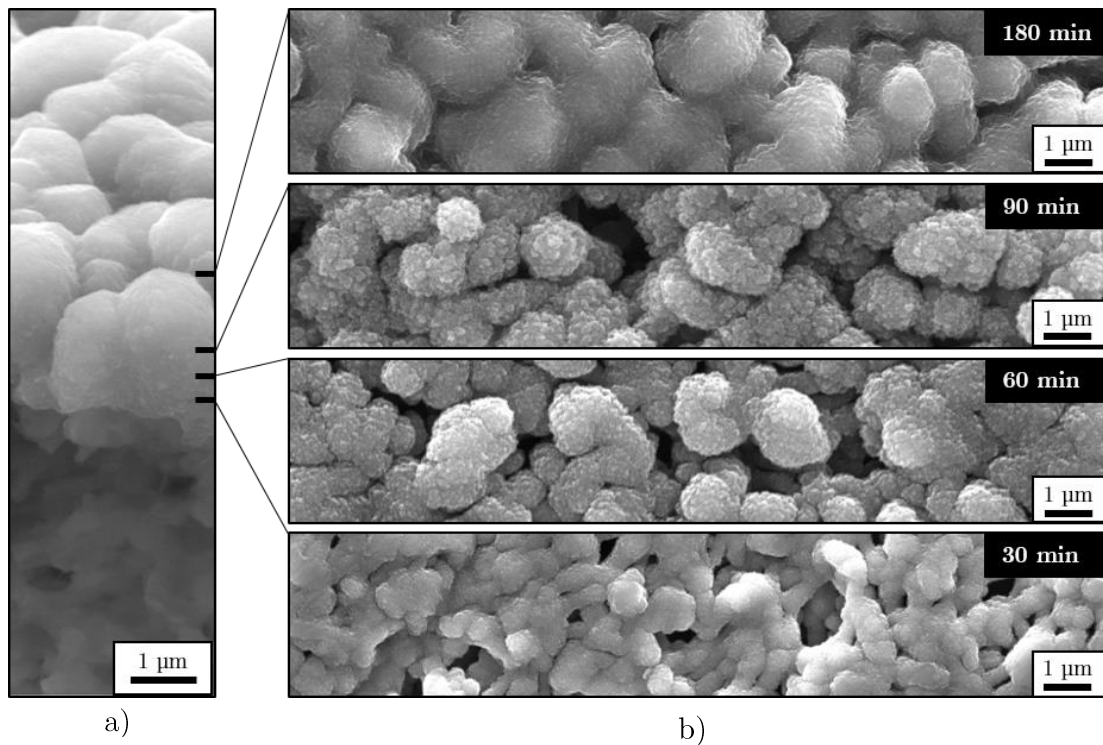
Figure 2. 17 - Growth of aluminum thin films deposited onto Millipore, function of the deposition time: a) cross section and b) top view.

For the first 30 min of deposition, aluminum thin film coats the wall surface of pores, and columns appear after 60 min. After 90 min of deposition, the columns coalesce, and finally after 180 min it is evident that some of big pores begin to close. Thus, when compared to Anopore and AAO, Millipore substrates require longer deposition times to

achieve the stages of film growth (nucleation, island growth, coalescence and column formation), due to the largest pore size.

Table 2. 8 - Average pore and column sizes of porous membranes onto Millipore.

	Pore size ± σ (nm)	Column size ± σ (nm)
Millipore_M_2.55_0_180_O	458 ± 28	1407 ± 262
Millipore_M_2.55_0_90_O	571 ± 103	1176 ± 218
Millipore_M_2.55_0_60_O	593 ± 57	1069 ± 222
Millipore_M_2.55_0_30_O	610 ± 138	568 ± 115

● Power density

The influence of power density and the type of substrate on the surface morphology of aluminum thin films is shown in Figure 2. 18, and the respective average pore and column sizes are summarized in Table 2. 9.
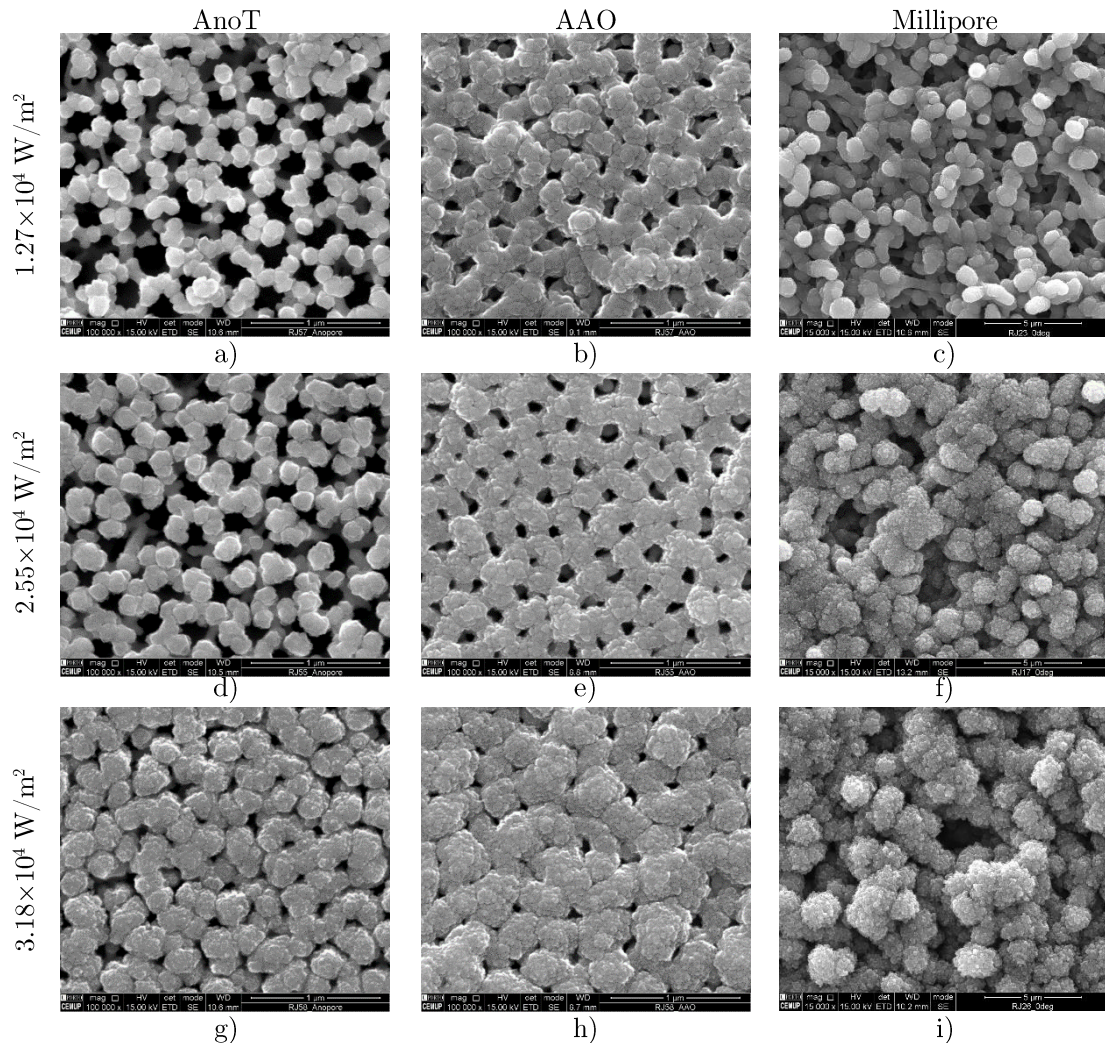
Figure 2. 18 - Morphology of aluminum thin films deposited onto AnoT, AAO and Millipore substrates, according to different power densities: a) AnoT_M_1.27_0_15_O; b) AAO_M_1.27_0_15_O; c) Millipore_M_1.27_0_90_O; d) AnoT_M_2.55_0_15_O; e) AAO_M_2.55_0_15_O; f) Millipore_M_2.55_0_90_O; g) AnoT_M_3.18_0_15_O; h) AAO_M_3.18_0_15_O and i) Millipore_M_3.18_0_90_O.

Table 2. 9 - Average pore and column sizes of aluminum thin films deposited by M with different power densities.

	Pore size $\pm \sigma$ (nm)	Column size $\pm \sigma$ (nm)
AnoT_M_1.27_0_15_O	146 $\pm$ 14	52 $\pm$ 8
AnoT_M_2.55_0_15_O	130 $\pm$ 10	139 $\pm$ 22
AnoT_M_3.18_0_15_O	79 $\pm$ 5	225 $\pm$ 31
AAO_M_1.27_0_15_O	83 $\pm$6	163 $\pm$ 27
AAO_M_2.55_0_15_O	80 $\pm$ 4	183 $\pm$ 27
AAO_M_3.18_0_15_O	48 $\pm$ 3	296 $\pm$ 66
Millipore_M_1.27_0_90_O	776 $\pm$ 174	886 $\pm$ 142
Millipore_M_2.55_0_90_O	571 $\pm$ 103	1176 $\pm$ 218
Millipore_M_3.18_0_90_O	558 $\pm$ 80	1623 $\pm$ 292

Regarding the Anopore substrate, the morphology of the thin film was preferably studied in the top surface of Anopore (AnoT) instead of the bottom surface (AnoB), due to the characteristics of pores and columns.

For all the substrates, the increasing in the power density from 1.27×10^4 W/m^2 to 3.18×10^4 W/m^2, leads to the growth of columns and consequently decreases the pore size. Whatever the substrate material, increasing the power density leads Ar$^+$ to reach the target with higher energy and therefore improve the flux of adatoms in the surface of the substrates. Thus, for the highest power density applied (3.18×10^4 W/m^2), the size of pores are 79, 48 and 558 nm in AnoT, AAO and Millipore, respectively.

● Substrate rotation

SEM images (Figure 2. 19) and average pore and column sizes (Table 2. 10) reveal a decrease in the columns size and consequently an increase of the pore size for the thin films deposited in rotational mode whatever the substrate selected.

With the substrates in the rotational mode (Figure 2. 2), the flux of adatoms reaching the surface varies throughout the cycle. Thus, the energy of adatoms deposited on the substrates far from the target decreases due to the occurrence of more collisions between atoms and Ar$^+$ ions, and some of them are not able to reach the substrate surface [140]. Consequently, the general flux of adatoms reaching the surface is lower in rotational mode than in the static mode. Furthermore, adatoms present at the substrate surface have increased capability to diffuse, tending to eliminate small defects in the thin films and apparently creating smoother surfaces (Figure 2. 19 d), e) and f)).
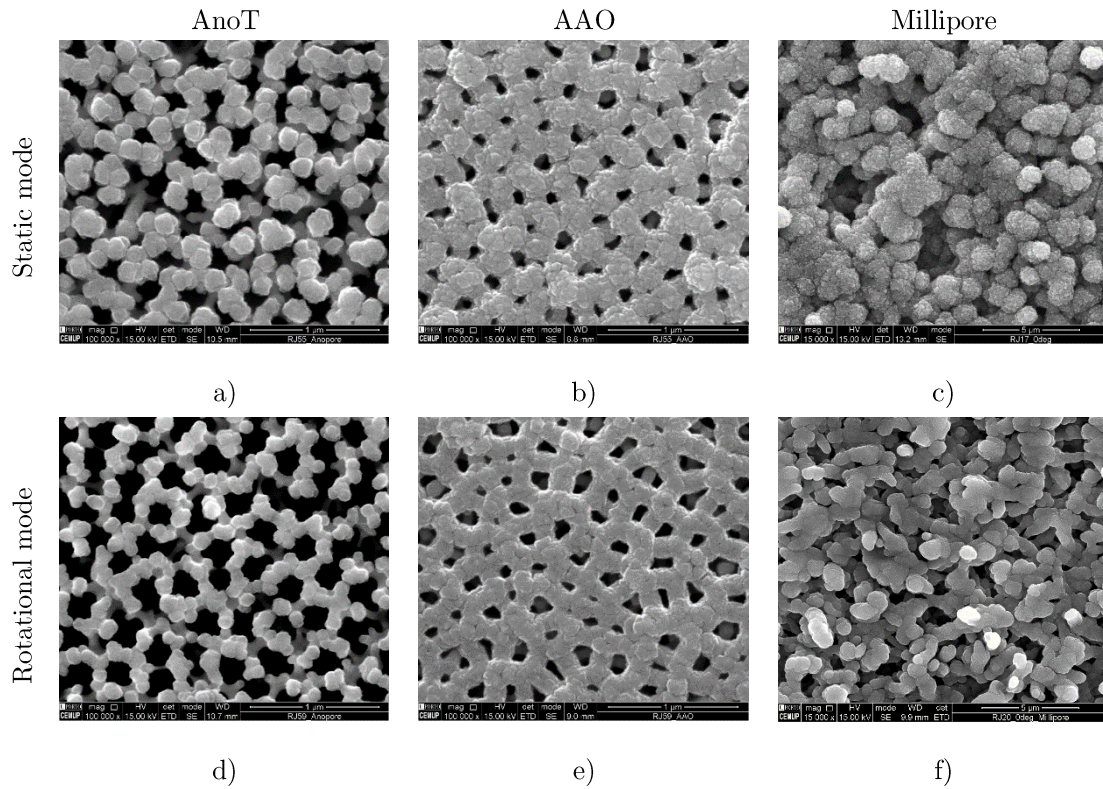
Figure 2. 19 - Morphology of aluminum thin films deposited onto AnoT, AAO and Millipore substrates, in static or rotational mode: a) AnoT_M_2.55_0_15_O; b) AAO_M_2.55_0_15_O; c) Millipore_M_2.55_0_90_O; d) AnoT_M_2.55_0_15_R; e) AAO_M_2.55_0_15_R and f) Millipore_M_2.55_0_90_R.

Table 2. 10 - Average pore and column sizes of aluminum thin films deposited by M in static or rotational mode.

	Pore size $\pm$ σ (nm)	Column size $\pm$ σ (nm)
AnoT_M_2.55_0_15_O	130 $\pm$ 10	139 $\pm$ 22
AnoT_M_2.55_0_15_R	168 $\pm$ 16	114 $\pm$ 17
AAO_M_2.55_0_15_O	80 $\pm$ 4	183 $\pm$ 27
AAO_M_2.55_0_15_R	93 $\pm$ 7	167 $\pm$ 19
Millipore_M_2.55_0_90_O	571 $\pm$ 103	1176 $\pm$ 218
Millipore_M_2.55_0_90_R	711 $\pm$ 161	802 $\pm$ 188

2.2.2.2 Surface area and porosity

The isotherm curves of membranes achieved by nitrogen adsorption, are similar when the thin film is deposited onto AnoB and AAO (Figure 2. 20). Both membranes reveal H4 type hysteresis [137] with non-coincident adsorption and desorption curves. This behavior suggests the occurrence of capillary condensation, with different filling and emptying of pores with the gas. This isotherm curve is common in structures with pores with a large range of sizes. The non stable value of gas volume adsorbed for $P/P_0=1$ suggests that biggest pores are not completely filled of nitrogen.

a)   b)
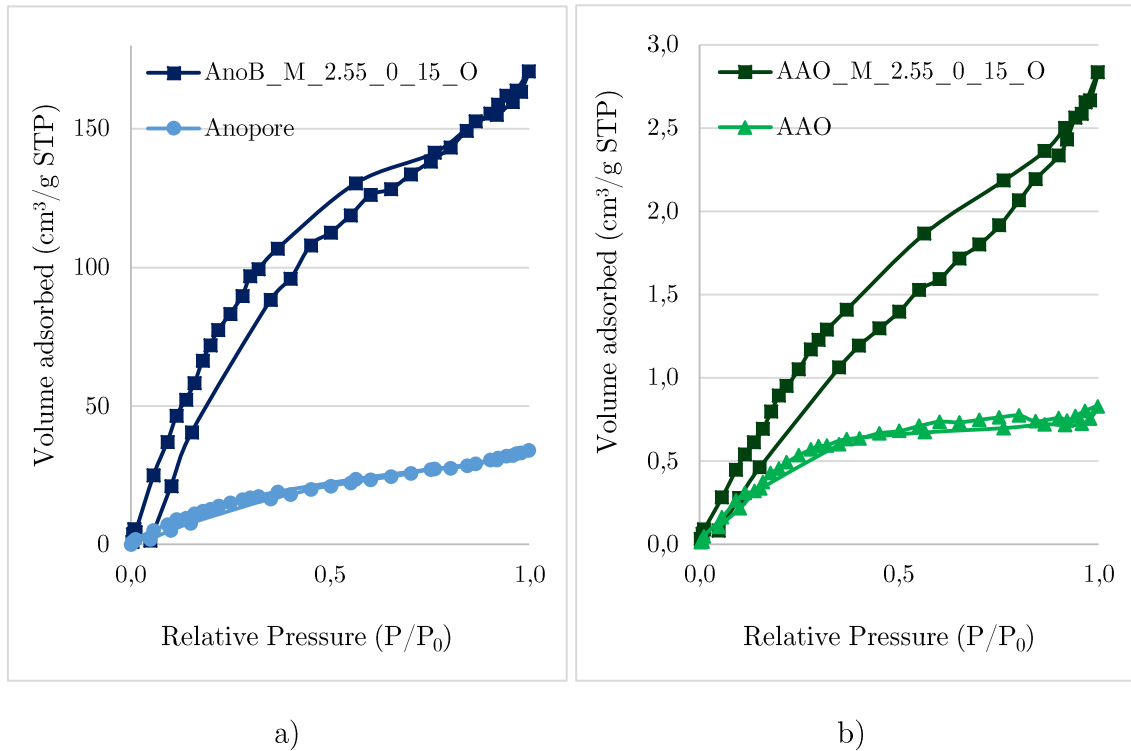
Figure 2. 20 - Nitrogen adsorption isotherms of nanoporous thin films and substrates, deposited by method M onto: a) AnoB and b) AAO.

The adsorbed volume of nitrogen is significantly greater after the sputtering deposition than in the respective substrates. This shows that the aluminum thin film improves the porosity of substrates. Moreover, the BET surface area and the total pore volume (Table 2. 11) are also greater after de coating.

Table 2. 11 - BET surface area and total pore volume of nanoporous structures produced by M and substrates.

	Surface area (m^2/g)	Total pore volume (cm^3/g)
AnoB_M_2.55_0_15_O	410.89	0.2600
Anopore	66.44	0.0530
AAO_M_2.55_0_15_O	5.89	0.0044
AAO	2.40	0.0013

The surface area and pore volume are much higher in AnoB_M_2.55_0_15_O than AAO_M_2.55_0_15_O, mainly due to the porosity characteristics of substrates (surface area $_{ANOPORE}$ > surface area $_{AAO}$ and pore volume $_{ANOPORE}$ > pore volume $_{AAO}$) and to the morphology of aluminum thin films when deposited onto AnoB.

<u>*2.2.2.3 Topography*</u>

The topographic characterization of Al thin films, deposited onto AnoB and AAO, provides further characterization of the surface of nanoporous membranes. AFM 3D images of 1×1 µm² are in agreement with the SEM images (Figure 2. 15 and Figure 2. 16), showing the closure of pores after 30 min of Al deposition onto AnoB, and sharpen and packed Al columns, with a typical zone T morphology (Thornton model [141]) of thin films deposited onto AAO (Figure 2. 21).
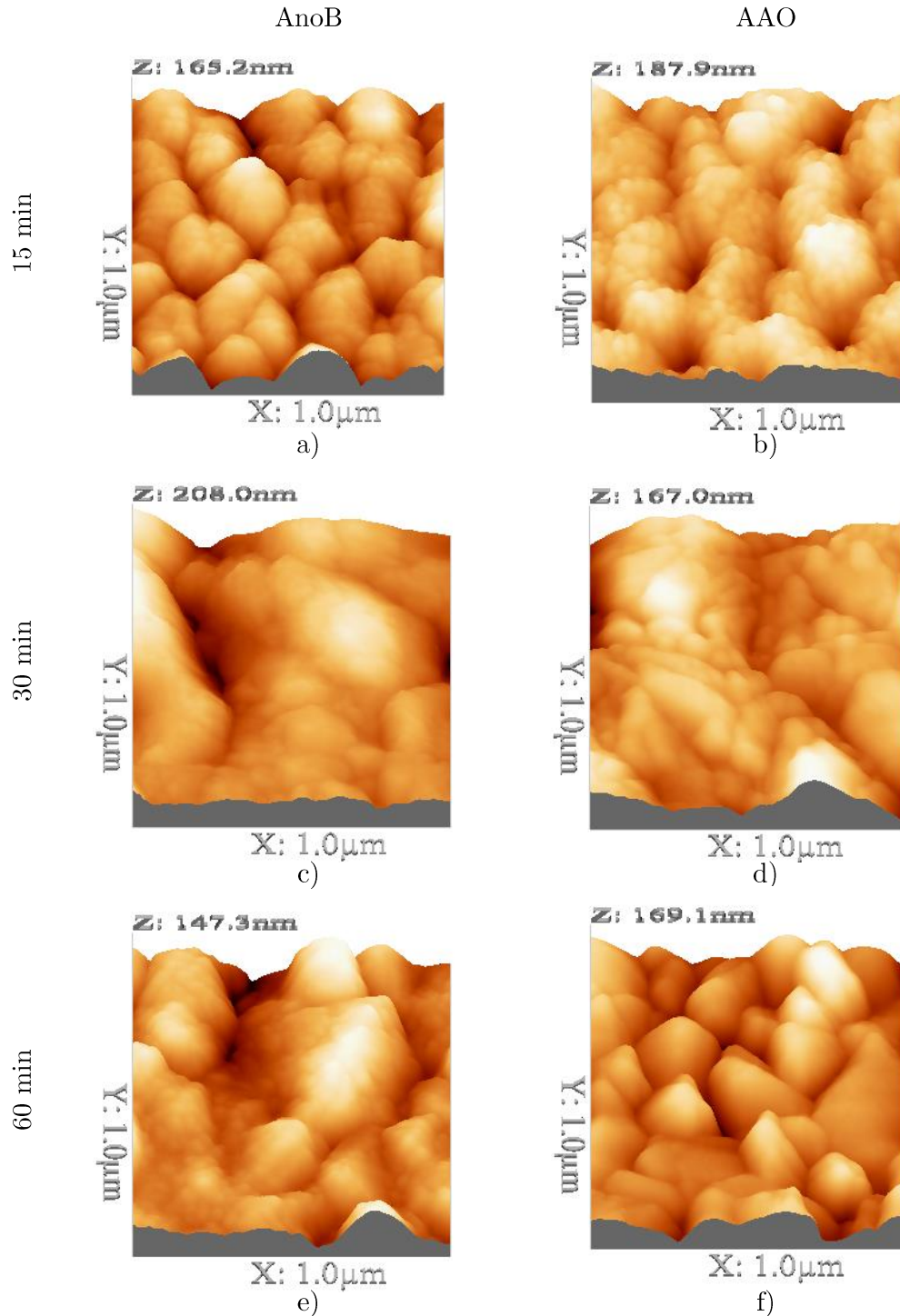
AnoB   AAO

Figure 2. 21 – Topography of nanoporous structures produced by M: a) AnoB_M_2.55_0_15_O; b) AAO_M_2.55_0_15_O; c) AnoB_M_2.55_0_30_O; d) AAO_M_2.55_0_30_O; e) AnoB_M_2.55_0_60_O and f) AAO_M_2.55_0_60_O.

For 15 min of deposition, AFM images reveal larger pore size in thin films deposited onto AAO than AnoB substrate. Moreover, the pore walls of AAO_M_2.55_0_15_O presents a more marked surface texture than those of AnoB_M_2.55_0_15_O, which is corroborated by the highest surface roughness values, S_a = 20 nm and S_{RMS} = 26 nm, for AAO (Table 2. 12). This behavior is in agreement with the substrates roughness (AnoB - S_a = 12 nm and S_{RMS} = 15 nm; AAO - S_a = 21 nm and S_{RMS} = 26 nm), once the trend of thin films is to reproduce the surface of substrate.

Table 2. 12 - Surface roughness of nanoporous structures produced by M.

	S_a (nm)	S_{RMS} (nm)
AnoB_M_2.55_0_15_O	19	24
AnoB_M_2.55_0_30_O	23	31
AnoB_M_2.55_0_60_O	19	25
AAO_M_2.55_0_15_O	20	26
AAO_M_2.55_0_30_O	19	23
AAO_M_2.55_0_60_O	19	25

Regarding the evolution of roughness with the deposition time, *Sun et al.* [138] report that for smaller pore sizes (which is related to longer periods of deposition), the surface roughness decrease. However, surprisingly the evolution of surface roughness of nanoporous structures produced by M over time does not follow a regular trend.

In fact, the roughness of thin films deposited onto AnoB have a slight increase from 15 to 30 min of sputtering deposition and decrease from the 30 to 60 min. During the first stage (15 to 30 min), the pores start to close, keeping some prominent defects, which could contribute to slight increase the surface roughness. The smaller pore sizes and the efforts to reduce such defects through the adatoms diffusion, result in the second stage (30 to 60 min) in the decrease of surface roughness.

Regarding the AAO, there are no significant changes of roughness after the deposition of Al thin film, although some protruded columns start to appear after 60 min of deposition. With the increase of the deposition time, which is correlated to the reduction of pore size (37 nm in 60 min), the roughness of surfaces decrease, which is in accordance with literature.

2.2.2.4 Tomography

Tomography allows a 3D observation of materials, revealing their internal structure. In this particular case, nanotomography is a valuable tool to study the internal morphology of the nanopores and their interconnectivity.

Therefore, the synchrotron X-ray nanotomography, which is a promising technique, was performed to study the internal characteristics of AnoB_M_2.55_0_10_O. Projection images of membrane obtained by the synchrotron X-ray nanotomography (Figure 2. 22)

represent the transmission of X-rays, with the different shades of gray depending on the chemical composition of the material and its thickness. The image of the top of the cylinder clearly shows the three different phases: porous Al_2O_3 substrate (Anopore); nanoporous Al thin films; and YSZ coating (chapter 2.1.2.4). In the extremities, the darkest phase corresponds to YSZ coating with a dense morphology, while the brightest phase is related to the porous Al_2O_3 structure. However, the nanoporous network of the Al thin film sandwiched between Al_2O_3 and YSZ is difficult to analyze.
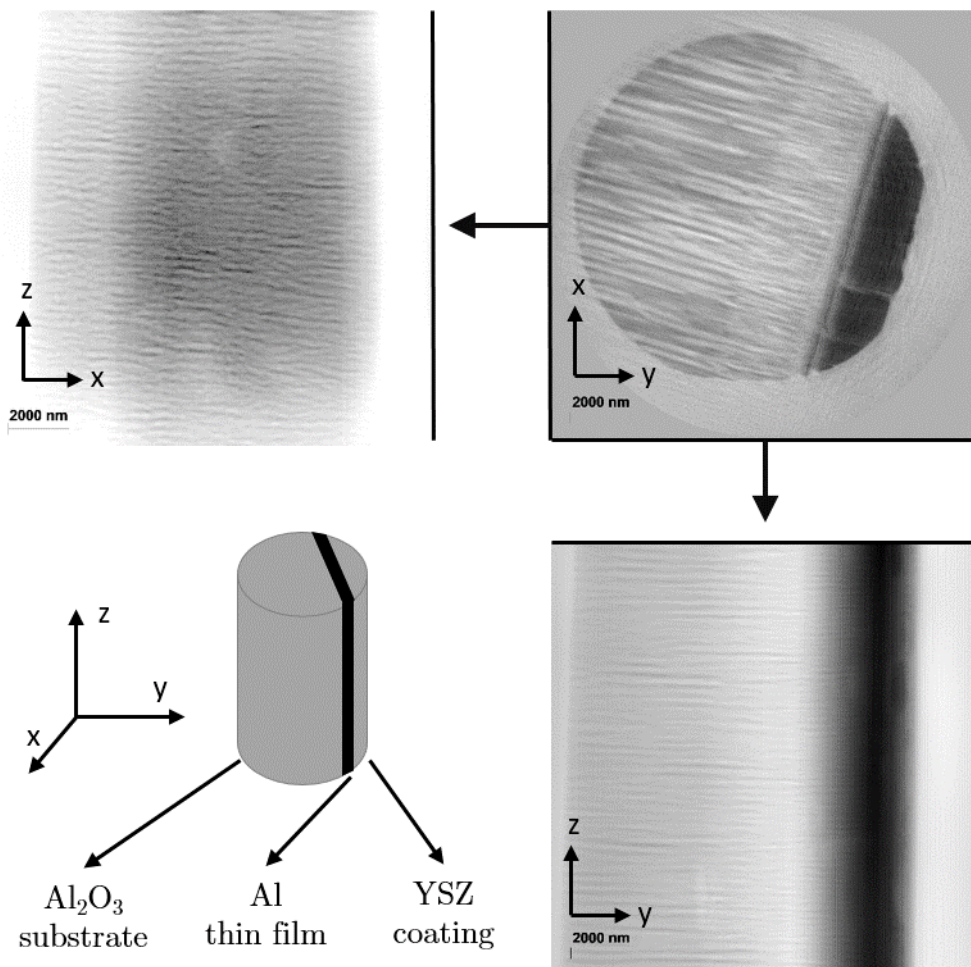
Figure 2. 22 - Projection images of AnoB_M_2.55_0_10_O, with a pixel size of 7 nm.

In fact, the image processing was not completely achieved, contributing to the poor display of the nanoporous structure and consequently becoming impossible a proper 3D reconstruction.

As already referred, the specimen is rotating while the images at different angles are acquired. However, in this experiment the rotation engine had some operational problems, which implies that images were not acquired in the angles where it was supposed to.

Thus, the Octave script[2] was not in accordance with the new positions of images, which did not lead to achieve optimized images.

Despite the porous structure of substrate is clearly visualized, in the top view image and also in the vertical projections of the cylinder, this characterization technique did not allow the expected quality of nanotomographic characterization of nanoporous membranes.

Nevertheless, the FIB nanotomography successfully got the 3D reconstruction of the same membrane, (Figure 2. 23). The 3D images reveal a structure of two-level open porosity, the alumina substrate and the aluminum thin film.

a)   b)
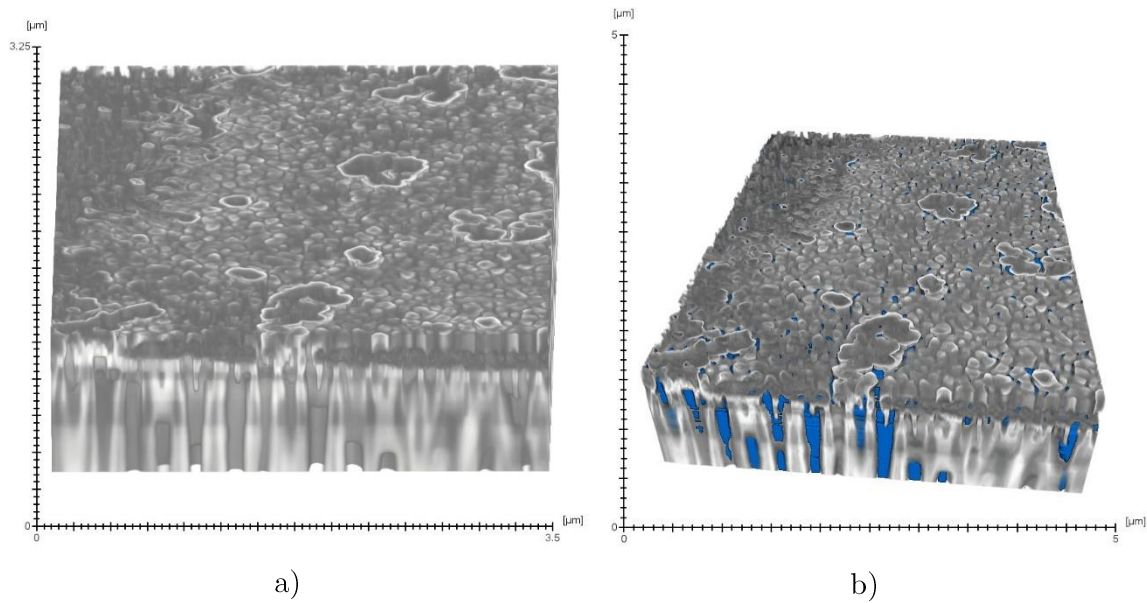
Figure 2. 23 - FIB reconstructed tomographies of AnoB_M_2.55_0_10_O (blue corresponds to the open porosity).

The pore walls of the substrate and the thin film are clearly distinguished from the voids, with the interface region where the substrate ends and the thin film starts being easily noticeable. The thin film gradually decreases the substrate pore size towards the surface, keeping the tunnel structures with the vertical pores, represented with the blue color in Figure 2. 23 b).

In this study, FIB nanotomography allowed to obtain the best resolution images. However both techniques, synchrotron X-ray nanotomography and FIB nanotomography, have advantages and disadvantages. Synchrotron X-ray nanotomography requires the prior preparation of the samples, since they must be as thin as possible allowing X-ray to pass through the material to obtain tomographic images. Conversely, FIB nanotomography does not require any pretreatment of the samples, but usually the technique demands longer periods of analysis. Besides being the

---

[2] The investigation group of ESRF ID16A beamline has developed a sequence of commands in programming language Octave to the phase retrieval.

technique with the highest resolution, FIB nanotomography also provides an overview of the whole material for then selecting the region of interest for a localized analysis. Nevertheless, FIB nanotomography is a destructive technique and if the equipment parameters are not the most suitable, it can degrade the exposed surface making difficult to properly display the material characteristics.

Despite the pointed advantages and disadvantages, both techniques are complementary and must be conducted together in order to contribute to a deeper characterization of the internal structure of material. In this case, to obtain better quality tomographic images by synchrotron X-ray nanotomography, the experimental procedures should be improved.

2.2.3 Nanoporosity by controlling sputtering conditions (F1)

2.2.3.1 Morphology

The morphology of thin films deposited by oblique angle deposition is easily controlled by various deposition parameters. Thus, it is studied the influence of substrate tilt, deposition time, power density, deposition pressure, substrate rotation and reactive sputtering on the nanoporosity of aluminum thin films deposited by F1.

Aluminum thin films were deposited onto both surfaces of Anopore, AAO, Millipore and bulk Si. The morphology of thin films deposited onto AnoB shows a thin layer of aluminum film at the interface substrate/thin film (Figure 2. 24). The small substrate pore size and the high inclination of substrate may be the cause of the U-shaped pores resultant of side wall deposition. By observation of SEM images is difficult to infer if the thin layer is open somewhere or otherwise completely closed. Since in filtering applications is required open porosity, regarding the Anopore substrate, in this study only the thin films deposited onto the top surface of the Anopore will be discussed.

a)   b)
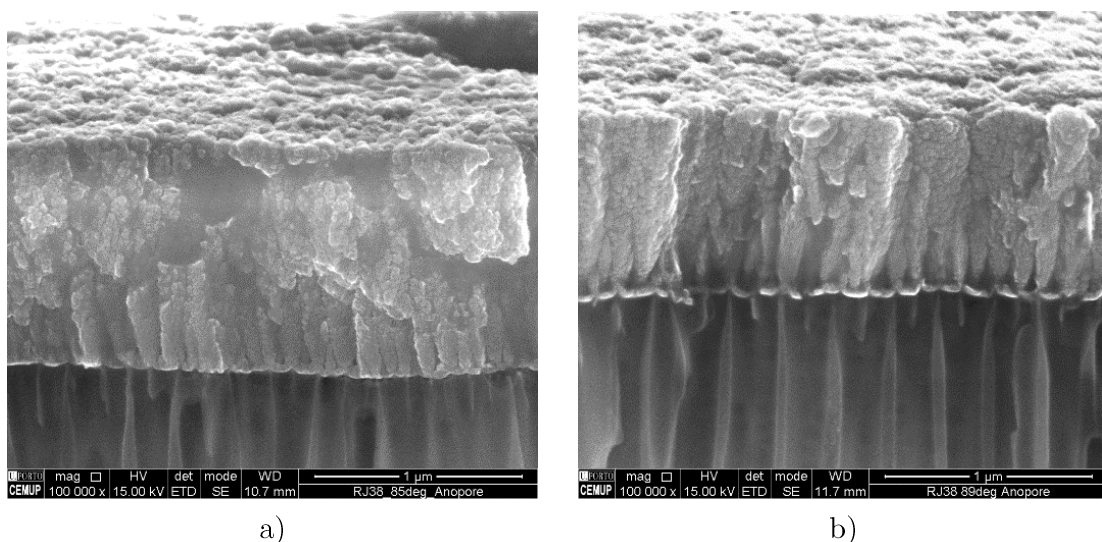
Figure 2. 24 - Cross section SEM images of: a) AnoB_F1_2.55_85_60_O and b) AnoB_F1_2.55_89_60_O.

- <u>Substrate tilt</u>

The morphologies of aluminum thin films deposited onto AnoT, AAO, Millipore and Si by F1 method are revealed by SEM (Figure 2. 25) and the sizes of pores and columns are evaluated by image processing (Table 2. 13). Note that the figures of Millipore substrates have magnification of 10.000 X, while in the other substrates is 100.000 X, due to already referred reasons.

Figure 2. 25 - Morphology of aluminum thin films deposited by method F1 onto AnoT, AAO, Millipore and Si respectively at: a), b), c) and d) 70°; e), f), g) and h) 85° and i), j), k) and l) 89°.

Substrates were placed in tilted positions at 70°, 85° and 89°. However, thin films deposited at 85° serve here as a starting point for comparison with other depositions in different sputtering conditions.[3]

---

[3] The four images (Figure 2. 25 e), f), g) and h)) are highlighted by the red rectangle in order to facilitate the reader consulting, as well as respective pore and column sizes. In addition, in the printable version a bookmark is provided having the same images and respective pore and column sizes.

Morphological images of the thin films deposited onto the four different substrates show the formation of columnar structures. From 70° to 89°, the columns tend to separate creating voids with increased size (AnoT: 21 – 36 nm; AAO: 32 – 54 nm; Millipore: 357 – 459 nm and Si: 30 – 45 nm).

In bibliography is clear that the substrate angle tilt dramatically alters the thin film morphology, due to the shadow effect [89]. In fact, the increasing of tilt angle results in an increased shadow length. Therefore, the spaces between columns (pores) increase and the thin films become more porous.

In contrast, the size of columns decreases, with the increase of the substrate tilt. The relationship between column size and substrate angle tilt seems to be inconsistent in literature. Some researchers refer a tendency of increased column size with substrate tilt [142], while others suggest the opposite [143]. Thus, this dependence could be related to specific characteristics of each material, resulting in different behaviors during sputtering deposition, e.g. surface diffusion.

Table 2. 13 - Average pore and column sizes of aluminum thin films deposited by F1 with different substrate tilts.

	Pore size ± σ (nm)	Column size ± σ (nm)
AnoT_F1_2.55_70_60_O	21 ± 3	146 ± 33
AnoT_F1_2.55_85_60_O	31 ± 3	101 ± 16
AnoT_F1_2.55_89_60_O	36 ± 3	81 ± 21
AAO_F1_2.55_70_60_O	32 ± 3	473 ± 79
AAO_F1_2.55_85_60_O	49 ± 3	313 ± 68
AAO_F1_2.55_89_60_O	54 ± 4	283 ± 72
Millipore_F1_2.55_70_60_O	357 ± 28	1018 ± 150
Millipore_F1_2.55_85_60_O	433 ± 31	976 ± 206
Millipore_F1_2.55_89_60_O	459 ± 33	886 ± 135
Si_F1_2.55_70_60_O	30 ± 3	125 ± 24
Si_F1_2.55_85_60_O	39 ± 3	113 ± 20
Si_F1_2.55_89_60_O	45 ± 3	106 ± 18

Therefore, two important mechanisms affect the morphology of thin films produced by oblique angle deposition: the shadow effect and the adatoms surface diffusion.

Besides the shadow effect, the surface diffusion also plays an important role in the growth of aluminum thin films produced by F1, due to the relative low meting point of aluminum (933 K), when compared to other metallic elements. Therefore, although aluminum thin films exhibit porosity with a pore size dependence of the substrate tilt, the columns are not isolated, as would be expected for such large angles. Cross section images of aluminum thin films deposited at 85° and 89° onto AnoT and AAO porous substrates (Figure 2. 26) reveal the nanoporous columnar structures with packed and merged columns, as a result of high surface diffusion.

AnoT   AAO

a)   b)

c)   d)
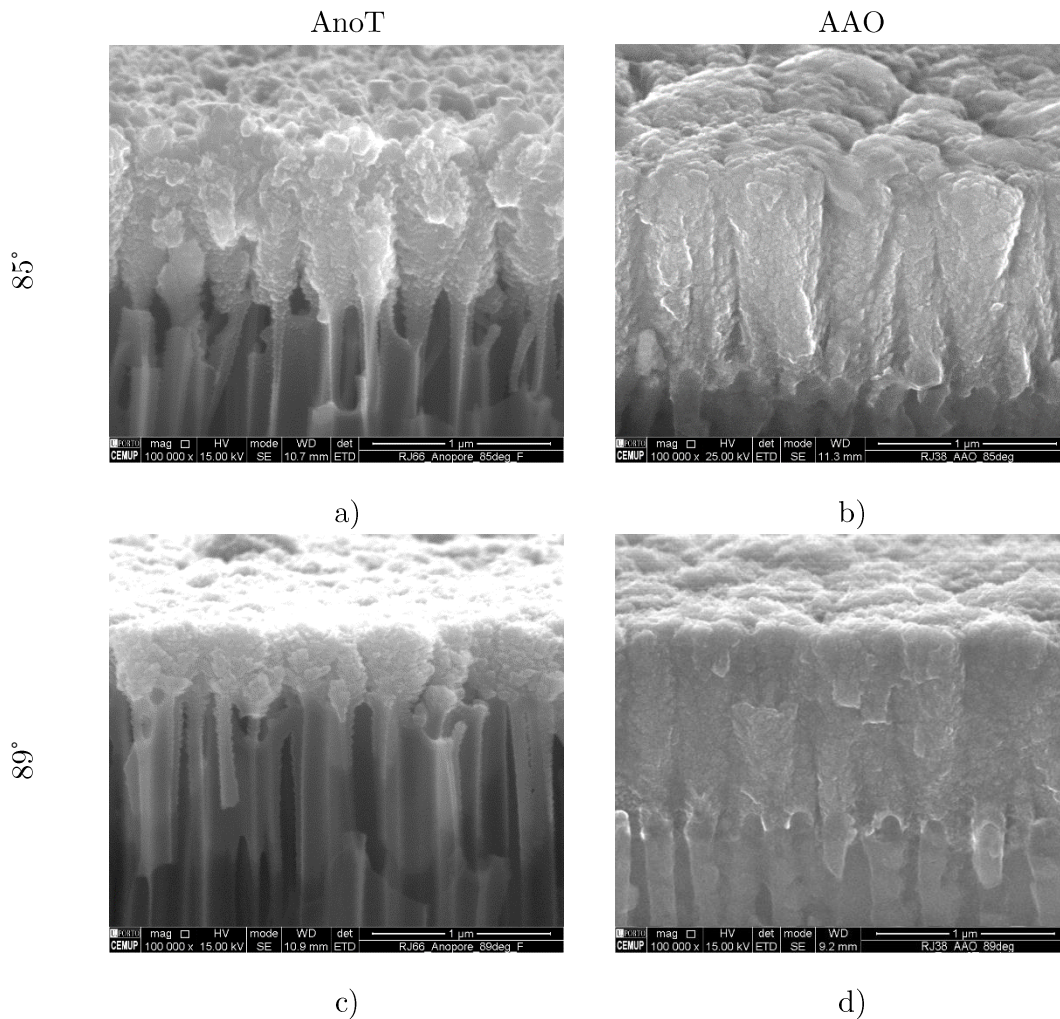
Figure 2. 26 - Cross section images of aluminum thin films deposited at 85° onto: a) AnoT and b) AAO
and at 89° onto: c) AnoT and d) AAO.

Moreover, columns are positioned almost perpendicularly to the substrate surface despite the deposition angles being almost 90°, while in literature usually the inclination of columns in other materials is much more pronounced [144]. This morphology can be explained by the surface trapping mechanism, which contradicts the atom straight trajectory of ballistic model, but instead considers that when atoms pass very close to the surface, their trajectory can be modified, with atoms being deposited at nearby locations.

Another factor must be also considered, the fact that the large area of material target contributes to large angular deposition flux distribution, which ultimately results in a sum of deposition material from diverse directions.

Aluminum thin films deposited by F1 present thicknesses of around 850 nm (85°) and 400 nm (89°) for AnoT substrates and around 1300 nm (85°) and 1000 nm (89°) for AAO substrates. Thus as expected, by increasing the tilt angle the thickness of thin films decreases, with thin films deposited onto AAO having larger thicknesses due to greatest surface density of substrate (bigger pore walls).

• Deposition time

Although it is reported that there are no correlation between some deposition parameters (e.g. gas pressure, power density, target-substrate distance...) [144] and the morphology of thin films, this study attempts to analyze in detail their role, when the substrate has controlled porosity.

The effect of deposition time on the morphology of thin films deposited by F1 is exhibited in SEM images of Figure 2. 27 (note that the figures of Millipore substrates have magnification of 10.000 X, while in the other substrates is 100.000 X) and respective pore and column sized are listed in Table 2. 14.

Within the four different substrates, different growing mechanisms are found. For the thin films deposited onto AnoT and Si, both the pore and the column sizes present a tendency to increase. Due to the competitive growth, characteristic of oblique angle depositions, some columns tend to extinguish because of high shadows of other columns, and some are even combined, forming larger single columns, becoming the columns much larger and consequently the voids between columns (pores) also increase in size, over time.

The same growing mechanism is observed in thin films deposited onto AAO, with the pore size increasing for longer periods of deposition. However, the size of columns does not follow the same principle. As the AAO substrates present sufficiently large pore walls, increasing the deposition time contributes to improve the roughness of the columns. This leads to the column bifurcation, where various small sub-columns grow on the surface of the column. Therefore, the final column size measured by the image processing software for 60 and 90 min, in fact corresponds to the size of the sub-columns, instead of the main columns.
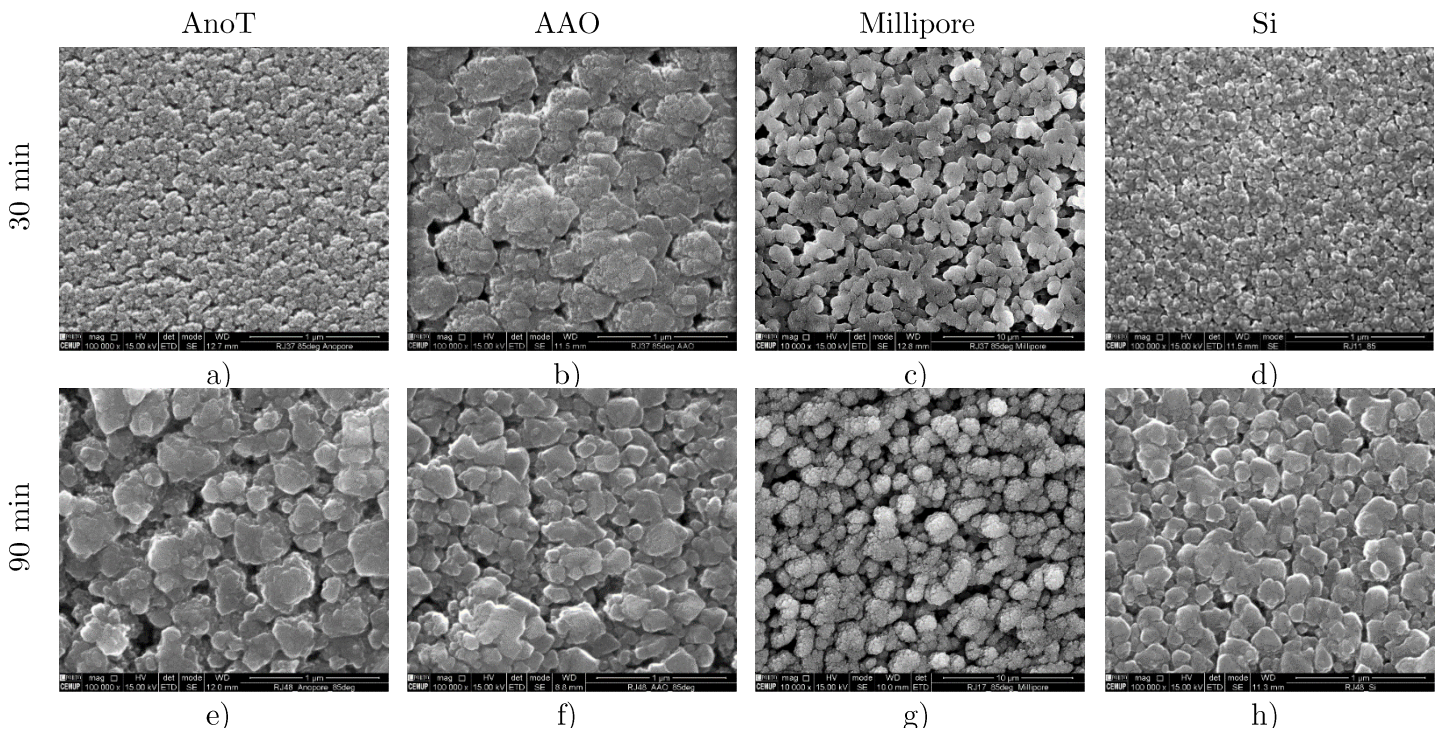
Figure 2. 27 - Morphology of aluminum thin films deposited by method F1 onto AnoT, AAO, Millipore and Si respectively during: a), b), c) and d) 30 min and e), f), g) and h) 90 min.

Table 2. 14 - Average pore and column sizes of aluminum thin films deposited by F1 with different times of deposition.

	Pore size $\pm$ σ (nm)	Column size $\pm$ σ (nm)
AnoT_F1_2.55_85_30_O	21 ± 3	93 ± 19
AnoT_F1_2.55_85_90_O	52 ± 3	307 ± 73
AAO_F1_2.55_85_30_O	48 ± 3	341 ± 78
AAO_F1_2.55_85_90_O	50 ± 4	213 ± 44
Millipore_F1_2.55_85_30_O	622 ± 102	931 ± 221
Millipore_F1_2.55_85_90_O	579 ± 67	1429 ± 263
Si_F1_2.55_85_30_O	17 ± 3	47 ± 7
Si_F1_2.55_85_90_O	41 ± 3	170 ± 54

The Millipore substrate exhibits another different growing mechanism. Due to their large average pore size (641 nm) the pore walls where the thin film can grow, are very distant. This suggests that for the first 60 min of deposition, adatoms try to decrease the pore size as happens with thin films deposited onto Millipore by M method, which is accompanied with an increase in the column size. However, from 60 to 90 min of deposition the pore size presents a different growing trend, with pore becoming larger. This indicates that it is most likely that at this point the competitive growth mediates the thin film growth, such as in thin films deposited onto AnoT and Si, with pores and columns increasing their size.

Therefore, it is clear that besides the deposition parameters, also the morphology of substrates plays a key role in the final morphology of the thin films.

● Power density

The power density is another deposition parameter that influences the morphology of thin films (Figure 2. 28).

For AnoT and Si substrates, by increasing the power density, the sizes of columns and pores increase (Table 2. 15). In fact, the greatest flux of adatoms reaching the surface may interfere with their surface diffusion which may lead to the initial creation of larger islands and consequently larger columns. SEM images also reveal that apparently the decrease in the number of pores, although with larger sizes, is related to the increase of the power densities. This is more evident in the AnoT_F1_3.18_85_60_O, where columns are merged and few pores are visible.

The same morphology evolution with the power density is observed in Al thin films deposited onto AAO. However the column size decreases by increasing the power density, which is due to the columns bifurcation. Similar behavior is observed with the increase of the deposition time.

	AnoT	AAO	Millipore	Si

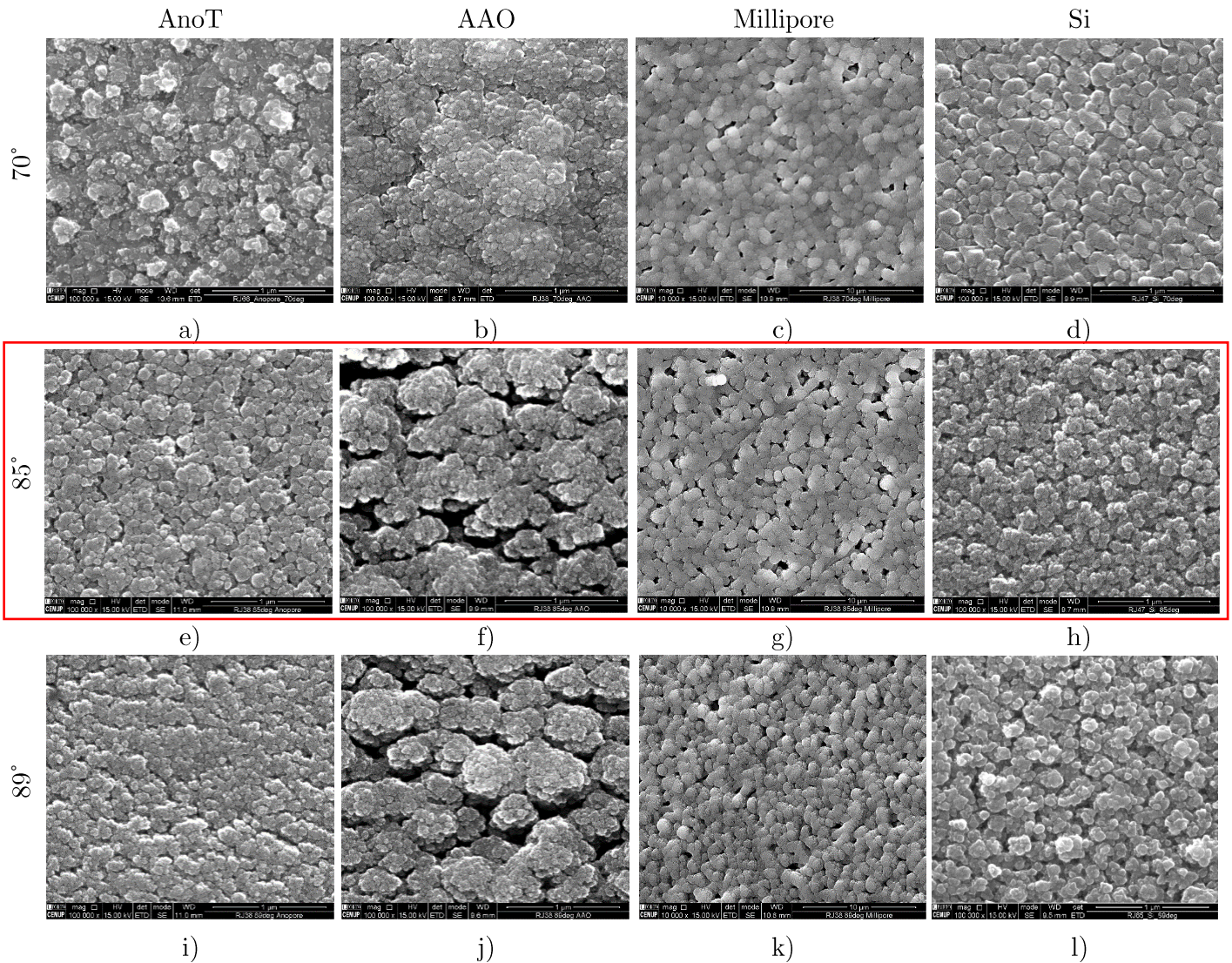<div align="center">a)   b)   c)   d)</div>

<div align="center">e)   f)   g)   h)</div>
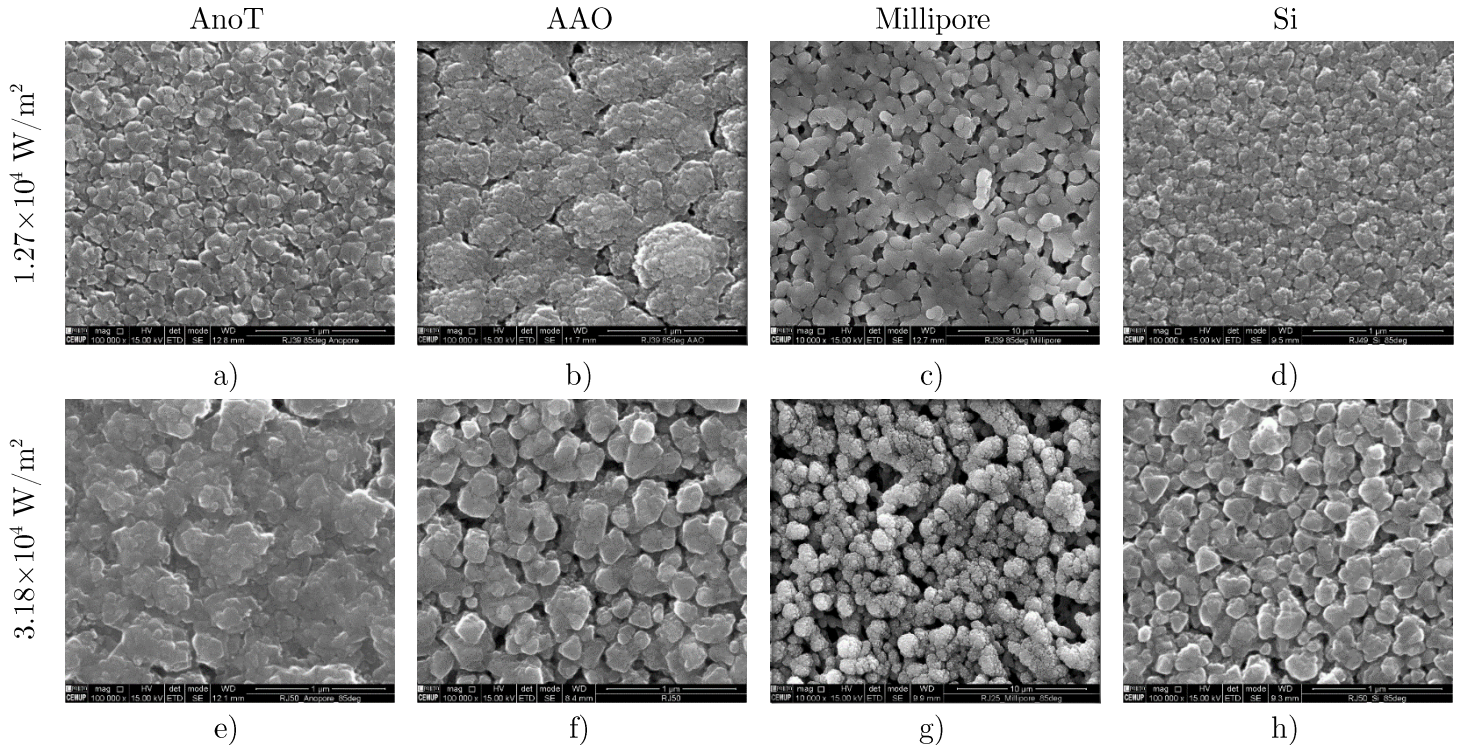
Figure 2. 28 - Morphology of aluminum thin films deposited by method F1 onto AnoT, AAO, Millipore and Si respectively with different power densities: a), b), c) and d) 1.27×10^4 W/m^2 and e), f), g) and h) 3.18×10^4 W/m^2.

Table 2. 15 - Average pore and column sizes of aluminum thin films deposited by F1 with different power densities.

	Pore size ± σ (nm)	Column size ± σ (nm)
AnoT_F1_1.27_85_60_O	19 ± 3	35 ± 7
AnoT_F1_3.18_85_60_O	45 ± 2	388 ± 46
AAO_F1_1.27_85_60_O	25 ± 3	332 ± 100
AAO_F1_3.18_85_60_O	75 ± 6	223 ± 50
Millipore_F1_1.27_85_60_O	534 ± 70	946 ± 197
Millipore_F1_3.18_85_60_O	634 ± 100	1247 ± 190
Si_F1_1.27_85_60_O	18 ± 3	96 ± 22
Si_F1_3.18_85_60_O	56 ± 3	140 ± 36

Although, the columns size of the thin films deposited onto Millipore has the same increasing trend of the other substrates when the power density increases, the pore size reveals no-dependence with power density, decreasing from 1.27×10^4 to 2.55×10^4 W/m^2 and increasing from 2.55×10^4 to 3.18×10^4 W/m^2. The same behavior was also detected by increasing the deposition time and it is a result of the substrate morphology itself. Moreover, the highest power density induces an increase in the columns roughness in the thin films deposited onto Millipore, which is the opposite of that observed for the other substrates.

• Deposition pressure

During the deposition, before the atoms reach the substrate they experience a significant number of collisions with gas particles. The distance between the target and the first collision is designated by mean free path. By increasing the deposition pressure, the probability of a vapour specie to collide with a gas particle increases while the mean free path shortens. When the collision occurs, the trajectory of species changes resulting in an angular divergent flux. This divergent flux, which is a result of increased gas pressure, suppresses the shadow effect created by tilting the substrates and the resultant morphology is unpredictable. In fact, *Barranco et al.* have already referred the no-correlation between the gas pressure and the morphology of thin films [144].

Therefore, the changing on the deposition pressure from 0.7 to 1.7 Pa leads to different growth mechanisms of aluminum thin films in selected substrates (Figure 2. 29).

By increasing the deposition pressure, pores become broader in AnoT and Millipore and narrower in AAO and Si. In contrast, columns sizes are enlarged for AnoT and reduced for AAO, Millipore and Si (Table 2. 16).
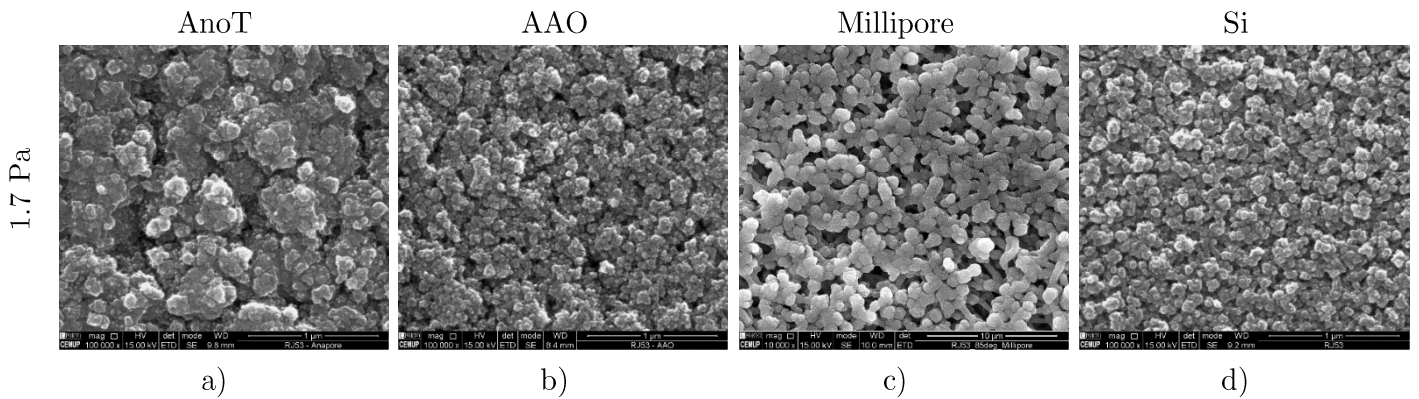
Figure 2. 29 - Morphology of aluminum thin films deposited by method F1 with a deposition pressure of 1.7 Pa onto: a) AnoT, b) AAO, c) Millipore and d) Si.

Table 2. 16 - Average pore and column sizes of aluminum thin films deposited by F1 with increased gas pressure of 1.7 Pa.

	Pore size $\pm$ σ (nm)	Column size $\pm$ σ (nm)
AnoT_F1_2.55_85_60_1.7Pa	45 ± 4	333 ± 67
AAO_F1_2.55_85_60_1.7Pa	40 ± 3	131 ± 31
Millipore_F1_2.55_85_60_1.7Pa	506 ± 43	906 ± 212
Si_F1_2.55_85_60_1.7Pa	24 ± 3	68 ± 11

● Substrate rotation

The rotation of the substrates modifies the distance target-substrate and the vapour flux direction and density, leading to a thin film growing from different directions. For longer target-substrate distances, the flux of adatoms reaching the substrate surface has a lower energy due to the collisions with Ar^+ ions. Furthermore, some adatoms cannot even reach the substrate. Thus, the adatoms arriving the surface are not enough to produce a compact thin film, which contributes to improve porosity (Figure 2. 30).

Therefore, the pore size is larger in rotational than in static mode for AnoT, AAO and Millipore (Table 2. 17). However, this does not occur in thin films deposited onto bulk Si, in which the pore size is smaller in rotational mode.

Conversely and as a consequence of larger pores, the column size is smaller in rotational than in the static mode, with an exception to the thin films deposited onto AnoT. Figure 2. 30 a) of AnoT_F1_2.55_85_60_R suggests that small columns have merged and formed large isolated columns.
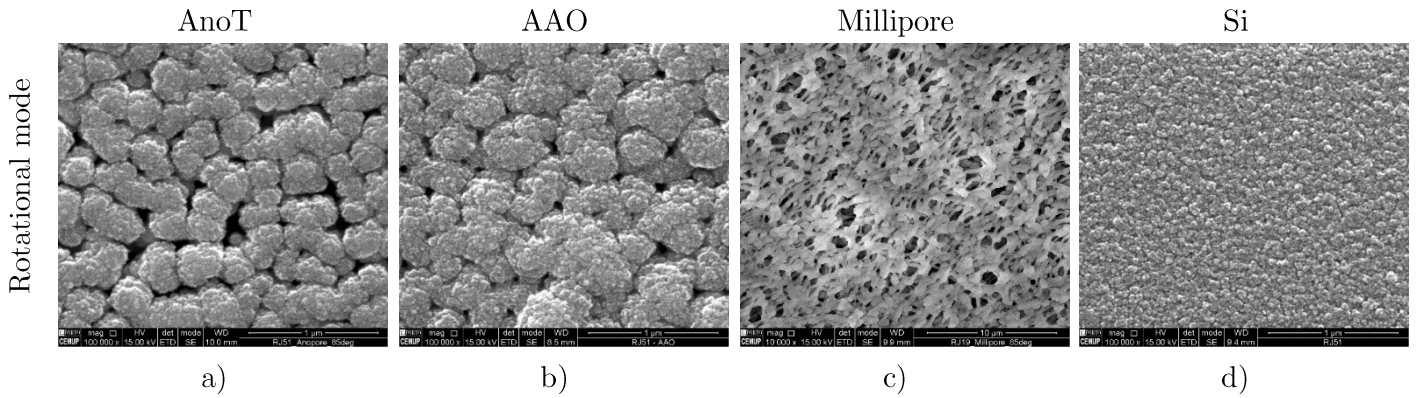
Figure 2. 30 - Morphology of aluminum thin films deposited by method F1 in rotational mode onto: a) AnoT, b) AAO, c) Millipore and d) Si.

Table 2. 17 - Average pore and column sizes of aluminum thin films deposited by F1 in rotational mode.

	Pore size $\pm$ σ (nm)	Column size $\pm$ σ (nm)
AnoT_F1_2.55_85_60_R	73 $\pm$ 6	252 $\pm$ 45
AAO_F1_2.55_85_60_R	52 $\pm$ 3	271 $\pm$ 74
Millipore_F1_2.55_85_60_R	500 $\pm$ 50	429 $\pm$ 192
Si_F1_2.55_85_60_R	15 $\pm$ 3	46 $\pm$ 12

Regarding the thickness of thin films, in rotational mode the Al films are thinner, being 250 nm in AnoT (static mode: 850 nm) and 400 nm in AAO (static mode: 1300 nm).

AnoT   AAO

a)   b)

c)   d)
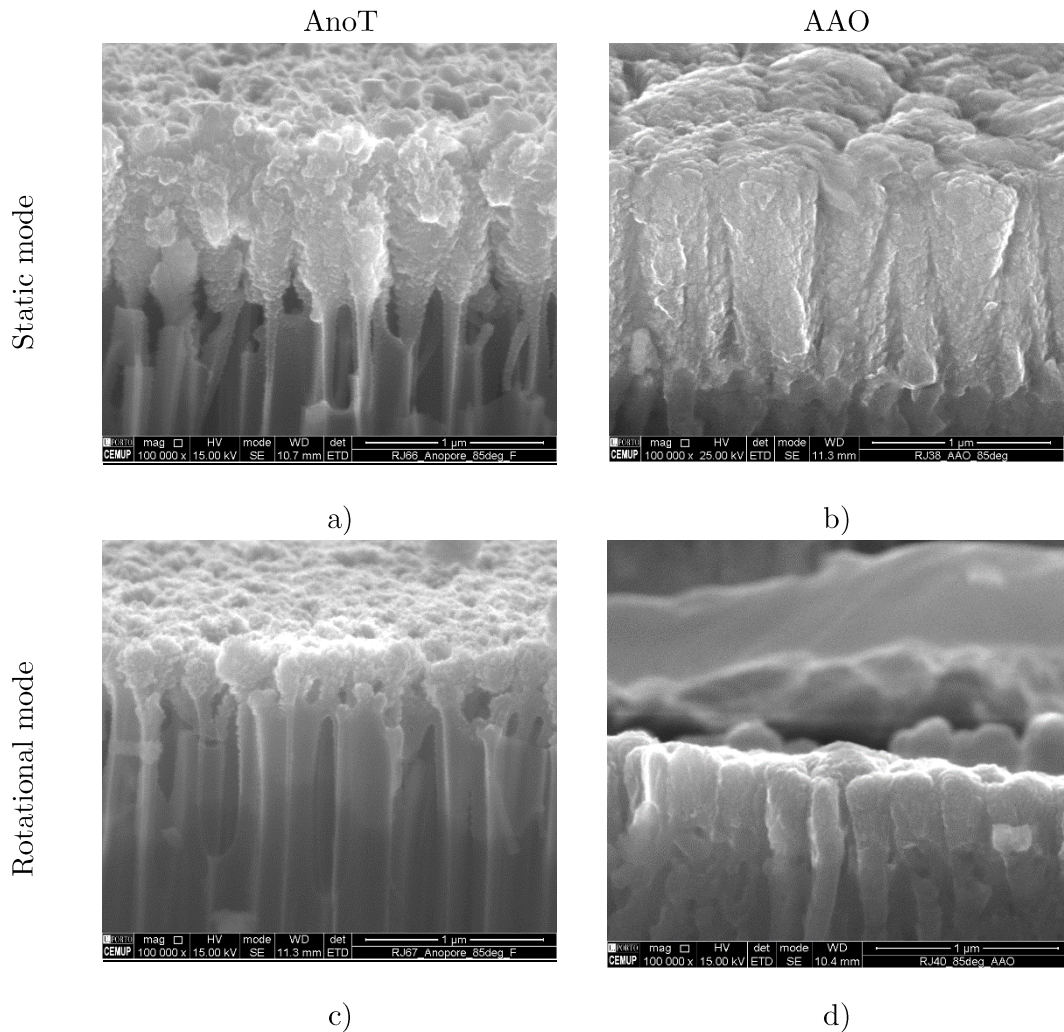
Figure 2. 31 - Cross section images of aluminum thin films deposited in static mode onto: a) AnoT and b) AAO and in rotational mode onto: c) AnoT and d) AAO.

● <u>Reactive sputtering</u>

The reactive sputtering deposition obliges to the introduction of new gaseous species (Nitrogen) in the chamber and consequently promotes chemical reactions between reactive gas and vapour species resulting from the target. New chemical compounds are deposited at the surface of substrates, originating a thin film with different morphology.

By adding 5% of Nitrogen into the chamber with Argon (deposition pressure constant) induces different morphologies on the surface of the columns (Figure 2. 32). Reactive deposition reveals for all the studied substrates, a smoother surface at the top of the columns, than in the thin films deposited with 100% of Ar. However, the reactive sputtering leads to nonlinear effects in the pore and column sizes. By depositing with gas composition of 95% Ar + 5% N, the pore size decreases in AAO and Si and increases in AnoT and Millipore. In addition, the column size increases for all the substrates studied.

AnoT   AAO   Millipore   Si

a)   b)   c)   d)
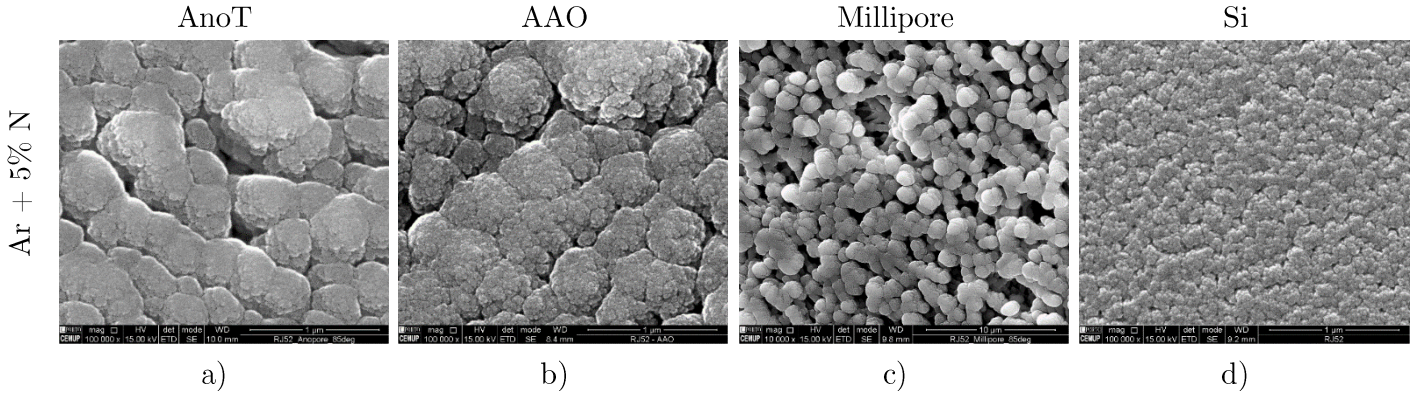
Figure 2. 32 - Morphology of aluminum thin films deposited by method F1 with a chamber gas composition of Ar + 5% N onto: a) AnoT, b) AAO, c) Millipore and d) Si.

Table 2. 18 - Average pore and column sizes of aluminum thin films deposited by F1 with 5% of N.

	Pore size ± σ (nm)	Column size ± σ (nm)
AnoT_F1_2.55_85_60_5%N	49 ± 3	367 ± 97
AAO_F1_2.55_85_60_5%N	42 ± 3	397 ± 162
Millipore_F1_2.55_85_60_5%N	641 ± 90	1018 ± 160
Si_F1_2.55_85_60_5%N	18 ± 3	124 ± 33

2.2.3.2 Surface area and porosity

The influence of the substrate material and the angle of deposition on the porosity of nanoporous thin films deposited by F1 method, were studied through the nitrogen adsorption isotherms (Figure 2. 33), the BET surface area and the total pore volume (Table 2. 19).

The nitrogen adsorption isotherms of substrates and nanoporous thin films are similar and type H4 [137], according to IUPAC. The hysteresis of adsorption/desorption curves reveals the possible occurrence of capillary condensation, with different filling and emptying of pores.

For the same deposition parameters (2.55×10^4 W/m², 85°, 60 min), different substrates lead to similar adsorption isotherm profiles, despite the different volume adsorbed. The volume adsorbed by the nanoporous thin films deposited by F1 on AnoT substrates is greater than on AAO or Si (Si_F1_2.55_85_60_O < AAO_F1_2.55_85_60_O < AnoT_F1_2.55_85_60_O). According to these results, the BET surface area and the total pore volume are also greatest for AnoT_F1_2.55_85_60_O, while thin films deposited onto Si reveal the lowest surface area and total pore volume.

Similar behavior is in accordance with the volume adsorbed, BET surface area and total pore volume of substrates, being Si (non-porous) < AAO < Anopore, highlighting the role of substrates in the morphology and porosity of nanoporous thin films.

With the increase of the substrate tilt from 85° to 89°, in Anopore substrate some prominent and almost isolated columns emerge from the thin film, resulting in increased volume adsorbed, BET surface area and total pore volume.
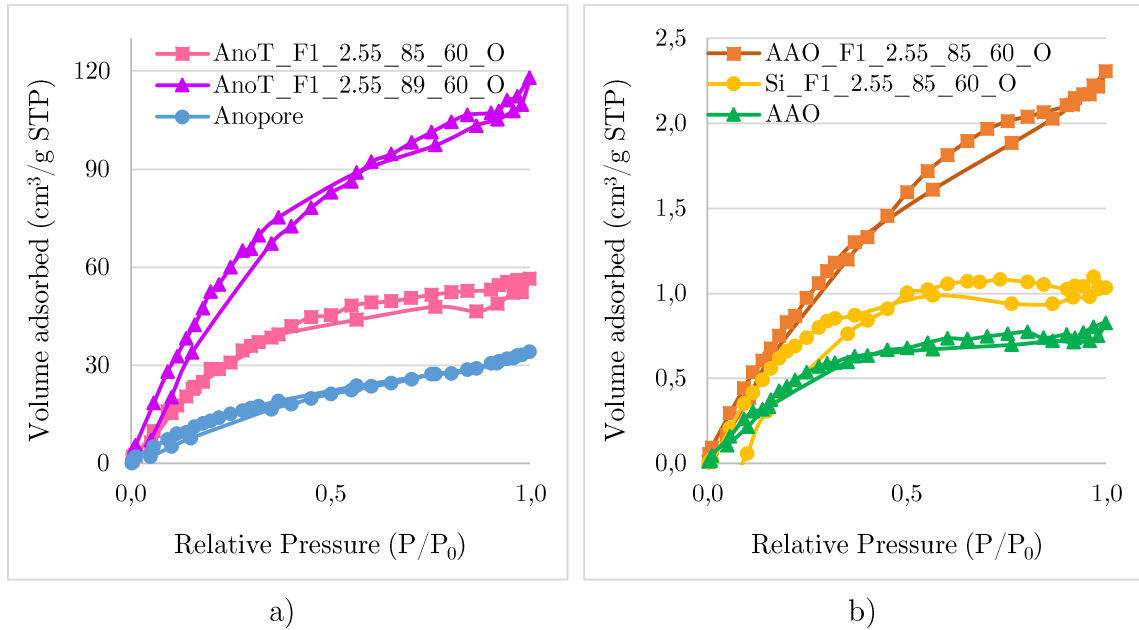
Figure 2. 33 - Nitrogen adsorption isotherms of nanoporous thin films and substrates, deposited by method F1 onto: a) AnoT and b) AAO and Si.

Table 2. 19 – BET surface area and total pore volume of nanoporous structures produced by F1 and substrates.

	Surface area (m²/g)	Total pore volume (cm³/g)
AnoT_F1_2.55_85_60_O	148.53	0.0880
AnoT_F1_2.55_89_60_O	285.14	0.1800
Anopore	66.44	0.0530
Si_F1_2.55_85_60_O	3.61	0.0016
AAO_F1_2.55_85_60_O	4.86	0.0036
AAO	2.40	0.0013

2.2.3.3 Topography

The topography and surface roughness of thin films deposited onto AnoT, AAO and Si tilted 85° and 89° are exhibited in Figure 2. 34 and Table 2. 20, respectively.

AFM scans of 1×1 μm² reveal the largest column size of thin films deposited onto AAO, while for AnoT and Si, the columns of thin films have the smallest sizes. Moreover, larger distances between peak and valley (pores) are detected in thin films which substrates are placed in tilter angles. In fact, the results of these topographic images are in accordance with SEM morphological images.
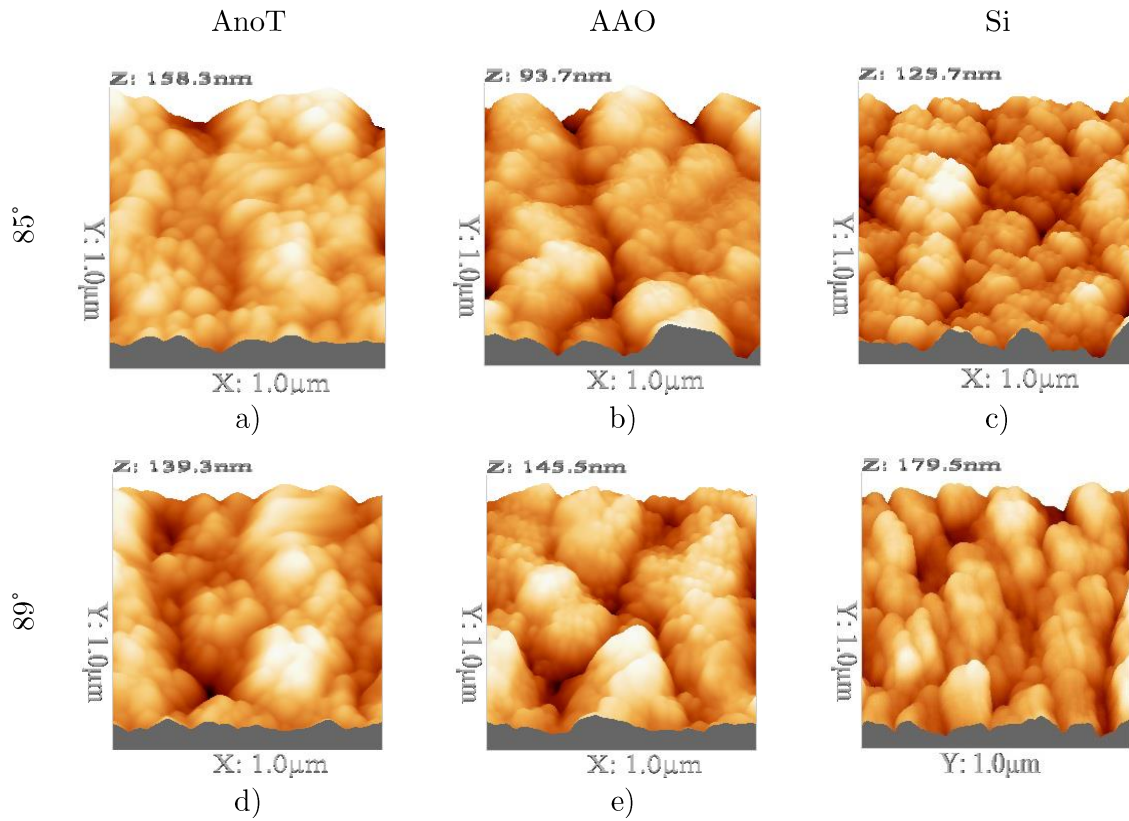
Figure 2. 34 - Topography of nanoporous structures produced by F1: a) AnoT_F1_2.55_85_60_O; b) AAO_F1_2.55_85_60_O; c) Si_F1_2.55_85_60_O; d) AnoT_F1_2.55_89_60_O; e) AAO_F1_2.55_89_60_O and f) Si_F1_2.55_89_60_O.

Table 2. 20 - Surface roughness of nanoporous structures produced by F1.

	S_a (nm)	S_{RMS} (nm)
AnoT_F1_2.55_85_60_O	15	19
AnoT_F1_2.55_89_60_O	19	24
AAO_F1_2.55_85_60_O	11	14
AAO_F1_2.55_89_60_O	21	26
Si_F1_2.55_85_60_O	16	20
Si_F1_2.55_89_60_O	22	28

By increasing the substrate tilt, the shadow effect is more pronounced leading to the expansion of pores size, which invariably gives rise to bigger pores [89]. This is expressed by the surface roughness values, which increases with increasing of the pore size and the substrate tilt from 85° to 89°, in AnoT, AAO and Si substrates.

Thin films tend to mimic the substrate surface, however for longer deposition times (thicker films) the substrate plays no influence, with the thin film imposing its own morphology and roughness. This is clearly shown in Table 2. 20, where the surface roughness of the thin films are completely independent of the surface roughness of

substrates (AnoT – S_a = 10 nm and S_{RMS} = 12 nm; AAO – S_a = 21 nm and S_{RMS} = 26 nm and Si - S_a = 1 nm and S_{RMS} = 1 nm).

2.2.3.4 Tomography

Nanotomography of nanoporous thin films (AnoT_F1_2.55_85_60_O, AnoT_F1_2.55_89_60_O and AnoT_F1_2.55_85_60_R) produced by F1 method were analyzed by synchrotron X-ray and FIB nanotomography.

The images of nanoporous structures of thin films analyzed by synchrotron X-ray nanotomography with 7 nm of pixel size are shown in Figure 2. 35, Figure 2. 36 and Figure 2. 37. The low quality of some projection images is manly related to the unsuccessful image processing, as already reported in chapter 2.2.2.4.

In spite of the synchrotron X-ray nanotomography image limitations, in all the three nanoporous thin films is visible the semi-cylindrical structure with different X-ray transmissions. The brightest phases are characteristic of porous alumina substrates and conversely the darkest phases are related to nanoporous aluminum thin films. These two phases are clearly discerned in the top view images, while in the vertical projections the limited quality precludes further detailed analysis.
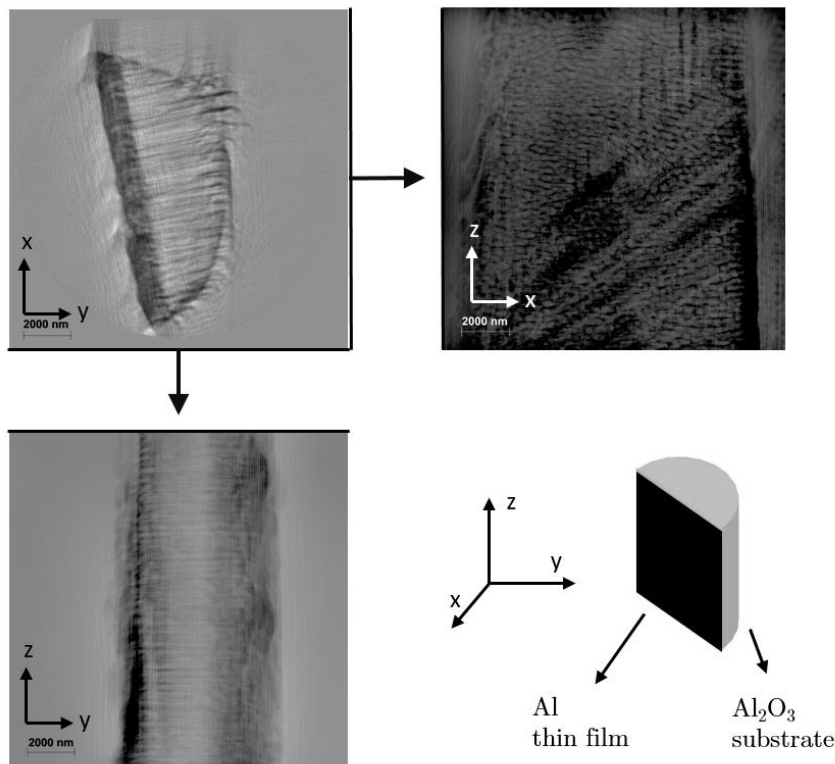
Figure 2. 35 - Projection images of AnoT_F1_2.55_85_60_O, with a pixel size of 7 nm.
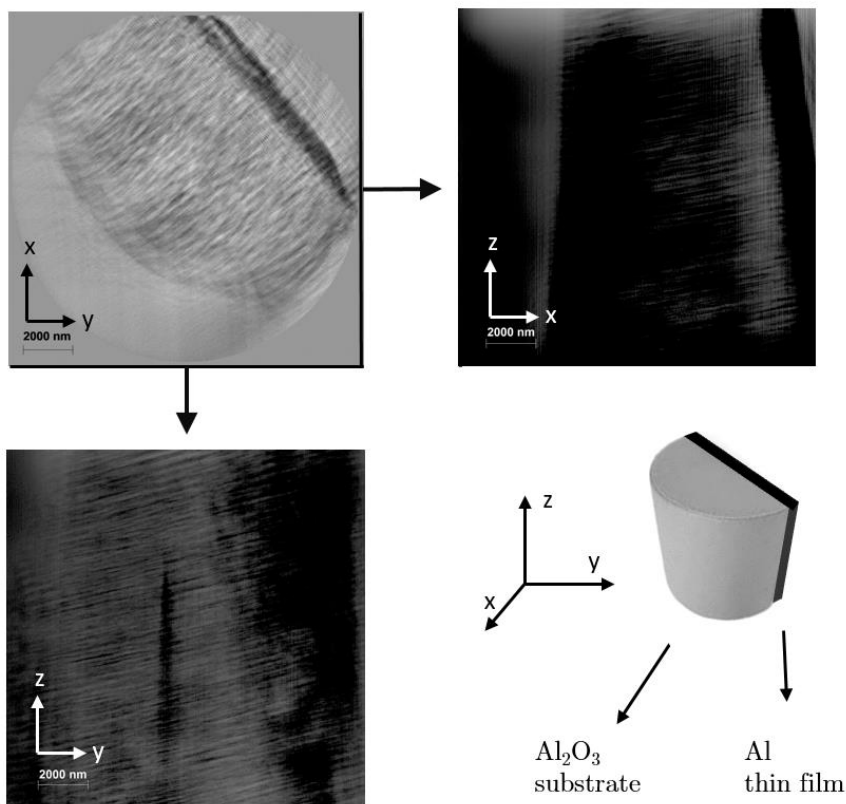
Figure 2. 36 - Projection images of AnoT_F1_2.55_89_60_O, with a pixel size of 7 nm.
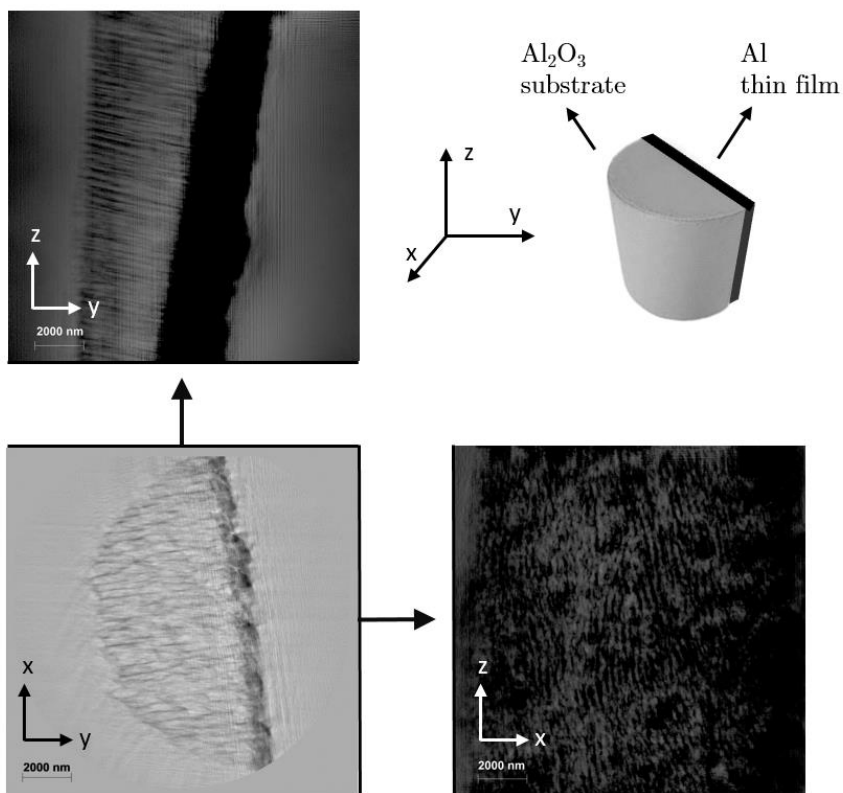
Figure 2. 37 - Projection images of AnoT_F1_2.55_85_60_R, with a pixel size of 7 nm.

Nevertheless, the images obtained by FIB nanotomography of AnoT_F1_2.55_85_60_O (Figure 2. 38), AnoT_F1_2.55_89_60_O (Figure 2. 39) and AnoT_F1_2.55_85_60_R (Figure 2. 40) exhibit a high interconnected porosity between the Anopore substrate and the nanoporous Al thin films.

a)   b)
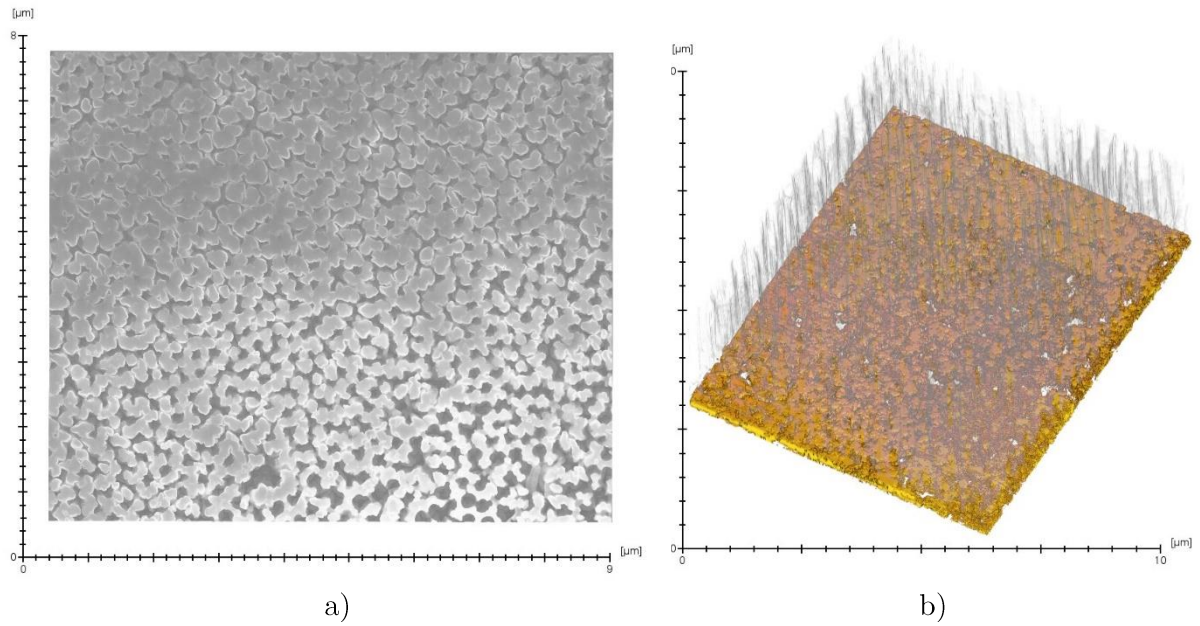
Figure 2. 38 - FIB nanotomographic images of AnoT_F1_2.55_85_60_O: a) top view and b) 3D reconstruction.

a)   b)
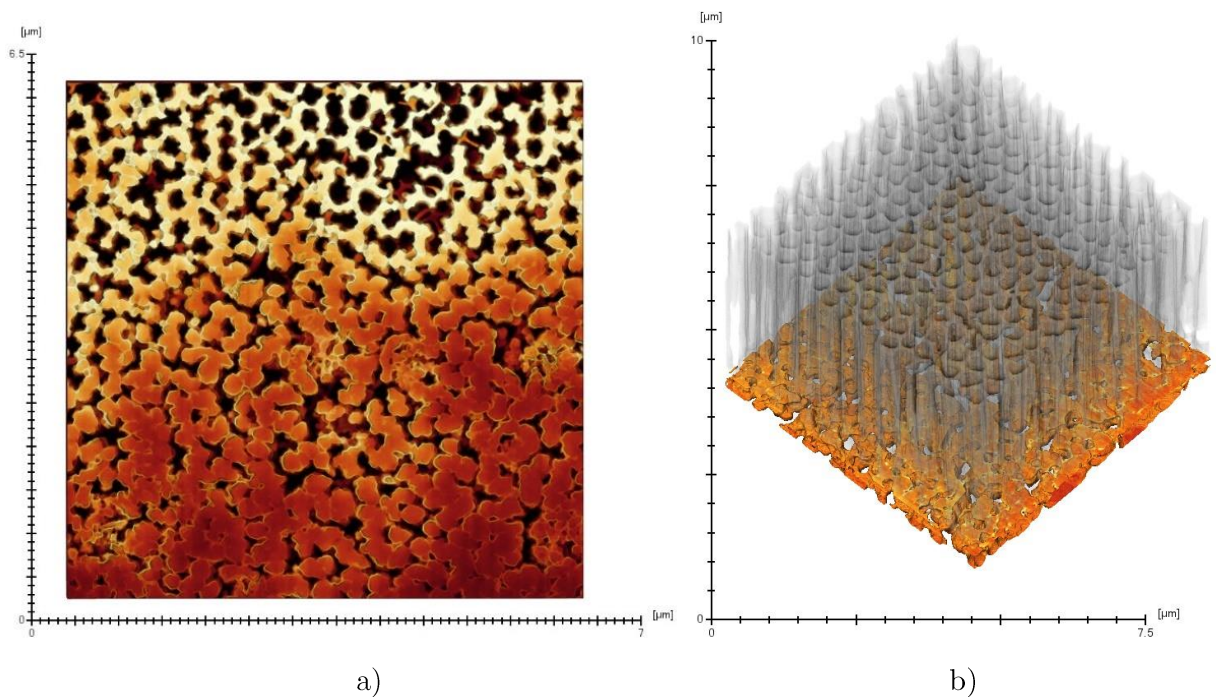
Figure 2. 39 - FIB nanotomographic images of AnoT_F1_2.55_89_60_O: a) top view and b) 3D reconstruction.

a)   b)
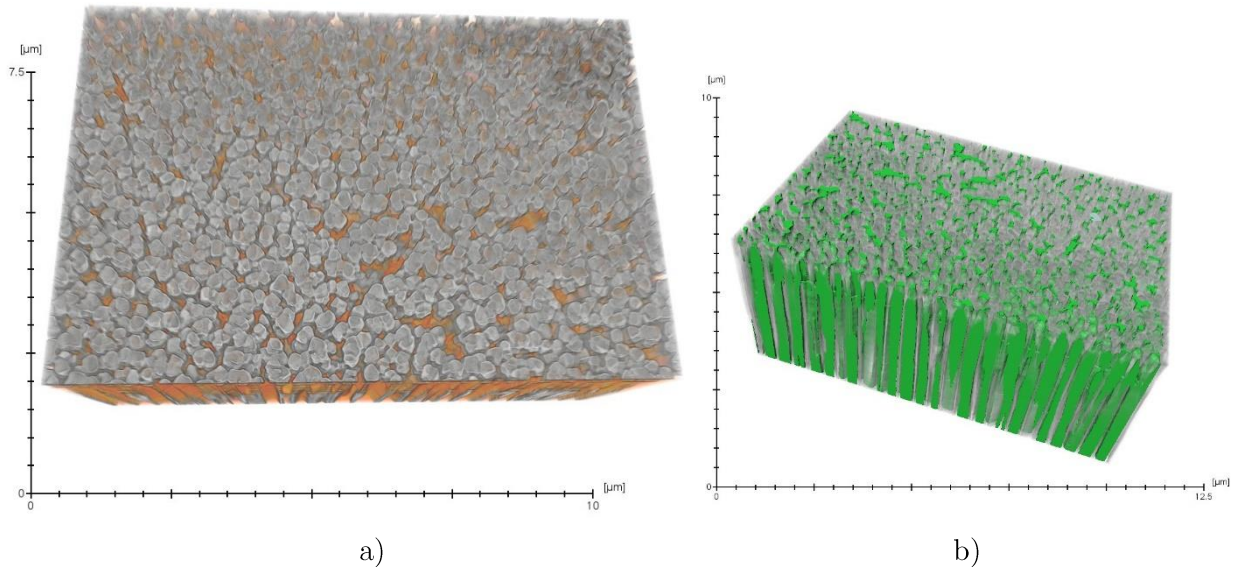
Figure 2. 40 - FIB nanotomographic images of AnoT_F1_2.55_85_60_R: a) top view and b) 3D reconstruction.

The top view images (Figure 2. 38 a), Figure 2. 39 a) and Figure 2. 40 a)) are in accordance with the results of SEM, showing the aluminum thin films (yellow in AnoT_F1_2.55_85_60_O, orange in AnoT_F1_2.55_89_60_O and gray in AnoT_F1_2.55_85_60_R) with columnar porous structures.

The 3D reconstructions (Figure 2. 38 b), Figure 2. 39 b) and Figure 2. 40 b)) reveal the two level porosity related to substrate and thin film. The interconnectivity of pores between thin films and substrates were investigated by analyzing the profile in depth of specific pores (Figure 2. 41) of AnoT_F1_2.55_85_60_O and AnoT_F1_2.55_89_60_O. Both porous structures are similar, showing the substrate pores decreasing in size, by the deposition of the aluminum thin film. However, after few nanometers of film thickness, the size of pores begins to increase. This is mainly due to the shadow effect caused by the tilt of the substrates. The deposition of aluminum thin films becomes the cylindrical shape of substrate pores into irregularly shaped pores.

Thus, one can be concluded that the pores of thin films and substrates are real interconnected, which is a feature of major importance regarding the need of open porosity and interconnectivity in air filtration. Moreover, the size of pores observed at the surface may be larger than actually they are in deeper regions.

Despite the limitations of synchrotron X-ray nanotomography, both techniques (synchrotron X-ray and FIB nanotomographies) are complementary and therefore must be used together for a complete characterization of the nanoporous structures.
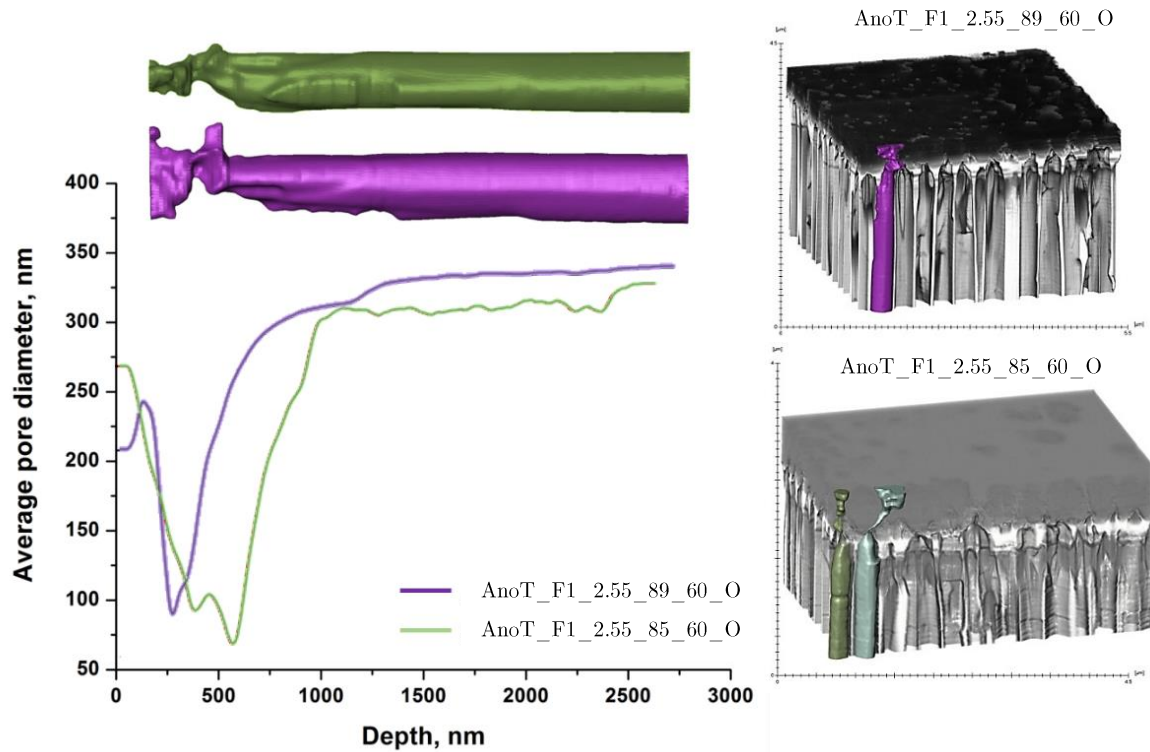
Figure 2. 41 - Diameter of pores in depth of aluminum thin films deposited onto AnoT by method F1 at 85° and 89°.

2.2.4 Nanoporosity by sputtering two materials – YSZ and Sn (F2)

2.2.4.1 Morphology

Thin films of YSZ and Sn deposited on F2a conditions (Figure 2. 42) present several micro/submicrometric Sn spheres dispersed in a matrix of YSZ. This behavior is characteristic of Sn deposition by rf sputtering onto copper substrates. Similar thin films have been already reported in other studies, where the Sn was deposited also by rf sputtering onto a copper substrate [145]. The spheres tend to grow by increasing the number of Sn foils on the target, which is related to the increase of Sn content in the thin films. More detailed observations of thin films surface (Figure 2. 42 b) and d)) reveal not only Sn spheres but also cavities/depressions with semispherical shapes. Those cavities do not overpass the thickness of the thin film, suggesting that thin film grows with Sn partially dissolved in the YSZ matrix and during the cooling, the Sn manifests a complete immiscibility [146]. After the deposition, Sn turns into liquid state evidencing the low wetability in the substrate. Therefore, due to the surface temperature Sn assumes spherical shapes with different dimensions. After the cooling, a large number of cavities with greater diameters than the spheres, is observed. Since this phenomenon is not reported in other works, it may occurs the detachment of the majority of Sn spheres from the thin film surface, probably due to the position of substrates in deposition chamber (substrate is on top and target bottom), which leads liquid/melted Sn to fall down.
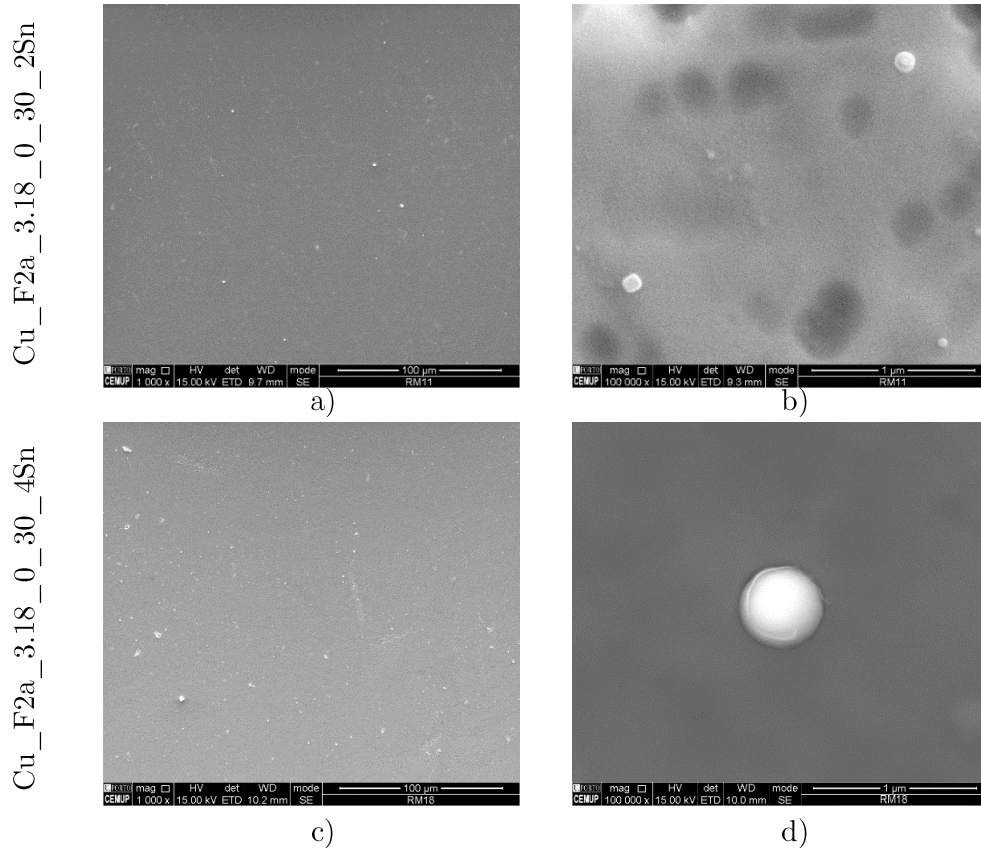
Figure 2. 42 - YSZ-Sn thin films by method F2a: a) and b) Cu_F2a_3.18_0_30_2Sn and c) and d) Cu_F2a_3.18_0_30_4Sn (SEM).

In what concerns the thin films deposited by the method F2b (homemade target 70 wt.% YSZ and 30 wt.% Sn), Figure 2. 43 reveals a different morphology compared to those observed in F2a (YSZ target with Sn foils) (Figure 2. 42). The surface of the thin film shows submicrometric or even nanometric columns/grains. In addiction, Sn spheres were not found in this thin film, despite a second phase is present in lower percentage. Thus, the Cu_F2b_3.18_0_30_O seems to have a significant content of Sn dissolved into the YSZ structure, where a new phase occurs, but with reduced dimensions.
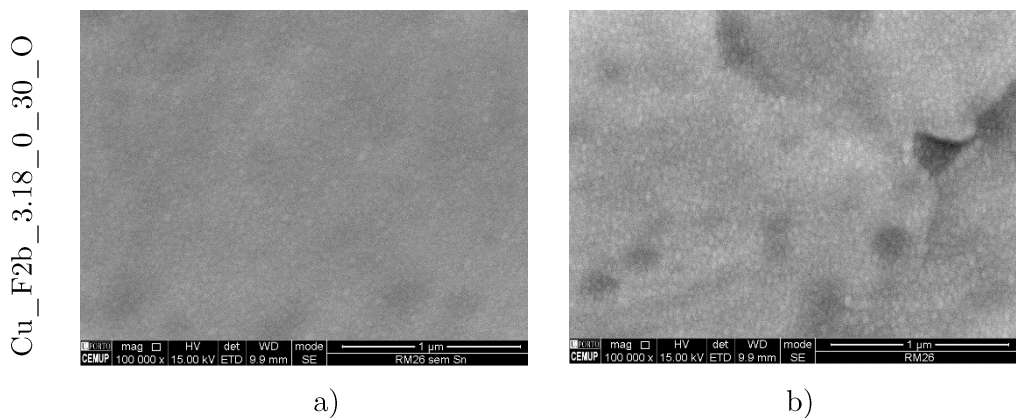
Figure 2. 43 – YSZ-Sn thin films by method F2b (SEM).

2.2.4.2 Topography

Topographic images of YSZ-Sn thin films deposited by F2a method with 2 foils of Sn reveal the influence of sputtering deposition time on surface topography (Figure 2. 44). The surfaces exhibit cavities, apparently resulting from Sn spheres detachment. These results are in accordance with the morphology of thin films (Figure 2. 42). By increasing the deposition time, thin films reveal the presence of a columnar structure, which is correlated to the increase of roughness (Table 2. 21). Both, surface roughness (S_a and S_{RMS}) increase from 3 to 8 nm and from 5 to 11 nm, respectively, as a function of the deposition time (30 - 90 min).

| 30 min | 60 min | 90 min |

a)   b)   c)
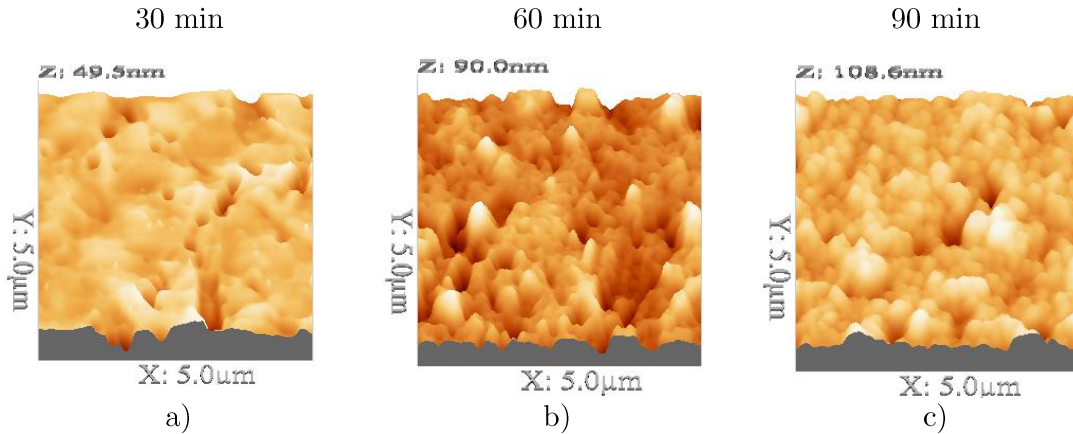
Figure 2. 44 - Topography of YSZ-Sn thin films deposited by F2a method with 2 foils of Sn: a) Cu_F2a_3.18_0_30_2Sn; b) Cu_F2a_3.18_0_60_2Sn and c) Cu_F2a_3.18_0_90_2Sn (scan of 5×5 µm^2).

Table 2. 21 - Surface roughness of nanoporous thin films deposited by method F2.

	S_a (nm)	S_{RMS} (nm)
Cu_F2a_3.18_0_30_2Sn	3	5
Cu_F2a_3.18_0_60_2Sn	8	11
Cu_F2a_3.18_0_90_2Sn	8	11
Cu_F2a_3.18_0_30_4Sn	9	12
Cu_F2b_3.18_0_30_O	9	11

By increasing the Sn content, the number of cavities increases and S_a and S_{RMS} are slightly incremented. However, thin films deposited by F2b show lower roughness values than those of F2a with 4 foils of Sn. This fact is probably due to the greatest number of cavities present at the surface of the thin films deposited by F2a, which are not so common in thin films deposited by F2b.

Topographic (Figure 2. 45 a), b), c) and d)) and phase (Figure 2. 45 e), f), g) and h)) images highlight the influence of the Sn content on the thin film structural evolution. Thin films with the lowest Sn content (Cu_F2a_3.18_0_30_2Sn and Cu_F2a_3.18_0_30_4Sn) have an YSZ single phase (Figure 2. 45 e) and f)) and some spheres of Sn at the surface, as shown in phase images. In the thin films with the highest Sn content (Cu_F2b_3.18_0_30_O), the surface exhibits a fine granular structure with

two distinct phases, probably corresponding to YSZ and Sn dissolved into the YSZ matrix. (Figure 2. 45 g) and h)).

Cu_F2a_3.18_0_30_2Sn Cu_F2a_3.18_0_30_4Sn   Cu_F2b_3.18_0_30_O
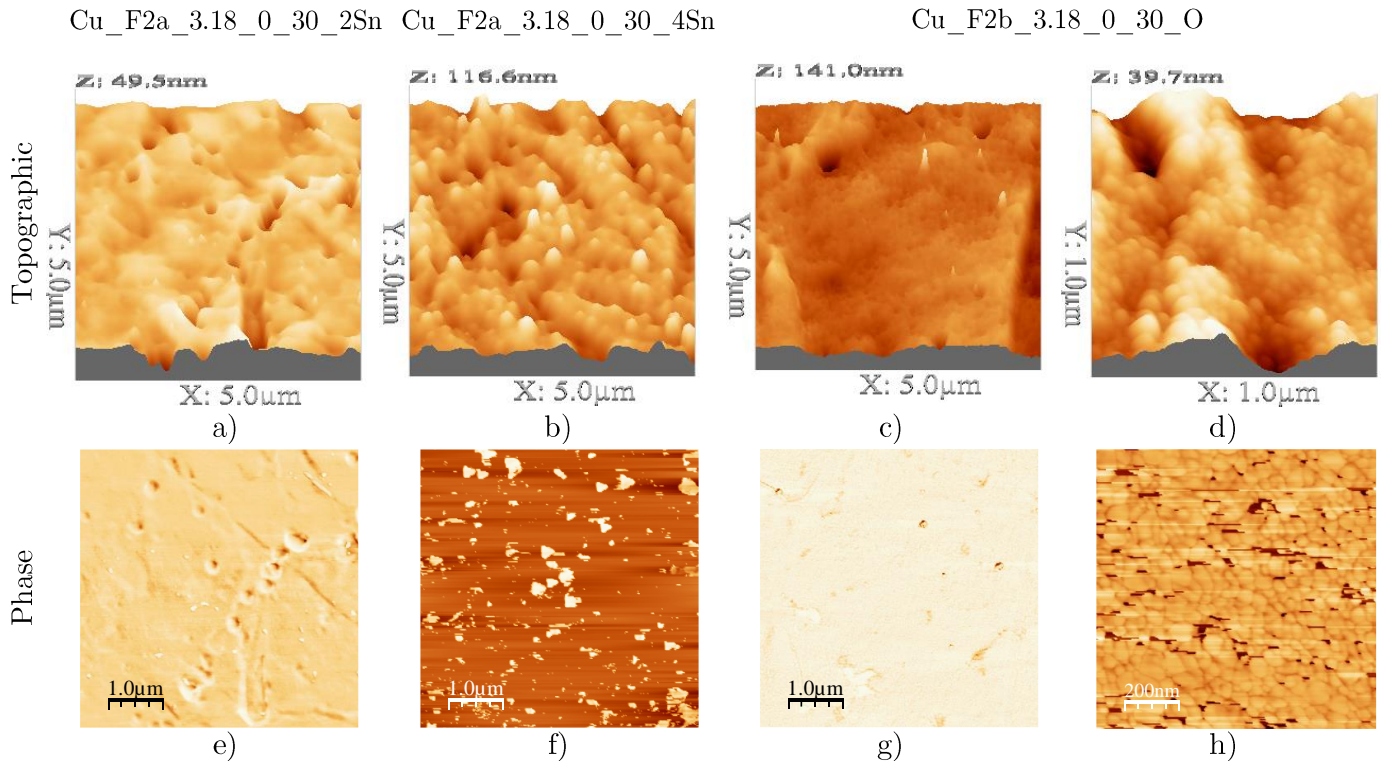
Figure 2. 45 - AFM topographic (a, b, c and d) and phase (e, f, g and h) images of YSZ-Sn thin films: a) and e) Cu_F2a_3.18_0_30_2Sn; b) and f) Cu_F2a_3.18_0_30_4Sn and c), d), g) and h) Cu_F2b_3.18_0_30_O.

2.2.4.3 Thickness and Phasic composition

The evolution of the thin films thickness with the deposition time, measured by AFM, shows that after 90 min of deposition, the thin film deposited with YSZ+4 Sn foils presents a higher growing rate than that with YSZ+2 Sn foils or with the homemade target (70 wt.% YSZ and 30 wt.% Sn) (Figure 2. 46).
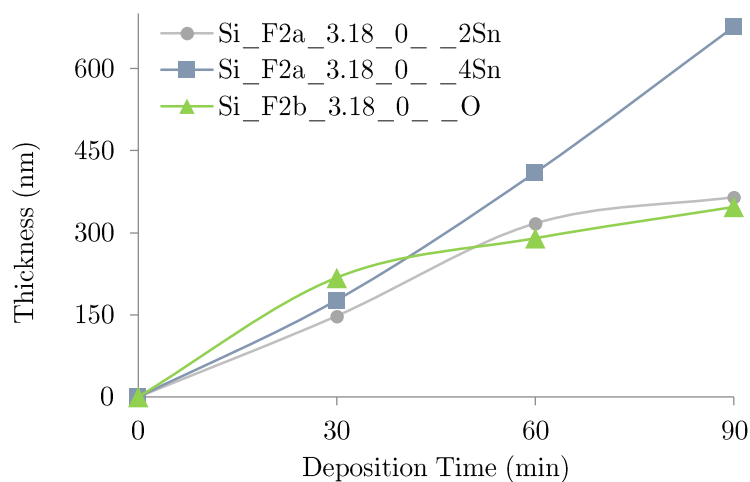
Figure 2. 46 - Growth of YSZ-Sn thin films deposited by F2.

For the first 30 min, thin films thickness increases by increasing the percentage of Sn, since large contents of metallic elements leads to increased ejection rates. However, after 30 min the growth of the thin film deposited by F2b shows a decrease in the deposition rate, which is maybe induced by higher content of oxides compounds.

Regarding the structure of YSZ-Sn thin films deposited by F2, diffractograms of thin films fabricated using the two different targets with different Sn contents, are shown in Figure 2. 47. Both, Si_F2a_3.18_0_180_2Sn and Si_F2a_3.18_0_180_4Sn present a crystallin structure corresponding to rhombohedral $Y_4Zr_3O_{12}$ (PDF No. 01-077-0743 Annex A).
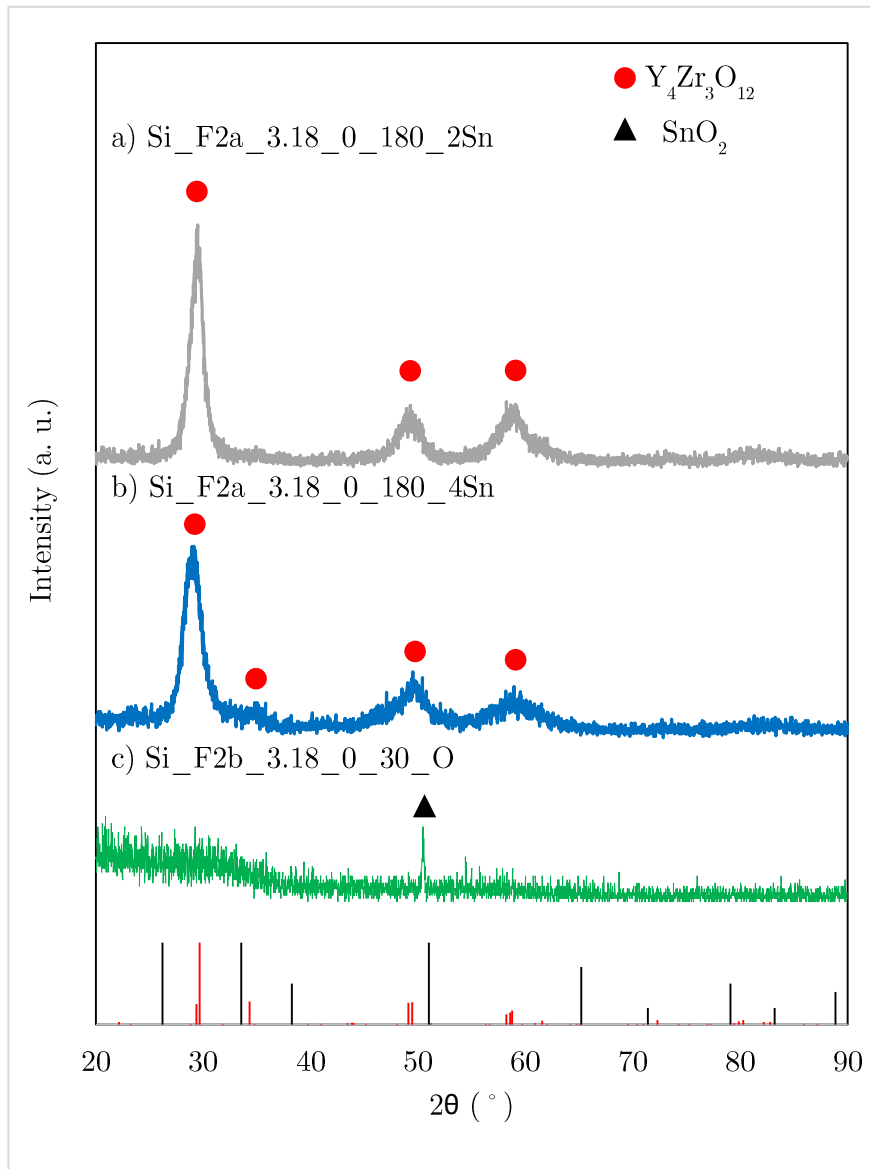
Figure 2. 47 - Diffractograms of YSZ-Sn thin films: a) Si_F2a_3.18_0_180_2Sn; b) Si_F2a_3.18_0_180_4Sn and c) Si_F2b_3.18_0_30_O.

By increasing the Sn content in the target from 2 foils of Sn to 4 foils, the peak at $2\theta = 34°$ becomes more evident and the "hump" at $2\theta \approx 59°$ becomes larger and less intense.

This suggests that the addition of Sn may result in fact in a substitutional incorporation of Sn in the matrix of YSZ, as supposed.

In contrast, the XRD pattern of Si_F2b_3.18_0_30_O shows an isolated peak at $2\theta \approx$ 51°, characteristic peak of SnO_2 (PDF No. 00-001-0625 Annex A) and corresponding to (211) with $I/I_0=100\%$. Regarding YSZ, no characteristic peak is shown, but an enlargement at early stages of 2θ evidences the amorphism, as a consequence of the thin thickness of the film (218 nm). Therefore, these results show the presence of two different phases: YSZ and SnO_2.

YSZ-Sn thin films were produced by method F2 aiming to produce a bi-phasic thin film to posterior removal of the sacrificial material (Sn) by a heat treatment. However, the aim is not attained whatever the deposition conditions. No open porosity is achieved after F2a deposition and the presence of tin oxides in thin films deposited by F2b became impossible the task of removing the Sn at a relatively low temperature (505 K).

2.3 Key conclusions

The aim of developing nanoporous structures efficient for filtration of NPs that are potentially harmful for the human health and environment, led to three main approaches: reducing the substrate pore size, controlling sputtering conditions and sputtering two materials with a great difference between melting temperatures. The main conclusions after a detailed characterization of nanoporous structures are listed below.

Membranes by method M:

- The pores are narrower and the columns are broader by increasing the deposition time or the power density and with substrate in static mode;
- By adjusting the deposition parameters, depending on the type of substrate, it is possible to obtain "new" membranes with nanopores (<100 nm), wherein the smallest pore size is 20 nm in AnoB_M_2.55_0_15_O;
- AnoB_M_2.55_0_15_O revealed to be the membrane with the best porosity characteristics for filtration: the largest surface area (410.89 m^2/g) and the greatest total pore volume (0.2600 cm^3/g);
- The roughness of membranes with Anopore or AAO substrates are not dependent on the deposition time;
- Tomographic images obtained by FIB nanotomography clearly reveal 3D porous structures with open porosity (from top to bottom).

Thin films by method F1:

- In general, the pore sizes are smaller and columns larger for lower substrate tilt, deposition time and power density and in static mode;
- The morphology of thin films deposited by F1 does not have a clear dependence on the deposition pressure and gas composition;

- The dimensions of pores are function of the substrate and the application envisaged: 19 nm for AnoT_F1_1.27_85_60_O, 25 nm for AAO_F1_1.27_85_60_O and 357 nm for Millipore_F1_2.55_70_60_O;
- In the same deposition conditions, the BET surface area and the total pore volume are larger for thin films deposited onto AnoT than AAO (AnoT_F1_2.55_85_60_O: surface area – 148.53 m^2/g; total pore volume – 0.088 cm^3/g)
- The greater the substrate tilt, the greater the surface area, the total pore volume and the surface roughness;
- Tomographic observations by X-ray synchrotron and FIB are complementary. FIB nanotomography shows the interconnected porous structures of thin films with irregularly shaped pores, but it is AnoT_F1_2.55_85_60_O and AnoT_F1_2.55_85_60_O that show a clear presence of open porosity from top to bottom.

Thin films by method F2:

- Whatever the alternative assumed, the co-deposition of YSZ and Sn results in thin films without application in filtration whatever the dimension of particles.

In conclusion, for the proof of concept will be used AnoT_F1_2.55_85_60_O thin film, because it revealed to be the membrane with suitable pores size, open porosity (top/bottom) and great number of open surface pores.

Chapter 3
Unintended Emission
of Nanoparticles

I n recent years the growing number of nanomaterials applications has led scientific community to make aware to the potential harmful effects of engineered nanoparticles to the human health. With the focus on nanotechnology, the presence of nanoparticles in conventional industries and other activities has been neglected. In fact, conventional industrial processes can be responsible for the emission of airborne NPs which at long term can compromise the workers' health. Therefore, it is of great interest the assessment of airborne occupational environments, as a way to understand the real health effects to the workers.

This chapter reports measurements (size distribution, total number of particles and surface area) performed in conventional industries based on additive and subtractive electrolytic processes: additive - aluminum surface treatments (anodizing and lacquering); and subtractive - subtractive manufacturing (electrical discharge machining (EDM) and laser machining) during 24 hours. Furthermore, other sources of NPs are assessed for short periods of time.

The PCR are evaluated for both industrial environments, in order to estimate the exposure of workers to particles that can be potentially harmful to their health.

Number and surface area, which are the most reliable characteristics to study the toxicity of NPs, are measured using different equipment. Therefore, the correlation between these parameters are studied in order to infer the possible limitations inherent to the characterization of airborne NPs in occupational environments.

Finally, the efficiencies of commercial filters (Anopore) and the filters developed in this study, are evaluated.

3.1 Experimental procedure

3.1.1 Activities and workplaces descriptions

Two main industrial environments were selected, both based on electrolytic processes (additive and subtractive). Data were collected in industries of aluminum surface treatments and of subtractive manufacturing. Moreover, other activities such as, laboratorial research, the industry of printing by lithography, the transportation and some daily life activities were also investigated.

3.1.1.1 Aluminum surface treatments

The industry of aluminum surface treatments, which comprises anodizing and lacquering methods, is dedicated to prevent the degradation of aluminum pieces, by creating a surface protective layer for environmental conditions and also to decorative purposes. Anodizing baths (AB) is an electrochemical process which induces the growth onto a surface of an oxide coating (Al_2O_3) to protect the aluminum surface, by immersing the aluminum pieces in different acidic baths. Lacquering is a decorative process which consists of two main steps: the aluminum piece is alternatively immersed in acidic baths (lacquering baths (LB)) and then the material is coated by an electrostatic polymeric paint (lacquering paint (LP)).

Four different workplaces belonging to the industry of aluminum surface treatments, labelled by A, B, C and D, were assessed in terms of particle size distribution, total number of particles and surface area over time. Figure 3. 1 shows the schemes of the workplaces floor plans and a general description of the factories is provided in Table 3. 1.
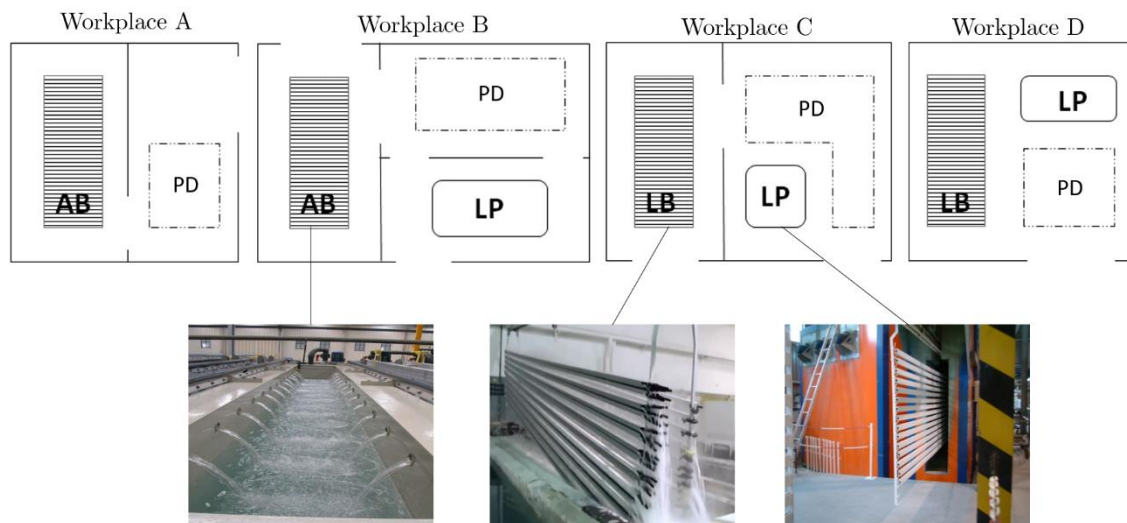
Figure 3. 1 - Schematic illustration of workplaces of aluminum surface treatments (AB - anodizing baths, LB - lacquering baths, LP - lacquering paint and PD - area for aluminum pieces preparation and drying).

Table 3. 1 - Overall description of Workplaces A, B, C and D.

Workplace	Anodizing Baths (AB)	Lacquering Baths (LB)	Paint (LP)	Operation Schedule	Number of pieces treated per hour	Control Strategies
A	X	-	-	7:00-19:00	1.93	Yes
B	X	-	X	6:00-0:00	22.2	Yes
C	-	X	X	6:00-12:00 and 14:00-1:00	2.45	Yes
D	-	X	X	8:00-12:00 and 13:00-17:00	4.17	No

Workplace A is a medium sized workplace where physical barriers and general ventilation systems are present. Moreover, workers use gloves and respirators as personal protective equipment. Workplace B also has physical barriers to separate different activities, ventilation systems, air filtration and washing facilities. Workers are educated to implement safety procedures and use personal protective equipment (gloves, certified respirators and protective clothing). In this site, LP is an engineering controlled process, as in the Workplace C. Workplace C has local exhaust ventilation, air filtration, physical barriers to separate LB and LP processes and workers use personal protective equipment (gloves and certified respirators). Workplace D is a small factory where no control strategy is applied. Workers do not use any personal protective equipment and there are no physical barriers or mechanically driven ventilation (only natural ventilation is present). Moreover, the LP is a manual process, being required the presence of at least one worker who is exposed to high levels of polymeric-based particles from the paints. Usually, when the work shift ends, workers clean their clothes near the LB area, with compressed air. In contrast, Workplaces A and C, as medium sized industries and Workplace B, as a large industrial site, all express concerned about environmental and workers' health protection, applying control strategies.

Both AB and LB processes consist of the aluminum pieces immersion in baths. Usually one worker is present at approximately 2 meters from the tanks with the task of handling the automatic immersion system and monitoring activities. The LP process in Workplace D is manual, and conversely in the other workplaces (B and C) is autonomous, with the worker being responsible to conduct the pieces to the system and to monitor the process. In all the workplaces, there are other workers in the surrounding areas, responsible for other tasks who are also exposed to the same occupational environment.

3.1.1.2 Subtractive manufacturing

Subtractive manufacturing is widely used in the mechanical industry for the purpose of cutting a certain material in a desired 3D shape. EDM is a subtractive process that applies a spark discharge between the tool electrode and the workpiece, submerged in a dielectric fluid, causing the material erosion. Two types of EDM are used in industry:

sinker EDM and wire EDM. In both, the methodology is similar, differing in the electrode material and configuration. In the sinker EDM, a machined electrode usually of graphite with the negative of desired shape, is the tool, while for the wire EDM is commonly used a brass wire to cut the workpiece.

Laser machining is also a subtractive process, in which the beam laser energy removes material from the workpiece by eroding the material.

Size distribution, total number and surface area of particles present in subtractive manufacturing processes environments, were studied in four different workplaces, here identified as Workplace E, F, G and H. The schematic floor plans and overall descriptions of workplaces are present in Figure 3. 2 and Table 3. 2, respectively.
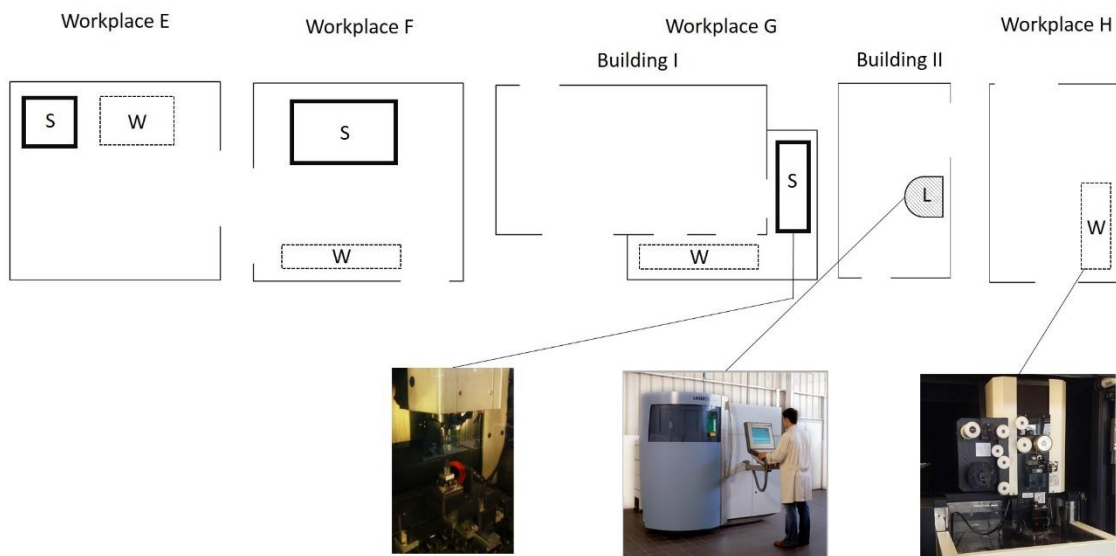
Figure 3. 2 - Schematic illustration of workplaces of subtractive manufacturing (S – sinker EDM, W – wire EDM and L – laser machining).

Table 3. 2 - Overall description of Workplaces E, F, G and H.

Workplace	EDM		Laser machining	Operation Schedule	Control Strategies
	Sinker	Wire			
E	X	X	-	8:00-17:00	Yes
F	X	X	-	8:00-18:30	No
G	X	X	X	8:00-17:00	Yes
H	-	X	-	9:00-13:00 and 14:00-17:30	Yes

Workplace E (medium sized industry) and Workplace H (small sized industry) have local exhaust ventilation, although there are no physical barriers to separate EDM environments from those dedicated to other activities. Conversely, Workplace F, as a small industry, does not apply any control strategy, nor even ventilation systems are used. From time to time, the front gate is kept open. In Workplace G, a large factory, sinker and wire EDM processes are separated in a closed room from the other activities. The room has ventilation systems and air filtration. The laser machine is placed in another room and the equipment includes an exhaust ventilation system with three
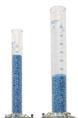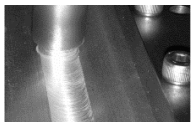
different filters with different levels of porosity, where the last one filters the smallest particles. Once a month, a worker cleans the filters with compressed air, instead of new filters being replaced periodically. None of the factories have workers using personal protective equipment.

Each machine requires the handling of at least one worker. Usually, the sinker EDM and laser machining equipment have one front door which is only open when it is necessary to make some intervention on the tool or the workpiece. In contrast, wire EDM is an open system.

3.1.1.3 Other sources

Other activities were monitored to make a quantitative determination of the emitted particles during these events. The descriptions of these activities are summarized in Table 3. 3.

Table 3. 3 - List of activities from different fields which environments were monitored.

Field		Activity	Description
Laboratorial research		Sputtering cleanroom	Airborne particles were characterized in a sputtering cleanroom where two sputtering equipment are installed. The facility has particles filters and temperature room control.
		Tap density	Method to determine the density of a specific powder by consecutively tapping it. Measurements were conducted during one experiment.
Industry		Welding	Assessment of particles emitted from friction stir welding of aluminum alloys.
		Printing in lithography	Aerosol evaluation during the printing of paper articles.
Transportation		Gas combustion in vehicles	Monitoring the particles released by a diesel and a gasoline car working at idle speed.
Daily life activities		Incense	Determination of airborne particles present during the burning of one piece of incense.
		Candle	Data recorded for several minutes with a lighted candle.
		Gel nails	A drill is used to remove the old gel nail before applying the new one. The particles released from this event were assessed.

3.1.2 Aerosol monitoring

Equipment used to monitor aerosol are a scanning mobility particle sizer (SMPS) and a nanoparticle surface area monitor (NSAM).

SMPS measures the size distribution per volume of air ($\#/cm^3$) of airborne particles through the determination of the particles electrical mobility diameter. Particles are electrically charged and separated by size in channels. A beam laser and a photodetector are used to count particles.

NSAM estimates the surface area of airborne particles deposited in human lung per volume of air ($\mu m^2/cm^3$). Charged particles are detected by an electrometer. Through a mathematical model, the particles charge measured by the electrometer is correlated to the surface area [147]. Depending on the voltage applied, the NSAM is able to determine particles deposited in the tracheobronchial (100 V) or alveolar (200 V) regions.

The measuring apparatus (Figure 3. 3), comprising a SMPS (TSI, Model 3034), a NSAM (TSI, Model 3550) and a computer with appropriate software (Aerosol Instrument Manager® and Nanoparticle Surface Monitor), was installed 2 meters away from the activities, collecting data continuously.

The SMPS 3034 with 54 sequence channels and working at 1L/min of inlet sample flow, was used to determine the concentration of particles with sizes ranging from 10 to 487 nm. For measurements of 24 hours or more, which is the case of industries of aluminum surface treatments and subtractive manufacturing, each sample corresponds to 3 scans (3 min/scan), totalizing 9 minutes of data acquisition. In the case of short period experiments, 1 sample consists of only 1 scan of 3 min. The NSAM was acquiring data every 10 seconds by applying an ion trap voltage of 200 V, in order to estimate the surface area of particles with sizes between 10 and 1000 nm which is deposited in the alveolar region.

Figure 3. 3 - Measuring apparatus: a) computer with appropriate software, b) NSAM 3550 and c) SMPS 3034.

For complementary information, the workers behavior and their activities during work shift were detailed recorded, as much as possible.

The SMPS 3034 was also used to estimate the efficiency of Anopore and AnoT_F1_2.55_85_60_O thin films developed in Chapter 2. The filters were inserted into a 13 mm syringe filter holder (*Sartorius Stedim biotech*), which was placed on the inlet tube of the SMPS. The filters efficiencies were calculated by determining the percentage of NPs which was retained, from the background experiment (upstream) to the experiment using the filter (downstream).

Ideally, these tests should be performed using an aerosol generator to produce a known concentration of NPs. As there is lack of that kind of equipment, measurements were taken in a closed laboratorial room where the concentration of particles does not show significant variation over time. The same procedure was performed in real industrial

environments, but with an unstable number of airborne particles over time, the final results had no scientific validity.

3.1.3 Data analysis

All data were statistically analyzed to determine the total number of particles (N), the weighted arithmetic mean ($\bar{x}$) and the standard deviation (σ) of number of airborne particles. These parameters were calculated according to the follow equations:

$$N = \sum_{l}^{u} n$$

<div align="right">Eq 3. 1</div>

$$\bar{x} = \frac{\sum_{l}^{u} nx}{N}$$

<div align="right">Eq 3. 2</div>

$$\sigma = \sqrt{\frac{\sum_{l}^{u}[x - \bar{x}]^2}{N}}$$

<div align="right">Eq 3. 3</div>

where:

N total number of particles

$\bar{x}$ weighted arithmetic mean

σ standard deviation

l minimum diameter

u maximum diameter

n number of particles

x diameter of particle

Considering the indoor environment, workers exposure level is ideally assessed with workers carrying personal measuring equipment. With the lack of such equipment, it was adopted the aerosol monitoring approach as an indicator of workers exposure.

The provisional NRVs suggested in literature [135] refer to the occupational exposition to nanomaterials, i.e., all materials which sizes are within 10-100 nm, and are time weighted average for 8 hours (TWA-8hr). Hence, data obtained by the SMPS were processed in order to determine the concentration of airborne particles considered nanometric (10-100 nm) for a period of 8 hours of industrial activity. The TWA-8hr corrected concentrations (C_C TWA-8hr) were calculated by the difference between concentrations during industrial activity (C_{IA} TWA-8hr) i.e., during working hours, and background concentrations (C_B TWA-8hr) i.e. measurements when there is no industrial activity (in-between processes, usually the overnight periods).

The precaution characterization ratio (PCR) was calculated according to equation 3.4.

$$PCR = \frac{C_{C\,TWA-8hr}}{NVR}$$

<div align="right">Eq 3. 4</div>

3.2 Results and discussion

3.2.1 Workplace aerosol monitoring for 24h

Industrial environments, such as the industry of aluminum surface treatments including anodizing and lacquering processes, and the industry of subtractive manufacturing by sinker and wire EDM and laser machining, were monitored for 24h. Size distribution of particles, total number and surface area deposited per human lung were determined.

3.2.1.1 Aluminum surface treatments

Characteristics of airborne particles emitted from aluminum surface treatments, which were assessed by means of SMPS 3034 and NSAM 3550, are summarized in Table 3. 4.

Table 3. 4 - Characteristics of particles present in workplaces of industry of aluminum surface treatments.

Industrial Process	Workplace	SMPS 3034					NSAM 3550
		10-100 nm ($\times 10^6$ particles /cm³) [%]	100-487 nm ($\times 10^6$ particles /cm³) [%]	Total ($\times 10^6$ particles /cm³)	Particle Size		Lung Deposited Surface Area (μm²/cm³)
					$\bar{x}$ (nm)	σ	
AB	A	1.11 [93.9%]	0.07 [6.1%]	1.18	44	2	1.2
	B	4.64 [93.1%]	0.34 [6.9%]	4.98	46	2	24.6
LB	C	3.80 [78.3%]	1.05 [21.7%]	4.85	77	2	167.4
	D	4.07 [87.8%]	0.57 [12.2%]	4.64	61	2	125.4
LP	B	6.11 [86.6%]	0.95 [13.4%]	7.06	63	2	113.9
	C	2.30 [87.4%]	0.33 [12.61]	2.63	66	2	68.0
	D	2.63 [88.5%]	0.34 [11,5%]	2.97	59	2	96.5

Anodizing Baths

Measurements carried out while AB process occurred in Workplaces A and B, are shown in Figure 3. 4.

Profiles of daily concentration of particles, as well as surface area have more intense peaks during industrial activity and low concentration of particles overnight. Workplace B presents the highest values of total number of particles (4.98×10^6 particles/cm³), particle size (46 nm) and surface area (24.6 μm²/cm³).

Figure 3. 4 - Size distribution, total number and surface area of airborne particles emitted for 24h during AB process: a) Workplace A and b) Workplace B.

Regarding the deposited surface area in human lung, particles emitted from AB in Workplace A (1.2 $\mu m^2/cm^3$) present much smaller values than any other process whatever the workplace. This is maybe related to the equipment resolution, since SMPS 3034 detects particles from 10 to 487 nm and NSAM 3550 measures particles which sizes are between 10 and 1000 nm. Hence, this may implies that the number of particles with diameters between 487 and 1000 nm is much lower in Workplace A than the others.

Besides, the smallest particles size (44 nm) and the greatest percentage of NPs (93.9%) in Workplace A, may endorse this assumption.

Lacquering baths

The LB process was monitored in Workplaces C and D and data collected are plotted in graphs of Figure 3. 5.

Workplace C (Figure 3. 5 a) and D (Figure 3. 5 b) present similar profiles of particles size distribution over time, despite concealed by the graphic scale of Workplace C. These profiles show high concentration of particles during the working period (day) and conversely, the number of particles at downtime (night) is substantially smaller. During the night, the particle size slightly increases, which may indicate the agglomeration/aggregation of particles, which are detected as larger single particles by the SMPS. For some authors this phenomenon is in most cases related to the atmospheric conditions, such as temperature and humidity [22]. Usually, the night period causes the decrease in temperature and the increase in relative humidity and both factors promote the formation of agglomerates or aggregates.

Figure 3. 5 - Size distribution, total number and surface area of airborne particles emitted for 24h during LB process: a) Workplace C and b) Workplace D.

Figure 3. 5 - Size distribution, total number and surface area of airborne particles emitted for 24h during LB process: a) Workplace C and b) Workplace D.

Workplace D is a small industrial site where there are no mechanically driven ventilation and no physical barriers separating LB and LP processes. This may lead the airborne particles emitted from both processes to move between the different industrial environments due to natural ventilation. Thus, particles detected near LB tanks may be released from LB and LP. At 17:32 is detected a highlighted peak of 24 900 particles/cm^3 which occurs after the shift ends and the workers clean their clothes and the painting area using compressed air.

The Workplace D has also the highest percentage of NPs (87.8%), which means an average particle size smaller in Workplace D (61 nm) than in Workplace C (77 nm). In contrast, due to longer work shifts, Workplace C presents a slightly higher total number of particles and higher surface area deposited per human lung. As expected, the total number of particles and the surface area seem to be correlated, presenting both similar profiles.

Lacquering paint

Airborne particles present in Workplaces B, C and D during LP, were assessed and results are represented in Figure 3. 6.

The intense industrial activity in Workplace B with 22.2 pieces surface treated per hour compared with 2.45 and 4.17 in Workplaces C and D respectively, results in higher values of particles concentration and surface area. For 24 hours the total number of particles is 7.06×10^6 particles/cm^3 and the surface area deposited in human lung is 113.9 μm^2/cm^3. At 21:12, Workplace B shows a peak in the total number of particles (9.8×10^4

particles/cm^3) which corresponds to the period of cleaning the factory. Workplaces C and D have a typical profile with large concentration of particles during industrial activity and low concentrations when the works are interrupted, although this gap is much more marked in Workplace D.

Figure 3. 6 - Size distribution, total number and surface area of airborne particles emitted for 24h during LP process: a) Workplace B, b) Workplace C and c) Workplace D.

Figure 3. 6 - Size distribution, total number and surface area of airborne particles emitted for 24h during LP process: a) Workplace B, b) Workplace C and c) Workplace D.

The painting system differs in the three workplaces, being automated in Workplaces B and C and manual in Workplace D. While with the automated system, the pieces are placed inside the chamber and painted by the machine without any human intervention, in the case of the manual painting the worker has to paint manually the pieces without any protection. Particles detected during LP, which is believed that are mainly polymeric-based particles from the paints, can easily disperse in air by turbulent eddy diffusion and advective air flow. However, when performing automated painting, particles are confined inside a chamber which promotes their collision and consequent agglomeration or aggregation, being detected as larger particles than actually single particles are. Thus, in Workplaces B and C particles have larger sizes (63 nm and 66 nm respectively) than in Workplace D (59 nm).

Results referring to the size distribution of particles emitted from AB, LB and LP processes in the four studied workplaces are compiled in Figure 3. 7.

AB process emits particles with the smallest diameters, while LB has the biggest particles. On the other hand, AB presents on average the lowest number of particles and LB the highest. However, LP process in Workplace B presents the largest number of particles, which may not be related to the process itself but rather than to the high level of productivity.
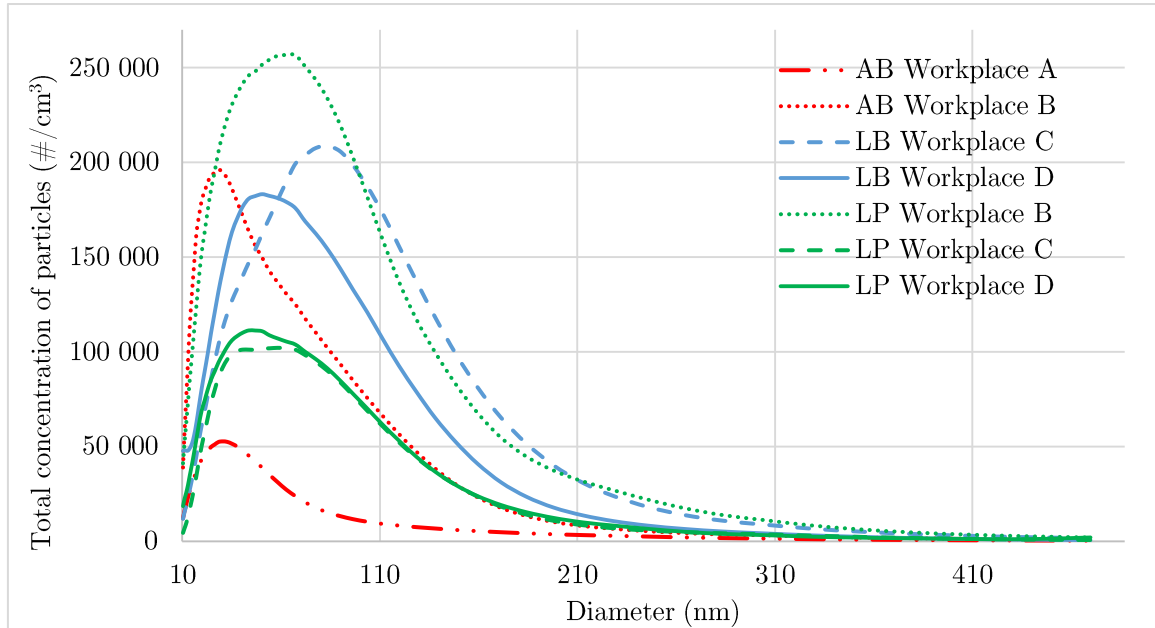
Figure 3. 7 - Size distribution of particles emitted from aluminum surface treatments.

In Table 3. 5 are summarized the particles concentrations during industrial activity (C_A), the background concentrations (C_B) and the corrected concentrations (C_C), as well as the $PCR_{TWA-8hr}$ calculated by equation 4.4.

Table 3. 5 - Concentrations of particles and PCR calculated for the AB, LB and LP processes in the 4 workplaces.

Industrial Process	Workplace	$C_{IA\ TWA-8hr}$ ($\times 10^4$ particles/cm³)	$C_{B\ TWA-8hr}$ ($\times 10^4$ particles/cm³)	$C_{C\ TWA-8hr}$ ($\times 10^4$ particles/cm³)	NRV ($\times 10^4$ particles/cm³)	PCR TWA-8hr
AB	A	1.1	0.2	0.9		0.23
	B	3.0	2.3	0.7		0.18
LB	C	2.9	1.2	1.7		0.43
	D	2.7	1.0	1.7	4	0.43
LP	B	4.0	3.4	0.6		0.15
	C	1.7	0.7	1.0		0.25
	D	4.0	0.9	3.1		0.78

For the determination of the PCR, the $NRV_{TWA-8hr}$ value of 4×10^4 particles/cm³ suggested by SER [135] was applied, assuming that studied nanomaterials belong to the class 3, which comprises biopersistent granular and fiber form nanomaterials in the range of 1-100 nm (examples: Al_2O_3, SiO_2 TiN, TiO_2...).

According to SER, $PCR_{TWA-8hr}$ should always be smaller or equal to 1. In all studied workplaces, PCR are within the provisional limits, with the PCR ranging from 0.15 to 0.78.

These results may suggest that: workers are exposed every day to high contents of NPs, even in conventional industrial processes, which may cause severe health problems; and/or the suggested provisional NRVs are unsuitable or methods used to the

determination of PCR are not the most appropriate, being required to carry out further studies in this area.

3.2.1.2 Subtractive manufacturing

The number, size and surface area of particles present in industry of subtractive manufacturing in various workplaces, are shown in Table 3. 6.

Table 3. 6 - Characteristics of particles present in workplaces of industry of subtractive manufacturing.

Industrial Process	Workplace	SMPS 3034					NSAM 3550
		10-100 nm ($\times 10^6$ particles /cm^3) [%]	100-487 nm ($\times 10^6$ particles /cm^3) [%]	Total ($\times 10^6$ particles /cm^3)	Particle Size		Lung Deposited Surface Area (μm^2/cm^3)
					$\bar{x}$ (nm)	σ	
Sinker EDM	E	6.07 [83.6%]	1.19 [16.4%]	7.26	76	2	-
	F	2.90 [90.6%]	0.30 [9.4%]	3.20	62	2	-
	G	13.57 [97.6%]	0.34 [2.4%]	13.91	43	2	-
Wire EDM	E	2.51 [86.6%]	0.39 [13.4%]	2.90	71	2	-
	F	3.41 [71.2%]	1.38 [28.8%]	4.79	88	2	-
	G	35.89 [99.1%]	0.32 [0.9%]	36.21	23	2	-
	H	2.67 [91.8%]	0.24 [8.2%]	2.91	49	2	69.5
Laser Machining	G	0.82 [92.1%]	0.07 [7.9%]	0.89	58	2	-

Sinker EDM

The daily size distribution of particles in Workplaces E, F and G during sinker EDM (Figure 3. 8) shows the industrial activity occurring throughout the day (24 hours) although workers only are present during the day.

The sinker EDM equipment has doors which are kept closed, although occasionally need to be open to some type of intervention on the working piece or the tool electrode. Thence, in the three workplaces during the day, there are some evidenced peaks of particles concentration which coincide with the doors opening, while during the night the particle number decreases, because in the absence of workers the doors of equipment are kept closed. Workplace G is the company which presents the largest total number of particles (13.91$\times 10^6$ particles/cm^3). Since this is the company applying more control strategies (physical barriers, ventilation and air filtration), this value should be greatly influenced by its productivity levels. Furthermore, sinker EDM in Workplace G is responsible for the emission of the largest percentage of NPs (97.6%) which means the smallest average particle size (43 nm).
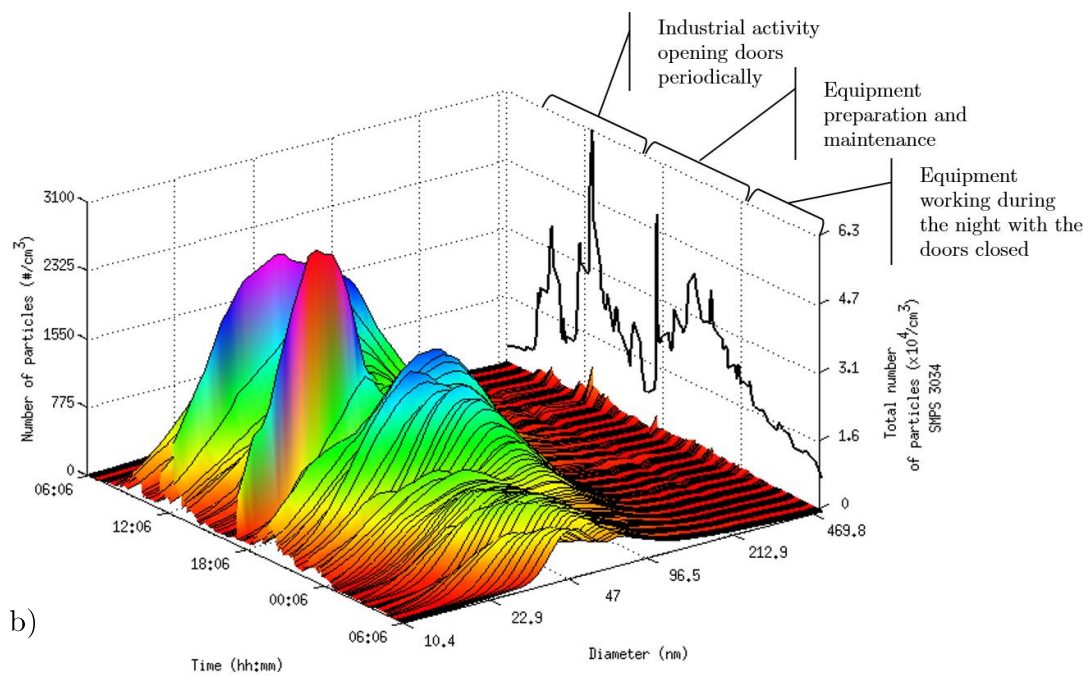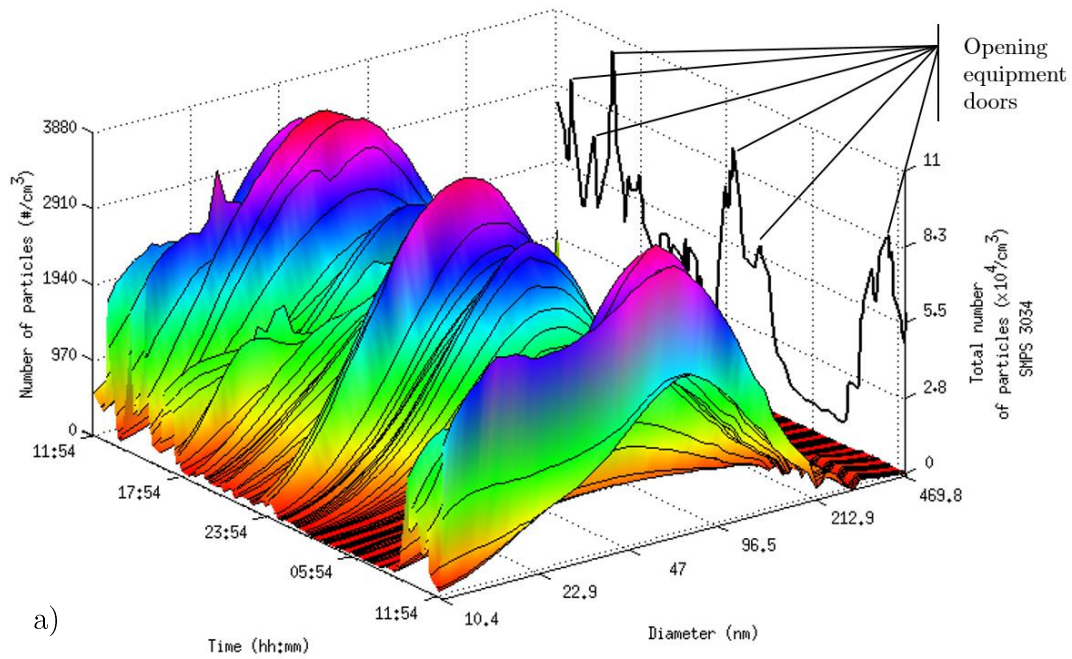
Figure 3. 8 - Size distribution and total number of airborne particles emitted for 24h during sinker EDM process: a) Workplace E, b) Workplace F and c) Workplace G.
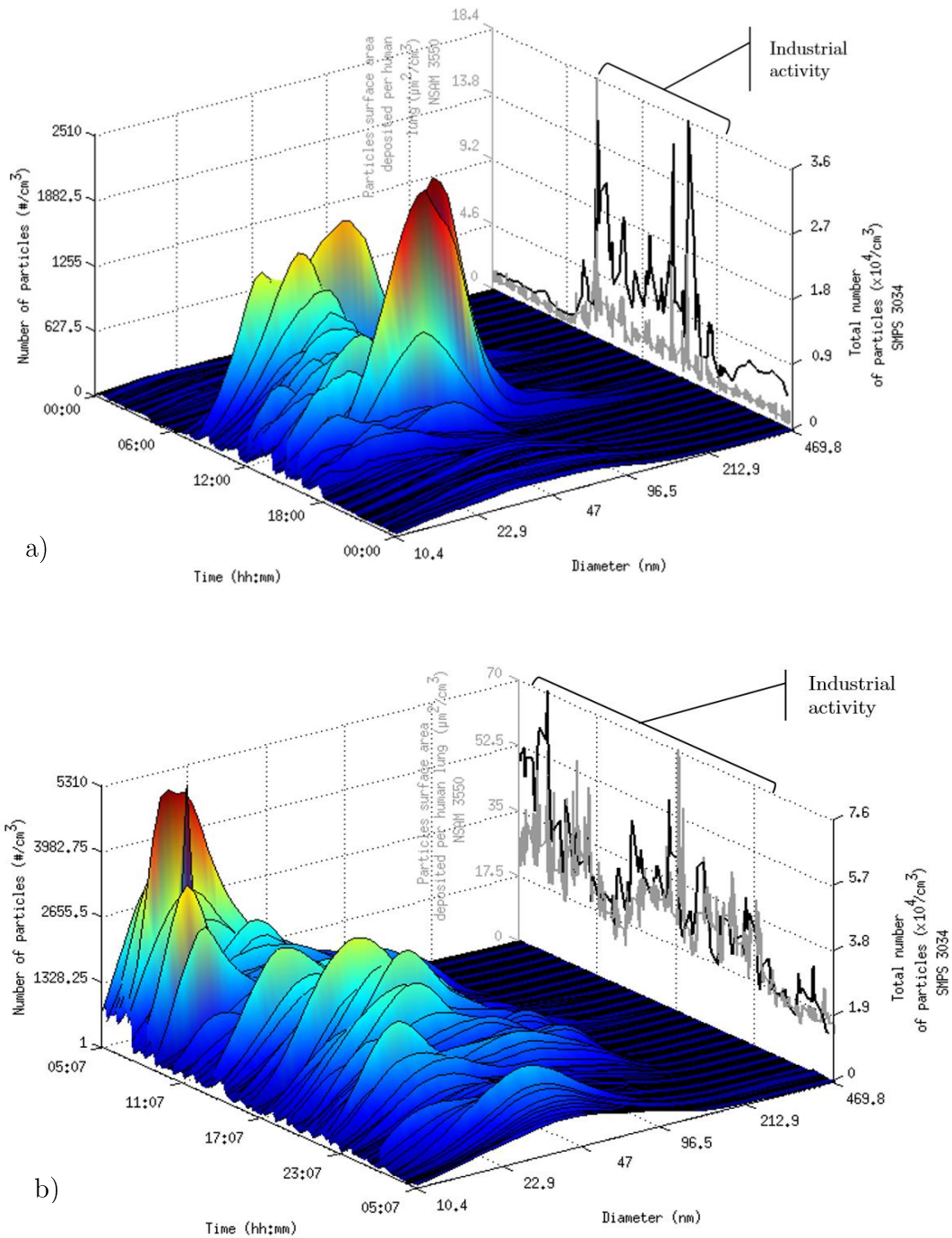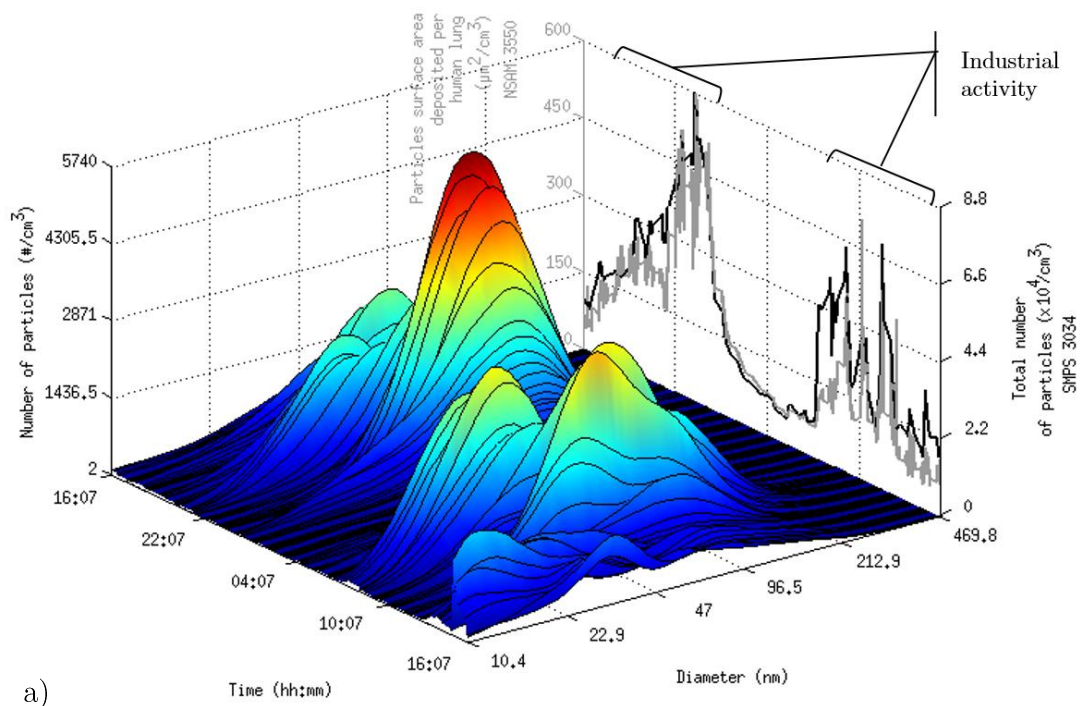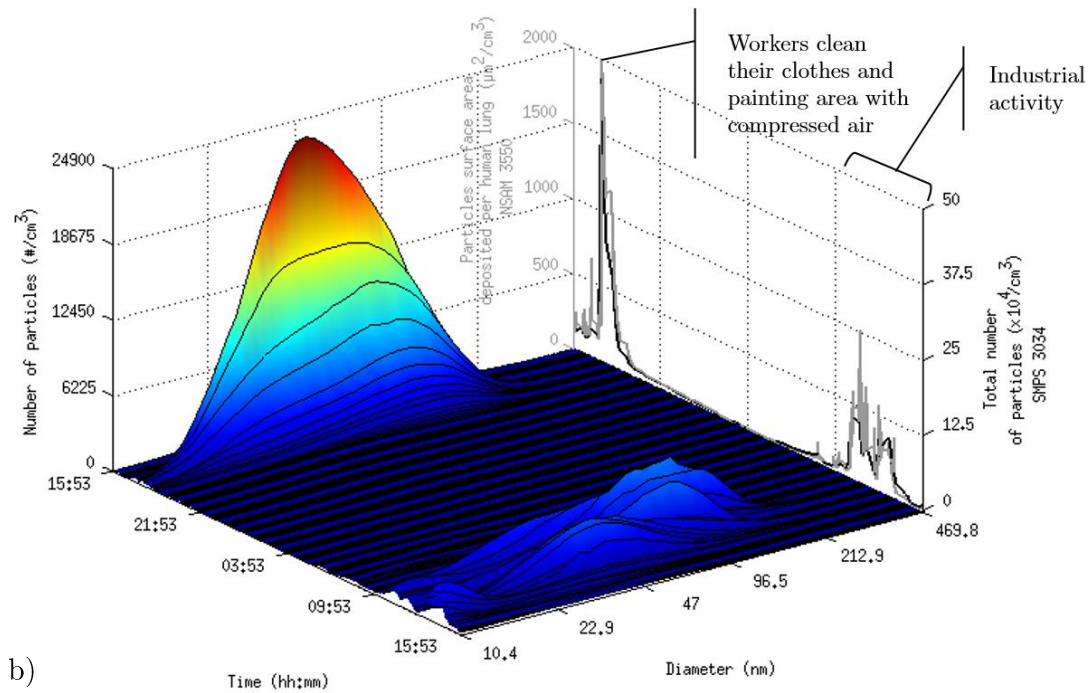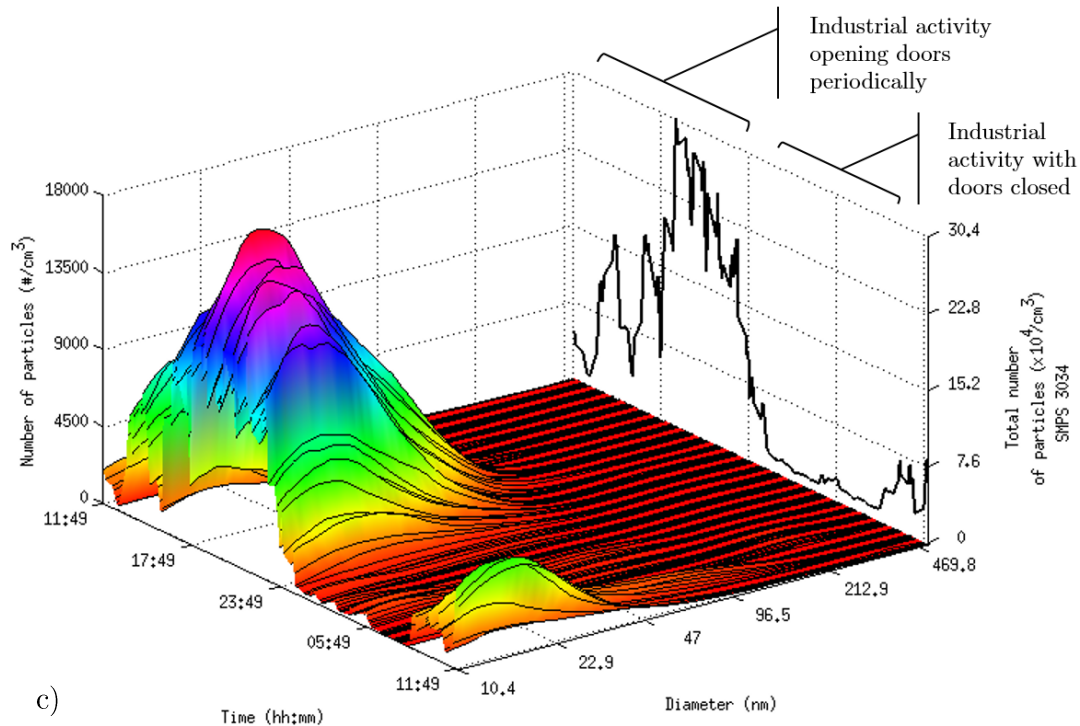
Figure 3. 8 - Size distribution and total number of airborne particles emitted for 24h during sinker EDM process: a) Workplace E, b) Workplace F and c) Workplace G.

Wire EDM

All analyzed factories, except Workplace H, perform industrial activity during 24 hours, even in the absence of workers. However, in the monitoring day in Workplace E, wire EDM equipment was turned off overnight. This can be observed in Figure 3. 9, with high concentrations of particles during the day and low overnight in Workplaces E and H, whereas in Workplaces F and G concentration profiles are relatively constant throughout the day. Like in the sinker EDM process, in the wire EDM is the Workplace G which presents the highest total number of particles (36.21×10^6 particles/cm³) and the greatest percentage of NPs (99.1%) which corresponds to an average particle size of 23 nm. In contrast, Workplace H represents one of the environments with lower total number of particles (2.91×10^6 particles/cm³) with a surface area of 69.5 µm²/cm³. This last value is in agreement with those achieved in the industry of aluminum surface treatments with similar number of particles. The surface area deposited per human lung has not been evaluated in the other industrial sites and processes.
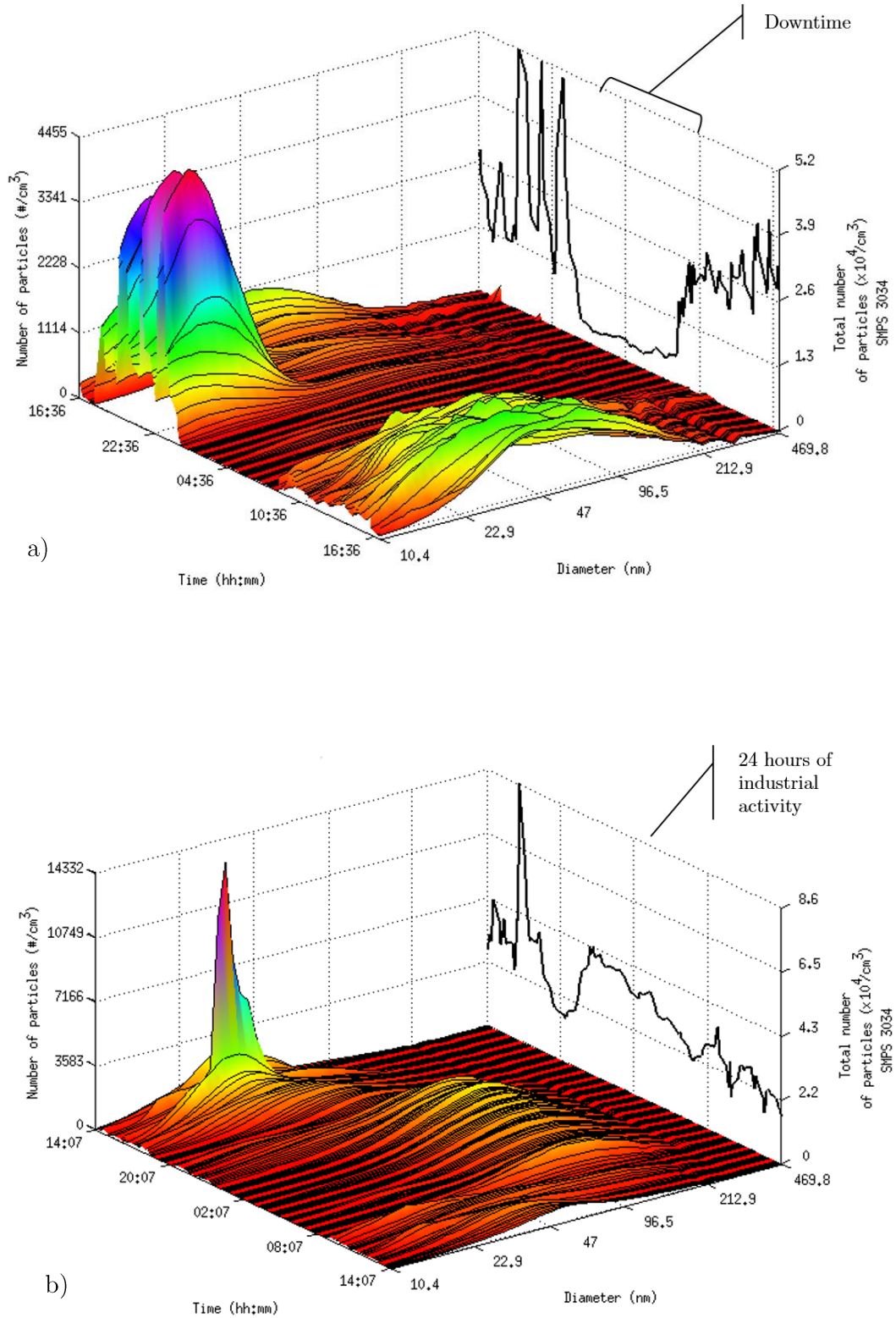
Figure 3. 9 - Size distribution and total number of airborne particles emitted for 24h during wire EDM process: a) Workplace E, b) Workplace F, c) Workplace G and d) Workplace H.
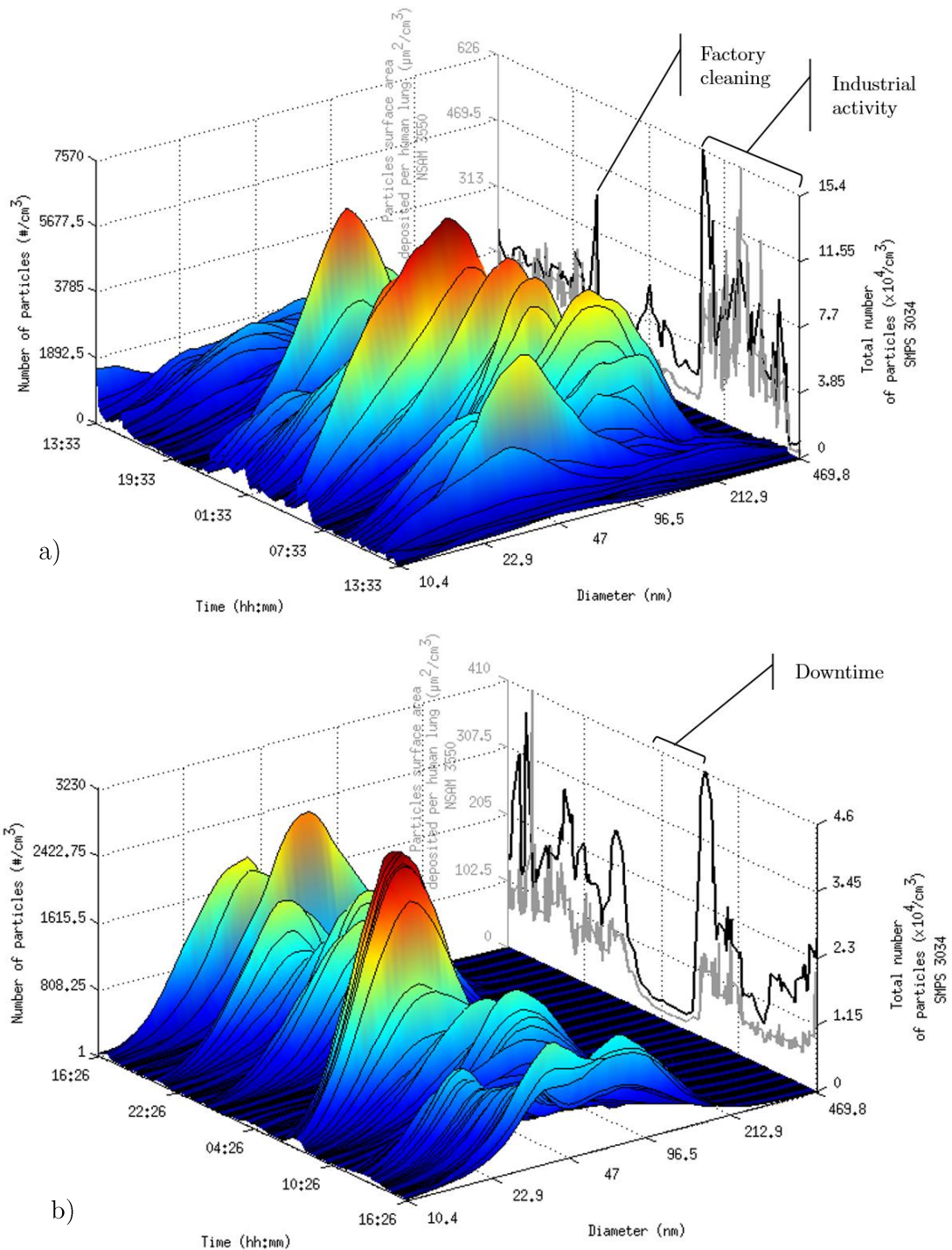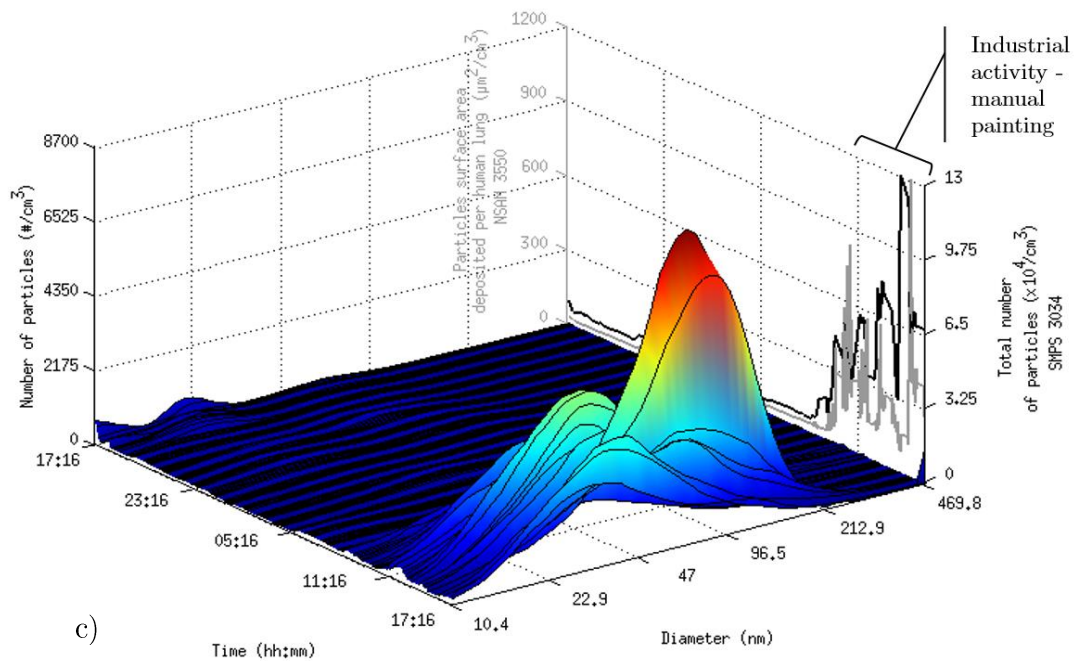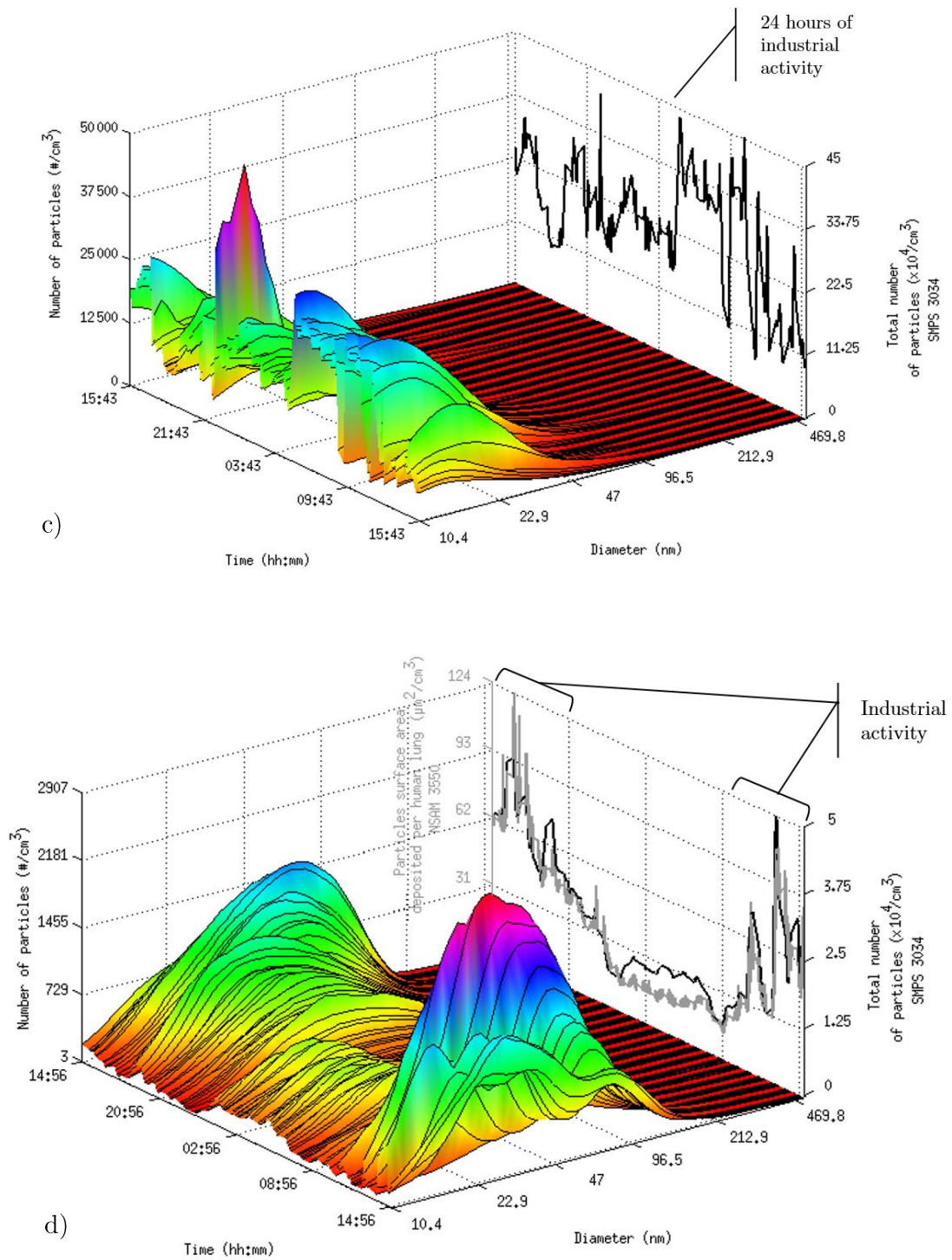
Figure 3. 9 - Size distribution and total number of airborne particles emitted for 24h during wire EDM process: a) Workplace E, b) Workplace F, c) Workplace G and d) Workplace H.

Laser machining

The laser machining process takes place only during the working hours and with the equipment having the doors closed. The particles concentration profile (Figure 3. 10) increases during the day, which coincides with the industrial activity period, and substantially decreases at night. Laser machining emits in 24 hours a total of 0.89×10^6 particles/cm^3 with an average particle diameter of 58 nm.
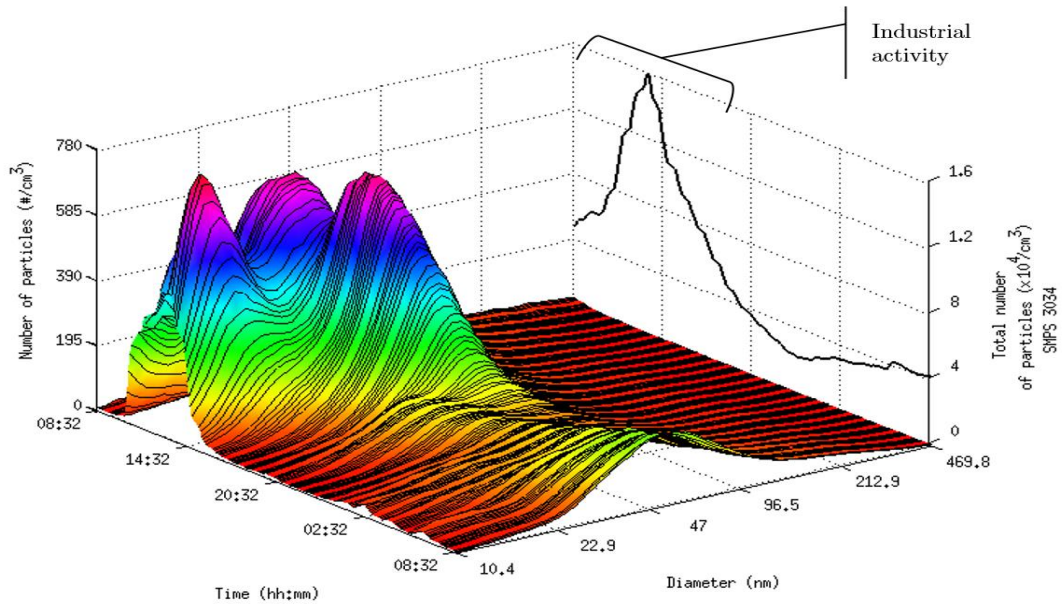
Figure 3. 10 - Size distribution and total number of airborne particles emitted for 24h during laser machining process in Workplace G.

However, compared to other processes, the laser machining is the one that releases the lowest number of particles (Figure 3. 11). Conversely, wire EDM in Workplace G is the process emitting the greatest number of particles and the smallest average size. Particles generated by sinker EDM in Workplace G have also a small average size. This condition
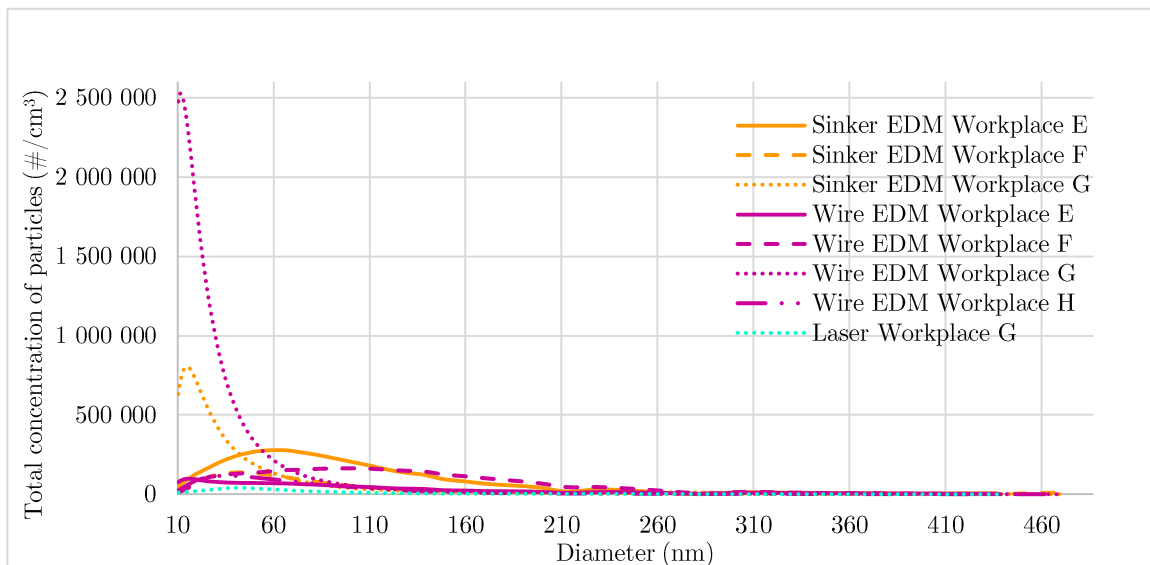
Figure 3. 11 - Size distribution of particles emitted from subtractive manufacturing.

can lead Workplace G to be considered the most potentially hazardous occupational environment to the health of workers. In average, the biggest particles are emitted by sinker EDM process.

The $C_{C\ TWA-8hr}$ values for the different processes in the 4 workplaces, were calculated in order to determine the PCR (Table 3. 7).

Table 3. 7 - Concentrations of particles and PCR calculated for the sinker EDM, wire EDM and laser machining processes in the 4 workplaces.

Industrial Process	Workplace	$C_{IA\ TWA-8hr}$ ($\times 10^4$ particles/cm³)	$C_{B\ TWA-8hr}$ ($\times 10^4$ particles/cm³)	$C_{C\ TWA-8hr}$ ($\times 10^4$ particles/cm³)	NRV ($\times 10^4$ particles/cm³)	PCR $_{TWA-8hr}$
Sinker EDM	E	6.2	0.8	5.4		1.35-2.70
	F	2.4	1.1	1.3		0.33-0.65
	G	12.0	1.6	10.4		2.60-5.20
Wire EDM	E	2.5	0.4	2.1		0.53-1.05
	F	3.1	2.4	0.7	2 - 4	0.18-0.35
	G	22.6	21.4	1.2		0.30-0.60
	H	2.1	1.1	1.0		0.25-0.50
Laser Machining	G	0.8	0.3	0.5		0.13-0.25

It is considered that airborne NPs present in the environments of the industry of subtractive manufacturing belong to class 2 (examples: Ag, Au, CoO, Fe, Fe_xO_y, Pb...) and class 3 (examples: Al_2O_3, SiO_2, TiN, TiO_2...) of nanomaterials, placing NRV in the range of 0.2 - 0.4$\times 10^5$ particles/cm³.

Despite the majority of studied workplaces have PCR within the stated reference values, sinker EDM in workplaces E and G reveal values of PCR that exceed the limit of 1. For this reason, this industrial process is potentially harmful for workers and thus further investigations are required

Number and surface area correlation

Currently, the number and the surface area are the most suitable metrics to characterize NPs, besides these are usually correlated. Surface area can be determined by direct methods (NSAM) or by estimation, knowing the particle size distribution (SMPS) and shape. However, some researchers [148] [149] have observed in some conditions that both parameters cannot always be well correlated.

In industries of aluminum surface treatments and subtractive manufacturing, the particle surface area deposited in human lung and the total number of particles seem to have similar profiles (Figures 3. 4 , 3. 5 , 3. 6, and 3. 9 d)). The graphic of Figure 3. 12 plots

the comparison between the number of particles detected by the SMPS 3034 and the surface area deposited in human lung estimated by the NSAM 3550.
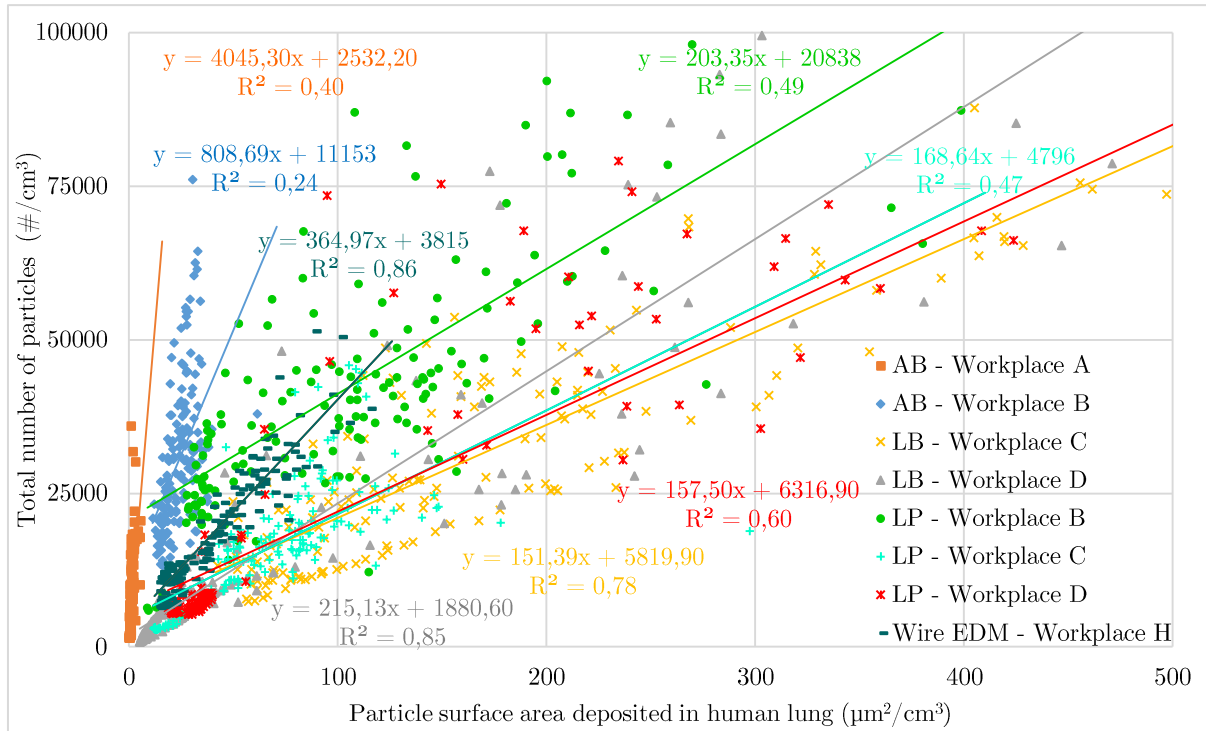
Figure 3. 12 - Correlation between particles surface area deposited in human lung and total number of particles measured in industries of aluminum surface treatments and subtractive manufacturing.

The linear regression allows the estimation of the coefficient of determination, R^2, for each process in different workplaces. For the LB and wire EDM processes, both parameters are fairly correlated ($0.78 < R^2 < 0.86$). The LP shows a weak correlation with R^2 ranging from 0.47 to 0.49. Finally, AB has very poor correlation between number and surface ($0.24 < R^2 < 0.40$). There is therefore a pattern result, already reported in literature [148], in which the lower the surface area of emitted particles is, the poorer is the correlation between both factors, although the wire EDM process is an exception. This fact reveals the equipment (NSAM) limitations, when working with low surface areas that can be associated with charger ion concentration or even with calibration issues.

3.2.2 Monitoring aerosol from diverse sources

Unintended NPs are released from the most diverse sources, e.g. laboratorial research and industrial activities, transportation or daily life activities.

In addition to the daily monitoring of the industrial processes, some examples of general activities responsible for the emission of NPs, are studied. Experiments performed for short periods of time are represented in Figure 3. 13, with the particle diameter as a function of the average concentration of particle for 3 min.

Activities, such as burning an incense or a candle or the combustion emission from a diesel car, are those releasing the largest number of particles. Thus, the gasoline vehicles

are the cleanest, emitting almost 50 times less particles in the range of 10-487 nm than the diesel ones. Conversely, the sputtering cleanroom is the monitored environment with the lowest presence of particles (0.08 particles/cm³), showing the effectiveness on the air filtration and ventilation systems. Moreover, the average particle size in all activities is lower than 100 nm, except in the case of the sputtering cleanroom (Table 3. 8).
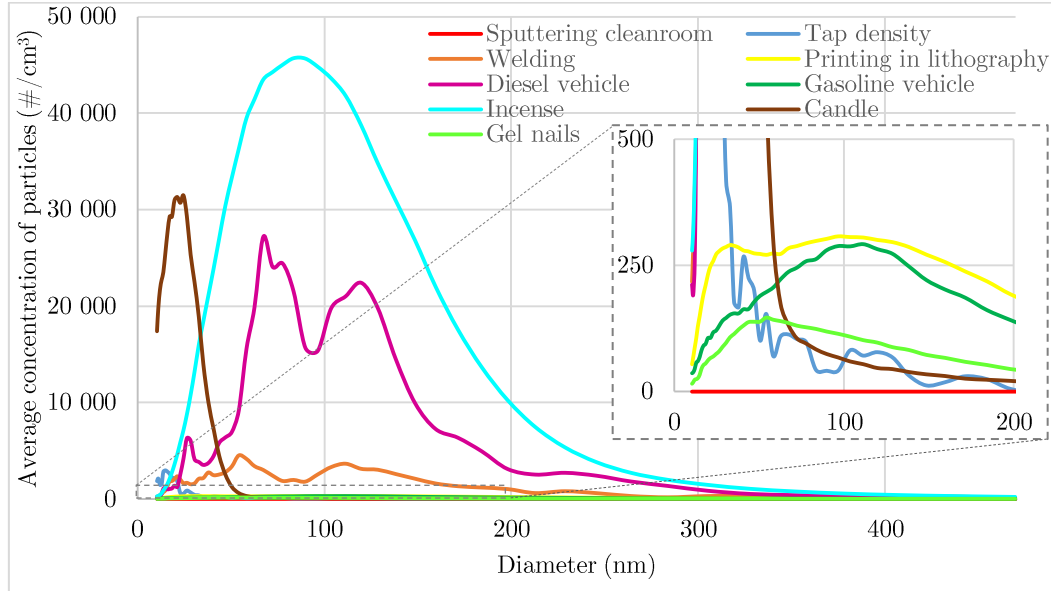
Figure 3. 13 - Size distribution of particles emitted from diverse activities, for 3 min.

Table 3. 8 - Number and size of particles released in different activities.

Activity	Average concentration of particles (#/cm³) (scan 3 min)	Particle size	
		$\overline{x}$ (nm)	σ
Incense	926 742.50	88	2
Candle	478 973.89	22	1
Diesel vehicle	382 280.02	93	2
Welding	91 487.68	79	2
Tap density	30 249.27	22	2
Printing in lithography	11 271.99	89	2
Gasoline vehicle	7 660.49	93	2
Gel nails	3 914.59	80	2
Sputtering cleanroom	0.08	137	2

The measured average particle sizes, considered as NPs, must be a potential cause of concern, since the daily activity of burning candles and the tap density laboratorial assay show to produce the smallest particles (22 nm). In this order of sizes, particles can easily enter into the human body by any exposure route. Therefore, it is of utmost importance to develop filters that are effectively able to retain NPs, in order to prevent possible health problems in workers.

3.2.3 Filters efficiency

Anopore and AnoT_F1_2.55_85_60_O thin film were evaluated in terms of efficiency in air filtration in a closed laboratorial room (Figure 3. 14).
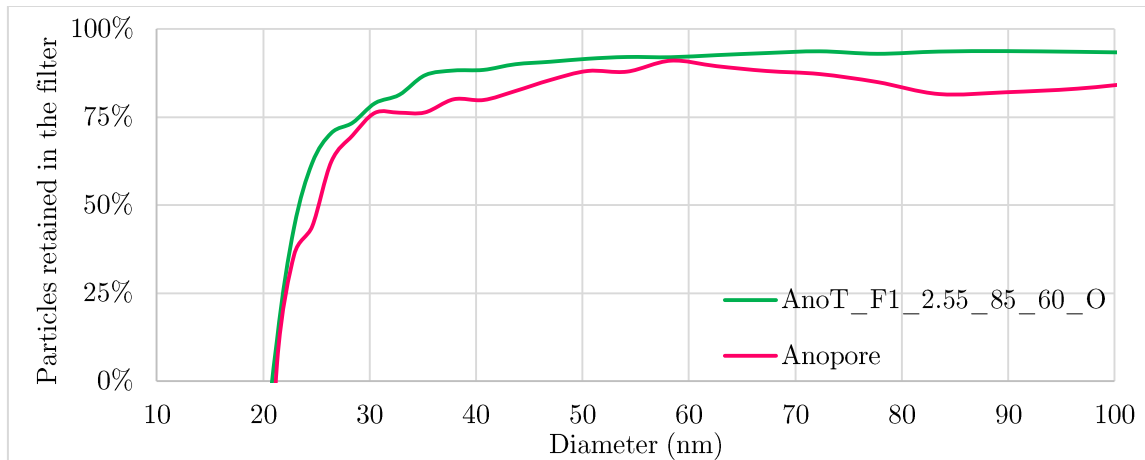
Figure 3. 14 - Efficiency of Anopore and AnoT_F1_2.55_85_60_O against NPs.

In the range 10-100 nm Anopore and AnoT_F1_2.55_85_60_O have similar profiles. However, AnoT_F1_2.55_85_60_O thin film shows a superior efficiency for all particle sizes and a more regular filtration efficiency in the evaluated size range. The maximum efficiency is 94% for particles sizing 90 nm (AnoT_F1_2.55_85_60_O). Both filters are able only to capture particles larger than 20 nm.

Since the SMPS is not an appropriate equipment to assess the filtration efficiency, for filters with small average pores, such as Anopore and AnoT_F1_2.55_85_60_O, the equipment has to increase the air velocity to maintain the inlet flow. This makes the particles to travel at much faster velocity than the normal inlet flow. This condition may interfere with the final results, and then further studies with appropriate filter testers are required.

3.3 Key conclusions

This chapter conducted to some main conclusions that are listed below:

- Conventional industrial processes are indeed an unexpected source of unintended NPs;

- Usually, the daily size distribution in occupational environments shows a typical profile with a large number of particles emitted during industrial activities and a low number of particles during downtime;

- In the industry of aluminum surface treatments, lacquering baths (LB) presents the greatest number of particles and surface area with particles having the smallest average diameter, while anodizing baths (AB) exhibits the lowest number of particles and surface area, having the biggest average particle size;

- In the industry of subtractive manufacturing, the laser machining is the process releasing the lowest number of particles, and in contrast the wire EDM emits the greatest number of particles with the smallest size, while in average the biggest particles are present in sinker EDM environments;

- PCR exceed the recommended value of 1 in sinker EDM of Workplaces E and G, suggesting that this industrial process exposes workers to a very high concentration of NPs;

- Equipment limitations were observed: single particles are not discerned when agglomerated/aggregated, and the surface area deposited in human lung is poor correlated to the total number of particles when NSAM 3550 works with lower surface areas. Further scientific efforts are required towards the development of reliable NPs characterization techniques and equipment;

- Filtering solution developed in this work has the ability to filter a great percentage of airborne NPs.

The results achieved in the current chapter have revealed the presence of great amounts of NPs in conventional occupational environments. The wire EDM was the most concerning activity, with the highest concentration of NPs and the smallest average particle size. With potential toxic characteristics, NPs must be fully studied concerning physicochemical properties and nanotoxicity, as a way of perceiving the real toxic effects on workers. In chapter 4 a complete physicochemical characterization of NPs emitted from wire EDM (Workplace G), is performed.

Chapter 4
Characterization
of Nanoparticles

T he potential risks of NPs for the human health and environment lead the scientific community to seek for still many unanswered questions, namely to understand the mechanisms that can trigger nanomaterials toxicity. Although nowadays, with the lack of knowledge in the nanotoxicity field, there is no widely accepted methodology, the physicochemical characterization of nanomaterials combined with toxicological studies is taken as an appropriate approach in the toxicity assessment of nanomaterials.

The physicochemical characteristics of NPs influence their absorption, distribution, metabolism, excretion and toxicity. Thus, a proper physicochemical characterization based on the 5 S's: Size, Size distribution, Shape, Structure and Surface is essential to link nanomaterials properties to the toxicological responses *in vitro*, *in vivo* and/or *in silico*. According to the recent trend, *in vitro* approaches are the preferred since they present many advantages, such as providing effective results with lower associated costs and reducing the animal testing.

This chapter covers the 5 S's characterization of NPs collected in an industrial environment of subtractive manufacturing, wire EDM in Workplace G. The studies of particle size distribution present in Chapter 3, had shown that the wire EDM process in Workplace G was the source of the greatest number of particles with the smallest average particle size, and for this reason was the industrial environment of most concern and then chosen for further characterization.

Furthermore, *in vitro* nanotoxicity assessment is performed by determining the cell viability and pro-inflammatory activity.

4.1 Experimental procedure

4.1.1 Collection of nanoparticles

NPs were collected by electrostatic precipitation in Workplace G, during wire EDM to perform physicochemical characterization and *in vitro* nanotoxicological assessment.

The Nanometer Aerosol Sampler (NAS) (TSI, model 3089) used in this experiment creates an electric field between particles and substrates of deposition, attracting particles to the substrate, which according to the manufacturer have sizes smaller than 100 nm. Four transmission electron microscopy (TEM) grids (Agar Scientific) of 200 mesh Cu coated with carbon film were mounted with carbon tape on the NAS electrode, to ensure electroconductivity. One TEM grid was used in dynamic light scattering (DLS)/ electrophoretical light scattering (ELS) test, which is a destructive technique, while the others were observed by TEM, analysed by SEM-EDS and finally used in *in vitro* assays.

The equipment was operating at 1.5 L/min of inlet sample flow and -5 kV of voltage, collecting NPs for 8 hours (labour hours) during 5 weekdays.

4.1.2 Characterization

4.1.2.1 5 S's: Size, Size distribution, Shape, Structure and Surface

The airborne NPs present in Workplace G during wire EDM and collected in TEM grids, were fully physicochemically characterized according to 5 S's, through diverse characterization techniques.

Size and size distribution were estimated by TEM, DLS and SMPS. In addition, TEM was also used to evaluate the shape and structure of NPs, while surface was assessed by ELS to determine the zeta potential. Furthermore, the metallic elemental composition was evaluated by scanning electron microscopy - Energy Dispersive X-ray Spectroscopy (SEM-EDS).

The list of equipment used in the characterization of NPs, are present in Table 4. 1.

Table 4. 1 - Techniques and equipment used in the physicochemical characterization of NPs.

Characteristic	Technique	Equipment
	DLS	Malvern Zeta Sizer Nano ZS series
Size and Size distribution	TEM	FEI, Model Tecnai G2
	SMPS	TSI, Model 3034
Shape	TEM	FEI, Model Tecnai G2
Structure	TEM	FEI, Model Tecnai G2
Surface	ELS	Malvern zeta Sizer, nano ZS series
Chemical Composition	SEM-EDS	FEI Quanta 400 FEG

Size and particle size distribution were evaluated by TEM analysis (accelerating voltage of 200 kV). Various images with different magnifications were recorded (5 000 X and 15 000 X) and were after processed with ImageTool 3.0 software. These images revealed also the different shapes of the NPs. Moreover, the selected area electron diffraction (SAED) pattern allowed to characterize the crystalline phases of NPs.

For the size and surface characterization, TEM grid with NPs was immersed in 5 mL of ultrapure water and particles were dispersed in an ultrasonic bath for 20 min. Then, the dispersion was analyzed by DLS and ELS in the same equipment, which was operating at a backscattering angle of 173° and a temperature of 298 K. For both techniques, 3 measurements of 12 scans, were conducted.

NPs were also observed by SEM, operating at 15 kV, and a set of aleatory particles with different sizes and shapes were used to evaluate their chemical composition.

4.1.2.2 Nanotoxicity assessment

NPs collected in Workplace G during wire EDM were tested _in vitro_ in order to study the potential nanotoxicological effects of these NPs when in contact with macrophages cells.

The NPs collected in two TEM grids were separately immersed in 10 µL of Dulbecco's Modified Eagle Medium (DMEM) (Sigma Aldrich) supplemented with 10% inactivated fetal bovine serum, 100 U/mL of penicillin, 100 µg/mL of streptomycin, 1.5 g/L of sodium bicarbonate and 3.5 g/L of D-glucose, then exposed to UV radiation during 15 min to promote the material sterilization and finally dispersed in an ultrasonic bath for 45 min. The same procedure was used in two TEM grids without NPs to serve as control (Figure 4. 1).
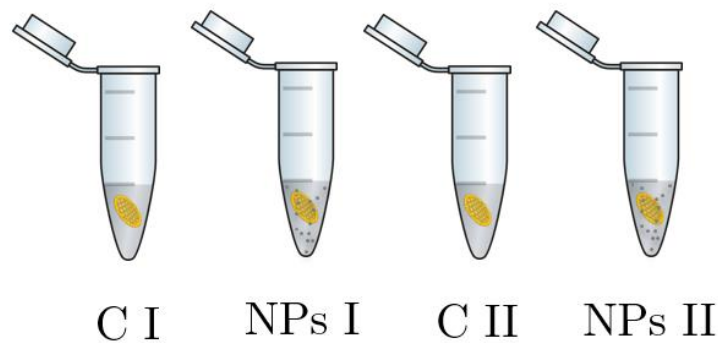
Figure 4. 1 - Scheme of TEM girds immersed in DMEM in Eppendorf.

Murine macrophages cells, Raw 264.7 (ATCC®, TIB71™), were cultured in DMEM, at a cellular density of 10 cells/mL. Raw 264.7 were cultivated in a 96-well plate (100 µL/well) and were kept at 310 K in a humidified atmosphere of 95% air and 5% CO_2 for 14 hours to allow cells adhesion.

Afterwards, the 100 µL of culture medium of each well were removed and eight conditions of analysis were performed:

- C_0 I – control 0 I: adding 100 µL of culture medium

- C_{10} I – control 10: adding 10 µL of solution without NPs + 90 µL of culture medium

- NP_{10} I – adding 10 µL of dispersion of NPs + 90 µL of culture medium

- C_0 II – control 0 II: adding 100 µL of culture medium

- C_7 II – control 7: adding 7 µL of solution without NPs + 93 µL of culture medium

- NP_7 II – adding 7 µL of dispersion of NPs + 93 µL of culture medium

- C_2 II – control 2: adding 2 µL of solution without NPs + 98 µL of culture medium

- NP_2 II – adding 2 µL of dispersion of NPs + 98 µL of culture medium

Then cells were incubated at 310 K in a humidified atmosphere of 95% of air with 5% of CO_2 during 24 hours.

This procedure was performed to evaluate the nanotoxicity of NPs *in vitro*, in terms of pro-inflammatory activity and cellular viability.

In the inflammatory process, and after activation with pro-inflammatory stimuli, macrophages produce nitric oxide (NO), which plays a key role mediating the inflammatory response [150]. Thus, the pro-inflammatory activity of several compounds can be assessed indirectly by determining the production of NO through the Griess method. In fact, the Griess assay quantifies the nitrite ions (NO_2^-) present in the cell culture supernatant, which are originated by the presence of NO in aqueous solutions.

Regarding the cellular viability, it can be determined through a reliable assay, the alamarBlue. This is composed by resazurin, which is an oxidation-reduction indicator. The characteristic blue color of resazurin is converted into a bright pink in the presence of metabolically active cells, which promote the reduction of resazurin into resorufin. In contrast, inactive cells keep the compound oxidized, which means with the same initial blue color. Thus, the direct reading of the color spectrum allows the identification of the level of cellular viability.

Therefore, after 24 hours of macrophages incubation in the presence of NPs, 170 µL of cell culture supernatant were collected and added to the same volume of Griess reagent (N-1-napthylethylenediamine 0.1% (m/v) + sulfanilamide 1% (m/v) in H_3PO_4 5% (v/v)) to measure the production of NO. Concomitantly, the remaining culture medium was discarded and 150 µL of DMEM with 10% of resazurin were added into the wells in order to evaluate cellular viability.

Pro-inflammatory activity tests (nitric oxide) were kept away from the light for 30 min and cellular viability assays (alamarBlue) were maintained at low temperature for 6 H.

Both were then read by spectrophotometry (Synergy™ HT, BioTek instruments, Winooski, VT) at 550 nm (pro-inflammatory activity) and 570 and 620 nm (cellular viability).

The values of pro-inflammatory activity and cellular viability are expressed as the percentage of C_0 (control 0 with only the culture medium), being C_0 considered in each assay, no production of NO and 100% of cellular viability.

4.2 Results and discussion

4.2.1 5 S's characterization

4.2.1.1 Size and Size distribution

The size of particles is one of the most important characteristics influencing the toxicity, being usually the smaller particles the much toxic ones.

The size distribution and average size of particles were evaluated by image processing of TEM images and DLS. Moreover, in chapter 3, the size distribution of particles present in Workplace G during the wire EDM were also measured through the SMPS.

Figure 4. 2 compares the profiles of size distribution measured by observation of TEM images and SMPS. Both have similar profiles, with the major amount of particles being smaller than 100 nm. In fact, the average particle size calculated by processing TEM images is 27 ± 1 nm, while that measured by SMPS is 23 ± 2 nm. These values are quite similar and indicate that both are reliable techniques in the evaluation of the size of particles.
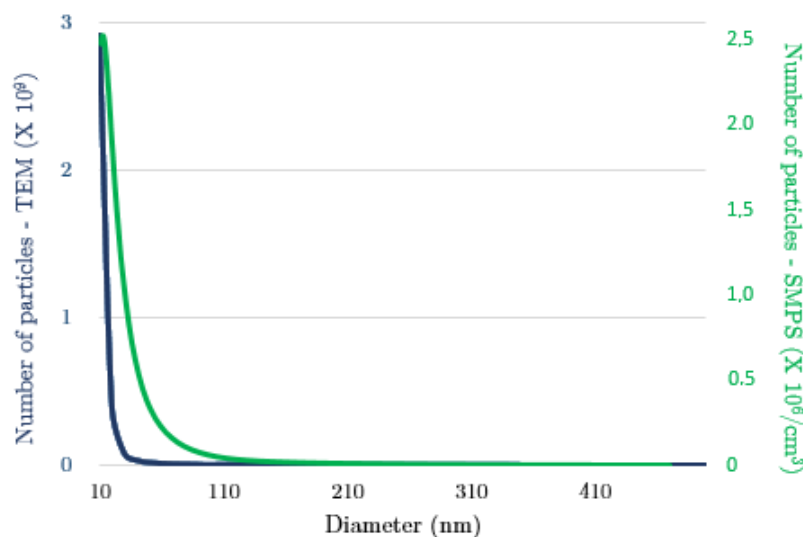
Figure 4. 2 - Size distribution of particles present in Workplace G during wire EDM, determined by TEM observation and by SMPS.

However, the particle size distribution achieved by DLS analysis (Figure 4. 3) has a different profile of Figure 4. 2.

The DLS results reveal two distributions in the ranges 40 – 150 nm and 150 – 700 nm, suggesting that particles present different behaviors in liquids and air. When particles are immersed in ultrapure water, they probably tend to agglomerate/aggregate, being then detected by DLS as larger particles. Therefore, the average particle size is also larger (349 nm) than those measured by TEM and SMPS.
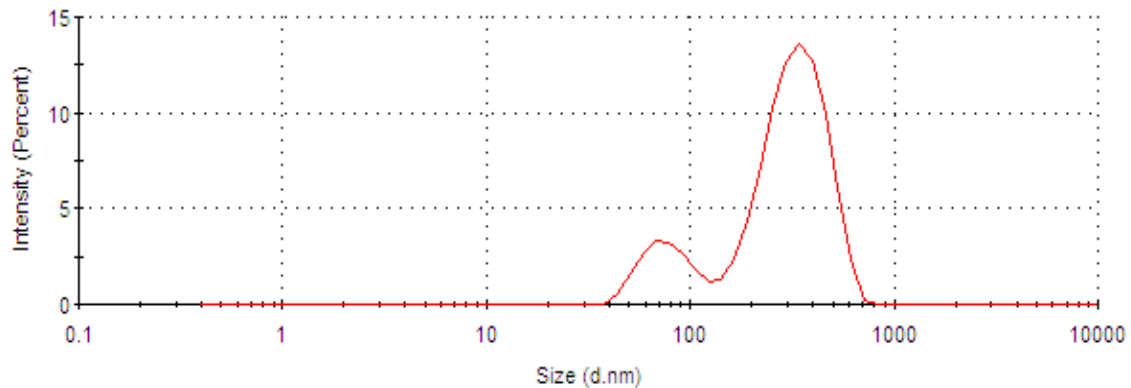
Figure 4. 3 - Size distribution of particles present in Workplace G during wire EDM, determined by DLS.

Usually, the toxicological *in vitro* tests are performed with different concentration of particles in the cell culture medium to study their effect in the cells. Although the number of particles (or even the surface area) is the best metric to be used, due to NPs being almost absent in mass, nowadays the mass continues to be used as a key characteristic to potentially induce toxicity. This is mainly due to the difficulty in determining the real number of particles present in the assay and thus to relate it to the toxicological responses.

In this study, the total number of particles is estimated by determining the number of particles analyzed in the TEM images and extrapolating this value to the total area of the TEM grid (the number and size throughout the TEM grid are homogeneous).

The final value is approximately **3.5×10^9 particles/grid**.

4.2.1.2 Shape

The shape is one of the NPs characteristics which also may influence toxicological responses [151]. In particular, the high aspect ratio NPs difficult the clearance mechanisms presenting increased toxicity.

The particles collected in Workplace G during wire EDM were observed by TEM and the images reveal two main types of shapes: the spherical shaped particles (Figure 4. 4) and the irregularly shaped particles (Figure 4. 5).

Spherical particles present an almost perfectly spherical shape and are frequently isolated. They exhibit a wide range of sizes within few nanometers to micrometers. Conversely, irregularly shaped particles reveal many undefined shapes which are mainly agglomerated/aggregated, with diverse sizes.

Chen et al. [152] had already reported similar airborne NPs, with irregular shapes and the existence of a great number of agglomerates/aggregates, detected in a factory with the same industrial process.
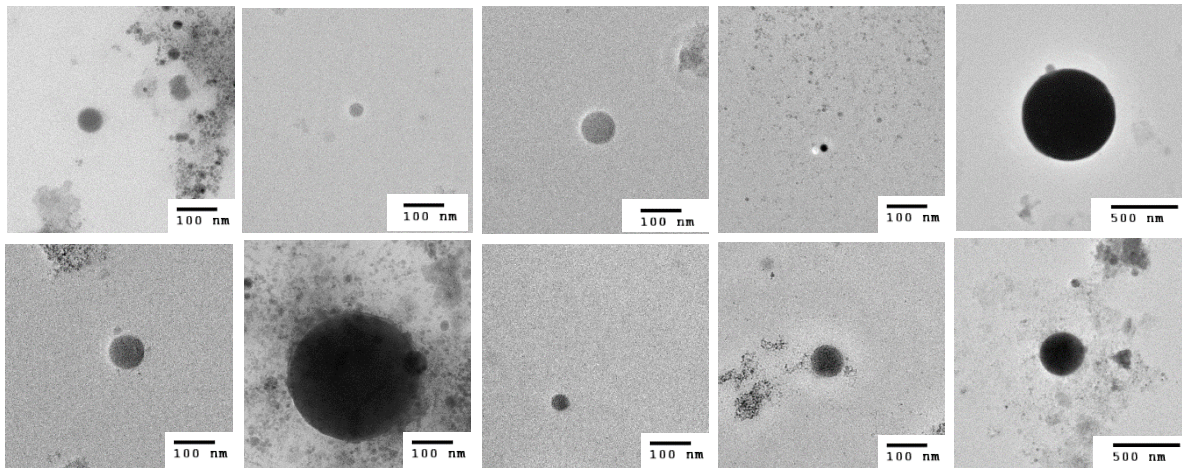
Figure 4. 4 - Spherical shaped particles (TEM).
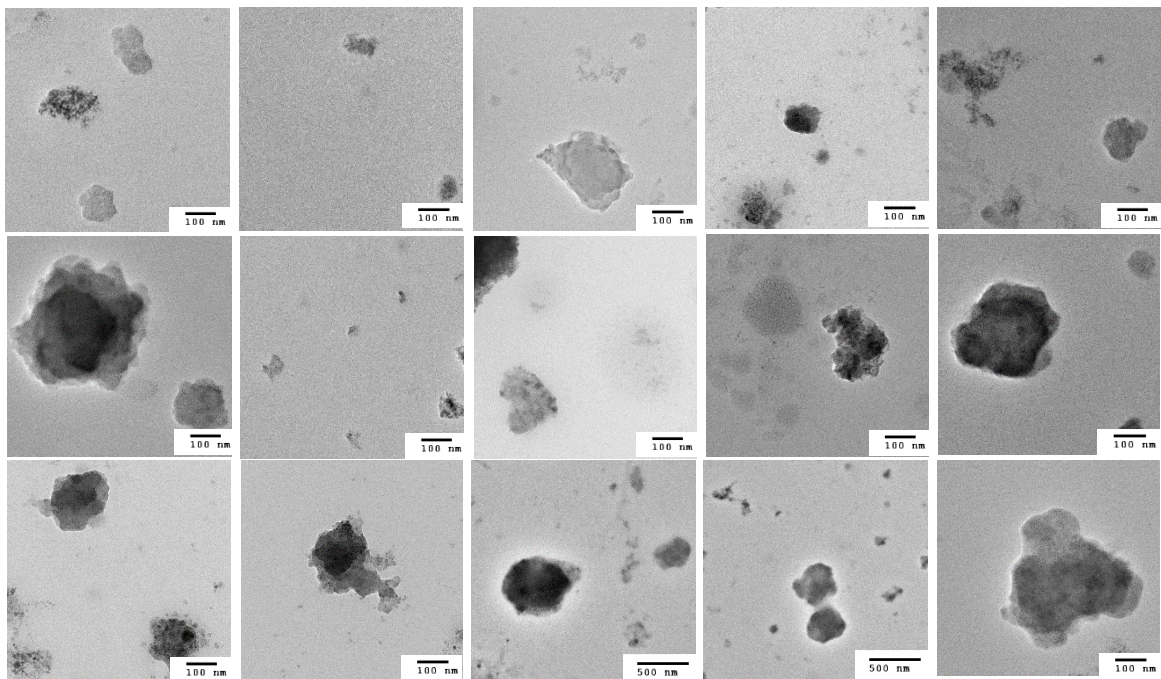
Figure 4. 5 - Irregularly shaped particles (TEM).

4.2.1.3 Structure

Representative TEM images and respective SAED are present in Figure 4. 6. According to the SAED images, it is evident the presence of both, crystalline (Figure 4. 6 a)) and amorphous (Figure 4. 6 b)) NPs. The thin ring visualized in Figure 4. 6 b) must be ignored, since it is considered optical artifact.

For technical reasons, it was not possible to measure the d-spacing and consequently to identify the planes of diffraction.

a)   b)
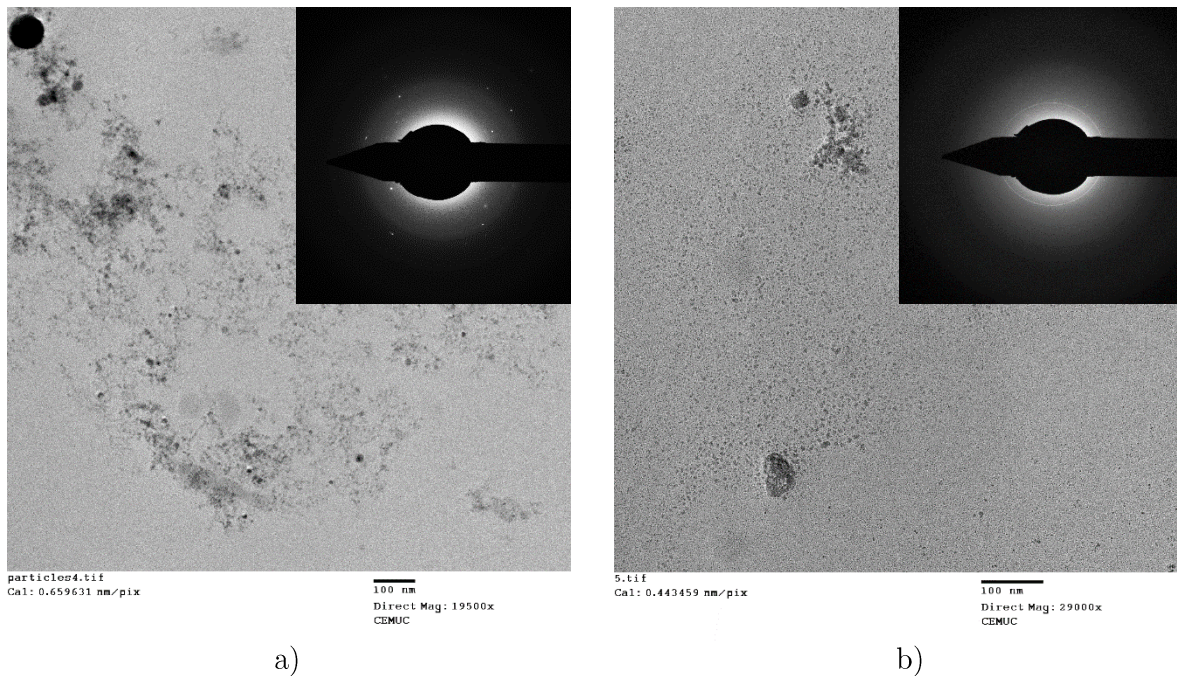
Figure 4. 6 – Examples of TEM images and SAED of NPs present in Workplace G with: a) crystalline and b) amorphous structures.

The chemical composition of NPs were evaluated to determine the weight content of chemical elements present in airborne NPs from Workplace G (Figure 4. 7). Although C, O, Si, Cl and S were detected, the most predominant elements are Cu, Al, Fe, Zn and Cr and trace amounts of Mo, Mg, Ca and K were detected. These outcomes indicate that the main source of NPs are the stainless steel working pieces (Fe and Cr) and the brass wire of EDM (Cu and Zn). The Al is probably originated from the dielectric fluid or other EDM activities.
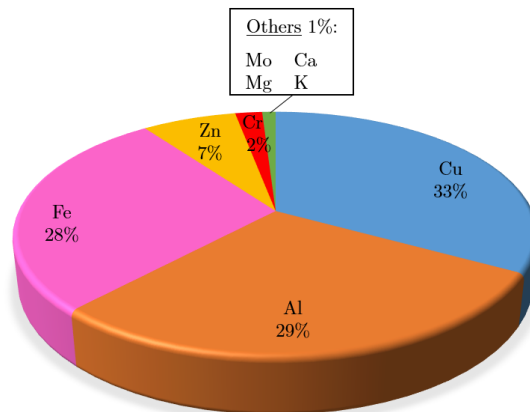
Figure 4. 7 – Percentage of metals present in NPs collected in Workplace G (wt.%).

Although the SEM-EDS results have shown the presence of several chemical elements, the chemical composition of particles varies according to their shape.

Regardless the Al element, the chemical composition of irregularly shaped particles are predominantly Cu (1 - 16 wt.%) and Zn (1 -14 wt.%) and the spherical shaped particles are mainly composed by Fe (2 - 45 wt.% and 3 - 35 wt.%), O (2 - 11 wt.% and 3 - 18 wt.%) and C (2 - 7 wt.% and 3 - 15 wt.%) (Figure 4. 8).
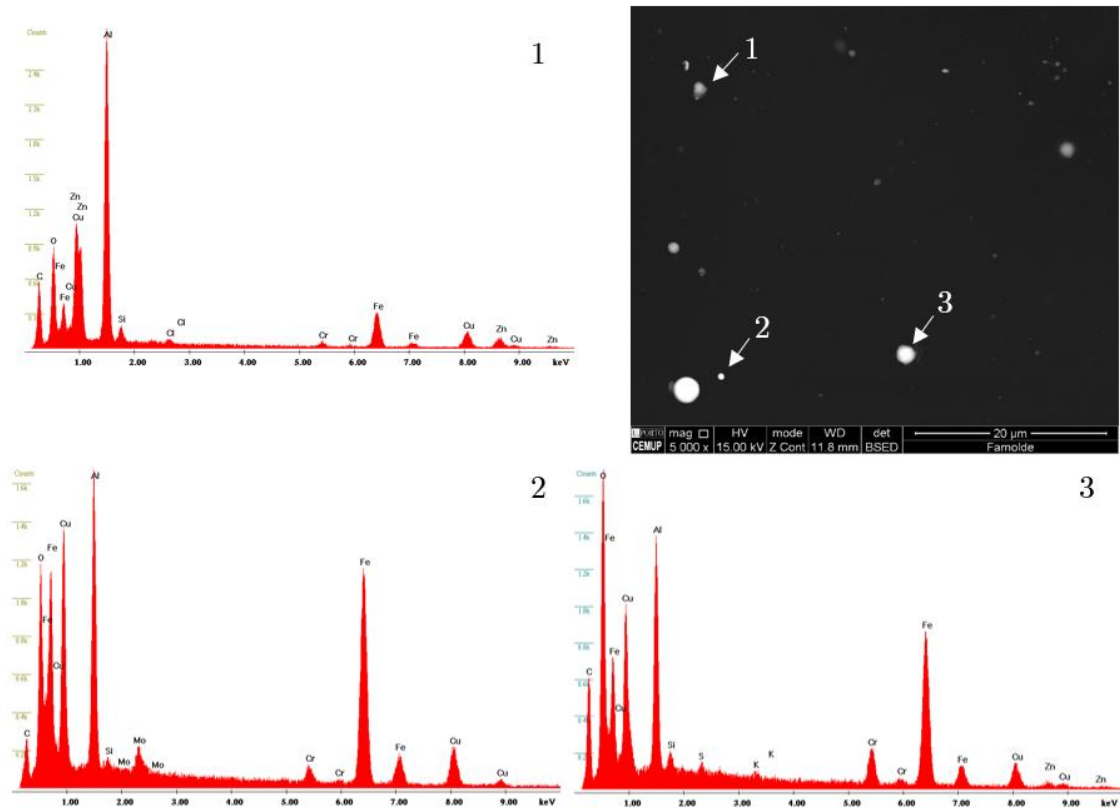
Figure 4. 8 - SEM-EDS spectra of particles with different shapes: 1) irregularly shaped and 2) spherical shaped.

According to nanotoxicological studies, Cu and Zn-based particles are those of most concern, since they induce high levels of toxicity both *in vitro* and *in vivo*. They cause massive oxidative stress, cell death and severe cytotoxic inflammation. Thence, it is of paramount importance to evaluate the effect of these NPs in cells, through *in vitro* assays, according to the trend to abolish animal testing.

4.2.1.4 Surface

The surface charge influences the toxicological responses of NPs. In fact, the positively charged particles are known for inducing higher levels of toxicity than the negatively charged ones. This can be explained by the overall negative charge of surface cells which promotes the cellular uptake of NPs [153].

However, recent studies have revealed that the opposite charges attraction may not be the only way of interaction between NPs and cellular membrane, at the nanoscale. *Troiano et al.* [154] have shown that negatively charged particles can be also a matter of concern regarding the potential toxicity, since they are also attracted to the membrane of the cells, according to a mechanism that is not yet well understood.

The surface of NPs was characterized by the determination of the surface charge through the zeta potential. Zeta potential remains in the range of negative values with an average value of -26.60 mV (Figure 4. 9).
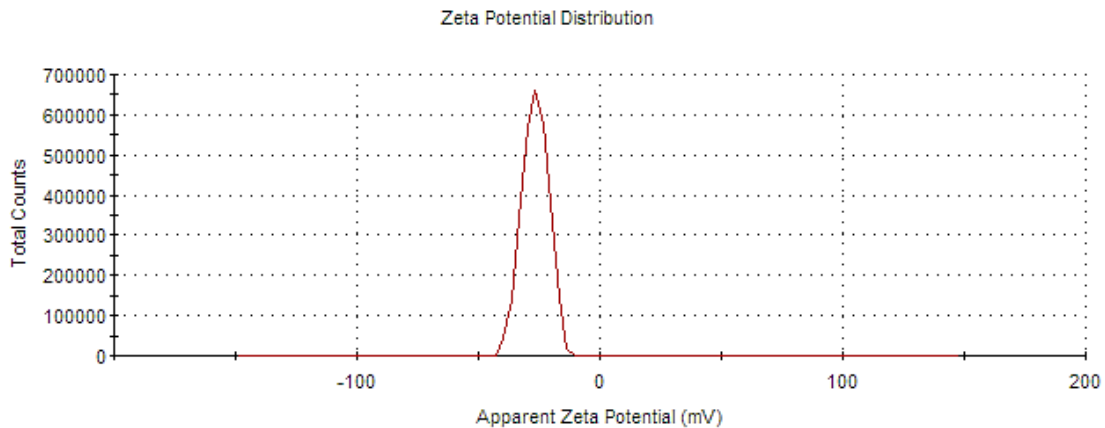
Figure 4. 9 – Zeta potential distribution of NPs collected in Workplace G during wire EDM.

As already referred, the fact of NPs present a negative charge is not predictive of the absence of toxicity, and thus further studies must be carried out, namely *in vitro* toxicological tests. On the other hand, the average zeta potential in the range of -30 mV to +30 mV is characteristic of instable particles which trend to agglomerate/aggregate [155]. However, caution must be taken in the interpretation of these results, since the zeta potential values are closely dependent on the characteristics of the NPs' medium (pH).

The tendency of NPs to agglomerate/aggregate in the air can be observed in the TEM images, where the airborne particles are frequently found agglomerated/aggregated (Figure 4. 10).
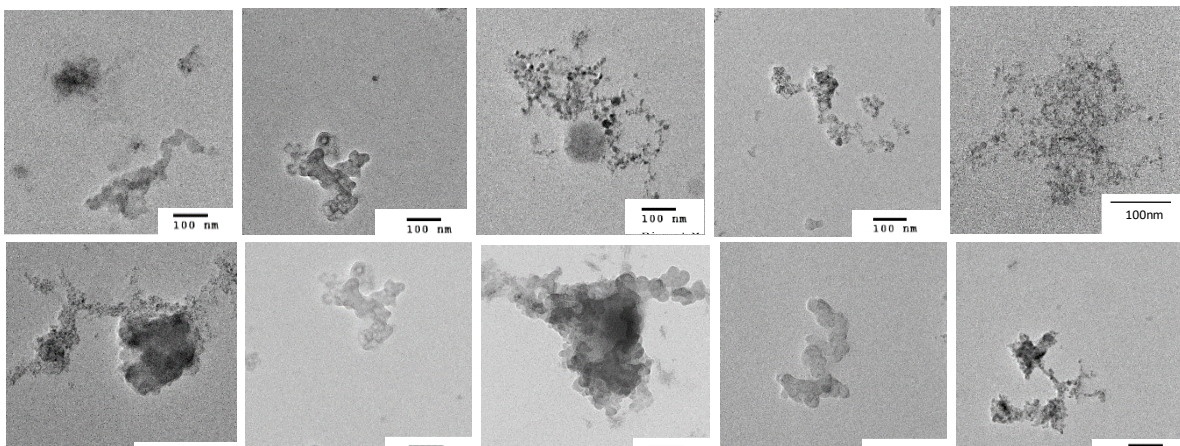
Figure 4. 10 - TEM images of agglomerates/aggregates of NPs present in Workplace G during wire EDM.

Moreover, in the DLS test, the great number of particles which sizes are larger than 100 nm (Figure 4. 3) corroborates that also in liquid medium (ultrapure water) particles are agglomerated/aggregated, since the majority of single particles observed in TEM are nanosized.

4.2.2 Nanotoxicity assessment

The high levels of NPs found in Workplace G during wire EDM should be a significant concern, regarding the human health and the environment. For this reason, the nanotoxicological potential of these NPs with known physicochemical characteristics are of paramount importance contributing to unveil the real health effects or even the triggered mechanisms of toxicity.

In this study, a preliminary approach is taken in this sense, having in mind that there is still much work to be done. Therefore, NO production assays and cellular viability were performed with different concentrations of NPs, as preliminary nanotoxicological studies. As a TEM grid contains approximately 3.5×10^9 particles, the final concentrations are:

- $NP_2 = 0.7 \times 10^7$ particles/µL;
- $NP_7 = 2.45 \times 10^7$ particles/µL;
- $NP_{10} = 3.5 \times 10^7$ particles/µL.

4.2.2.1 Production of nitric oxide

The pro-inflammatory activity of macrophages is evaluated by determining the additional production of nitric oxide relatively to the control, when the cells are in contact with potential toxic NPs from wire EDM (Figure 4. 11).
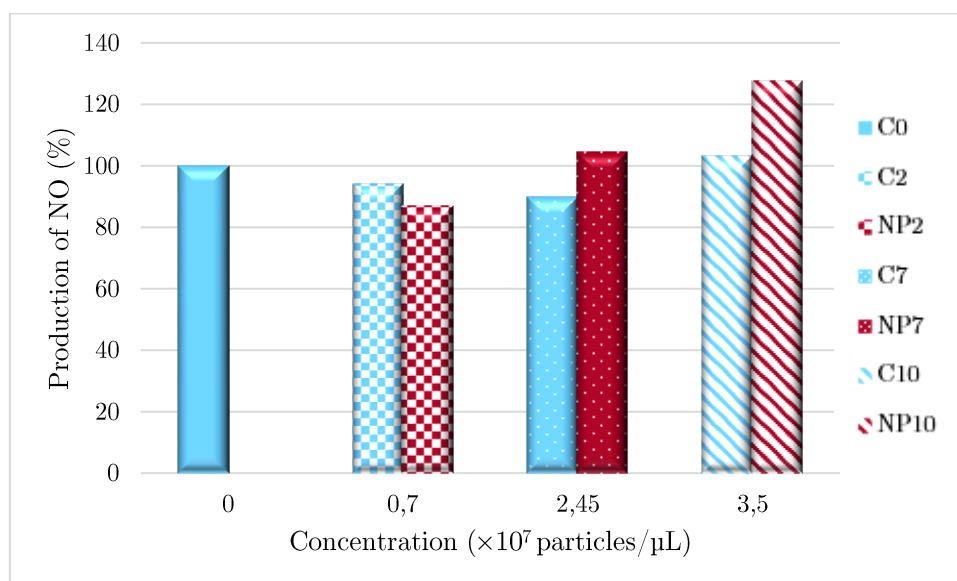
Figure 4. 11 – Pro-inflammatory activity of Raw 264.7 cells incubated with different concentrations of NPs, determined through the production of nitric oxide.

For the lowest concentration of NPs (0.7×10^7 particles/µL), the results demonstrate that there is no production of NO, shown in % of C_0, having values lower than the control C_0. In contrast, the other two concentrations of NPs tested (2.45×10^7 particles/µL and 3.5×10^7 particles/µL) increase the production of nitric oxide by macrophages, relatively to respective controls without NPs ($NP_7 > C_7$ and $NP_{10} > C_{10}$). The increase in the production of NO observed in NP_7 and NP_{10} is about 14% and 25% relatively to C_7 and C_{10} and 4% and 27% compared to C_0.

These results indicate that the highest concentration of NPs (3.5×10^7 particles/µL) induces an immunostimulatory effect on Raw 264.7 cells.

4.2.2.2 Cellular viability

The influence of NPs collected in Workplace G in the macrophage cellular viability is depicted in Figure 4. 12.
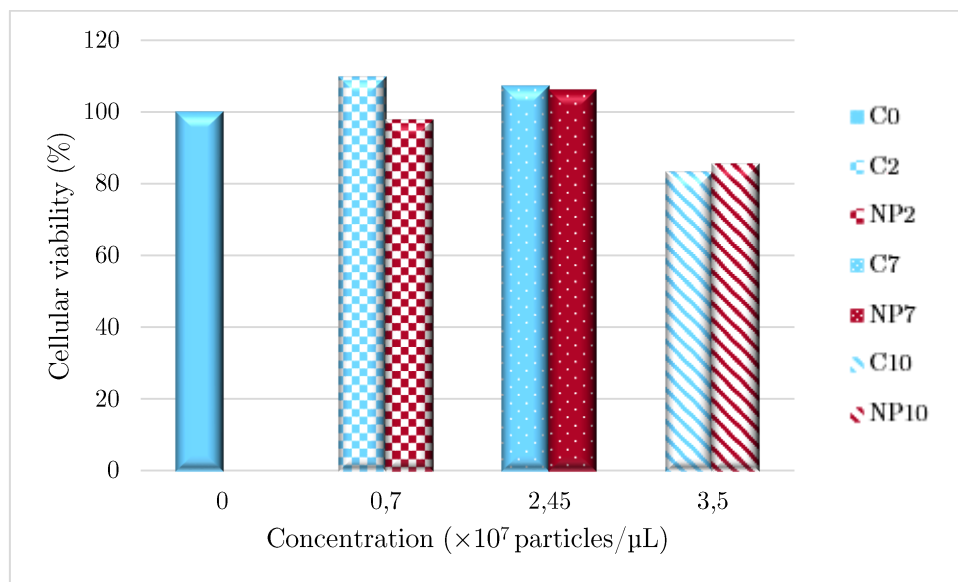
Figure 4. 12 - Viability of Raw 264.7 cells incubated with different concentrations of NPs, determined through alamarBlue assay.

The results are shown in % comparing to the C_0, the control assay without stimuli. The cellular viability is not affected by introducing lower concentrations of NPs in the cell culture medium, with C_2, C_7 and NP_7 being even superior than C_0.

In contrast, for higher concentrations (3.5×10^7 particles/µL), the outcomes are slightly lower than the control C_0. However, the decrease in cellular viability is observed in both, C_{10} and NP_{10}.

Therefore, the preliminary results of cellular viability are inconclusive, revealing that most probably the concentrations of NPs studied are considered non-toxic.

However, this does not imply that higher concentrations of these NPs could not cause toxicity effects. *Chen et al.* [156] studied the cellular viability of human alveolar epithelial cells (16HBE) when in contact with particles collected from an industrial environment of wire EDM. Regarding the cellular viability, they showed that particles smaller than 100 nm present toxic effects for an unknown dose, with cellular viability of particles from wire EDM being always lower than NPs of background (without industrial activity). They were not able to determine the mass of particles smaller than 56 nm due to equipment limitations in the case of low mass.

The NPs from wire EDM collected in Workplace G reveal do not affect the cellular viability, despite having increased the production of NO, which is related to pro-inflammatory mechanisms.

However, only one sample was used for each concentration, which may lead to possible non representativeness or misreads. These results cannot be considered reliable since it was not possible to properly study the nanotoxicological trend in a large number of samples and thus to determine the standard deviation.

Therefore, the cellular viability and production of nitric oxide assayed in these airborne NPs are merely indicative of a possible toxic effect, and must be analysed with caution, since further tests are required to prove their nanotoxicity.

4.3 Key conclusions

In this chapter airborne NPs present in Workplace G and originated from wire EDM, are characterized regarding their physicochemical characteristics and nanotoxicological effects in macrophage cells. The main conclusions are:

- The size distributions of particles in air, determined by TEM and SMPS, are identical, while particles in water assessed by DLS, present a different profile of size distribution, due to their agglomeration/aggregation in liquid mediums. The average particle sizes are: 27 nm (TEM), 23 nm (SMPS) and 349 nm (DLS);
- The total number of particles per grid is 3.5×10^9;
- Particles have spherical and irregular shapes;
- Regarding the structure of NPs, they are present in both forms, crystalline and amorphous;
- The chemical composition revealed the presence of metals (Cu, Zn and Fe) from EDM wire and steel working pieces, with the chemical composition varying with the shape of the particles;
- The average zeta potential, which features the NPs surface in water, is -26.60 mV, being characteristic of instable particles that tend to agglomerate/aggregate;
- The preliminary results of *in vitro* studies performed to nanotoxicity assessment, demonstrated an increase of NO production for the highest concentration of NPs (3.5×10^7 particles/µL), related to pro-inflammatory responses.

Conclusions
& Future Work

The presence of unintended NPs in workplaces, which represent a potential risk for the health of humans, and the mechanisms to prevent the unnecessary exposure, were studied and addressed in this work. With this aim, nanoporous structures with the aptitude of efficiently filtering NPs, were produced and tested. Moreover, conventional industrial environments were assessed regarding the size distribution, total number and surface area of airborne NPs, which were then characterized according to the physicochemical characteristics and the potential toxic effect *in vitro*.

Nanoporous structures were produced by rf magnetron sputtering deposition of thin films onto porous (Anopore, AAO and Millipore) and bulk substrates (Cu and Si=standard), being used three different approaches:

- M – reducing the substrate pore size by depositing aluminum thin films;
- F1 – controlling sputtering conditions of aluminum thin films deposition, such as: deposition time, power density, deposition pressure, sputtering gases and rotation and tilt of the substrate;
- F2 – depositing YSZ and Sn with posterior removal of the sacrificial material (Sn).

Method M produced V-shaped columns with narrowed pore size by increasing deposition time, power density and keeping the substrate in static mode. Therefore, pores with minimal sizes of 58 nm in AnoT, 20 nm in AnoB, 37 nm in AAO and 458 nm in Millipore, were achieved. The deposition of the Al thin film onto porous substrates increased the surface area and the total pore volume, which are important characteristics for filtration applications. The AnoB_M_2.55_0_15_O led to the best results (410.89 m^2/g of surface area and 0.2600 cm^3/g of pore volume). Moreover, FIB 3D nanotomography proved the existence of open porosity from top to bottom allowing the air flow passage.

In the F1 approach, columns grow by oblique angle deposition resulting in pores with smaller sizes for lower substrate tilt and power density, shorter times of deposition and substrates in static mode. The deposition pressure and reactive sputtering do not seem to have any influence on the pore sizes. The smallest pore sizes achieved in different substrates were: 19 nm in AnoT, 25 nm in AAO and 357 nm in Millipore (15 nm in Si). Great values of surface area (AnoT_F1_2.55_85_60_O: 148.53 m^2/g and AnoT_F1_2.55_89_60_O: 285.14 m^2/g) and pore volume (AnoT_F1_2.55_85_60_O: 0.0880 cm^3/g and AnoT_F1_2.55_89_60_O: 0.1800 cm^3/g) were achieved by depositing the aluminum thin films onto AnoT. The open porosity was also observed in nanoporous structures produced by F1.

The production of nanoporous structures by F2 method was not possible. F2a originated YSZ thin films with surface Sn spheres, while F2b produced a thin film of YSZ+SnO_2. These conditions hindered the removal of sacrificial material (Sn) and thus the creation of porous structures.

Therefore, nanoporous structures were produced by methods M and F1, having pores smaller than 100 nm and allowing the filtration of NPs. However, not only the pore size, but also the surface area, pore volume and roughness play important roles in retention of NPs. Therefore, to achieve a better filtration performance, morphological characteristics of nanoporous structures must be a compromise between pore size, surface area, pore volume and roughness. By method M, AnoB_M_2.55_0_15_O revealed the smallest pores and the best porosimetry characteristics (BET surface area and pore volume). On the other hand, method F1 also produced nanosized pores, being selected AnoT_F1_2.55_85_60_O (pore size: 31 nm; surface area: 148.53 m^2/g; pore volume: 0.0880 cm^3/g; S_a: 15 nm and S_{RMS}: 19 nm) as one of the most promising nanoporous structures where open porosity, from top to bottom, was observed. Since AnoT_F1_2.55_85_60_O has a higher number of open pores than AnoB_M_2.55_0_15_O, the first was elected the filter with the best properties and thus was assessed regarding the filtration efficiency.

The filtration solution developed in this thesis presents advantages in relation to commercially available filters, which have mainly submicrometric sized pores. Commercial filters capture particles by impaction, interception and diffusion, while here is proposed an approach of filtering only by interception, which means that the particles crossing the filter are restricted to those with sizes smaller than the pores. This ultimately may represent a greater filtration performance of produced filters compared to the commercial ones. Moreover, commercial solutions having smaller pores hinder the passage of air due to the high ratio thickness/pore size. This issue can be overcome by having a microporous substrate coated with a nanoporous thin film.

The developed filters with nanoporosity can be applied in conventional industrial environments, where there is the release of unintended airborne NPs, in air filtration systems to protect workers health and environment. With this purpose, conventional industrial activities were investigated, regarding the particle size distribution, total

number and surface area of airborne particles released unintentionally from the conventional industrial processes. Industrial activities such as, AB, LB and LP in the industry of aluminum surface treatments, wire and sinker EDM and laser machining in the industry of subtractive manufacturing, were monitored for 24 hours. Moreover, daily life activities were also evaluated.

As expected, the outcomes revealed that conventional industrial processes emit unintended NPs, with an increased number of particles being detected during industrial activities and at downtime without industrial activities, the number of airborne NPs being lower.

The smallest particles were released during AB (industry of aluminum surface treatments) and wire EDM (industry of subtractive manufacturing), while the greatest number of particles were emitted during LB (industry of aluminum surface treatments) and wire EDM (industry of subtractive manufacturing). Moreover, the great total number of particles during the 8 hours of working represents a high workers exposure, with PCR values being greater than 1 in sinker EDM in Workplaces E and G.

The efficiency of nanoporous structures of aluminum produced by F1 (AnoT_F1_2.55_85_60_O) was tested during the emission of NPs from the wire EDM (the conventional industrial process that releases the greatest number of NPs with the smallest average size), being achieved the impressive maximum retention of about 95% of particles for 90 nm, despite particles smaller than 20 nm not being filtered.

The assessment of a combination of NPs in real occupational environments and the use of number and surface –based metrics to characterize airborne NPs are the major strengths in regards to the state of the art. However, although the promising results achieved, this study presented some limitations. Equipment limitations hindered the distinction between agglomerates/aggregates and single NPs and the correlation between number of particles (SMPS) and surface area (NSAM) were poor.

In the same occupational environment where filtration performance of nanoporous structures were tested (wire EDM in Workplace G), airborne NPs were collected in TEM grids to 5 S's (Size, Size distribution, Shape, Structure and Surface) characterization and assessment of *in vitro* toxicity.

The average size of particles determined by TEM was 27 nm, by SMPS was 23 nm and by DLS was 349 nm, suggesting that particles tend to agglomerate/aggregate as corroborated by the zeta potential of surface (-26.60 mV) which is characteristic of instable particles. Particles with spherical and irregular shapes, crystalline and amorphous, were detected. The results of SEM-EDS analysis revealed the presence of Cu and Zn from the brass wire and Fe from the steel working piece.

Therefore, it is demonstrated the presence of NPs with Cu and Zn in their chemical composition, which in literature are reported to be those exhibiting higher toxicity effects *in vitro* and *in vivo*.

Preliminary *in vitro* studies were then performed in order to determine the cellular viability and the production of nitric oxide, which is related to pro-inflammatory responses. Although the results must be careful analyzed since few samples were assayed, the preliminary results showed an increase in the nitric oxide production of around 25% (for the highest concentration of NPs) and no effects in the cellular viability. These outcomes suggest that unintended NPs emitted from wire EDM, a conventional industrial process, may represent a risk for the health of workers, and thus need to be further studied.

The *in vitro* studies carried out in this work are in line with the recent trend of abolishing animal testing and additionally *in vitro* results are considered reliable, contributing with relevant insights to the toxicity predictive computational models (*in silico*).

This work has involved the *in vitro* assessment of toxicity of NPs with different sizes, shapes, chemical compositions and structures, contributed to more realistic results than those usually found on recent R&D works that are mainly focused in particles with specific characteristics.

Notwithstanding all the promising results achieved, further intensive research should be pursued. As future work some tasks are suggested:

- The filtration efficiency of nanoporous structures, produced by sputtering aluminum onto porous substrates by method F1, was conducted by introducing the filter in the inlet tube of SMPS and analyzing the size distribution of particles with and without the filter. This method present some limitations, since the size distribution of particles is not regular over time which implies that a different size distribution profile can be related to the filtration by nanoporous structures, or simply because the number of emitted particles has changed. Moreover placing a filter in the inlet tube, reduces the air flow forcing the equipment to increase the air suction. Therefore, the filtration of nanoporous structures developed in this thesis should be assessed using a system that releases a known and regular concentration of NPs, coupled with a detector that maintains a uniform inlet flux over time;

- Regarding the workers exposure in occupational environments, personal monitoring must be performed with proper equipment that is carried by the workers for the 8 hours of working. This will allow to monitor the personal exposure, as a complement of area monitoring stated in this thesis;

- Although the number and surface –based metrics are the most appropriated in characterizing NPs, the majority of the studies in the field only considers the mass. Consequently, the outcomes attained in this work cannot be compared with other works. Then, to determine the mass of NPs would be essential as a complement of 5 S's characterization;

- *In vitro* results were preliminary, considering that only two samples were assessed. Thus, it is of paramount importance to evaluate the toxicity of NPs in more samples and in different concentrations to infer the real toxic effects.

- The development of nanotoxicological predictive models, by means of computational intelligent algorithms, is an important step towards a reliable and scalable tool to provide information on nanotoxicity. Nevertheless, contributions on physicochemical characterization and *in vitro* toxicity of NPs are necessary to implement predictive models.

As a final conclusion, the nanoporous structures produced by sputtering showed to efficiently filtrate NPs and conventional industrial processes are indeed sources of unintended NPs being these NPs potentially harmful for the human health and environment. The outcomes of this thesis are an important contribute to establish definitive exposure limits and to provide significant insights in nanotoxicological predictive models.

References

[1] European Commission, "Types and uses of nanomaterials, including safety aspects," SWD (2012) 218 final, Brussels, 2012.

[2] V. H. Grassian, Nanoscience and Nanotechnology: Environmental and Health Impacts, John Wiley & Sons, 2008.

[3] S. Kaluza, B. Honnert, E. Jankowska and et al., "Workplace exposure to nanoparticles," European Agency for Safety and Health at Work (EU-OSHA), 2009.

[4] S. Bastian, W. Busch, D. Kühnel and et al., "Toxicity of Tungsten Carbide and Cobalt-Doped Tungsten Carbide Nanoparticles in Mammalian Cells in Vitro," *Environmental Health Perspectives,* vol. 117, no. 4, pp. 530-536, 2009.

[5] E. V. Esquivel and L. E. Murr, "A TEM analysis of nanoparticulates in a Polar ice core," *Material Characterization,* vol. 52, no. 1, pp. 15-25, 2004.

[6] ISO/TS 80004-2:2015, "Nanotechnologies - Vocabulary - Part 2: Nano-objects," 2015.

[7] SCENIHR, "The Scientific Aspects of the Existing and Proposed Definitions Relating to Products of Nanoscience and Nanotechnologies," 2007.

[8] SCCP, "Safety of Nanomaterials in Cosmetic Products," 2007.

[9] IUPAC, "IUPAC glossary," [Online]. Available: https://sis.nlm.nih.gov/enviro/iupacglossary/glossaryn.html. [Accessed 01 03 2016].

[10] G. Oberdörster, "Pulmonary effects of inhaled ultrafine particles," *International Archives of Occupational and Environmental Health,* vol. 74, no. 1, pp. 1-8, 2000.

[11] G. Oberdörster, E. Oberdörster and J. Oberdörster, "Nanotoxicology: an emerging discipline evolving from studies of ultrafine particles," *Environmental Health Perspectives,* vol. 113, 2005.

[12] A. Maynard , P. Baron, M. Foley e et al., "Exposure to carbon nanotube material: aerosol release during the handling of unrefined single-walled carbon nanotube material," *Journal of Toxicology and Environmental Health, Part A,* vol. 67, n⁰ 1, pp. 87-107, 2004.

[13] J. Twist, "BBC news online science and technology staff," 28 July 2004. [Online]. Available: http://news.bbc.co.uk/2/hi/science/nature/3920685.stm. [Accessed 2 August 2013].

[14] ISO/TR 27628, "Workplace atmospheres - Ultrafine, nanoparticle and nano-structured aerosols - Inhalation exposure characterization and assessment," 2007.

[15] F. Morency, S. Hallé, L. Dufresne and C. Émond, "Evaluation of diffusion models for airborne nanoparticles transport and dispersion," *Transactions on Engineering Sciences,* vol. 59, pp. 111-120, 2008.

[16] C. Ostiguy, G. Lapointe, L. Ménard and et al., "Nanoparticles Actual Knowledge about Occupational Health and Safety Risks and Prevention Measures," IRSST, 2006.

[17] R. J. Aitken, K. S. Creely and C. L. Tran, "Nanoparticles: An occupational hygiene review," Institute of Occupational Medicine, Edinburgh, 2004.

[18] S. Friedlander, Smoke, Dust and Haze, 2nd ed., New York: John Wiley and Sons, 2000.

[19] G. Hidy, Aerosols: an industrial and environmental science, Academic Press, Inc., 1984.

[20] G. Olivares, C. Johanssona, J. Ström and H. Hansson, "The role of ambient temperature for particle number concentrations in a street canyon," *Atmospheric Environment,* vol. 41, p. 2145–2155, 2007.

[21] L. Morawska, Z. Ristovski, E. R. Jayaratne and et al., "Ambient nano and ultrafine particles from motor vehicle emissions: Characteristics, ambient processing and implications on human exposure," *Atmospheric Environment,* vol. 42, no. 35, pp. 8113-8138, 2008.

[22] M. Jamriskaa, L. Morawskaa and K. Mergersen, "The effect of temperature and humidity on size segregated traffic exhaust particle emissions," *Atmospheric Environment,* vol. 42, no. 10, pp. 2369-2382, 2008.

[23] S. Kim, S. Shen, C. Sioutas and et al., "Size Distribution and Diurnal and Seasonal Trends of Ultrafine Particles in Source and Receptor Sites of the Los Angeles Basin," *Journal of the Air & Waste Management Association,* vol. 52, pp. 297-307, 2002.

[24] S. Zhao, Y. Yu, D. Yin and J. He, "Meteorological dependence of particle number concentrations in an urban area of complex terrain, Northwestern China," *Atmospheric Research,* Vols. 164-165, pp. 304-317, 2015.

[25]   A. Hamed, H. Korhonen, S. Sihto and et al., "The role of relative humidity in continental new particle formation," *Journal of Geophysical Research,* vol. 116 (D3), 2011.

[26]   M. Maricq, N. Xu and R. Chase, "Measuring Particulate Mass Emissions with the Electrical Low Pressure Impactor," *Aerosol Science and Technology,* vol. 40, pp. 68-79, 2006.

[27]   M. Nabi, R. Brown, Z. Ristovski and J. Hustad, "A comparative study of the number and mass of fine particles emitted with diesel fuel and marine gas oil (MGO)," *Atmospheric Environment,* vol. 57, pp. 22-28, 2012.

[28]   T. Seto, S. Kim, Y. Otani and et al., "New particle formation and growth associated with East-Asian long range transportation observed at Fukue Island, Japan in March 2012," *Atmospheric Environment,* vol. 74, pp. 29-36, 2013.

[29]   J. Byeon and J. Kim, "Particle emission from laser printers with different printing speeds," *Atmospheric Environment,* vol. 54, pp. 272-276, 2012.

[30]   L. H. Schmoll, T. M. Peters and P. T. O'Shaughnessy, "Use of a condensation particle counter and an optical particle counter to assess the number concentration of engineered nanoparticles," *Journal of occupational and environmental hygiene,* vol. 7, no. 9, pp. 535-545, 2010.

[31]   L. Cena and T. M. Peters, "Characterization and control of airborne particles emitted during production of epoxy/carbon nanotube nanocomposites," *Journal of occupational and environmental hygiene,* vol. 8, no. 2, pp. 86-92, 2011.

[32]   Y. Wang, P. Tsai, C. Chen and et al., "Size distributions and exposure concentrations of nanoparticles associated with the emissions of oil mists from fastener manufacturing processes," *Journal of hazardous materials,* vol. 198, pp. 182-187, 2011.

[33]   S. Derrough, G. Raffin, D. Locatelli and et al., "Behaviour of nanoparticles during high temperature treatment (Incineration type)," in *Journal of Physics: Conference Series,* 2013.

[34]   T. Klein, E. Buhr, K. Johnsen and C. Frase, "Traceable measurement of nanoparticle size using a scanning electron microscope in transmission mode (TSEM)," *Measurement Science and Technology,* vol. 22, no. 9, p. 094002, 2011.

[35]   M. Gini, C. Helmis and K. Eleftheriadis, "Cascade Epiphaniometer: An instrument for aerosol "Fuchs" surface area size distribution measurements," *Journal of Aerosol Science,* vol. 63, pp. 87-102, 2013.

[36] G. Buonanno, L. Morawska, L. Stabile and A. Viola, "Exposure to particle number, surface area and PM concentrations in pizzerias," *Atmospheric Environment,* vol. 44, no. 32, pp. 3963-3969, 2010.

[37] G. Oberdörster, "Toxicology of ultrafine particles: in vivo studies," *Philosophical Transactions of the Royal Society A,* vol. 358, pp. 2719-2740, 2000.

[38] European Comission, *The appropriateness of existing methodologies to assess the potential risks associated with engineered and adventitious products of nanotechnologies,* 2006.

[39] V. Gómez, S. Irusta, F. Balas and J. Santamaria, "Intense generation of respirable metal nanoparticles from a low-power soldering unit," *Journal of Hazardous Materials,* Vols. 256-257, pp. 84-89, 2013.

[40] J. F. Gomes, P. C. Albuquerque, R. M. Miranda and et al., "Comparison of deposited surface area of airborne ultrafine particles generated from two welding processes," *Inhalation Toxicology,* vol. 24, no. 11, pp. 774-781, 2012.

[41] A. Voliotis, S. Bezantakos, M. Giamarelou and et al., "Nanoparticle emissions from traditional pottery manufacturing," *Environmental Science: Processes & Impacts,* vol. 16, pp. 1489-1494, 2014.

[42] R. Chen, X. Shi, W. Rang and et al., "Airborne Nanoparticle Pollution in a Wire Electrical Discharge Machining Workshop and Potential Health Risks," *Aerosol and Air Quality Research,* vol. 15, pp. 284-294, 2015.

[43] L. Wallace and W. Ott, "Personal exposure to ultrafine particles," *Journal of Exposure Science and Environmental Epidemiology,* vol. 21, pp. 20-30, 2011.

[44] M. Bezek and J. Vaupotič, "The role of human activities on number concentration and size distribution of particles in indoor air".

[45] Q. Zhang, R. Gangupomu, D. Ramirez and Y. Zhu, "Measurement of Ultrafine Particles and Other Air Pollutants Emitted by Cooking Activities," *International Journal of Environmental Research and Public Health,* vol. 7, pp. 1744-1759, 2010.

[46] Safe Work Australia, "Nanoparticles from Printer Emissions in Workplace Environments," 2011.

[47] R. M. Healy, I. P. O'Connor, S. Hellebust and et al., "Characterisation of single particles from in-port ship emissions," *Atmospheric Environment,* vol. 43, no. 40, pp. 6408-6414, 2009.

[48] G. Buonanno, M. Bernabei, P. Avino and et al., "Occupational exposure to airborne particles and other pollutants in an aviation base," *Environmental Pollution,* vol. 170, pp. 78-87, 2012.

[49] G. A. Ban-Weiss, M. M. Lunden, T. W. Kirchstetter and R. A. Harley, "Size-resolved particle number and volume emission factors for on-road gasoline and diesel motor vehicles," *Journal of Aerosol Science,* vol. 41, no. 1, pp. 5-12, 2010.

[50] H. E. Burroughs and S. J. Hansen, Managing indoor air quality, 5 ed., The Fairmont Press, Inc., 2011, p. 359.

[51] ISO/TS 80004-4:2011, "Nanotechnologies — Vocabulary — Part 4: Nanostructured materials," 2011.

[52] S. L. Candelaria, Y. Shao, W. Zhou and et al., "Nanostructured carbon for energy storage and conversion," *Nano Energy,* vol. 1, no. 2, pp. 195-220, 2012.

[53] C. Yu, F. Jia, Z. Ai and L. Zhang, "Direct Oxidation of Methanol on Self-Supported Nanoporous Gold Film Electrodes with High Catalytic Activity and Stability," *Chemistry of Materials,* vol. 19, no. 25, pp. 6065-6067, 2007.

[54] K. Laatikainen, J. Pakarinen, M. Laatika and et al., "Preparation of silica-supported nanoporous manganese oxides," *Separation and Purification Technology,* vol. 75, no. 3, pp. 377-384, 2010.

[55] E. Gultepe, D. Nagesha, S. Sridhar and M. Amiji, "Nanoporous inorganic membranes or coatings for sustained drug delivery in implantable devices," *Advanced Drug Delivery Reviews,* vol. 62, no. 3, pp. 305-315, 2010.

[56] T. Waitz, B. Becker, T. Wagner and et al., "Ordered nanoporous SnO2 gas sensors with high thermal stability," *Sensors and Actuators B: Chemical,* vol. 150, no. 2, pp. 788-793, 2010.

[57] P. Shao and R. Y. M. Huang, "Polymeric membrane pervaporation," *Journal of Membrane Science,* vol. 287, pp. 162-179, 2007.

[58] P. Gibson, H. Schreuder-Gibson and D. Rivin, "Transport properties of porous membranes based on electrospun nanofibers," *Colloids and Surfaces A: Physicochemical and Engineering Aspects,* Vols. 187-188, pp. 469-481, 2001.

[59] J. Hayashi, H. Mizuta, M. Yamamoto and et al., "Pore size control of carbonized BPDA-pp' ODA polyimide membrane by chemical vapor deposition of carbon," *Journal of Membrane Science,* vol. 124, no. 2, pp. 243-251, 1997.

[60] S. Maphutha, K. Moothi, M. Meyyappan and S. E. Iyuke, "A carbon nanotube-infused polysulfone membrane with polyvinyl alcohol layer for treating oil-containing waste water," *Scientific Reports,* vol. 3, 2013.

[61] S. Kim and E. Marand, "High permeability nano-composite membranes based on mesoporous MCM-41 nanoparticles in a polysulfone matrix," *Microporous and Mesoporous Materials,* vol. 114, no. 1-3, pp. 129-136, 2008.

[62] T. C. Merkel, B. D. Freeman, R. J. Spontak and et al., "Ultrapermeable, Reverse-Selective Nanocomposite Membranes," *Science,* vol. 296, pp. 519-522, 2002.

[63] T. Sharma, Y. Hu, M. Stoller and et al., "Mesoporous silica as a membrane for ultra-thin implantable direct glucose fuel cells," *Lab on a chip,* vol. 11, pp. 2460-2465, 2011.

[64] H. Miyata, T. Noma, M. Watanabe and K. Kuroda, "Preparation of Mesoporous Silica Films with Fully Aligned Large Mesochannels Using Nonionic Surfactants," *Chemistry of materials,* vol. 14, pp. 766-772, 2002.

[65] J. M. Gomez-Vega, M. Iyoshi, K. Y. Kim and et al., "Spin casted mesoporous silica coatings for medical applications," *Thin Solid Films,* Vols. 398-399, pp. 615-620, 2001.

[66] K. Niesz, P. Yang and G. A. Somorjai, "Sol-gel synthesis of ordered mesoporous alumina," *Chemical Communications,* pp. 1986-1987, 2005.

[67] M. M. Yusuf, H. Imai and H. Hirashima, "Preparation of Porous Titania Film by Modified Sol-Gel Method and its Application to Photocatalyst," *Journal of Sol-Gel Science and Technology,* vol. 25, no. 1, pp. 65-74, 2002.

[68] G. Q. Lu and G. X. S. Zhao, Nanoporous Materials: Science and Engineering, vol. 4 on Series of Chemical Engineering, Imperial College Press, 2004.

[69] J. L. Plawsky, J. K. Kim and E. F. Schubert, "Engineered nanoporous and nanostructured films," *Materials today,* vol. 12, pp. 36-45, 2009.

[70] V. V. Guliants, M. A. Carreon and Y. S. Lin, "Ordered mesoporous and macroporous inorganic films and membranes," *Journal of Membrane Science,* vol. 235, pp. 53-72, 2004.

[71] F. Keller, M. S. Hunter and D. L. Robinson, "Structural Features of Oxide Coatings on Aluminum," *Journal of the Electrochemical Society,* vol. 100, no. 9, pp. 411-419, 1953.

[72] H. Masuda and K. Fukuda, "Ordered Metal Nanohole Arrays Made by a Two-Step Replication of Honeycomb Structures of Anodic Alumina," *Science,* vol. 268, pp. 1466-1468, 1995.

[73] G. D. Sulka, "Highly Ordered Anodic Porous Alumina Formation by Self-Organized Anodizing," in *Nanostructured Materials in Electrochemistry,* Wiley-VCH Verlag GmbH & Co. KGaA, 2008, pp. 1-116.

[74] M. Kushwaha, "A comparative Study of Different Electrolytes for Obtaining Thick and Well-ordered nano-porous Anodic Aluminium Oxide (AAO) Films," *Procedia Materials Science,* vol. 5, pp. 1266-1273, 2014.

[75] S. Ono and N. Masuko, "Evaluation of pore diameter of anodic porous films formed on aluminum," *Surface and Coatings Technology,* Vols. 169-170, pp. 139-142, 2003.

[76] A. Jagminienė, G. Valinčius, A. Riaukaitė and A. Jagminas, "The influence of the alumina barrier-layer thickness on the subsequent AC growth of copper nanowires," *Journal of Crystal Growth,* vol. 274, no. 3-4, pp. 622-631, 2005.

[77] N.-Q. Zhao, X.-X. Jiang, C.-S. Shi and et al., "Effects of anodizing conditions on anodic alumina structure," *Journal of Materials Science,* vol. 42, no. 11, pp. 3878-3882, 2007.

[78] Y. Zhao, M. Chen, Y. Zhang and et al., "A facile approach to formation of through-hole porous anodic aluminum oxide film," *Materials Letters,* vol. 59, no. 1, pp. 40-43, 2005.

[79] T. Masuda, H. Asoh , S. Haraguchi and S. Ono , "Fabrication and Characterization of Single Phase α-Alumina Membranes with Tunable Pore Diameters," *Materials,* vol. 8, pp. 1350-1368, 2015.

[80] H. Föll, "Electronic Materials - Script," Kiel University, [Online]. Available: http://www.tf.uni-kiel.de/matwis/amat/elmat_en/index.html. [Accessed 14 March 2016].

[81] P. L. Johnson and D. Teeters, "Fabrication of nanobaskets by sputter deposition on porous substrates and uses thereof". United States of America Patent US 7736724 B1, 15 June 2010.

[82] R. W. Davis, M. Ronaghi and A. Talasaz, "Array-based bioactivated nanopore devices". Patent US20120142016 A1, 12 June 2012.

[83] H. Xu and A. Goedel, "Preparation of ultrathin free-standing porous metal films," *Small,* vol. 1, pp. 808-812, 2005.

[84] F. Chen and A. H. Kitai, "Growth of nanoporous silicon dioxide thin films using porous alumina substrates," *Thin Solid Films,* vol. 517, pp. 622-625, 2008.

[85] P. -S. Cheow, E. Ting, M. Tan and C. -S. Toh, "Transport and separation of proteins across platinum-coated nanoporous alumina membranes," *Electrochimica Acta,* vol. 53, pp. 4669-4673, 2008.

[86] C. Morant, F. Márquez, T. Campo and et al., "Niobium and hafnium grown on porous membranes," *Thin Solid Films,* vol. 518, pp. 6799-6803, 2010.

[87] Z. Yao, C. Wang, Y. Li and N. -Y. Kim, "AAO-assisted synthesis of highly ordered, large-scale TiO2 nanowire arrays via sputtering and atomic layer deposition," *Nanoscale Research Letters,* vol. 10, p. 166, 2015.

[88] C. -C. Lai, C. -J. Chang, Y. -S. Huang and et al., "Desalination of saline water by nanochannel arrays through manipulation of electrical double layer," *Nano Energy,* vol. 12, pp. 394-400, 2015.

[89] M. M. Hawkeye, M. T. Taschuk and M. J. Brett, Glancing Alngle Deposition of Thin Films, John Wiley & Sons, Ltd, 2014.

[90] Z. Michalcik, M. Horakova, P. Spatenka and et al., "Photocatalytic Activity of Nanostructured Titanium Dioxide Thin Films," *International Journal of Photoenergy,* vol. 2012, pp. 1-8, 2012.

[91] A. Flanagan, R. Herrmann, K. Merdan e et al., "Medical devices for releasing therapeutic agent and methods of making the same". United States of America Patente US20090123517 A1, 14 May 2009.

[92] A. Trajkovska-Broach, Y. Sun, W. Kokonaski, P. P. Monticone and N. Schneeberg, "Electrochromic films and related methods thereof". Patent US 20150027613 A1, 29 January 2015.

[93] B. Zhang, Y. Yu, Z. Wang and J. Zhang, "Structure evolution from nanocolumns to nanoporous of nitrogen doped amorphous carbon films deposited by magnetron sputtering," *Applied Surface Science,* vol. 256, pp. 6506-6511, 2010.

[94] V. -H. Pham, T. -S. Jang, H. -D. Jung, H. -E. Kim and Y. -H. Koh, "Creation of nanoporous tantalum (Ta)-incorporated titanium (Ti) surface onto Ti implants by sputtering of Ta in Ar under extremely high negative substrate biases," *Journal of Materials Chemistry,* vol. 22, pp. 24798-24804, 2012.

[95] D. Choi, Y. Han, B. Lee and et al., "Use of a Columnar Metal Thin Film as a Nanosieve with Sub-10 nm Pores," *Advanced Materials,* vol. 24, pp. 4408-4413, 2012.

[96] C. M. Zhou and D. Gall, "Development of two-level porosity during glancing angle deposition," *Journal of Applied Physics,* vol. 103, p. 14307, 2008.

[97] D. Choi, B. Lee and H. Yang, "Simple Fabrication of Microfluidic Channel with Nanoporous formed by Conventional Physical Vapor Deposition," in *Proceedings of 10th IEEE International Conference on Nanotechnology,* Korea, 2010.

[98] D. Deniz and R. J. Lad, "Temperature threshold for nanorod structuring of metal and oxide films grown by glancing angle deposition," *Journal of Vacuum Science & Technology A,* vol. 29, p. 011020, 2011.

[99] Y. Liu, J. Liu, S. Sohn and et al., "Metallic glass nanostructures of tunable shape and composition," *nature communications,* vol. 6, 2015.

[100] M. Tai, A. Gentle , K. Silva and et al., "Thermal Stability of Nanoporous Raney Gold Catalyst," *Metals,* vol. 5, no. 3, pp. 1197-1211, 2015.

[101] P. D. Swartzentruber, *Microstructure and work function of dispenser cathode coatings: effects on thermoionic emission,* University of Kentucky: PhD thesis, 2014.

[102] J. Spradlin, W. -K. Lye, M. Reed and M. Hudson, "Nanoporous layers using thermal dealloying". Unites States of America Patent US20060193889 A1, 31 August 2006.

[103] K. Fukutani, K. Tanji, T. Saito and T. Den, "Phase-separated Al-Si thin films," *Journal of Applied Physics,* vol. 98, pp. 033507-1 - 033507-7, 2005.

[104] X. Lu, T. J. Balk, R. Spolenak and E. Arzt, "Dealloying of Au-Ag thin films with a composition gradient: Influence on morphology of nanoporous Au," *Thin Solid Films,* vol. 515, pp. 7122-7126, 2007.

[105] W. -C. Li and T. J. Balk, "Achieving finer pores and ligaments in nanoporous palladium-nickel thin films," *Scripta Material,* vol. 62, pp. 167-169, 2010.

[106] C. Nahm, H. Choi, J. Kim and et al., "A simple template-free 'sputtering deposition and selective etching' process for nanoporous thin films and its application to dye-sensitized solar cells," *Nanotechnology,* vol. 24, p. 365604, 2013.

[107] R. Kraehnert, E. Ortel, B. Paul and et al., "Electrochemically dealloyed platinum with hierarchical pore structure as highly active catalytic coating," *Catalysis Science & Technology,* vol. 5, pp. 206-216, 2015.

[108] C. Buzea, I. I. Pacheco and K. Robbie, "Nanomaterials and nanoparticles: Sources and toxicity," *Biointerphases,* vol. 2, no. 4, pp. 17-71, 2007.

[109] P. H. M. Hoet, I. Brüske-Hohlfeld and O. V. Salata, "Nanoparticles – known and unknown health risks," *Journal of Nanobiotechnology,* vol. 2, no. 12, 2004.

[110] S. Takenaka, E. Karg, C. Roth and et al., "Pulmonary and Systemic Distribution of Inhaled Ultrafine Silver Particles in Rats," *Environmental Health Perspectives,* vol. 109, no. 4, pp. 547-551, 2001.

[111] C. S. Yah, G. Simate and E. Iyuke, "REVIEW Nanoparticles toxicity and their routes of exposure," *Pakistan Journal of Pharmaceutical Sciences,* vol. 25, no. 2, pp. 477-491, 2012.

[112] J. V. Georgieva, D. Kalicharan, P. Couraud and et al., "Surface Characteristics of Nanoparticles Determine Their Intracellular Fate in and Processing by Human Blood–Brain Barrier Endothelial Cells In Vitro," *Molecular Therapy,* vol. 19, no. 2, pp. 318-325, 2011.

[113] R. Asmatulu, Nanotechnology Safety, Elsevier, 2013.

[114] H. S. Sharm and A. Sharm, "Neurotoxicity of Engineered Nanoparticles from Metals," *CNS & Neurological Disorders - Drug Targets,* vol. 11, pp. 65-80, 2010.

[115] A. Peters, B. Veronesi, L. Calderón-Garcidueñas and et al., "Translocation and potential neurological effects of fine and ultrafine particles a critical update," *Particle and Fibre Toxicology,* vol. 3, pp. 1-13, 2006.

[116] A. Nemmar, M. F. Hoylaerts, H. M. Hoet and et al., "Ultrafine Particles Affect Experimental Thrombosis in an In Vivo Hamster Model," *American Journal of Respiratory and Critical Care Medicine,* vol. 166, pp. 998-2002, 2002.

[117] M. Schulenburg, "Nanoparticles - small things, big effects opportunities and risks," Federal Ministry of Education and Research, Berlin, 2008.

[118] Y. Xie, T. R. Bagby, M. S. Cohen and M. L. Forrest, "Drug delivery to the lymphatic system: importance in future cancer diagnosis and therapies," *Expert Opinion on Drug Delivery,* vol. 6, no. 8, pp. 785-792, 2009.

[119] J. F. Hillyer and R. M. Albrecht, "Gastrointestinal Persorption and Tissue Distribution of Differently Sized Colloidal Gold Nanoparticles," *Journal of Pharmaceutical Sciences,* vol. 90, no. 12, pp. 1927-1936, 2001.

[120] C. S. J. Campbell, L. R. Contreras-Rojas, M. B. Delgado-Charro and R. H. Guy, "Objective assessment of nanoparticle disposition in mammalian skin after topical exposure," *Journal of Controlled Release,* vol. 162, no. 1, pp. 201-207, 2012.

[121] J. Z. Rappoport, J. Preece and K. Chipman, "How do manufactured nanoparticles enter cells?," 2011. [Online]. Available: http://www.maths-in-medicine.org/uk/2011/nanoparticles/description.pdf.

[122] D. Ramakrishna and R. Pragna, "Nanoparticles: is toxicity a concern?," [Online]. Available: http://www.ifcc.org/media/110324/01%20Nanoparticle%20-%20Is%20Toxicity%20a%20concern.pdf. [Accessed 25 August 2013].

[123] M. Chidambaram and K. Krishnasamy, "Nanotoxicology: Toxicity of engineered nanoparticles and approaches to produce safer nanotherapeutics," *International Journal of Pharma Sciences,* vol. 2, no. 4, pp. 117-122, 2012.

[124] M. Park, *Nanotoxicology – an in vitro approach (PhD thesis),* Vleuten, 2012.

[125] M. R. Wilson, J. H. Lightbody, K. Donaldson and et al., "Interactions between Ultrafine Particles and Transition Metals in Vivo and in Vitro," *Toxicology and Applied Pharmacology,* vol. 184, pp. 172-179, 2002.

[126] C. M. Sayes, R. Wahi, P. A. Kurian and et al., "Correlating nanoscale titania structure with toxicity: a cytotoxicity and inflammatory response study with

human dermal fibroblasts and human lung epithelial cells," *Toxicological Sciences,* vol. 92, no. 1, pp. 174-185, 2006.

[127] H. L. Karlsson, M. S. Toprak and B. Fadeel, "Toxicity of Metal and Metal Oxide Nanoparticles," in *Handbook on the Toxicology of Metals,* Academic Press, 2015, pp. 75-112.

[128] S. Lanone, F. Rogerieux, J. Geys and et al., "Comparative toxicity of 24 manufactured nanoparticles in human alveolar epithelial and macrophage cell lines," *Particle and Fibre Toxicology,* vol. 6, no. 14, pp. 1-12, 2009.

[129] H. Zhang, Z. Ji, T. Xia and et al., "Use of Metal Oxide Nanoparticle Band Gap To Develop a Predictive Paradigm for Oxidative Stress and Acute Pulmonary Inflammation," *ACS Nano,* vol. 6, pp. 4349-4368, 2012.

[130] D. A. Winkler, E. Mombelli, A. Pietroiusti and et al., "Applying quantitative structure-activity relationship approaches to nanotoxicology: Current status and future potential," *Toxicology,* vol. 313, pp. 15-23, 2013.

[131] D. J. Paustenbach, "ILO Encyclopaedia of Occupational Health and Safety," 2011. [Online]. Available: http://www.ilo.org/oshenc/part-iv/occupational-hygiene/item/575-occupational-exposure-limits. [Accessed 14 August 2013].

[132] D. Dankovic, E. Kuempel and M. Wheeler, "An Approach to Risk Assessment for TiO2," *Inhalation Toxicology,* vol. 19, pp. 205-212, 2007.

[133] P. A. Schulte, V. Murashov, R. Zumwalde and et al., "Occupational exposure limits for nanomaterials: state of the art," *Journal of Nanoparticles Research,* vol. 12, pp. 1971-1987, 2010.

[134] Institute for Occupational Safety and Health of the German Social Accident Insurance (IFA), "Criteria for assessment of the effectiveness of protective measures," [Online]. Available: http://www.dguv.de/ifa/fachinfos/nanopartikel-am-arbeitsplatz/beurteilung-von-schutzmassnahmen/index-2.jsp. [Accessed 25 August 2016].

[135] Social and Economic Council (SER), "Provisional nano reference values for engineered nanomaterials," 2012. [Online]. Available: http://www.ser.nl/~/media/Files/Internet/Talen/Engels/2012/2012_01/2012_01.ashx.

[136] S. -H. Yoon, Membrane Bioreactor Processes: Principles and Applications, CRC Press, Taylor & Francis Group, 2015.

[137] M. Thommes, K. Kaneko, A. V. Neimark and et al., "Physisorption of gases, with special reference to the evaluation of surface area and pore size distribution (IUPAC Technical Report)," De Gruyter, 2015.

[138] J. -N. Sun, Y. Hu, W. E. Frieze, W. Chen and D. W. Gidley, "How Pore Size and Surface Roughness Affect Diffusion Barrier Continuity on Porous Low-k films," *Journal of The Electrochemical Society,* vol. 150, no. 5, pp. F97-F101, 2003.

[139] S. Thomas, S. H. Al-Harthi, R. V. Ramanujan and et al., "Surface evolution of amorphous nanocolumns of Fe–Ni grown by oblique angle deposition," *Applied Physics Letters* , vol. 94, no. 6, p. 063110, 2009.

[140] N. Panich and Y. Sun, "Effect of substrate rotation on structure, hardness and adhesion of magnetron sputtered TiB2 coating on high speed steel," *Thin Solid Films,* vol. 500, pp. 190-196, 2006.

[141] J. A. Thornton, "The microstructure of sputter deposited coatings," *Journal of Vacuum Science and Technology A,* vol. 4, pp. 3059-3065, 1986.

[142] M. T. Taschuk, K. M. Krause, J. J. Steele and M. A. Summers, "Growth scaling of metal oxide columnar thin films deposited by glancing angle depositions," *Journal of Vacuum Science & Technology B,* vol. 27, pp. 2106-2111, 2009.

[143] C. Buzea, G. Beydaghyan, C. Elliott and K. Robbie, "Control of power law scaling in the growth of silicon nanocolumn pseudo-regular arrays deposited by glancing angle deposition," *Nanotechnology,* vol. 16, pp. 1986-1992, 2005.

[144] A. Barranco, A. Borras, A. R. Gonzalez-Elipe and A. Palmero, "Perspectives on oblique angle deposition of thin films: From fundamentals to devices," *Progress in Materials Science,* vol. 76, pp. 59-153, 2016.

[145] Z. Lingzhi, H. Shejun, L. Weishan, L. Liming and H. Xianhua, "Lithium intercalation/de-intercalation behavior of a composite Sn/C thin film fabricated by magnetron sputtering," *Rare Metals,* vol. 27, no. 5, pp. 507-512, 2008.

[146] B. D. C. Bell, S. T. Murphy, P. A. Burr, R. W. Grimes and M. R. Wenman , "Accommodation of tin in tetragonal ZrO2," *Journal of Applied Physics,* vol. 117, p. 084901, 2015.

[147] ICRP, "Human respiratory tract model for radiological protection," *Annals of the ICRP,* vol. 24, pp. 1-3, 1994.

[148] M. Levin, O. Witschger, S. Bau and et al., "Can We Trust Real Time Measurements of Lung Deposited Surface Area Concentrations in Dust from Powder Nanomaterials?," *Aerosol and Air Quality Research,* vol. 16, pp. 1105-1117, 2016.

[149] W. A. Heitbrink, D. E. Evans, B. K. Ku and et al., "Relationships Among Particle Number, Surface Area, and Respirable Mass Concentrations in Automotive Engine MAnufacturing," *Journal of Occupational and Environmental Hygiene,* vol. 6, pp. 19-31, 2009.

[150] C. A. Davies, S. A. Rocks, M. C. O' Shaughnessy, D. Perrett and P. G. Winyard, "Analysis of Nitrite and Nitrate in the Study of Inflammation," in *Inflammation Protocols*, Humana Press, 2003, pp. 305-320.

[151] K. W. Powers, M. Palazuelos, B. M. Moudgil and S. M. Roberts, "Characterization of the size, shape, and state of dispersion of nanoparticles for toxicological studies," *Nanotoxicology,* vol. 1, no. 1, pp. 42-51, 2007.

[152] R. Chen, X. Shi and R. Bai, "Airborne Nanoparticle Pollution in a Wire Electrical Discharge Machining Workshop and Potential Health Risks," *Aerosol and Air Quality Research,* vol. 15, pp. 284-294, 2015.

[153] G. F. Nordberg, B. A. Fowler and M. Nordbe, Handbook on the Toxicology of Metals, 4th ed., vol. I, Academic Press, 2015.

[154] J. M. Troiano, L. L. Olenick and T. R. Kuech, "Direct Probes of 4 nm Diameter Gold Nanoparticles Interacting with Supported Lipid Bilayers," *Journal of Physical Chemistry C,* vol. 119, no. 1, pp. 534-546, 2015.

[155] R. Marsalek, "Particle size and Zeta Potential of ZnO," *APCBEE Procedia ,* vol. 9, pp. 13-17, 2014.

[156] R. Chen, X. Shi, Bai R. and et al., "Airborne Nanoparticle Pollution in a Wire Electrical Discharge Machining Workshop and Potential Health Risks," *Aerosol and Air Quality Research,* vol. 15, pp. 284-294, 2015.

[157] R. Dimper, H. Reichert, P. Raimondi and et al., *ESRF upgrade programme phase II (2015-2020) - technical design study,* Grenoble: ESRF, 2014.

| References

142

Appendix A
Synchrotron radiation

Nanotomography is a technique used to characterize at the nano level the entire internal structure of a certain material, through the penetration of waves, usually X-rays, in the structure to be studied.

When the beam crosses the material, it is attenuated by dispersion and absorption according to the Lambert-Beer law:

$$I = I_0 e^{-\mu x}$$ (Eq A. 1)

Where I_0 and I are the intensity of the incident beam and the emerging beam, respectively, µ is the attenuation coefficient and x the material thickness.

The mapping of the attenuation coefficients throughout the material allows its detailed 3D imaging, by the reconstruction of 2D sections.

Conventional tomography is performed using conventional X-ray sources, however in the case of nanotomography, which requires greater spatial resolution, X-ray synchrotron radiation presents major benefits. Synchrotron radiation, emitted from charged particles forced to circulate in storage rings, has much greater intensity of the beam and the smaller beam angular divergence.

In this work, nanoporous thin films were characterized by nanotomography, which was performed at nano-imaging beamline ID16-A of the ESRF.

This technique is based in 2 main steps:

- Signal acquisition (Figure A. 1)

The synchrotron X-ray beam comes across the rotating material and a charge-coupled device (CCD) (FReLoN camera) acquires photons from the attenuated beam. X-rays are converted into visible light and then projected onto the CCD.

- Computational processing

Image reconstruction is performed by converting the projections onto 2D images. Then, these images can be "stacked" creating a 3D image of the material.
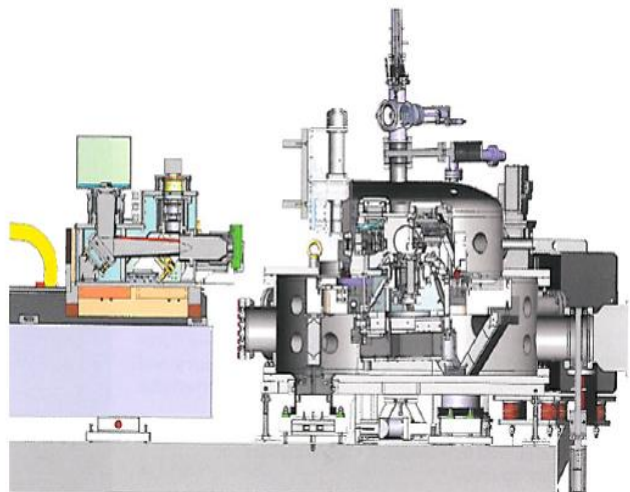
Figure A. 1 - ESRF ID16A nano-imaging beam line end-station [155].

Name and formula

Reference code:	01-077-0743
ICSD name:	Yttrium Zirconium Oxide
Empirical formula:	$O_{12}Y_4Zr_3$
Chemical formula:	$Y_4Zr_3O_{12}$

Crystallographic parameters

Crystal system:	Rhombohedral
Space group:	R-3
Space group number:	148
a (Å):	9,7380
b (Å):	9,7380
c (Å):	9,1150
Alpha (°):	90,0000
Beta (°):	90,0000
Gamma (°):	120,0000
Calculated density (g/cm^3):	5,46
Volume of cell (10^6 pm^3):	748,56
Z:	3,00
RIR:	7,77

Subfiles and Quality

Subfiles:	Inorganic
	Corrosion
	Modelled additional pattern
Quality:	Calculated (C)

Comments

ICSD collection code:	039484
Test from ICSD:	At least one TF missing.

References

Primary reference:	*Calculated from ICSD using POWD-12++*, (1997)
Structure:	Red'ko, V.P., Lopato, L.M., *Izv. Akad. Nauk SSSR, Neorg. Mater.*, **27**, 1905, (1991)

Peak list

| No.	h	k	l	d [A]	2Theta[deg]	I [%]
1	1	0	1	6,19025	14,297	0,1
2	1	1	0	4,86900	18,205	3,4
3	0	1	2	4,00948	22,153	2,8
4	0	2	1	3,82701	23,224	0,4
5	2	0	2	3,09513	28,822	0,6
6	0	0	3	3,03833	29,373	25,2
7	1	2	-1	3,00884	29,667	100,0
8	3	0	0	2,81112	31,807	0,3
9	2	1	-2	2,61205	34,303	27,8
10	1	1	-3	2,57764	34,776	1,0
11	2	2	0	2,43450	36,892	0,2
12	3	1	-1	2,26559	39,754	1,0
13	1	0	4	2,19986	40,994	0,7
14	1	3	-2	2,08094	43,452	1,4
15	3	0	3	2,06342	43,840	2,0
16	4	0	1	2,05411	44,049	1,1
17	0	2	4	2,00474	45,193	0,4
18	0	4	2	1,91351	47,476	0,2
19	2	2	-3	1,89986	47,839	0,2
20	2	3	-1	1,89258	48,034	0,5
21	1	2	-4	1,85376	49,106	26,1
22	1	4	0	1,84031	49,489	27,0
23	3	2	-2	1,78091	51,257	1,7
24	2	0	5	1,67332	54,818	0,2
25	0	5	1	1,65852	55,349	0,2
26	3	1	-4	1,63220	56,321	0,9
27	3	3	0	1,62300	56,669	0,3
28	2	1	-5	1,58247	58,257	12,5
29	1	4	-3	1,57408	58,598	14,7
30	4	2	-1	1,56994	58,767	16,8
31	4	0	4	1,54756	59,703	0,8
32	0	0	6	1,51917	60,935	1,8
33	2	4	-2	1,50442	61,598	4,9
34	1	5	-1	1,49419	62,066	0,6
35	2	3	-4	1,47486	62,972	0,1
36	1	1	-6	1,45022	64,168	0,3
37	5	1	-2	1,43737	64,811	1,0
38	3	3	-3	1,43156	65,107	0,3
39	6	0	0	1,40556	66,465	0,1
40	0	4	5	1,37899	67,918	0,1
41	3	4	-1	1,37067	68,387	0,1
42	0	5	4	1,35570	69,249	0,2
43	2	5	0	1,35042	69,558	0,3
44	3	0	6	1,33649	70,390	0,3
45	3	2	-5	1,32680	70,981	0,8
46	4	2	-4	1,30602	72,287	5,1
47	2	2	-6	1,28882	73,408	0,1
48	0	6	3	1,27567	74,291	0,3
49	1	6	1	1,27346	74,441	0,2
50	1	5	-4	1,26143	75,274	0,4
51	0	2	7	1,24417	76,505	0,2
52	1	6	-2	1,23774	76,975	0,3
53	5	2	-3	1,23402	77,250	0,9
54	4	4	0	1,21725	78,517	0,1
55	1	2	-7	1,20544	79,438	1,8
56	2	4	-5	1,19987	79,880	3,4
57	7	0	1	1,19438	80,322	5,1
58	3	4	-4	1,18444	81,136	0,1

146

```
59    4    1    -6    1,17156    82,219    3,3
60    0    7     2    1,16476    82,804    2,7
61    3    1    -7    1,13772    85,228    0,2
62    6    2    -2    1,13279    85,688    0,1
63    4    4     3    1,12994    85,956    0,4
64    6    1    -4    1,12001    86,906    0,1
65    1    7     0    1,11703    87,196    0,3
66    3    3    -6    1,10911    87,978    0,1
67    4    0     7    1,10788    88,101    0,2
68    4    3    -5    1,10355    88,537    0,2
69    2    0     8    1,09993    88,905    0,1
```

Stick Pattern
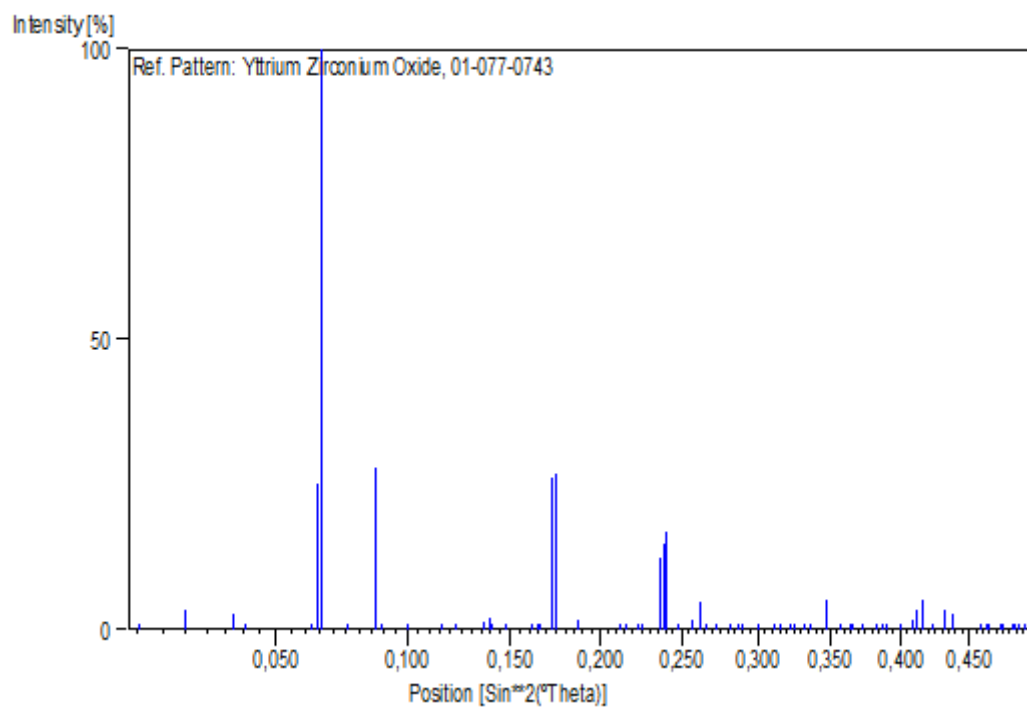
Name and formula

Reference code: 01-071-0652

Mineral name: Cassiterite
ICSD name: Tin Oxide

Empirical formula: O_2Sn
Chemical formula: SnO_2

Crystallographic parameters

Crystal system: Tetragonal
Space group: P42/mnm
Space group number: 136

a (Å):   4,7380
b (Å):   4,7380
c (Å):   3,1865
Alpha (°):   90,0000
Beta (°):   90,0000
Gamma (°):   90,0000

Calculated density (g/cm^3):   6,99
Volume of cell (10^6 pm^3):   71,53
Z: 2,00

RIR: 9,98

Subfiles and Quality

Subfiles: Inorganic
Mineral
Alloy, metal or intermetalic
Corrosion
Modelled additional pattern
Quality: Calculated (C)

Comments

ICSD collection code: 009163

References

Primary reference: *Calculated from ICSD using POWD-12++*, (1997)
Structure: Baur, W.H., Khan, A.A., *Acta Crystallogr., Sec. B*, **27**, 2133, (1971)

Peak list

No.	h	k	l	d [A]	2Theta[deg]	I [%]
1	1	1	0	3,35027	26,585	100,0
2	1	0	1	2,64414	33,874	75,6
3	2	0	0	2,36900	37,950	21,2
4	1	1	1	2,30892	38,977	3,5
5	2	1	0	2,11890	42,635	1,2
6	2	1	1	1,76442	51,771	56,4
7	2	2	0	1,67514	54,754	13,0
8	0	0	2	1,59325	57,825	6,4
9	3	1	0	1,49829	61,877	11,7
10	2	2	1	1,48274	62,599	0,2
11	1	1	2	1,43884	64,737	12,2
12	3	0	1	1,41506	65,962	15,2
13	3	1	1	1,35588	69,238	0,2
14	2	0	2	1,32207	71,274	6,0
15	2	1	2	1,27342	74,444	0,2
16	3	2	1	1,21484	78,703	9,0
17	4	0	0	1,18450	81,131	2,9
18	2	2	2	1,15446	83,709	6,1
19	4	1	0	1,14913	84,186	0,3
20	3	3	0	1,11676	87,223	2,8
21	3	1	2	1,09148	89,779	7,3

Stick Pattern